Investigating the use of novel fluorescent nanosensors to measure chemical changes in bacterial surroundings

Mark Perkins

Thesis submitted to the University of Nottingham for the degree of Doctor of Philosophy

January 2021

Abstract

The formation and persistence of microbial biofilms play an important role in infection and the biofouling of the environment. In order to eradicate these complex structures, further characterisation of the microniches that form within biofilms is vital. This study aimed to investigate whether fluorescent nanosensors could map pH and oxygen gradients in microbial biofilms.

Chapter One outlined the interaction of both neutral and cationic pH-sensitive, polyacrylamide nanosensors with the opportunistic pathogen *Pseudomonas aeruginosa*. When added to both planktonic cultures and biofilms, cationic pH-sensitive nanosensors co-localised with *P. aeruginosa* where they were likely interacting with extracellular components coating the bacterial cells. In a *P. aeruginosa* biofilm, this co-localisation led to thicker biofilm formation. Conversely, neutral pH-sensitive nanosensors became dispersed within a planktonic culture; whilst in a biofilm the neutral nanosensors formed distinct aggregation between the microcolonies.

Chapter Two showed the optimisation of oxygen-sensitive polyacrylamide nanosensor use with *P. aeruginosa*. During planktonic growth, *P. aeruginosa* produced the auto-fluorescent virulence factor, pyoverdine, which matched the fluorescence spectra used to detect platinum (II) porphyrin, the oxygen-sensitive fluorophore used to functionalise polyacrylamide nanoparticles. By using PAO1-NΔ*pvdD,* the oxygen-sensitive nanosensors were capable of measuring real-time oxygen consumption in planktonic culture. However, incorporation into a *P. aeruginosa* biofilm required further optimisation to prevent microcolony disruption.

Finally, Chapter Three used *Streptococcus mutans*, a predominant acid-producing oral bacteria, to determine whether the pH-sensitive nanosensors could detect pH changes induced by glucose treatment. Confocal laser scanning microscopy revealed that the addition of 1% w/v glucose to an established *S. mutans* biofilm, embedded with pH-sensitive nanosensors, resulted in a gradual reduction in the fluorescence intensity ratio during a 30 min period. This reduction in the fluorescence intensity ratio indicated a reduction in pH of the biofilm over time as the glucose was fermented.

These findings will help to improve technologies used to detect, measure, and map both pH and oxygen gradients in microbial biofilms in order to develop potential methods of biofilm treatment that either bypass or utilise these gradients.

Acknowledgements

For Mum. Made possible with the help of Lori, Dad, Sarah, Rachel, Birte, Dean, Kim and Jon.

Table of Contents

Abstract 2
Acknowledgements 4
1. Introduction 9
1.1. What is a biofilm 9
1.2. Environmental biofouling 10
1.2.1. Developing Anti-biofouling Materials 10
1.3. Biofilm formation and dispersal 14
1.4. Components of the biofilm matrix 16
1.5. Environmental factors for chemical gradients 18
1.6. Analysing environmental factors in microbial biofilms 20
1.6.1. *In vitro* biofilm systems 21
1.6.2. Tools for biofilm analysis 22
2. Aims and Objectives 25
3. Materials 26
3.1. Bacterial strains 26
3.2. Chemicals and Equipment 28
4. Methods 30
4.1. Nanosensor fabrication 30
4.1.1. Nanosensor fabrication with Rhodamine Red-X 31
4.1.2. Oxygen nanosensors fabrication 31
4.2. Characterisation of nanosensors 32
4.2.1. Zeta Potential and size 32
4.2.2. pH nanosensor calibration 33
4.2.3. Oxygen nanosensor calibration 34
4.3. Confocal Laser Scanning Microscopy (CLSM) and fluorescence microscopy systems 34
4.4. Super-Resolution imaging of nanosensors with PAO1-N WT 35
4.5. Growth assays 35
4.5.1. Toxicity of polyacrylamide nanosensors with PAO1-N WT 35
4.5.2. Toxicity of cationic polyacrylamide nanosensors with *S. mutans* strain NCTC 10449 36
4.5.3. Photostability of OG, FAM, TAMRA and Rhodamine Red-X 37
4.5.4. pH measurements over time 38
4.6. Oxygen consumption assays 39
4.6.1. Detecting auto-fluorescence in PAO1 strains 39

4.6.2. Measuring growth and auto-fluorescence in different bacterial species 39
4.6.3. Measuring growth and auto-fluorescence in *Pseudomonas* mutants .. 40
4.6.4. Testing different bacterial species with oxygen nanosensors 41
4.6.5. Measuring PAO1-NΔ*pvdD* growth and oxygen consumption with varying concentrations of potassium nitrate 42
4.7. *Streptococcus mutans* starvation assay 43
4.8. *Pseudomonas aeruginosa* static biofilm set-up 44
4.8.1. *P. aeruginosa* static biofilm set-up with pH nanosensors..... 44
4.8.2. Acetic acid challenge 44
4.8.3. *P. aeruginosa* static biofilm set-up with oxygen nanosensors 45
4.9. *S. mutans* Biofilm set-up with pH nanosensors 46
4.9.1. Examining sucrose supplementation in D282 and NCTC 10449 biofilm formation 46
4.9.2. Examining the addition of cationic polyacrylamide nanosensors to an established biofilm in comparison to incubation with the inoculum 48
4.9.3. Nanosensor responsiveness to pH challenge 48
4.9.4. Glucose challenge in *S. mutans* biofilm 49
4.10. Anti-biofouling polymer assays 50
4.10.1. OxoPlate and oxygen nanosensor microplate set-up 50
4.10.2. Crystal Violet assay 54
5. Characterisation of pH-sensitive, polyacrylamide nanosensors with *Pseudomonas aeruginosa* 55
5.1. Introduction 55
5.1.1. Potential effects of pH..... 55
5.1.2. Tools for pH calculations 58
5.2. Results 65
5.2.1. Neutral and cationic polyacrylamide nanosensors were manufactured to determine whether charge alters the interaction of bacteria with nanoparticles 65
5.2.2. Both fluorescence Spectrometer and TECAN plate reader accurately verified the pH-sensitivity of the polyacrylamide nanosensors 66
5.2.3. PAO1-N WT growth is unaffected by low concentrations of polyacrylamide nanosensors 70
5.2.4. Cationic polyacrylamide nanosensors interact and coat planktonic PAO1-N WT when incubated overnight 72
5.2.5. TAMRA and Rhodamine Red-X are not photo stable over an extended period 77

5.2.6. Extracellular pH decreases over time as PAO1-N WT metabolises available carbon sources 79

5.2.7. Generation of static biofilm models of PAO1-N WT with polyacrylamide nanosensors highlight their effects on the biofilm formation and their dispersal throughout the biofilm 82

5.2.8. Acetic acid treatment is readily detectable by embedded nanosensors in a PAO1-N WT biofilm..... 87

5.3. Discussion..... 89

6. Optimisation of oxygen-sensitive, polyacrylamide nanosensor manufacture and their use with *Pseudomonas aeruginosa* 98

6.1. Introduction 98

6.1.1. The role of oxygen in microbial biofilms 98

6.1.1.1. Oxygen availability and biofilm formation 98

6.1.1.2. Oxygen availability and bacterial signalling 100

6.1.2. Adaptation to oxygen stresses 101

6.1.3. Biogeography in biofilms 104

6.1.4. Potential effects of oxygen availability 105

6.1.5. Current tools for oxygen detection 108

6.2. Results 115

6.2.1. Determining the particle size and charge of the oxygen-sensitive polyacrylamide nanosensors 115

6.2.2. The quenching of fluorescence from platinum (II) porphyrin by oxygen is reversible 115

6.2.3. Auto-fluorescence at 650 nm is present in PAO1 strains 117

6.2.4. Increase in fluorescence at 650 nm only seen in *P. aeruginosa* 118

6.2.5. Pyoverdine appears to cause auto-fluorescence 120

6.2.6. Oxygen consumption varies drastically between bacterial species... 122

6.2.7. Oxygen consumption plateaus with increasing concentrations of potassium nitrate 126

6.2.8. Oxygen nanosensors disrupt PAO1-N microcolony formation in biofilms 128

6.2.9. Amphiphilic polymers significantly reduce bacterial attachment and biofilm formation 135

6.3. Discussion..... 149

7. Proof of Principle – Mapping pH changes in *Streptococcus mutans* biofilms using fluorescent, ratiometric, pH-sensitive polyacrylamide nanosensors 166

7.1. Introduction 166

7.1.1. The importance of chemical gradients in biofilms..... 166

7.1.2. Oral biofilms and *Streptococcus mutans* 167
7.1.3. Nanosensors in oral biofilm studies 172
7.2. Results 174
7.2.1. *S. mutans* growth is uninhibited by polyacrylamide nanosensors at low concentrations 174
7.2.2. The introduction of glucose and sucrose drastically reduces the pH of the medium when added to starved, planktonic *S. mutans* 176
7.2.3. Sucrose supplementation improves microcolony formation in a *S. mutans* biofilm 178
7.2.4. The addition of cationic, polyacrylamide nanosensors with the inoculum results in the formation of distinct structures within the biofilm 181
7.2.5. Cationic nanosensors show responsiveness to various pH solutions 183
7.2.6. The glucose challenge resulted in a significant reduction in fluorescence intensity when introduced to an *S. mutans* biofilm 185
7.3. Discussion 187
8. Conclusions and Future Work 197
8.1. Conclusions 197
8.2. Future Work 201
8.2.1. A biological system for oxygen nanosensors 202
8.2.2. Oral care and pH 205
9. References 208
10. Supplemental 225

1. Introduction

1.1. What is a biofilm

A common misconception of microbial living is that bacteria exist as individual organisms in a 'planktonic state'. Rather, microorganisms such as *Pseudomonas aeruginosa*, a Gram-negative rod-shaped bacterium, and *Streptococcus mutans*, a Gram-positive coccus bacterium, have been shown to naturally accumulate on a wide variety of surfaces; where they form sessile, sedentary communities (Geesey et al., 1977, Costerton et al., 1999). This accumulation of microorganisms of mono- or poly-microbial aggregates are commonly referred to as a biofilm (Flemming and Wingender, 2010). Biofilms have been defined as a population of adherent bacterial cells, to themselves and surfaces, that are enclosed by a matrix (Costerton, 1995). Since their initial discovery by Anton van Leuwenhoek in the 17th century (by studying his own dental plaque), biofilms have been an integral source of microbiological research, as biofilm-associated bacteria differ from their planktonic form both phenotypically and functionally, as seen when analysing gene transcription (Donlan, 2002).

The impact of expanding our understanding of complex microbial communities is wide ranging, as the formation and persistence of these communities has a profound effect in both medicine and the environment. As an example, *P. aeruginosa* can typically be found as biofilms in soils, coastal habitats, on plants and on animals (Stover et al., 2000). However, *P. aeruginosa* can also be found in the form of antimicrobial-resistant biofilms in the lung of cystic fibrosis (CF) patients (Moreau-Marquis et al., 2008). Once established, the *P. aeruginosa* biofilm can contribute to the pathophysiology of disease by secreting virulence factors and effector proteins to alter immune responses and cause cell injury or

death (Govan and Deretic, 1996, Driscoll et al., 2007). Another example of a microbial biofilm contributing to the pathophysiology of a disease is with *S. mutans,* a primary species of tooth decay, surviving as a biofilm in oral cavities such as tooth surfaces and dental materials (Klein et al., 2009, Waters et al., 2014). Microbes are also capable of forming biofilms on inanimate, manmade biomaterials devices; such as catheters, endocardial pacemakers, orthopaedic prostheses and intraocular lens, which can hinder the performance of the device as well as lead to the development of an infection (Bazaka et al., 2012, Passerini et al., 1992). The formation of undesirable biofilms on man-made, abiotic products is typically termed as biofouling (Kumar and Anand, 1998).

1.2. Environmental biofouling

Biofouling is not only limited to a medical setting; environmental biofouling can lead to contamination in the food and dairy industry, as well as the contamination of water systems such as drinking water reservoirs (Kumar and Anand, 1998) (Xu et al., 1998). Biofouling can be detrimental to systems reliant on the passage of water; for instance, biofouling can decrease the heat transfer in cooling towers and cause a general deterioration of materials in industrial or home water piping systems such as washing machines (Flemming, 2002, Donlan, 2002).

1.2.1. Developing Anti-biofouling Materials

An important aspect of the prevention of biofouling is the development of materials that can inhibit the attachment of microbes. A prime example of a material susceptible to biofouling are silicone catheters; as catheters are pervious to biofouling due to the material used (Polydimethylsiloxane – PDMS). Due to the

hydrophobicity of PDMS, bacterial attachment is improved (Fletcher and Loeb, 1979), which has led to research into coating catheters with anti-biofilm materials (Tyler et al., 2017) or the altering the topography of PDMS to inhibit attachment (Graham et al., 2013). Further work is required to expand the library of suitable, biocompatible, non-toxic materials that prevent biofouling in both catheter design as well as other susceptible systems such as washing machines (Munk et al., 2001, Gattlen et al., 2010).

Of particular interest is the development of polymers capable of coating surfaces to provide anti-biofouling properties. Some materials that have previously been used include Poly(2-ethyl-2-oxazoline) (PEOX), Poloaxmers, and Poly(ethylene glycol) (PEGs)-based polymers.

PEOX are hydrophilic polymer chains of varying lengths. Previous research by Roosjen et al. (2004) had shown that PEOX coatings reduced the adhesion of both bacteria and yeast in static conditions, whilst Tauhardt et al. (2014) showed, using a flow-cell system, that PEOX coatings had reduced the adhesion of five water-borne bacterial species with high potential to form biofilms; yet cell viability was largely unchanged.

Poloxamers are Poly(ethylene oxide)-block-poly(propylene oxide)-block-poly(ethylene oxide) (PEO-PPO-PEO) block copolymers where the end tail PEO regions are hydrophilic and the central PPO region is hydrophobic, creating an amphiphilic polymer. These amphiphilic copolymers have been demonstrated to prevent the attachment of bacteria. In particular, the Poloxamer, F127, has been shown to be effective in the prevention of bacterial attachment of *Escherichia coli* strain D21 to F127-coated, hydrophobic, *N*-octadecyltrichlorosilane (OTS)-pre-treated glass (Razatos et al., 2000); and the attachment of both

Staphylococcus epidermis and *Serratia marcescens* on F127-coated glass slides, pre-treated with polystyrene (Marsh et al., 2002). Another example of F127 used as an anti-biofouling material was by Nejadnik et al. (2008) who used F127 to coat silicone rubber. Both *Staphylococcus aureus* and *S. epidermis* attachment was significantly reduced, whilst *P. aeruginosa* attachment was unaffected. Other Poloxamers have been tested as an anti-biofouling material; Poloxamer 338 (P388) has been shown to reduce the adherence of two *E. coli* strains under both static and flow conditions when compared to uncoated silicone urinary catheter (two-way Foley catheter), whilst having no significant effect on planktonic growth (Stirpe et al., 2020).

Finally, Poly(ethylene glycol) (PEGs) can either form self-assembled monolayers (SAMs) or can be combined with PEGMA/GMA and LMA to create random copolymers. These random copolymers are amphiphilic, with the LMA monomer providing the hydrophobic group and the other two groups providing the hydrophilic groups. Similar to the PEO regions of the Poloxamer materials, the PEG region of these copolymers form a linear brush layer, whilst the PEGMA region forms a bottlebrush structure (**Figure *1.2.1-1***) (Cheng et al., 2005, Gunkel et al., 2011). The effect of PEG-based polymers preventing bacterial protein adsorption were first described by Prime and Whitesides (1991) whilst increased chain length as a preventative measure was described by Prime and Whitesides (1993).These PEG-based coatings have been demonstrated as suitable material for the prevention of bacterial attachment. For example, Harris et al. (2004) coated titanium surfaces with poly(L-lysine)-*grafted*-poly(ethylene glycol) (PLL-*g*-PEG) functionalised with peptides of the RGD (Arg-Asp-Gly) motif. These PLL-PEG-RGD coated surfaces reduced the attachment of *S. aureus* when compared to the uncoated titanium surface. Another example, by Ozcelik et al. (2017), showed

significant reduction in the attachment of *P. aeruginosa* and *S. aureus* to polystyrene coated with poly(ethylene glycol) diglycidyl ether (PEDGE) incorporated with the Quorum Sensing Inhibitor (QSI), 5-methylene-1-(prop-2-enoyl)-4-(2-fluorophenyl)-dihyropyrrol-2-one (DHP). The inhibition of Quorum Sensing (QS) is important, as it is a vital interbacterial communications mechanism responsible for the development and maturation of a biofilm (Sauer et al., 2002, Muras et al., 2020). Therefore, the action of this PEG-based polymer with a QSI incorporated can have a two-fold affect; the first is to prevent bacterial attachment, and the second is to inhibit biofilm formation.

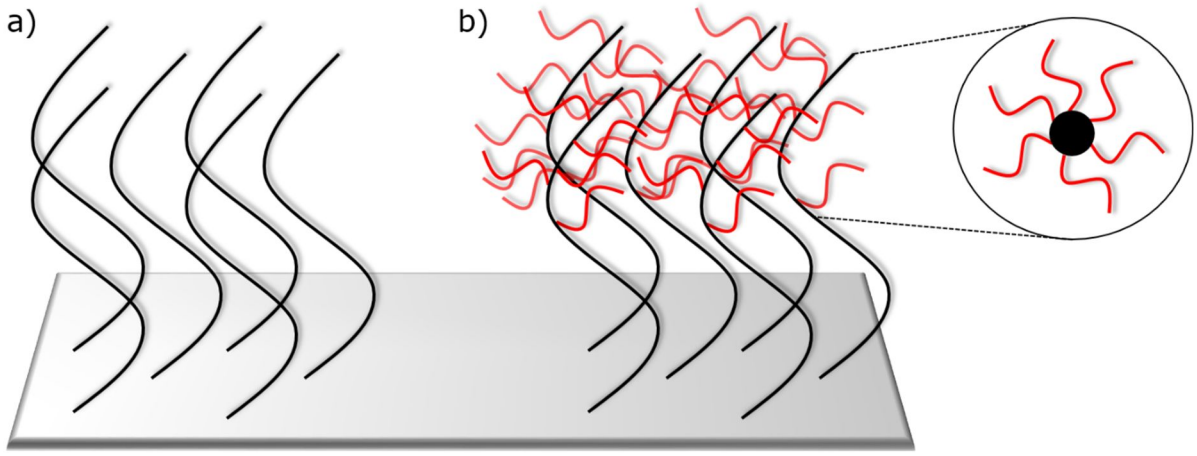

Figure 1.2.1-1: Schematic representation of linear PEG brushes (a) and PEGMA bottlebrushes with its 3D architecture (b) – adapted from (Maan et al., 2020)

1.3. Biofilm formation and dispersal

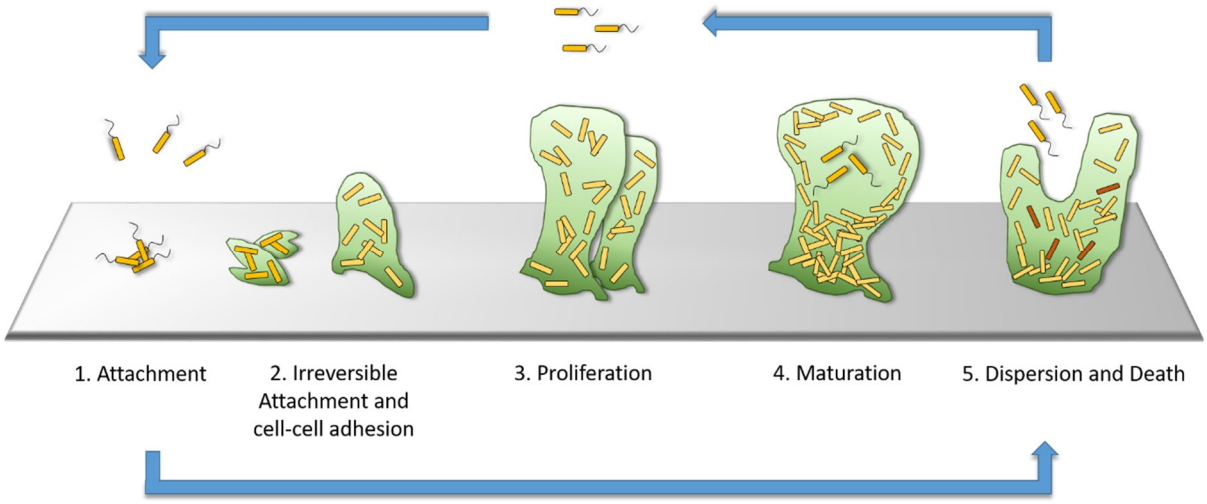

Figure 1.3-1: Biofilm establishment and the maturation process leading the dispersal – Stage 1, initial attachment; stage 2, irreversible attachment and cell-cell adhesion; stage 3, proliferation; stage 4, maturation; stage 5, dispersion and death (brown cells in image).

In order to improve the development of anti-biofouling materials, understanding how biofilm formation occurs is essential. **Figure *1.3-1*** represents the five stages involved in the formation of a biofilm, using *P. aeruginosa* as an example. The initial establishment of a *P. aeruginosa* biofilm begins with the attachment of planktonic cells to a surface, where they form a monolayer. Motility and the velocity of the suspending medium dictate whether bacteria adhere or attach to a surface. Non-motile bacteria adhere to surfaces at low and moderate velocities, whilst at higher velocities non-motile bacteria are transported away. For motile bacteria, attachment can occur at any fluid velocity (Tuson and Weibel, 2013). Attachment and early biofilm formation under flow are therefore often reliant on flagellar-based swimming, type IV pili and Cup fimbriae for *P. aeruginosa* (O'Toole and Kolter, 1998, Mikkelsen et al., 2011). Once the cell has made contact with the surface, proteins such as SadB are required for the transition from reversible to irreversible attachment (Caiazza and O'Toole, 2004). This irreversible attachment

then leads to microcolony formation by clonal growth and/or aggregation. Surface contact leads to changes in gene expression, with upregulation of factors favouring a sessile lifestyle, including components found within the extracellular matrix such as the exopolysaccharides Psl and Pel and the protein CdrA (Borlee et al., 2010, Kostakioti et al., 2013). A number of factors including type IV pili twitching and GacA, the response regulator for the GacS/GacA/RsmA system, are required for the formation of *P. aeruginosa* microcolonies (O'Toole et al., 2000, Parkins et al., 2001, Caiazza and O'Toole, 2004). Expression of GacA results in the upregulation of *rsmY* and *rsmZ,* which suppresses RsmA activity and allows *pel* and *psl* gene expression (Mikkelsen et al., 2011). These microcolonies can then transition to a mature antimicrobial-resistant population encased in extracellular polymeric substances, which can contribute to antimicrobial tolerance and protection from the immune system (Ramsey and Whiteley, 2004, Rybtke et al., 2015).

The formation of patterns within a biofilm can also enable survival and innate tolerance to adverse conditions. Nutrient availability and environmental cues can influence the pattern of biofilm formation (Parsek and Tolker-Nielsen, 2008); whilst the development of the distinct architecture in a mature biofilm can be attributed to cell-to-cell signalling via the *las* quorum-sensing system (Davies et al., 1998). Finally, cell death plays an important role in the continued differentiation and dispersion of subpopulations of a biofilm (Webb et al., 2003). Voids within microcolonies can form via cell lysis, which can contribute "public goods" such as cytosolic proteins and extracellular DNA (eDNA) to the surrounding biofilm (Turnbull et al., 2016); or, individual cells and aggregates can slough off from a mature biofilm where they are dispersed, in a planktonic state, to attach and establish another biofilm elsewhere (Rumbaugh and Sauer, 2020).

1.4. Components of the biofilm matrix

Complex multicellular biofilms consist of numerous microbial cells, which are embedded within a self-produced matrix containing extracellular polymeric substances, providing heterogeneity and creating multiple microenvironments (Sutherland, 2001). This self-produced matrix is referred to as the extracellular matrix (ECM). The ECM of a biofilm can provide physical stability and increased adhesion via the expression of exopolysaccharides (Ryder et al., 2007), whilst retaining secreted enzymes, cellular debris and genetic material (Flemming and Wingender, 2001). During periods of starvation, the ECM can even be degraded by their own producer bacteria or other microorganisms present (Zhang and Bishop, 2003). The ECM is also capable of conferring a significant increase in antimicrobial resistance, with a tolerance to antimicrobial treatments of up to 1000-fold more than planktonic cells (Flemming and Wingender, 2010). The resultant ECM is a dynamic system constructed by the organism in response to the local environment (Flemming and Wingender, 2001).

The structural composition of the ECM can vary depending upon the microbial species involved; for example, the ECM of *Bacillus subtilis* is more proteinaceous than *P. aeruginosa*, whilst *P. aeruginosa* is characterised by more carbohydrate components (Harimawan and Ting, 2016). However, the components that are invariably present within the ECM are exopolysaccharides, proteins, nucleic acids and lipids (Wei and Ma, 2013). Each component of the ECM has a different function, resulting in a spatially heterogeneous and diffusion-limiting matrix that can protect and secure the microbes within (Klein et al., 2015). As biofilms can be formed by multiple microbial species, including fungi, some biofilms are better characterised than others are. The following examples of ECM components are

focused on *P. aeruginosa*, with additional species-specific examples given where relevant.

P. aeruginosa produces exopolysaccharides (EPS) such as Psl, Pel, and alginate that provide stability via cell-to-cell and cell-to-surface interactions during the formation and survival of a biofilm (Colvin et al., 2012, Sharma et al., 2014). In mucoid strains of *P. aeruginosa*, the predominant EPS produced is alginate (Hentzer et al., 2001). These mucoid strains, typically isolated from CF patients, often over-express alginate which promotes cell attachment (Govan and Deretic, 1996, Orgad et al., 2011). In non-mucoid strains, both Psl and Pel are the principle EPS expressed (Wozniak et al., 2003). Psl is essential for biofilm formation in the *P. aeruginosa* strain PAO1 (Jackson et al., 2004) where it is required for the adherence to abiotic surfaces and other bacterial cells (Ryder et al., 2007). Psl also sequesters iron, which serves as a signal for biofilm formation and development (Yu et al., 2016). For the *P. aeruginosa* strain PA14, Pel is shown to be an essential component of the pellicle form of a biofilm, which forms at the air-liquid interface in a static culture (Friedman and Kolter, 2004). Each polysaccharide is important during the establishment of a biofilm; however, a redundancy between Psl and Pel when serving as structural scaffolds in mature biofilms has been shown (Colvin et al., 2012). This redundancy can protect against any possible mutation that could affect the expression of one of the exopolysaccharides.

There are also a range of proteins present in the ECM that have either been actively secreted or are present due to the lysis of bacteria within the biofilm (Turnbull et al., 2016). These proteins appear to have a key role in the assembly of the ECM (Klein et al., 2015). An example is the protein CdrA, which has been found in the matrix fraction of *P. aeruginosa* biofilms (Borlee et al., 2010). CdrA

has been shown to crosslink either Psl and/or tethers Pel to the bacterial cell wall, promoting stability of the biofilm. However, CdrA is not dependent on the presence of EPS, as it is capable of forming proteinaceous matrices in the absence of EPS (Reichhardt et al., 2018). Another example is the exoenzyme glucosyltransferase, secreted in *S. mutans.* Glucosyltransferase plays an important role in the accumulation of microorganisms on enamel surfaces via the *in situ* production of glucans. These glucans then present suitable binding regions for the oral microorganisms (Bowen and Koo, 2011).

Finally, eDNA has been shown to promote biofilm establishment and the stability of the biofilm (Das and Manefield, 2012). A novel mechanism of eDNA has been identified which shows the ability of eDNA to chelate Mg^{2+} within the biofilm. This creates a localised cation-limited environment, which in turn induces the expression of LPS-modification genes leading to the resistance to certain antimicrobials (Mulcahy et al., 2008) (Discussed in further detail later).

Altogether, the ECM creates a complex combination of extracellular polymeric substances which allow the embedded microorganisms to attach to both biotic and abiotic surfaces (Karatan and Watnick, 2009), protect itself from host immunity, such as oxidative stress (Wood, 2016), and to survive in oligotrophic conditions, occasionally supplied by a eutrophic environment (Kim and Lee, 2016).

1.5. Environmental factors for chemical gradients

As well as determining the general make-up of the ECM and the individual components present, an understanding of the formation of distinct and dynamic chemical environments within a biofilm is also required.

Donlan (2002) described biofilms as discrete microniches; which leads to the formation of various microenvironments within a single biofilm. For example, the formation of dynamic pH gradients to create physiological heterogeneity can be attributed to environmental factors such as the availability of nutrients (Allan et al., 1999) and their resultant metabolites (Hidalgo et al., 2009); whilst the physiological structure and distribution of cells and nutrients within a biofilm can create dynamic oxygen gradients (Xu et al., 1998). Through the use of a phosphate limited nutrient media, Allan et al. (1999) were able to show reduction in pH when comparing the biofilm with the bulk fluid; whilst the accumulation of metabolites such as tricarboxylic acids and CO_2 from the catabolism of carbon sources such as glucose can cause a decrease in pH (Hidalgo et al., 2009). Components of the ECM can also affect the pH of the biofilm; for example, eDNA can influence the acidification of *P. aeruginosa* in planktonic cultures and biofilms (Wilton et al., 2016). Lastly, using an oxygen microelectrode De Beer et al. (1994) were able to demonstrate the formation of vertical and horizontal voids formed in mature biofilms, where oxygen concentrations where higher than the surrounding anaerobic cell clusters.

Biofilms are typically formed by multiple species of bacteria (Elias and Banin, 2012). With multispecies biofilms, spatial distribution of bacterial species can result in various combinations of organisation. These combinations can either be separate mono-species microcolonies, co-aggregation, or distinct layers of each species (Nielsen et al., 2000, Elias and Banin, 2012). These combinations of possible spatial distributions are often a result of metabolite availability as well as the bacterial species present. For example; the first species may require a metabolite from the second species, leading to aggregation for access to the metabolite (Nielsen et al., 2000). Oxygen availability can also dictate the location

of different bacteria within a multispecies biofilm. For example, oral biofilms consist of a host of microbes, with a range of aerobic and anaerobic respiration. Biogeography studies have shown that distinct strata can form in *in vitro* oral biofilms, with aerobic bacteria forming towards the surface and anaerobic bacteria towards the bottom/centre (Welch et al., 2016).

It is therefore possible that different organisations of multiple species could lead to the formation of distinctly different microenvironments within a biofilm. These multiple species may then generate their own optimal microenvironment depending on organisation, availability of nutrients, and other species present, which may lead to either antagonism or synergism between the different species. All of which may create more well-defined regions of both pH and oxygen within a biofilm. A better understanding of these microenvironments would lead to the improvement of treatment methods to combat these distinct microbial biofilms.

1.6. Analysing environmental factors in microbial biofilms

In order improve our understanding of these microenvironments; research has been carried out to detect chemical gradients that can form in microbial biofilms. To continue on this research, two important aspects for the analysis of microbial biofilms must be considered. The first is the *in vitro* system used to produce a biofilm, and the second are the tools used to analyse the chemical composition of a microbial biofilm. Using an accurate and non-invasive technique to measure chemical gradients in a mature *in vitro* biofilm can lead to the development and production of treatment methods that can either use these unique microenvironments to their advantage; or, to bypass these microniches to eradicate the bacteria directly.

1.6.1. *In vitro* biofilm systems

As mentioned above, the first aspect for analysing chemical gradients within a microbial biofilm is choosing a suitable *in vitro* system to grow a mature biofilm. Current research into biofilm formation presents an issue when considering what system would be suitable to use. Glass bottomed chambers, multi-well plates, and coverslips have been used as surfaces for biofilm formation after a period of incubation (Hidalgo et al., 2009, Murphy et al., 2014, Ruhal et al., 2015, Wilton et al., 2016)**.** These systems allow access to the biofilm so that further analysis can be carried out. Examples include quantifying live and dead cells by real-time PCR (Alvarez et al., 2013, Kean et al., 2017), multiplex fluorescence *in situ* hybridisation (M-FISH) to monitor the 3D spatial distribution of multispecies biofilm (Karygianni et al., 2014, Welch et al., 2016), or spectroscopic techniques such as Time-of Flight Secondary Ion Mass Spectroscopy (ToF-SIMS) (Hua et al., 2015) and Raman spectroscopy (Bodelon et al., 2016). The use of these analytical techniques can provide greater detail of the composition and distribution of microbes and their biomolecules found within a biofilm (Masyuko et al., 2014). Glass bottomed chambers, multi-well plates, and coverslips also do not restrict the imaging process such as Confocal Laser Scanning Microscopy (CLSM) and Super-Resolution Microscopy as these surfaces are clear.

In order to mimic systems with a flow of nutrients and microbes that can contribute to infection or biofouling, flow chambers or cells are a common system that allows for the movement of media and bacteria (Klausen et al., 2003, Hunter and Beveridge, 2005, De Rienzo et al., 2016). These systems provide a constant flow of media and bacteria to mimic natural flow rates and can be imaged in order to visualise the biofilm. However, they can typically be sealed systems and so post-analytical techniques would be difficult to perform after incubation.

For determining changing chemical gradients, the current tools available such as glass bottomed chambers and single-channel flow cells are adequate for our goals.

1.6.2. Tools for biofilm analysis

The second aspect for analysing chemical gradients within a microbial biofilm is choosing a compatible tool that is suitable for the detection of chemical gradients. Research into the dynamic formation of ion gradients within bacterial biofilms, including pH and oxygen gradients; have been reported in previous studies, and will be discussed in further detail below. Whilst this research has been able to characterise potential chemical gradients, they have used procedures which are either intrusive, potentially interfering with the results, or lacking resolution required for accurate chemical readings. Particular techniques to study the ion gradients of biofilms include microelectrodes (Schachtele and Jensen, 1982, Lingstrom et al., 1993, De Beer et al., 1994) or microsensors (von Ohle et al., 2010, James et al., 2016). A limiting factor is that microsensors typically cannot provide horizontal pH gradients or spatial resolution in biofilms (Hidalgo et al., 2009). However, microsensors are typically inexpensive and have improved in size of tip diameter and spatial resolution in recent years (Revsbech, 2005, Billings et al., 2015).

One particular avenue of interest are nanoparticles. Research into the novel application of nanoparticles has increased in recent years, including as an alternative to common treatment methods for the removal of biofilms, such as antimicrobials/antibiotics. An emphasis on inorganic nanocomposites, including silver, gold and magnetic iron oxide nanoparticles, has seen increased antimicrobial effects. For example, a polylysine/silver nanoparticle composite has

been used as an effective antibacterial towards both *P. aeruginosa* and *S. aureus,* without toxicity to mammalian cells or the emergence of bacterial resistance over a 30 passage period (Dai et al., 2016). Similarly, mixed charged zwitterionic gold nanoparticles, coupled with near-infrared (NIR) light irradiation has been used to treat *S. aureus* biofilms through photothermal therapy (Hu et al., 2017). Finally, the antimicrobial, methicillin, has been encapsulated in multiple suparamagnetic iron oxide nanoparticles (SPIONs) to create iron oxide-encapsulating polymersomes (IOPs). These IOPs were shown to penetrate a *S. epidermis* biofilm in the presence of a neodymium magnet, leading to extensive cell death within the boundaries of the magnetic field (Geilich et al., 2017). Whilst this last example highlights the use of nanoparticles as a delivery system as well as possessing antibacterial properties, nanoparticles have also been used to coat surfaces to prevent initial biofouling. For instance, titanium discs coated with zinc nanoparticles alone and with zinc nanoparticles in an equal mix with hydroxyapatite (HA) were shown to significantly reduce the biofilm mass and thickness of aerobes, anaerobes and *Streptococcus spp.* when compared to uncoated titanium discs, albeit only after 96 h incubation (Abdulkareem et al., 2015).

Whereas these previous examples have used inorganic nanoparticles for either the treatment or prevention of biofilms, further work has used biopolymers as a means of encapsulation for the delivery of antimicrobials. For example, alginate has been used to encapsulate the antimicrobial, ciprofloxacin, whilst the QSI, 3-amino-7-chloro-2-nonylquinazo-lin-4(3*H*)-one (ACNQ), was attached, via a pH-responsive hydrazine linker, to the surface of the alginate nanoparticle (Singh et al., 2019). ACNQ was used to inhibit QS during biofilm formation, whilst ciprofloxacin was incorporated to treat mature *P. aeruginosa* biofilms.

Whilst research has developed into using nanoparticles as a treatment method, this thesis is interested in nanoparticles as an optical tool for the study of chemical gradients. Various analytes have been studied in recent years, such as ions; including lithium (Galyean et al., 2018) and potassium (Jewell et al., 2020a), as well as pH (Hidalgo et al., 2009, Fulaz et al., 2019) and oxygen (Jewell et al., 2019, Jewell et al., 2020b). These studies have used fluorescent-based nanosensors to detect changes in microbial biofilms and will be discussed in greater detail in the following work.

2. Aims and Objectives

The first aim of this thesis was to develop both neutral and cationic pH-sensitive, polyacrylamide nanosensors and to determine their interaction with *P. aeruginosa*. The objectives were, 1). Detect any possible inhibition either neutral or cationic nanosensors had on the growth of *P. aeruginosa*, 2). Determine whether the neutral and cationic nanosensors remained extracellular, 3). Confirm real-time measurements of pH with various metabolites, 4). Determine the interaction of the neutral and cationic nanosensors in a *P. aeruginosa* biofilm, and 5). Measure pH changes in a *P. aeruginosa* biofilm with an acetic acid challenge.

The second aim of this thesis was to measure oxygen consumption and availability in a range of bacteria, using oxygen-sensitive polyacrylamide nanosensors. The objectives were, 1) Determine the suitability of the oxygen-sensitive nanosensors with the *P. aeruginosa* strain PAO1-N, 2). Detect variations in oxygen consumption in planktonic culture, 3). Determine the interaction of the oxygen-sensitive nanosensors in a *P. aeruginosa* biofilm, and 4). Elucidate the effectiveness of anti-biofouling materials on the bacterial attachment and biofilm formation of four bacterial species using oxygen consumption as a marker.

The final aim of this thesis was to detect and map pH changes in both planktonic and biofilm stages of *S. mutans,* using the pH-sensitive nanosensors in conjunction with accessible imaging techniques; including confocal laser scanning microscopy (CLSM) and fluorescence microscopy. The objectives were, 1). Detect pH changes generated by *S. mutans* in planktonic culture, 2). Generate a reproducible method that produced a robust biofilm incorporating the polyacrylamide nanosensors, and 3). Detect pH changes in a biofilm during a challenge with glucose.

3. Materials

3.1. Bacterial strains

Each experiment used freshly streaked agar plates, with isolates taken directly from an incubated plate to create an overnight culture. Plates were stored at 4°C if required for other work.

Pseudomonas aeruginosa strain PAO1-Nottingham wildtype (PAO1-N WT), PAO1-Washington (PAO1-W), PAO1-Lausanne (PAO1-L), PAO1-Denmark (PAO1-DK) and PAO1 C++ were initially streaked out from a -80°C stock onto Luria Broth (LB) agar and incubated at 37°C, for 24 h. Overnight cultures were made directly from incubated plates to insure isolates were fresh. 5 mL LB media and an individual colony picked with a sterile 10 µm loop from the streaked plate. The culture was incubated overnight at 37°C in a shaking incubator. Both *P. aeruginosa* strains CW4T1 (pyocyanin mutant) and PA14 as well as the PAO1 mutant strains (PAO1-N∆*pchEF*, PAO1-N∆*pvdD*, PAO1 C++∆*pvdD* and PAO1 C++∆*pvdD*∆*pchEF*) were also grown in the same manner.

Escherichia coli strain DH5α was initially streaked out from a -80°C stock onto Luria Broth (LB) agar and incubated at 37°C, for 24 h. Overnight cultures were made directly from incubated plates to insure isolates were fresh. 5 mL LB media and an individual colony picked with a sterile 10 µm loop from the streaked plate. The culture was incubated overnight at 37°C in a shaking incubator.

Staphylococcus aureus strain SH1000 was initially streaked out from a -80°C stock onto brain heart infusion (BHI) agar and incubated at 37°C, for 24 h. Overnight cultures were made directly from incubated plates to insure isolates were fresh. 5 mL BHI media and an individual colony picked with a sterile 10 µm loop from

the streaked plate. The culture was incubated overnight at 37°C in a shaking incubator.

Streptococcus mutans strain D282 was initially streaked out from a -80°C stock onto Todd Hewitt agar and incubated at 37°C, 5% CO_2, for 48 h. Overnight cultures were made using 5 mL Todd Hewitt (TH) media and an individual colony picked with a sterile 10 µm loop from the streaked plate. The culture was incubated overnight at 37°C in a static incubator. *S. mutans* strain NCTC 10449 was streaked out from a 80°C stock onto BHI agar and incubated at 37°C, 5% CO_2, for 48 h. Overnight cultures were made directly from incubated plates to insure isolates were fresh. 5 mL BHI media and an individual colony picked with a sterile 10 µm loop from the streaked plate. The culture was incubated overnight at 37°C in a static incubator.

3.2. Chemicals and Equipment

Oregon Green 488 carboxylic acid succinimidyl Ester, 5-isomer (OG), 5-(6)-carboxyfluorescein succinimidylester (FAM), 5-(6)-carboxytetramethylrhodamine succinimidylester (TAMRA) and Rhodamine Red™-X, succinimidylester-5-isomer, 4', 6-Diamidino-2-Phenylindole, Dihydrochloride (DAPI) and SYTO™9 green fluorescent nucleic acid strain were obtained from *Invitrogen,* USA. Acrylamide 99% minimum, *N,N'*-methylenebis(acrylamide) (bisacrylamide), polyoxyethylene(4)lauryl ether (Brij L4), (3-acrylamidopropyl) trimethylammonium chloride (ACTA), Diotylsulfosuccinate sodium (AOT), ammonium persulphate (APS), *N,N,N,N*-tetramethyl-ethylenediamine (TEMED), RPMI-1640, Lysogeny Broth (LB), Fetal Bovine Serum (FBS), L-gutamine 5x M9 minimal salts, Magnesium Sulphate, Citric acid, Potassium Phosphate, Glucose, Sucrose, Succinate and Xylose were purchased from *Sigma Aldrich*, USA. *N*-(3-Aminopropyl)methacrylamide hydrochloride (APMA) was obtained from *Polysciences Inc*, Germany. Hexane, Sodium Borate, Ethanol absolute (99.5%), Sodium Chloride, phosphate buffer saline (PBS), Sodium Sulphite, Acetic acid, Bacto agar and Bacto casamino acids were obtained from *Fisher Scientific*, UK. Calcium Chloride, Potassium Nitrate and Xylitol were obtained from *VWR International,* USA. Todd Hewitt broth and brain heart infusion broth (BHI) were obtained from *Thermo Fisher,* UK. was purchased from *Merck,* UK. Platinum (II) porphyrin was kindly supplied by Dr. Francesca Giuntini from Liverpool John Moores University.

TetraSpeck™ Fluorescent Microspheres Sampler Kit was obtained from *Thermo Fisher*, UK. Glass-bottom Microwell Dishes (35 mm petri dish, 20 mm microwell, No. 1.5 coverglass, 0.16-0.19 mm) were obtained from *MatTek corporation,* USA. Gas permeable moisture barrier seals (96) were

purchased from *4titude,* UK. Ibidi 15 µ-slide 8-well plates were purchased from *Ibidi,* Germany. Microplate, 96-well, PS, F-bottom (chimney well) µClear, Black, Med. Binding. And Sensoplate, 24-well, PS, F-bottom, Glass bottom, Black plates were obtained from *Greiner bio-one,* Austria. Immersol 518F & Immersol W were purchased from *Zeiss,* Germany. 96-well multiplate OxoPlates, OP96U, were obtained from *PreSens,* Germany.

Unless otherwise mentioned, all the chemicals that used throughout this study were of analytical grade.

4. Methods

4.1. Nanosensor fabrication

The initial step before nanosensor fabrication was the conjugation of the succinimidyl ester derivative of each fluorophore individually to APMA. This step was performed by dissolving 5 mg APMA into 2.5 mL of Sodium Borate buffer (50 mM, pH 9.5) followed by 1 mg of each fluorophore (OG, FAM, TAMRA) being dissolved in 200 µL of the resultant APMA solution. Each dye was prepared in individual glass vials, covered with aluminium foil. The reaction mixtures were left stirring for 24 h at room temperature before being stored at -20°C until further use.

For the synthesis of pH sensitive polyacrylamide nanosensors, hexane was deoxygenated for at least 30 min, using argon, under continuous stirring conditions. 3.080 g of Brij L4 and 1.590 g of AOT were weighed out and mixed together in a 250 mL round bottomed flask whilst being purged under argon for 15 min; followed by the addition of 42 mL of the deoxygenated hexane. The flask was left to continually stir as the mix was sealed within an argon environment using syringe needles and a balloon. This was proceeded by the addition of the acrylamide (513.0 mg), bisacrylamide (152.0 mg) and ACTA (119 µL) for cationic polyacrylamide nanosensors, or 540 mg acrylamide and 160 mg bisacrylamide for neutral polyacrylamide nanosensors. This was dissolved in 1.5 mL water, followed by the addition of the APMA-fluorophore conjugates made previously. 15 µL of OG-APMA, 15 µL of FAM-APMA, and 60 µL TAMRA- APMA were added and the mixture was purged under argon before being delivered by syringe into the 250 mL flask containing the emulsion of hexane, AOT and Brij L4. Finally, 15 µL

of TEMED and 30 µL of APS were added and the stirring continued in the dark, under a sealed argon environment for 2 h.

In order to isolate the nanosensors, the hexane was removed using a rotary evaporator at 30°C before 30 mL of ethanol (100%) was added to the flask contents. The mixture was transferred to a falcon tube and centrifuged at 6000 rpm for 3 min. The supernatant was disposed of and the pellet was re- suspended in 30 mL of 90% ethanol before being centrifuged again. The pellet was re- suspended in 30 mL of 100% ethanol and spun down (repeated twice). Finally, the pellet was re- suspended in 10 mL 100% ethanol and transferred to a 250 mL round bottomed flask before being dried using a rotary evaporator at 30°C. The dried nanosensors were stored at -20°C until further use.

4.1.1. Nanosensor fabrication with Rhodamine Red-X

For polyacrylamide nanosensors containing Rhodamine Red-X as a reference dye, the above method was followed with Rhodamine Red-X replacing TAMRA. 1 mg of Rhodamine Red-X was dissolved in 200 µL of an APMA solution and 60 µL of this solution was added instead of TAMRA. Only cationic polyacrylamide nanosensors containing Rhodamine Red-X were made.

4.1.2. Oxygen nanosensors fabrication

The nanoparticles used to covalently attach the platinum (II) porphyrin to were manufactured as shown above with amended volumes of acrylamide (502 mg) and bisacrylamide (149 mg). Additional APMA (31 mg) was included to provide a free amine group for the ester linked porphyrin to covalently attach to the surface

of the nanoparticle. Also, TAMRA (60 µL) was encapsulated in order to provide a reference.

For functionalisation, the polyacrylamide nanoparticles were suspended in sodium borate buffer (50 mM, pH 9.5) at 20 mg mL^{-1} with 1 mg mL^{-1} platinum (II) porphyrin. The solution was covered with aluminium foil, with the reaction mixture left stirring for 24 h at room temperature. After incubation, the solution was diluted in ethanol (100%). The mixture was transferred to a falcon tube and centrifuged at 6000 rpm for 10 min. The supernatant was disposed of and the pellet was re- suspended in 30 mL of 100% ethanol before being centrifuged again (repeated five times). Finally, the pellet was re- suspended in 10 mL 100% ethanol and transferred to a 250 mL round bottomed flask before being dried using a rotary evaporator at 30°C. The dried nanosensors were stored at -20°C until further use.

4.2. Characterisation of nanosensors

4.2.1. Zeta Potential and size

The zeta potential and size of the polyacrylamide nanosensors were calculated using the Malvern DLS Zetasizer. For determining both the size and zeta potential of the polyacrylamide nanosensors, 1 mg mL^{-1} suspensions of nanosensors were prepared in 10% phosphate buffered solution (PBS). For zeta potential, samples were loaded into a DTS1070 folded capillary cell (Malvern); whilst for size, samples were transferred into disposable 4 mL cuvettes.

4.2.2. pH nanosensor calibration

The pH calibration was performed by suspending polyacrylamide nanosensors in deionised H_2O at 2 mg mL^{-1} before being diluted to a working concentration of 1 mg mL^{-1} in the pH buffers. Fluorescence intensity was measured using the Agilent Fluorescence Spectrometer. The settings used can be found in **Table *4.2.2-1***.

Table 4.2.2-1: Excitation and emission settings for the emission scan of polyacrylamide nanosensors using the Agilent Fluorescence Spectrometer

Parameters	OG/FAM	TAMRA
Excitation wavelength (nm)	488	540
Emission scan (nm)	500-600	550-650
Slit size	5	5
Voltage (mV)	660	660

An alternative method for pH calibration was with a TECAN plate reader (Infinite® 200 PRO, TECAN). Using a black Greiner CELLSTAR® F-bottom 96-well microplate (Greiner Bio-one), 1 mg mL^{-1} polyacrylamide nanosensors, in the pH buffers ranging from 2.5-8, were loaded and single reads taken using the settings in **Table *4.2.2-2***.

Table 4.2.2-2: Excitation and emission settings for the emission scan of polyacrylamide nanosensors using a TECAN plate reader

Parameters	OG/FAM	TAMRA	Rhodamine Red-X
Excitation wavelength (nm)	488	540	570
Emission scan (nm)	520	580	590
Gain	Optimal	Optimal	Optimal

4.2.3. Oxygen nanosensor calibration

To confirm the change in fluorescence intensity by oxygen, platinum (II) porphyrin functionalised polyacrylamide nanosensors were diluted in 1:10 PBS to 1 mg mL^{-1}. The nanosensor solution was deoxygenated, using argon, under continuous stirring conditions. Fluorescence intensity was measured using the Agilent Fluorescence Spectrometer, whilst the oxygen saturation of the nanosensor solution was determined using an oxygen sensor probe from *Ocean Insight*. Once the solution reached atmospheric oxygen saturation, oxygen was bubbled into the solution to detect fluorescence intensity changes above atmospheric oxygen conditions.

4.3. Confocal Laser Scanning Microscopy (CLSM) and fluorescence microscopy systems

To generate the biofilm images, a Zeiss LSM 700 compact confocal laser scanning microscope was used fitted with HAL 100C lamp for light illumination and a Zeiss alpha-Plan-Apochromat, 20x/0.8na, 40x/1.2na Water or 63x/1.46na Oil objective lens. Images were captured by using AxioCam digital microscope camera connected to ZEN software and analysed using Zen blue software. For the planktonic images, a Nikon Eclipse Ti inverted fluorescence microscope was used with a CFI60 40x/0.6na objective lens. Images were captured by using Cool Snap™ MYO digital microscope camera connected to NIS Elements software and analysed using ImageJ.

4.4. Super-Resolution imaging of nanosensors with PAO1-N WT

Overnight cultures were set up as described in 3.1.

1 mL of PAO1-N WT was incubated with either 1 mg mL^{-1} cationic polyacrylamide nanosensors, neutral polyacrylamide nanosensors, or alone in LB as a control (O/N, 37°C shaking). After incubation, samples of each culture were washed to provide a comparison to unwashed samples. Culture samples were centrifuged and the pellet re-suspended in LB before being repeated a second time.

4.5 µL of the bacterial sample was loaded onto a 1 % agarose cube (1x1x0.5 µL). 0.5 µL of TetraSpeck™ 0.1µm Microspheres (diluted to 200 µM in Milli-Q H_2O) was loaded on the agarose samples for six samples in total (cationic; washed and unwashed, neutral; washed and unwashed, cells alone; washed and unwashed). The agarose cubes were placed onto MatTek 35 mm dishes with a 20 mm glass microwell and imaged using a Zeiss PS1 Super Resolution Microscope with a 63x water-immersion objective. Images were processed using Zen software for illumination and alignment adjustments.

4.5. Growth assays

4.5.1. Toxicity of polyacrylamide nanosensors with PAO1-N WT

1 mL of PAO1-N WT inoculum from an O/N culture was centrifuged at 13,000 rpm for 1 min, the pellet was washed in 1 mL PBS and re-centrifuged at 13,000 rpm for 1 min. The pellet was re-suspended in 1 mL of LB medium and the optical density at 600 nm (OD_{600}) measured. PAO1-N WT was then diluted to an OD_{600}=0.5 in LB.

Initial concentrations of 30 mg mL^{-1} and 2 mg mL^{-1} for both cationic and neutral nanosensors were made in LB medium. All four suspensions were filter sterilised using a Minisart® 0.22 µm PES filter. The final concentrations required were 25, 10, 5, 1, 0.5, & 0.1 mg mL^{-1} with PAO1-N WT at an OD_{600}=0.05. Both 25 mg mL^{-1} cationic and neutral nanosensors in LB (no PAO1-N WT), PAO1-N WT at an OD_{600}=0.05 in LB and finally LB alone were used as controls.

Samples were loaded into a Greiner CELLSTAR® F-bottom 96-well microplate and the absorbance measured using a TECAN plate reader. Absorbance at 600 nm was measured after 5 sec orbital shaking and 5 sec settle time every 15 min for 96 cycles, with the temperature held between 36.5°C and 37.5°C.

The resultant absorbance data was normalised by dividing the first OD_{600} measurement by itself to create a value of 1; then the proceeding values were divided by the first value.

The Area Under the Curve (AUC) was calculated as the sum of all data points recorded for each condition, *i.e.* each measurement taken from time-point 0-18 h to produce the sum of 72 values. This method was used for all AUCs calculated.

4.5.2. Toxicity of cationic polyacrylamide nanosensors with *S. mutans* strain NCTC 10449

1 mL of *S. mutans* NCTC 10449 inoculum from an O/N culture was centrifuged at 13,000 rpm for 1 min, the pellet was washed in 1 mL PBS and re-centrifuged at 13,000 rpm for 1 min. The pellet was re-suspended in 1 mL of BHI medium and the optical density at 600 nm (OD_{600}) measured. *S. mutans* was then diluted to an OD_{600}=0.5 in BHI.

Initial concentrations of 15 mg mL^{-1} and 2 mg mL^{-1} for both cationic and neutral nanosensors were made in BHI medium. All four suspensions were filter sterilised using a Minisart® 0.22 µm PES filter. The final concentrations required were 10, 5, 1, 0.5, & 0.1 mg mL^{-1} with *S. mutans* at an OD_{600}=0.05. Both 10 mg mL^{-1} cationic and neutral nanosensors in BHI (NCTC 10449), *S. mutans* at an OD_{600}=0.05 in BHI and finally BHI alone were used as controls.

Samples were loaded into a Greiner CELLSTAR® F-bottom 96-well microplate and covered with a permeable gas membrane (*4titude* 96-well cover). The absorbance and fluorescence intensity measured using a TECAN plate reader. Absorbance at 600 nm was measured after 5 sec orbital shaking and 5 sec settle time every 15 min for 21 h, with the temperature held between 36.5°C and 37.5°C, with CO_2 at 5%. Fluorescence intensity was measured at ex:488 nm, em:520 nm & ex:540 nm, em:580 nm.

4.5.3. Photostability of OG, FAM, TAMRA and Rhodamine Red-X

2 mg mL^{-1} cationic polyacrylamide nanosensors containing either TAMRA or Rhodamine Red-X were suspended in 1:10 PBS then diluted in pH buffers from 2.5-8 for a final concentration of 1 mg mL^{-1}. Samples were loaded into a Greiner CELLSTAR® F-bottom 96-well plate and covered with an *4titude* gas permeable membrane (96-well). Fluorescence intensity was measured using a TECAN microplate reader. The fluorescence intensity of OG, FAM (ex:488 nm; em:520 nm), Rhodamine Red-X and TAMRA (ex:540 nm, em:580 nm) were measured after 5 sec orbital shaking and 5 sec settle time every 15 min for 21 h, with the temperature held between 36.5°C and 37.5°C. The excitation and emission settings can be found in **Table *4.2.2-2***. Experiments extended to include

measurements every hour rather than every 15 min and also with a reduced temperature (25°C down from 37°C).

4.5.4. pH measurements over time

PAO1-N WT at OD_{600} of 0.05 with either M9 glucose or M9 succinate set up with 1 mg mL^{-1} cationic polyacrylamide nanosensors containing Rhodamine Red-X as a reference dye. pH buffers from 2.5-8 containing 1 mg mL^{-1} polyacrylamide nanosensors were also set up to measure the emission of OG, FAM, TAMRA over 21 h. Samples were loaded into a Greiner CELLSTAR® F-bottom 96-well plate and covered with an *4titude* gas permeable membrane (96-well). Both the absorbance and fluorescence intensity was measured using a TECAN microplate reader. For growth, absorbance at 600 nm was measured after 5 sec orbital shaking and 5 sec settle time every 15 min for 21 h, with the temperature held between 36.5°C and 37.5°C. For pH determination, the fluorescence intensity for OG, FAM (ex:488 nm; em:520 nm), Rhodamine Red-X and TAMRA (ex:540 nm, em:580 nm) was taken every 15 min. The excitation and emission settings can be found in **Table *4.2.2-2***.

The pH was calculated using measurements from pH 2.5-8 buffers with 1 mg mL^{-1} cationic polyacrylamide nanosensors. A ratio between OG/FAM fluorescence intensity and Rhodamine Red-X fluorescence intensity (em:580 nm) is created. From the fluorescence intensity ratio, a linear regression was calculated every 1 h (*i.e.* 22 are calculated for 0-21 h). The next step was to determine the fluorescence intensity emission from the wells containing PAO1-N WT. Another ratio between OG/FAM fluorescence intensity and Rhodamine Red-X fluorescence intensity was created, which can be converted to a pH value using the 'rolling' linear regression calculated. The difference between pH values from M9 glucose & M9 succinate, with and without PAO1-N WT, were subtracted to produce the final pH values.

4.6. Oxygen consumption assays

4.6.1. Detecting auto-fluorescence in PAO1 strains

The PAO1 strains from Nottingham, Washington, Lausanne and Denmark were prepared as described in 3.1. 1 mL of inoculum was centrifuged at 13,000 rpm for 1min, the supernatant was disposed of and the pellet was washed in 1 mL PBS and re-centrifuged at 13,000 rpm for 1 min. The pellet was re-suspended in 1 mL of M9 succinate + 1% w/v casamino acids and the optical density at 600 nm (OD_{600}) measured. PAO1-N was then diluted to an OD_{600}=0.5 in M9 succinate + 1% w/v casamino acids. A final OD_{600} of 0.05 for each PAO1 strain was used, either in the presence or in absence of 1 mg mL^{-1} oxygen nanosensors. Samples were loaded into a Greiner CELLSTAR® F-bottom 96-well black-walled microplate and the absorbance measured using a TECAN plate reader. For growth, absorbance at 600 nm was measured after 5 sec orbital shaking and 5 sec settle time every 15 min for 21 h, with the temperature held between 36.5°C and 37.5°C. For oxygen determination, the fluorescence intensity for TAMRA (ex:540 nm; em:580 nm) and porphyrin (ex:405 nm; em:650 nm) was taken every 15 min.

4.6.2. Measuring growth and auto-fluorescence in different bacterial species

The *E. coli* strain DH5α, the *S. aureus* strain SH1000 and PAO1-N were prepared as described in 3.1. 1 mL of inoculum was centrifuged at 13,000 rpm for 1min, the supernatant was disposed of and the pellet was washed in 1 mL PBS and re-centrifuged at 13,000 rpm for 1 min. The pellet was re-suspended in 1 mL of M9 glucose and the optical density at 600 nm (OD_{600}) measured. Each strain was then diluted to an OD_{600}=0.5 in M9 glucose. A final OD_{600} of 0.05 for each strain was

used, either in the presence or in absence of 1 mg mL^{-1} oxygen nanosensors. Samples were loaded into Greiner CELLSTAR® F-bottom 96-well black-walled microplate and the absorbance measured using a TECAN plate reader. For growth, absorbance at 600 nm was measured after 5 sec orbital shaking and 5 sec settle time every 15 min for 21 h, with the temperature held between 36.5°C and 37.5°C. For oxygen determination, the fluorescence intensity for TAMRA (ex:540 nm; em:580 nm) and porphyrin (ex:405 nm; em:650 nm) was taken every 15 min.

4.6.3. Measuring growth and auto-fluorescence in *Pseudomonas* mutants

The *P. aeruginosa* strains PAO1-N, PAO1 C++, PA14, CW4T1 (pyocyanin mutant), Δ*pvdD* (PAO1-N), Δ*pvdD* (PAO1 C++), Δ*pchEF* (PAO1-N) and Δ*pvdD*Δ*pchEF* (PAO1 C++) were prepared as described in 3.1. 1 mL of inoculum was centrifuged at 13,000 rpm for 1 min, the supernatant was disposed of and the pellet was washed in 1 mL PBS and re-centrifuged at 13,000 rpm for 1 min. The pellet was re-suspended in 1 mL of M9 succinate + 1% w/v casamino acids and the optical density at 600 nm (OD_{600}) measured. PAO1-N was then diluted to an OD_{600}=0.5 in M9 succinate + 1% w/v casamino acids. A final OD_{600} of 0.05 for each *P. aeruginosa* strain was used. Samples were loaded into a Greiner CELLSTAR® F-bottom 96-well black-walled microplate and the absorbance measured using a TECAN plate reader. For growth, absorbance at 600 nm was measured after 5 sec orbital shaking and 5 sec settle time every 15 min for 21 h, with the temperature held between 36.5°C and 37.5°C. For oxygen determination, the fluorescence intensity for TAMRA (ex:540 nm; em:580 nm) and porphyrin (ex:405 nm; em:650 nm) was taken every 15 min.

4.6.4. Testing different bacterial species with oxygen nanosensors

Using the *E. coli* strain DH5α, the PAO1 strains PAO1-N and PAO1-NΔ*pvdD*, and the *S. aureus* strain SH1000, 1 mL of each inoculum was centrifuged at 13,000 rpm for 1 min, the supernatant was disposed of and the pellet was washed in 1 mL PBS and re-centrifuged at 13,000 rpm for 1 min. The pellets were re-suspended in 1 mL of M9 glucose and the optical density at 600 nm (OD_{600}) measured. Each strain was then diluted to an OD_{600}=0.5 in M9 glucose. A final OD_{600} of 0.05 for each strain was used, either in the presence or in absence of 1 mg mL^{-1} oxygen nanosensors. For '0%' and '20%' oxygen controls, 1 mg mL^{-1} nanosensors in M9 glucose was used for '20%' and 40 mg mL^{-1} sodium sulphite was dissolved in 1 mg mL^{-1} oxygen nanosensors for '0%'. Samples were loaded into a Greiner CELLSTAR® F-bottom 96-well black-walled microplate and the absorbance measured using a TECAN plate reader. The microplate was covered with a gas permeable membrane (*4titude* – Moisture barrier seal 96). For growth, absorbance at 600 nm was measured after 5 sec orbital shaking and 5 sec settle time every 15 min for 21 h, with the temperature held between 36.5°C and 37.5°C. For oxygen determination, the fluorescence intensity for TAMRA (ex:540 nm; em:580 nm) and porphyrin (ex:405 nm; em:650 nm) was taken every 15 min.

Fluorescence intensity ratio values were calculated by dividing the em:650 nm reading by the em:580 nm reading for each time point. The resultant fluorescence intensity ratio was normalised by dividing the first fluorescence intensity ratio value by itself to create a value of 1; then the proceeding values were divided by the first value.

4.6.5. Measuring PAO1-NΔ*pvdD* growth and oxygen consumption with varying concentrations of potassium nitrate

Using the PAO1 strain PAO1-NΔ*pvdD* 1 mL of inoculum was centrifuged at 13,000 rpm for 1 min, the supernatant was disposed of and the pellet was washed in 1 mL PBS and re-centrifuged at 13,000 rpm for 1 min. The pellet was re-suspended in 1 mL of M9 salts and the optical density at 600 nm (OD_{600}) measured. PAO1-NΔ*pvdD* was then diluted to an OD_{600}=0.5 in M9 minimal media with 1% w/v casamino acids alone or 1% w/v casamino acids with increasing concentrations of KNO_3 (5 mM, 10 mM & 20 mM). A final OD_{600} of 0.05 was used, either in the presence or in absence of 1 mg mL^{-1} oxygen nanosensors. Samples were loaded into a Greiner CELLSTAR® F-bottom 96-well black-walled microplate and the absorbance measured using a TECAN plate reader. For '0%' and '20%' oxygen controls, 1 mg mL^{-1} nanosensors in M9 salts was used for '20%' and 40 mg mL^{-1} sodium sulphite was dissolved in 1 mg mL^{-1} oxygen nanosensors for '0%'. The microplate was covered with a gas permeable membrane (*4titude* – Moisture barrier seal 96). For growth, absorbance at 600 nm was measured after 5 sec orbital shaking and 5 sec settle time every 15 min for 21 h, with the temperature held between 36.5°C and 37.5°C. For oxygen determination, the fluorescence intensity for TAMRA (ex:540 nm; em:580 nm) and porphyrin (ex:405 nm; em:650 nm) was taken every 15 min. Fluorescence intensity ratio values were calculated by dividing the em:650 nm reading by the em:580 nm reading for each time point. The resultant fluorescence intensity ratio was normalised by dividing the first fluorescence intensity ratio value by itself to create a value of 1; then the proceeding values were divided by the first value.

4.7. *Streptococcus mutans* starvation assay

1 mL of *S. mutans* strain NCTC 10449 inoculum was centrifuged at 13,000 rpm for 1 min, the pellet was washed in 1 mL PBS and re-centrifuged at 13,000 pm for 1 min. The pellet was re-suspended in PBS for 30 min as a starvation step. The cells were spun down again and re-suspended in saline. A cell suspension at OD_{600}=0.5 mixed with 1 mg mL^{-1} cationic nanosensors in saline was aliquoted into a Greiner CELLSTAR® F-bottom 24-well black walled microplate. Imaging was performed using a Nikon wide field fluorescence microscope with the 60x/0.6na magnification (40x objective with 1.5x additional magnification). An image was taken (brightfield, 460 nm for OG/FAM & 550 nm for TAMRA) for time point 0 min before either glucose, sucrose, xylose, xylitol (all 1% w/v final conc.) or saline was added to the respective wells. Images were taken every 5 min for 30 min. Wells with no cells were treated with each carbohydrate solution and imaged to confirm the absence of any change in fluorescence intensity brought on through the solutions themselves.

The calibration was performed using a Greiner CELLSTAR® F-bottom 24-well black walled sensoplate where pH buffers from pH 8 to pH 2.5 were mixed with cationic polyacrylamide nanosensors for a final concentration of 1 mg mL^{-1}. Images were taken from each pH with (460 nm) and (550 nm) using the same exposure settings as the experiment. The fluorescence intensity ratio from each pH was plotted and the linear regression calculated to determine the pH values from the fluorescence intensities generated during the experiment.

4.8. *Pseudomonas aeruginosa* static biofilm set-up

4.8.1. *P. aeruginosa* static biofilm set-up with pH nanosensors

1 mL of PAO1-N WT inoculum was centrifuged at 13,000 rpm for 1 min, the pellet was washed in 1 mL PBS and re-centrifuged at 13,000 rpm for 1 min. The pellet was re-suspended in 1 mL of RPMI (supplemented with 10% FBS and 500 µL L-Glutamine) and the optical density at 600nm (OD_{600}) measured. PAO1-N WT was then diluted to an OD_{600}=0.5 using the RPMI. For the nanosensors, 1 mg mL^{-1} was used as the working concentration and the polyacrylamide nanosensors were filter sterilised using 0.22 µm PES filters. Finally, the working OD_{600} of PAO1-N WT was 0.05. A combination of cells and nanosensors were loaded into individual wells of µ-slide 8-well glass bottomed chambers (Ibidi) and a control of PAO1-N WT alone at OD_{600} = 0.05 was loaded too. The chamber was stored in a box covered in aluminium foil and place in a static incubator at 37°C for 48 h.

After incubation, the media was removed and replaced with fresh medium. The fluorescent nuclear stain 4',6-diamidino-2-phenylindole (DAPI) was then applied at 30 µg mL^{-1} where indicated. The biofilms were imaged using a Zeiss confocal laser scanning microscope and the appropriate excitation settings for the fluorescence channels (DAPI=405 nm, OG/FAM=488 nm, TAMRA=555 nm). Images were processed using Zen software (Zeiss).

4.8.2. Acetic acid challenge

1 mL of PAO1-N WT inoculum was centrifuged at 13,000 rpm for 1 min, the pellet was washed in 1 mL PBS and re-centrifuged at 13,000 pm for 1 min. The pellet was re-suspended in 1 mL of RPMI (supplemented with 10% FBS and 500 µL L-Glutamine) and the optical density at 600nm (OD_{600}) measured. *P. aeruginosa*

was then diluted to an OD_{600}=0.5 using RPMI. For the nanosensors, 1 mg mL^{-1} was used as the working concentration and the polyacrylamide nanosensors were filter sterilised using 0.22 µm PES filters. Finally, the working OD_{600} of *P. aeruginosa* was 0.05. A combination of cells and nanosensors were loaded into individual wells of µ-slide 8-well glass bottomed chambers (Ibidi) and a control of *P. aeruginosa* alone at OD_{600} = 0.05 was loaded too. The chamber was stored in a box covered in aluminium foil and place in a static incubator at 37°C for 48 h.

After incubation, the media was removed and replaced with fresh medium, and DAPI at 30 µg mL^{-1}. The biofilms were imaged using CLSM with a 63x/1.46na objective and the appropriate excitation settings for the fluorescence channels (DAPI=405 nm, OG/FAM=488 nm, TAMRA=555 nm). For the acetic acid treatment, 100 µL of 3% acetic acid was added to the medium after initial pre-treatment imaging. Further images were captured after 30 min incubation in the acetic acid. Images were processed using Zen software (Zeiss) and fluorescence intensities calculated using ImageJ software.

4.8.3. *P. aeruginosa* static biofilm set-up with oxygen nanosensors

Using the PAO1 strains PAO1-N and PAO1-NΔ*pvdD*. 1 mL of inoculum was centrifuged at 13,000 rpm for 1 min, the supernatant was disposed of and the pellet was washed in 1 mL PBS and re-centrifuged at 13,000 rpm for 1 min. The pellet was re-suspended in 1 mL of M9 succinate and the optical density at 600 nm (OD_{600}) measured. The PAO1 strains were then diluted to an OD_{600}=0.5 using M9 succinate. For the oxygen-sensitive nanosensors, 1 mg mL^{-1} was used as the working concentration. Finally, the working OD_{600} of *P. aeruginosa* was 0.05. A combination of cells and the oxygen nanosensors were loaded into individual wells

of μ-slide 8-well glass bottomed chambers (Ibidi) and a controls of PAO1-N and PAO1-NΔ*pvdD* alone at OD_{600} = 0.05 was loaded too. The chamber was stored in a box covered in aluminium foil and place in a static incubator at 37°C for 48 h.

After incubation, the media was removed and replaced with fresh medium. The fluorescent nuclear stain SYTO™9 was then applied for a final concentration of 0.3 μM. The biofilms were imaged using a CLSM at 20x/0.8na objective and the appropriate excitation settings for the fluorescence channels (Porphyrin=405 nm, Styo9=488 nm, TAMRA=555 nm). Images were processed using Zen software (Zeiss) and fluorescence intensities calculated using ImageJ software.

4.9. *S. mutans* Biofilm set-up with pH nanosensors

4.9.1. Examining sucrose supplementation in D282 and NCTC 10449 biofilm formation

1 mL of *S. mutans* strain D282 inoculum was centrifuged at 13,000 rpm for 1 min, the pellet was washed in 1 mL PBS and re-centrifuged at 13,000 pm for 1 min. The pellet was re-suspended in either Todd Hewitt (TH) media alone or TH + 1% w/v sucrose. Cell suspensions of *S. mutans* D282 (OD_{600}=0.05) were mixed with cationic polyacrylamide nanosensors at a working concentrations of 1 mg mL^{-1} (initially filtered using 0.22 μm PES filters), diluted in either TH alone or TH + 1% w/v sucrose. Biofilms were also set up with D282 alone, either with a 1% w/v sucrose supplement or without. Biofilms were set up using 15 μ-slide 8 well glass bottomed chambers (Ibidi). The chamber was incubated for 48 h static incubation, 37°C, 5% CO_2. The media was then removed and replaced with TH without sucrose supplementation and incubated for a further 24 h. Imaging was performed using CLSM with the 63x/1.46na objective. The TH media was removed and replaced

with saline (0.9% NaCl) and the nucleic acid stain 4',6-diamidino-2-phenylindole (DAPI) at 30 μg mL^{-1} was added in order to detect cells during the process. The biofilms were imaged using the appropriate excitation settings for the fluorescence channels (DAPI=405 nm, OG/FAM=488 nm, TAMRA=555 nm). Images were processed using Zen software (Zeiss).

For NCTC 10449 1 mL inoculum was centrifuged at 13,000 rpm for 1 min, the pellet was washed in 1 mL PBS and re-centrifuged at 13,000 pm for 1 min. The pellet was re-suspended in either BHI alone or BHI + 1% w/v sucrose. Cell suspensions of NCTC 10449 (OD_{600}=0.05) were mixed with cationic polyacrylamide nanosensors at a working concentrations of 1 mg mL^{-1} (initially filtered using 0.22 μm PES filters), diluted in either BHI alone or BHI + 1% w/v sucrose. Biofilms were also set up with NCTC alone, either with a 1% w/v sucrose supplement or without. Biofilms were set up using μ-slide 8 well glass bottomed chambers (Ibidi). The chamber was incubated for 48 h static incubation, 37°C, 5% CO_2. The media was then removed and replaced with 50% BHI without sucrose supplementation and incubated for a further 24 h. Imaging was performed using CLSM with the 40x/1.2na objective. The BHI Media was removed and replaced with saline (0.9% NaCl) and the nucleic acid stain 4',6-diamidino-2-phenylindole (DAPI) at 30 μg mL^{-1} was added in order to detect cells during the process. The biofilms were imaged using the appropriate excitation settings for the fluorescence channels (DAPI=405 nm, OG/FAM=488 nm, TAMRA=555 nm). Images were processed using Zen software (Zeiss).

4.9.2. Examining the addition of cationic polyacrylamide nanosensors to an established biofilm in comparison to incubation with the inoculum

Using the *S. mutans* strain D282, 1 mL of inoculum was centrifuged at 13,000 rpm for 1 min, the pellet was washed in 1 mL PBS and re-centrifuged at 13,000 pm for 1 min. The pellet was re-suspended in TH + 1% w/v sucrose. The biofilm was grown in an Ibidi glass chamber and set up with a cell suspension of D282 at OD_{600}=0.05 alone or mixed with 1 mg mL^{-1} cationic nanosensors in TH media + 1% w/v sucrose. After 48 h incubation at 37°C, 5% CO_2, the TH media + 1% w/v sucrose from each well was removed. For the wells with nanosensors already present, fresh TH media was added. To the wells with D282 alone, 1 mg mL^{-1} cationic polyacrylamide nanosensors in TH media was added. The chamber was incubated for another 24 h before imaging. Imaging was performed using CLSM with the 63x/1.46na objective. The media was removed and replaced with H_2O, with DAPI (1 mg mL^{-1}) added to detect cells during the process. The biofilms were imaged using the appropriate excitation settings for the fluorescence channels (DAPI=405 nm, OG/FAM=488 nm, TAMRA=555 nm). Images were processed using Zen software (Zeiss).

4.9.3. Nanosensor responsiveness to pH challenge

1 mL of D282 inoculum was centrifuged at 13,000 rpm for 1 min, the pellet was washed in 1 mL PBS and re-centrifuged at 13,000 pm for 1 min. The pellet was re-suspended in TH + 1% w/v sucrose. The biofilms were grown in an Ibidi glass chamber and set up with a cell suspension of D282 at OD_{600}=0.05 mixed with 1 mg mL^{-1} cationic nanosensors in TH media + 1% w/v sucrose and incubated for

48 h, 37°C, 5% CO_2. Imaging was performed using CLSM with the 63x/1.46na objective. The media was removed and replaced with H_2O, with DAPI (1 mg mL^{-1}) added to detect cells during the process. Initial snapshots of a single plane of focus were taken before a combination of pH solutions were added. Condition 1) pH 4 added at time point 0 min, pH 7 added at 5 min, pH 6 added at 10 min, pH 5 at 15 min and finally pH 4 at 20 min; condition 2) pH 6 added at time point 0 min, pH 5 added at 5 min, pH 4 added at 10 min, pH 7 at 15 min and finally pH 6 at 20 min. Subsequent snapshots were taken every minute for 25 min. The biofilms were imaged using the appropriate excitation settings for the fluorescence channels (DAPI=405 nm, OG/FAM=488 nm, TAMRA=555 nm). Images were processed using Zen software (Zeiss) and fluorescence intensities calculated using ImageJ software.

4.9.4. Glucose challenge in *S. mutans* biofilm

1 mL of D282 inoculum was centrifuged at 13,000 rpm for 1 min, the pellet was washed in 1 mL PBS and re-centrifuged at 13,000 pm for 1 min. The pellet was re-suspended in TH + 1% w/v sucrose. The biofilms were set up with a cell suspension of D282 at OD_{600}=0.05 mixed with 1 mg mL^{-1} cationic polyacrylamide nanosensors in TH media + 1% w/v sucrose and incubated for 48 h, 37°C, 5% CO_2. After 48 h, the media was replaced with TH media alone and incubated for a further 24 h. The imaging was performed using CLSM with the 63x/1.46na objective. The media was removed and replaced with saline (0.9% NaCl) whilst DAPI (1 mg mL^{-1}) added to detect cells during the process. A plane of interest was found and either glucose (1% w/v), or water was added. Images were taken every minute for 20 min then 25 and 30 min. After 30 min, a 4.5 pH buffer was added

to each well and an image was taken every min for 5 min. All images were taken with ex: 488 nm, em: 520 nm & ex: 540 nm, em: 580 nm. Duplicate images were taken at 0 min and 5 min post pH treatment with the addition of ex:405 nm, em: 420 nm to detect the cells. The biofilms were imaged using the appropriate excitation settings for the fluorescence channels (DAPI=405 nm, OG/FAM=488 nm, TAMRA=555 nm). Images were processed using Zen software (Zeiss) and fluorescence intensities calculated using ImageJ software.

4.10. Anti-biofouling polymer assays

4.10.1. OxoPlate and oxygen nanosensor microplate set-up

An adapted Calgary Biofilm Device (CBD) assay was performed using either an OxoPlate or oxygen-sensitive nanosensors to measure oxygen consumption during incubation. PA14, PAO1-N, *E. coli* strain ATCC 10536 and *S. aureus* strain ATCC 6538 were streaked out on TSB agar and incubated at 37°C for 18 h. 5 mL TSB medium was inoculated with an individual colony from each strain and incubated for 18 h at 37°C, at shaking 150 rpm. The optical density of each overnight was measured at 600 nm (OD_{600}) before each strain was diluted to an OD_{600}=0.05 using TSB media.

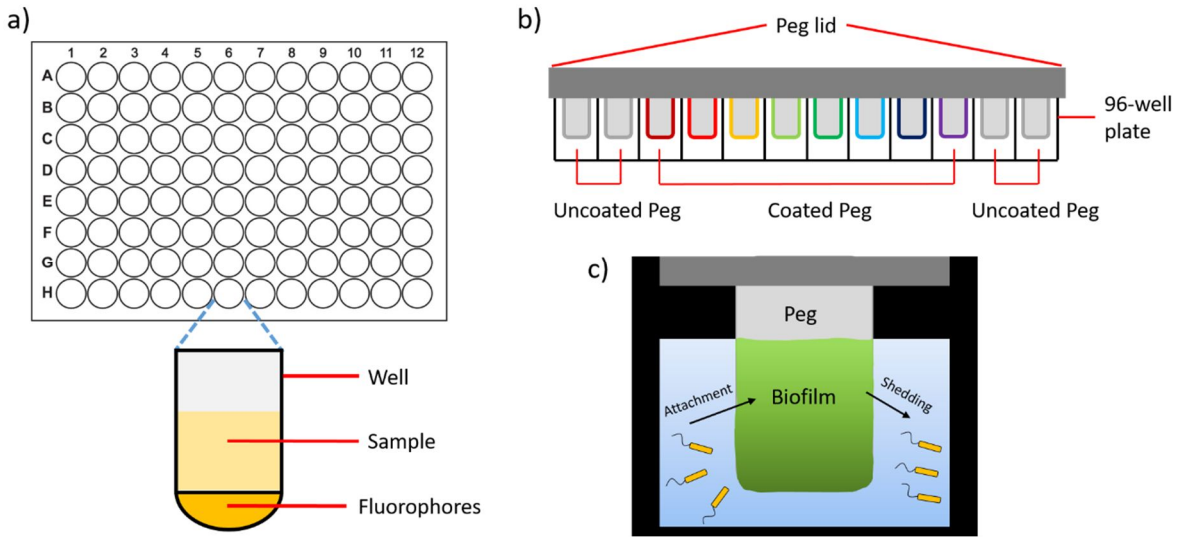

Figure 4.10.1-1: OxoPlate and polymer-treated Peg-lid schematic – a) The top-view of a 96-well OxoPlate with a side-view of an individual well. The oxygen-sensitive fluorophores are entrapped in a thin polymer film that sits at the bottom of the well. The film contains two different fluorophores, an indicator, and a reference fluorophore. The fluorescence intensity of the indicator depends on the oxygen content in the sample, whilst the fluorescence intensity of the reference is independent of oxygen content. **b)** The side-view of a coated peg-lid placed on top of a 96-well plate. Each individual peg sits within an individual well of the plate. The colours denote pegs coated in a polymer. **c)** Each individual peg is submerged in a sample during incubation. If bacteria is present, the peg provides a surface for bacterial attachment and biofilm formation. This peg-lid can then be transferred to either an OxoPlate or 96-well plate for analysis in a microplate reader.

Table 4.10.1-1: Material compositions used for peg-lid coatings

Row	Material No.	Treatment	Compositions
1		None	
2		None	
3	1	PEOX 200 kDa	Poly(2-ethyl-2-oxazoline) 200 kDa
4	2	PEOX 500 kDa	Poly(2-ethyl-2-oxazoline) 500 kDa
5	3	Pluronic F127	Poly(ethylene oxide)-block-poly(propylene oxide)-block-poly(ethylene oxide)
6	4	Pluronic P123	Poly(ethylene oxide)-block-poly(propylene oxide)-block-poly(ethylene oxide)
7	5	N/A	N/A
8	6	P20	Poly(PEGMA1000/LMA/PEG500), A:B P20
9	7	P26	Poly(GMA/LMA/PEG600), A:B P26
10	8	PDMS	Poly(dimethylsiloxane), hydroxy terminated 110 kDa
11		None	
12		None	

a)

	Uncoated	*Uncoated*	*Material 1*	*Material 2*	*Material 3*	*Material 4*	*Material 5*	*Material 6*	*Material 7*	*Material 8*	*Uncoated*	*Uncoated*	
	1	**2**	**3**	**4**	**5**	**6**	**7**	**8**	**9**	**10**	**11**	**12**	
A	C100	Media	Media	Media	Media	Media	Media	Media	Media	Media	Cells Alone	Planktonic	
B	C100	Media	Cells Alone	Cells Alone	Cells Alone	Cells Alone	Cells Alone	Cells Alone	Cells Alone	Cells Alone	Cells Alone	Planktonic	Species 1
C	C100	Virkon	Cells Alone	Cells Alone	Cells Alone	Cells Alone	Cells Alone	Cells Alone	Cells Alone	Cells Alone	Cells Alone	Planktonic	
D	C100	Virkon	Cells Alone	Cells Alone	Cells Alone	Cells Alone	Cells Alone	Cells Alone	Cells Alone	Cells Alone	Cells Alone	Planktonic	
E	C0	Virkon	Cells Alone	Cells Alone	Cells Alone	Cells Alone	Cells Alone	Cells Alone	Cells Alone	Cells Alone	Cells Alone	Planktonic	
F	C0	Virkon	Cells Alone	Cells Alone	Cells Alone	Cells Alone	Cells Alone	Cells Alone	Cells Alone	Cells Alone	Cells Alone	Planktonic	Species 2
G	C0	Media	Cells Alone	Cells Alone	Cells Alone	Cells Alone	Cells Alone	Cells Alone	Cells Alone	Cells Alone	Cells Alone	Planktonic	
H	C0	Media	Media	Media	Media	Media	Media	Media	Media	Media	Cells Alone	Planktonic	

KEY

Bacteria	TSB	PI alone
No bacteria	TSB + NS	PI + NS

b)

	Uncoated	*Uncoated*	*Material 1*	*Material 2*	*Material 3*	*Material 4*	*Material 5*	*Material 6*	*Material 7*	*Material 8*	*Uncoated*	*Uncoated*	
	1	**2**	**3**	**4**	**5**	**6**	**7**	**8**	**9**	**10**	**11**	**12**	
A	C100	NS Alone	NS Alone	NS Alone	NS Alone	NS Alone	NS Alone	NS Alone	NS Alone	NS Alone	Cells Alone	Planktonic	
B	C100	NS Alone	Cells Alone	Cells Alone	Cells Alone	Cells Alone	Cells Alone	Cells Alone	Cells Alone	Cells Alone	Cells Alone	Planktonic	
C	C100	Virkon	Cells + NS	Cells + NS	Cells + NS	Cells + NS	Cells + NS	Cells + NS	Cells + NS	Cells + NS	Cells + NS	Planktonic	Species 1
D	C100	Virkon	Cells + NS	Cells + NS	Cells + NS	Cells + NS	Cells + NS	Cells + NS	Cells + NS	Cells + NS	Cells + NS	Planktonic	
E	C0	Virkon	Cells + NS	Cells + NS	Cells + NS	Cells + NS	Cells + NS	Cells + NS	Cells + NS	Cells + NS	Cells + NS	Planktonic	
F	C0	Virkon	Cells + NS	Cells + NS	Cells + NS	Cells + NS	Cells + NS	Cells + NS	Cells + NS	Cells + NS	Cells + NS	Planktonic	Species 2
G	C0	NS Alone	Cells Alone	Cells Alone	Cells Alone	Cells Alone	Cells Alone	Cells Alone	Cells Alone	Cells Alone	Cells Alone	Planktonic	
H	C0	NS Alone	NS Alone	NS Alone	NS Alone	NS Alone	NS Alone	NS Alone	NS Alone	NS Alone	Cells Alone	Planktonic	

Figure 4.10.1-2: Plate layout for biofilm peg-lid assay – a) plate layout for the OxoPlate work. Plates were split along a horizontal axis to contain one bacterial species in the top portion (A-D) and a second species in the bottom portion (E-H). Six plates were produced for the four species used. **b)** plate layout for the oxygen nanosensor work. Plates were split along a horizontal axis to contain one bacterial species in the top portion (A-D) and a second species in the bottom portion (E-H). Two plates were produced for the four species used.

OxoPlate plate design is found in **Figure *4.10.1-2***a) whilst with oxygen nanosensor plate design is found in **Figure *4.10.1-2***b). Initial set-up for OxoPlate and nanosensor plate was identical. Cells were loaded at 0.05OD into assigned wells of a Grenier bio-one flat bottomed 96-well plate (red text in **Figure *4.10.1-2***) before a peg-lid, coated with test materials (**Error! Reference source not found.**), was placed onto the microplate, submerging each peg into culture, as described in **Figure *4.10.1-1***. The microplate and peg-lid were incubated for 5 h at 37°C. After incubation, a washing step was performed; the peg-lids were

placed into 96-well plates containing deionised H_2O for 10 min before being transferred to a second plate containing deionised H_2O for a further 10 min.

For the OxoPlate work, TSB media was loaded into assigned wells of an OxoPlate OP96U, 96-well multiplate (columns 2 to 11, **Figure *4.10.1-2***a). For the controls, planktonic cells (0.05OD) were loaded in column 12, virkon was added to TSB media in column 2, row C-F, deionised H_2O (C100) was added to column 1, row A-D and 20 mg mL^{-1} sodium sulphite in deionised H_2O (C0) was added to column 1, row E-H.

For the nanosensor work, TSB alone was loaded into assigned wells of a Grenier bio-one, flat-bottomed, black walled 96-well plate (grey sections in **Figure *4.10.1-2***b), whilst 0.5 mg mL^{-1} oxygen nanosensors in TSB were loaded in green section of **Figure *4.10.1-2***b. For column 12, planktonic cells in TSB at 0.05OD were loaded in A, B, G & H (orange), whilst planktonic cells at 0.05OD in 0.5 mg mL^{-1} oxygen nanosensors in TSB were loaded in C-F (blue). Virkon was added to nanosensors in TSB media in column 2, row C-F. For C100 and C0, 0.5 mg mL^{-1} oxygen nanosensors were suspended in deionised H_2O (C100) or 20 mg mL^{-1} sodium sulphite in deionised H_2O (C0).

The plates were loaded into a robotic system, Cheryl2, in order to measure multiple plates via a Varioskan plate reader. The robotics and the plate reader were housed in a cytomat incubator, held at 37^{o}C. Fluorescence intensity was measured every 30 min for 20 h. For the OxoPlate, fluorescence intensity was measured at ex:540 nm, em:590 nm for the reference dye & ex:540 nm, em:650 nm for the indicator dye; whilst for the oxygen nanosensor plates, fluorescence intensity was measured at ex:405 nm, em:650 nm for the platinum (II) porphyrin and ex:540 nm, em:580 nm for TAMRA.

Fluorescence intensity ratio values were calculated by dividing the em:650 nm reading by the em:580 nm reading (for nanosensor work) and em:650 nm by em:590 nm (for OxoPlate work) for each time point. The resultant fluorescence intensity ratio was normalised by dividing the first fluorescence intensity ratio value by itself to create a value of 1; then the proceeding values were divided by the first value.

4.10.2. Crystal Violet assay

0.05% Crystal Violet in H_2O was aliquoted into 96-well plates, before placing the bacteria-incubated peg-lids into the wells and incubating for 30 min. Material coated peg-lids without bacterial incubation were used as a control to remove background absorption from crystal violet staining the material. Peg-lids were transferred to a wash plate with H_2O for 30 min, before being transferred to new H_2O wash plate for another 30 min; before being left to dry. To process the stained peg-lids, 95% ethanol was aliquoted into 96-well plates and the peg-lids were transferred into the wells and incubated for 30 min. To measure the absorption from the crystal violet, a microplate reader was used at 590 nm.

5. Characterisation of pH-sensitive, polyacrylamide nanosensors with *Pseudomonas aeruginosa*

5.1. Introduction

5.1.1. Potential effects of pH

The heterogeneous environment produced within the matrix of a biofilm is a potential side effect of environmental changes facing the embedded microorganisms. Any change in the microenvironment will have an effect on biofilm function and survival, as these changes will be sensed by embedded bacteria and potentially trigger a response that alters the physiology of said bacteria. For example, the contraction in multispecies biofilm thickness has been observed (*Klebsiella pneumoniae*, *Pseudomonas fluorescens*, and *P. aeruginosa*) when irrigation with acidic media (pH 3) occurs, suggesting that localised changes in pH can alter the physical properties of the matrix (Stoodley et al., 1997). Environmental pH is also a contributing factor for the selection and establishment of biofilms. For example, the optimal pH for the planktonic growth of Group B *Streptococcus*, an asymptomatic coloniser in the acidic vagina of pregnant women, is at pH 6.5; however, for Group B *Streptococcus* biofilm formation, the optimal pH is 4.5 (Ho et al., 2013). This indicates a selection condition in the acidic range for optimal bacterial survival, as vaginal pH varies between pH 3.8 to 4.5 (Mania-Pramanik et al., 2008).

As well as environmental pH contributing to the establishment of a biofilm, the generation of an acidic environment by the biofilm itself can also contribute to the pathophysiology of a disease. For example, a change in pH within the lumen of the lung has been detected in patients with cystic fibrosis (CF); when examining both the exhaled breath condensate and airway surface liquid, the pH was lower

in CF patients compared with healthy controls (Tate et al., 2002). This is of importance as CF patients are prone to chronic polymicrobial infections that are characterised by the formation of a biofilm that can incorporate a range of microbes including both *P. aeruginosa* and *S. aureus* (Harrison, 2007, Moreau-Marquis et al., 2008, Filkins and O'Toole, 2015, Hotterbeekx et al., 2017). Therefore, the presence of a biofilm in CF patients may contribute to the lowering of the pH in the airway, causing airway inflammation. In another example, the ECM of an oral biofilm not only provides mechanical support and cohesiveness to a surface, it can also facilitate the formation of highly acidic microenvironments within the biofilm if acidogenic bacteria such as *S. mutans* and Lactobacilli are present. These acidic microenvironments are critical for the pathogenesis of dental caries (Klein et al., 2015). Altogether, these examples might indicate that the generation of an acidic environment may contribute to the pathogenicity of each bacteria.

As well as potentially contributing to the pathophysiology of a disease, could an acidic environment have a protective effect on the biofilm? The ECM does provide short-term protection against the initial diffusion of antimicrobials, such as β-lactams and aminoglycosides into the biofilm (Mulcahy et al., 2008). However not all antimicrobials (*e.g.* fluoroquinolones) have reduced penetration (Costerton et al., 1999). Previous research studied the effects of low pH and cation ion supplementation on the activity of quinolones and aminoglycosides against *P. aeruginosa* (Blaser and Luthy, 1988). Low pH and Ca^{2+} and Mg^{2+} supplements were able to antagonise the action of both classes of antibiotics, however, this study was only carried out on planktonic culture which are more sensitive to antimicrobials when compared to bacteria in biofilms (Flemming and Wingender, 2010). A second study determined the effects of pH on the antimicrobial

susceptibility of planktonic and biofilm-grown clinical *P. aeruginosa* isolates. During planktonic growth under acidic conditions (pH 5.5), tobramycin bactericidal activity against the isolates was reduced, whilst ceftazidime activity was unaffected by changes in pH. Conversely, both tobramycin and ceftazidime were ineffective at eradicating biofilms formed at each pH used (pH 5.5, 6.5, 7 & 7.4) (Moriarty et al., 2007). However, this may be as a result of aminoglycosides, such as tobramycin, exhibiting reduced penetration through the ECM of the biofilm (Tseng et al., 2013). Another example of antimicrobial resistance via pH changes was shown by Wilton et al. (2016); who demonstrated that the acidification of a *P. aeruginosa* culture by eDNA resulted in higher minimal inhibitory concentrations (MICs) for aminoglycosides. The action of eDNA was shown to be two-fold; the acidification of the environment together with cation chelation, both of which induces the expression of genes, including spermidine synthesis, controlled by PhoPQ and PmrAB, a two-component systems (TCS) used to detect limiting Mg^{2+}. The acidification and cation limitation leads to aminoarabinose modification of the lipopolysaccharide (LPS) lipid A moiety (Mulcahy et al., 2008, Wilton et al., 2016). The modification of LPS with aminoarabinose removes the anionic phosphate residues, which in turn masks LPS from interaction with cationic antimicrobials (Hamad et al., 2012). Therefore, aminoarabinose modification, along with the production of spermidine, can reduce outer membrane permeability, which in turn can limit the antimicrobial peptide binding, membrane damage and killing of *P. aeruginosa* by aminoglycosides. Interestingly, the acidic environment produced by eDNA can be neutralised using L-arginine or sodium bicarbonate, whilst the cation limitation can be neutralised by Mg^{2+}; all of which restores aminoglycoside sensitivity (Wilton et al., 2016).

Finally, as well as having a potential effect on the function of antimicrobials, low pH may also have an effect on QS, which would have knock-on effect on biofilm formation and virulence. As mentioned earlier, QS is an interbacterial communications mechanism that is partially responsible for the development of a biofilm in its later stages (Sauer et al., 2002). Research indicates that the threshold of *N*-acylhomoserine lactone (AHL) concentration is dependent on local pH and temperature. The turnover of AHL is attributed to pH-dependent lactonolysis (opening of the homoserine lactone ring). At a pH of <5, AHLs appear to be more stable than at between pH 6 to 8 where some AHL hydrolysis is likely to occur (Yates et al., 2002).

5.1.2. Tools for pH calculations

As mentioned in 1.6.2**,** various tools have been used to measure pH gradients in microbial biofilms including microelectrodes (Schachtele and Jensen, 1982, Lingstrom et al., 1993, De Beer et al., 1994) or microsensors (von Ohle et al., 2010, James et al., 2016). However, these tools are often intrusive or cannot provide horizontal pH gradients and spatial resolution in biofilms (Hidalgo et al., 2009). To move away from these intrusive methods, research has focused on the use of pH-sensitive fluorophores, which can be added to a biofilm. These biofilms can then be imaged via fluorescent microscopy and a quantitative measurement of the pH can be calculated by using the fluorescent intensity of the fluorophore. For instance, the pH-sensitive fluorophore, seminaphthorhodafluor-4F 5-(and-6)-carboxylic acid (C-SNARF-4), has been used to examine the pH microenvironment of biofilms formed by *P. aeruginosa* (Hunter and Beveridge, 2005). The protonation of C-SNARF-4 shifts the emission spectra so that increasing the ion

concentration increases the fluorescent intensity at one wavelength and decreases it at another (the fluorescent emissions for SNARF-4 are measured at 580 nm and 640 nm). As the pH increases from pH 5.6 to 7.6, the intensity at 640 nm increases whilst the intensity at 540 nm decreases. Calculating the ratio from these two wavelengths, a quantitative measurement of pH can be assigned. However, the reported range that this fluorophore is capable of achieving was only between pH 5.6 to 7.6. This lacks the pH range that is offered by the combination of Oregon Green 488 and 6-Carboxyfluorescein fluorophores that has been used in studies by the Aylott lab (Chauhan et al., 2013). C-SNARF-4, used by Hunter and Beveridge (2005), was also used freely with no encapsulation; this can be problematic due to the possible dissemination of the fluorophore and the fluorescence lifetime, which has been shown to change due to pH (Burdikova et al., 2015). Free fluorophores, such as C-SNARF-4, can also interact with non-specific proteins which will interfere with the fluorescence (Graber et al., 1986). However, studies have continued using C-SNARF-4 as a free fluorophore to detect pH changes in bacterial biofilms (Schlafer et al., 2015, Wilton et al., 2016, Schlafer et al., 2011, Dige et al., 2016, Schlafer and Dige, 2016). In a more recent study; C-SNARF-4 was used in combination with Oregon Green 488 in a novel study into the pH heterogeneity within a natural cheese matrix (Burdikova et al., 2015). The introduction of Oregon Green 488 meant that the pH range could be increased to as low as pH 3.5. However, the two fluorophores were again used freely which could lead to inappropriate fluorescence from non-specific binding of proteins. It is also not possible to confirm whether the two fluorophores are co-located, therefore the emission measured will be depend on which fluorophore is present.

More recently, fluorescent silica nanoparticle sensors, or more commonly referred to as nanosensors, have been used to image pH microenvironments in biofilms.

Hidalgo et al. (2009) manufactured pH-sensitive core-shell silica nanosensors using the pH-insensitive dye, Cy5, as the core. The Cy5 was coated in a silica shell that had the pH-sensitive dye, fluorescein, incorporated into. This provided ratiometric readings between pH 4.5-8 and was used to image pH changes in *E. coli* biofilms. Another example of fluorescent silica nanosensors has been used to study the pH gradients formed within *P. fluorescens* biofilms. These nanosensors again contained the pH-sensitive fluorophore, fluorescein, and a pH-insensitive dye, rhodamine B, to provide ratiometric analysis of the pH gradients, between pH 4.5-7.5, throughout a biofilm (Fulaz et al., 2019).

Similarly, studies by the Aylott Lab have used the pH-sensitive fluorophores Oregon Green 488 (OG) (pH~3.50 to 6.00) and 5-(and-6)-Carboxyfluorescein (FAM) (pH ~5.00 to 8) in conjunction with the pH-insensitive fluorophore 5-(and-6)-Carboxytetramethylrhodamine (TAMRA). These three fluorophores (**Figure *5.1.2-1***a) are covalently linked, via a succinimidyl ester group, to an inert cross-linked matrix and encapsulated, in polyacrylamide, to form pH-sensitive nanosensors (**Figure *5.1.2-1***b).

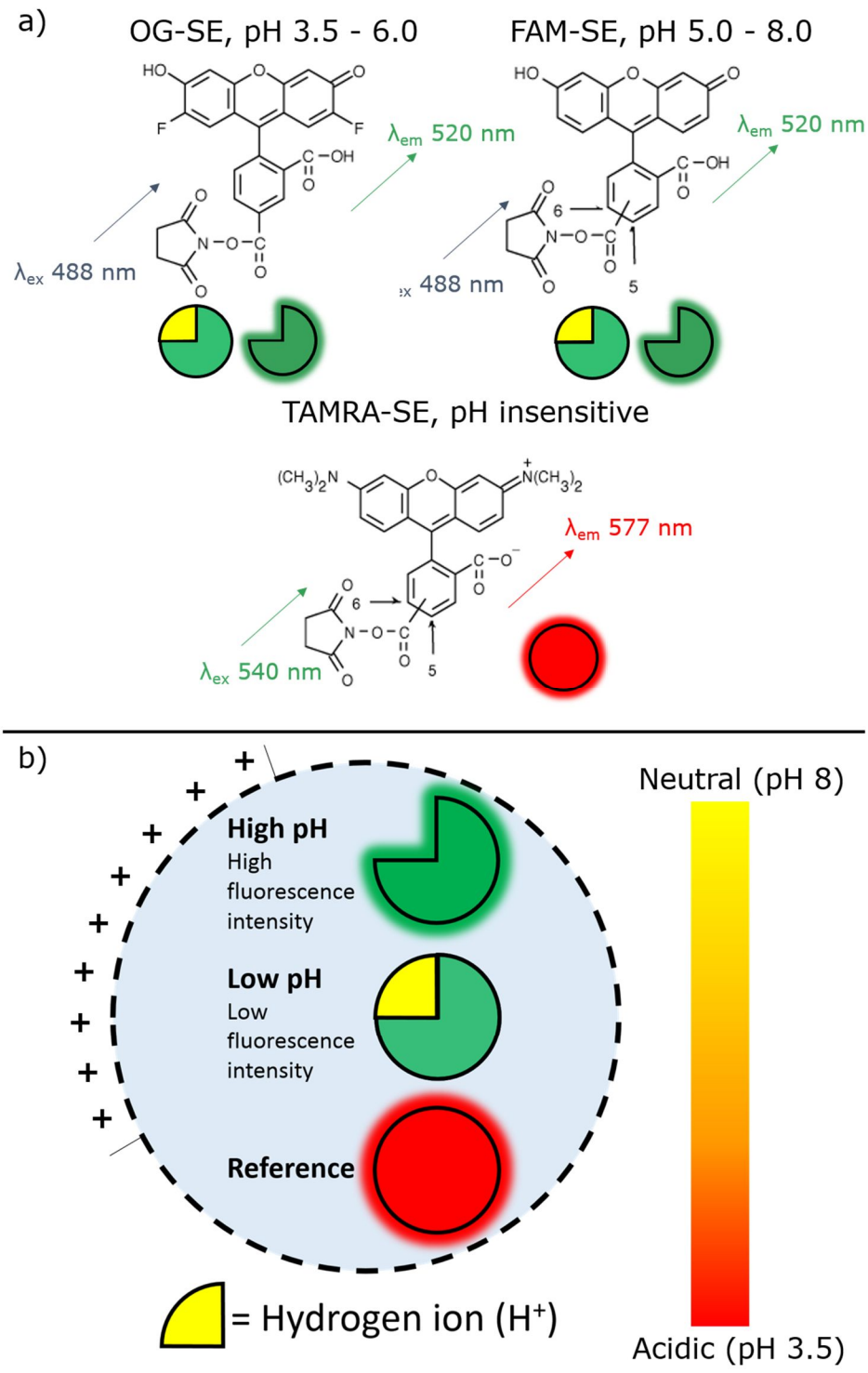

Figure 5.1.2-1: a) Chemical structure of the three fluorophores (OG, FAM & TAMRA), with the succinimidyl ester group, used in the polyacrylamide nanosensors. b) Representative diagram of nanosensors and their mode of action – The matrix protects both the fluorophores and the cellular components. As free protons pass through the matrix, they quench the fluorescence of OG and FAM. The fluorescence from TAMRA remains unaffected. (3-acrylamidopropyl) trimethylammonium chloride (ACTA) is added to provide a net positive surface charge. Modified from Chauhan et al. (2013)

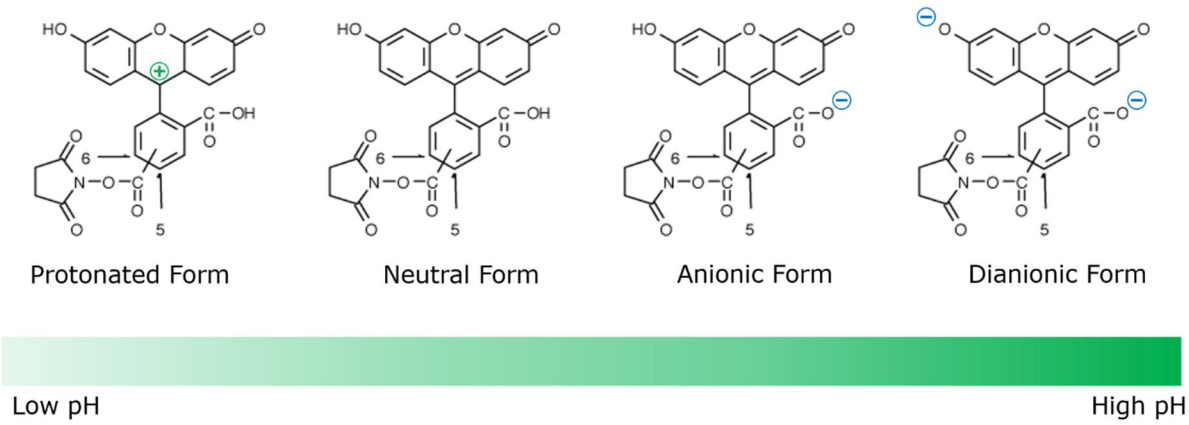

Figure 5.1.2-2: Fluorescent and non-fluorescent form of 5-(and-6)-Carboxyfluorescein (FAM) at different pH – The fluorophore FAM can exist in four forms; protonated, neutral, anionic and dianionic. At high pH, FAM is in its dianionic form, leading to high fluorescence intensity. As the pH decreases, free protons can protonate FAM, leading to the quenching of fluorescence. At its protonated form, FAM fluorescence is completely quenched.

Both FAM and OG are derivatives of fluorescein, a commonly used fluorophore. The pK_a of FAM is 6.5 whilst the pK_a of OG is 4.6. This difference is due to the fluorination of OG, as shown in **Figure *5.1.2-2***a. The addition of fluorine to fluorescein has been shown to cause ionisation at a lower pH due to strong electron-withdrawing properties of the fluorine (Sun et al., 1997). When the pH is higher than the pK_a, the fluorophore is deprotonated, producing high fluorescence intensity. As the pH decreases below the pK_a, the fluorophore becomes protonated, causing quenching of the fluorescence, as shown in ***Figure 5.1.2-1***. Therefore, when OG and FAM are present within a matrix, a wider pH range can be created as the quenching of FAM fluorescence is initiated first, followed by OG. The matrix also provides protection to the fluorophores from cellular components whilst also protecting biological components from free fluorophores (Chauhan et al., 2013). These ratiometric pH-sensitive nanosensors have been used to characterise the dynamic pH conditions of the pharyngeal and intestinal lumen of

Caenorhabditis elegans between the physiological ranges of pH 3 to 8 (Chauhan et al., 2013) and intracellular metabolism of glucose in *Saccharomyces cerevisiae* (Elsutohy et al., 2017). Rather than calculate a fluorescence intensity ratio from two emission wavelengths, as shown by Hunter and Beveridge (2005) and Burdikova et al. (2015), the intensity of emission at 520 nm is compared to the intensity of emission at 577 nm from the pH insensitive fluorophore TAMRA. As the protonation of Oregon Green and FAM increases, the intensity of emission at 520 nm decreases, whilst the intensity of emission at 577 nm remains the same as the pH changes, therefore a ratio can be generated. The final pH resolution is ±0.17 pH units, providing an accurate and non-invasive measurement of dynamic pH changes (Chauhan et al., 2013).

Finally, size and charge may also play a part in the functionality of nanosensors. The hydrophobic/hydrophilic properties of nanoparticles can influence the spatial distribution (Mauline et al., 2013), whilst size is important for the homogenous distribution of nanosensors within a biofilm (Hidalgo et al., 2009). Charge is an important factor for the penetration of antimicrobials or nanoparticles as bacterial biofilms have a net negative charge due to components of the ECM (Zhang et al., 2011). One product of the ECM that provides a negative charge is eDNA, which is present at low basal levels in *P. aeruginosa* culture during initial and mid-log phase of growth, before large quantities are released in the late-log phase of growth (Allesen-Holm et al., 2006). As well as secreting molecules with a negative charge, bacterial cells typically possess a net negative surface charge (Jucker et al., 1996, Gottenbos et al., 1999), due to the presence of carboxyl, phosphate and amino groups (vanderWal et al., 1997) and also lipopolysaccharides (LPS) (Langley and Beveridge, 1999). These surface expressed molecules, as well as eDNA, provide the net negative charge of a bacterial biofilm, which can have an impact on the

initial penetration and the dissemination of both charged antimicrobials and nanoparticles in a biofilm (Javanbakht et al., 2016). For example, penetration of the cationic antimicrobial, tobramycin was shown to be limited in *P. aeruginosa* biofilms, whilst the penetration of a neutral antimicrobial ciprofloxacin was not restricted (Tseng et al., 2013). The restriction of nanoparticle penetration due to particle charge has also been demonstrated; the self-diffusion of anionic nanoparticles into *P. fluorescens* biofilm was reduced due to charge as well as increasing size (Peulen and Wilkinson, 2011). It is therefore important to study the differences between nanoparticle charges to determine which is most suitable for this work.

Altogether, using these encapsulated fluorophores as pH-sensitive nanosensors can offer an unintrusive analytical tool that can produce a spatial distribution of pH ranges within a biological sample such as a biofilm.

5.2. Results

5.2.1. Neutral and cationic polyacrylamide nanosensors were manufactured to determine whether charge alters the interaction of bacteria with nanoparticles

Neutral and cationic nanosensors were produced in order to determine which charge would be suitable for measuring and mapping external pH changes in microbial biofilms.

To verify that the neutral and cationic polyacrylamide nanosensors were appropriately synthesised, each batch was prepared for post-production characterisation to determine the zeta potential and size, as described in 4.2.1. The average yield, size, zeta potential and polydispersal index (PDI) for each nanosensor is listed in **Table *5.2.1-1***.

Table 5.2.1-1: Average yield, size, charge and PDI of cationic and neutral polyacrylamide nanosensors

Parameters	Neutral nanosensors	Cationic nanosensors
Size (nm)	38.18 (±2.88)	44.61 (±2.35)
PDI (A.U.)	0.200 (±0.160)	0.173 (±0.099)
Zeta Potential (mV)	-3.09 (±2.25)	18.18 (±2.359)
Yield (mg)	947.37 (±105.12)	578.26 (±124.21)

Batch-to-batch production of both cationic and neutral polyacrylamide nanosensors was reproducible, resulting in comparable yields as well as consistent size and charge.

5.2.2. Both fluorescence Spectrometer and TECAN plate reader accurately verified the pH-sensitivity of the polyacrylamide nanosensors

To verify that the nanosensors would respond to pH changes, both neutral and cationic polyacrylamide nanosensors were prepared for pH calibration as described in 4.2.2.

The Agilent Fluorescence Spectrometer was initially used to generate an emission scan, as described in **Table *4.2.2-1***. **Figure *5.2.2-1***a) shows an emission scan for neutral nanosensors at 1 mg mL^{-1} in citrate/phosphate buffers ranging from pH 2.5–8, whilst b) shows an emission scan for cationic nanosensors.

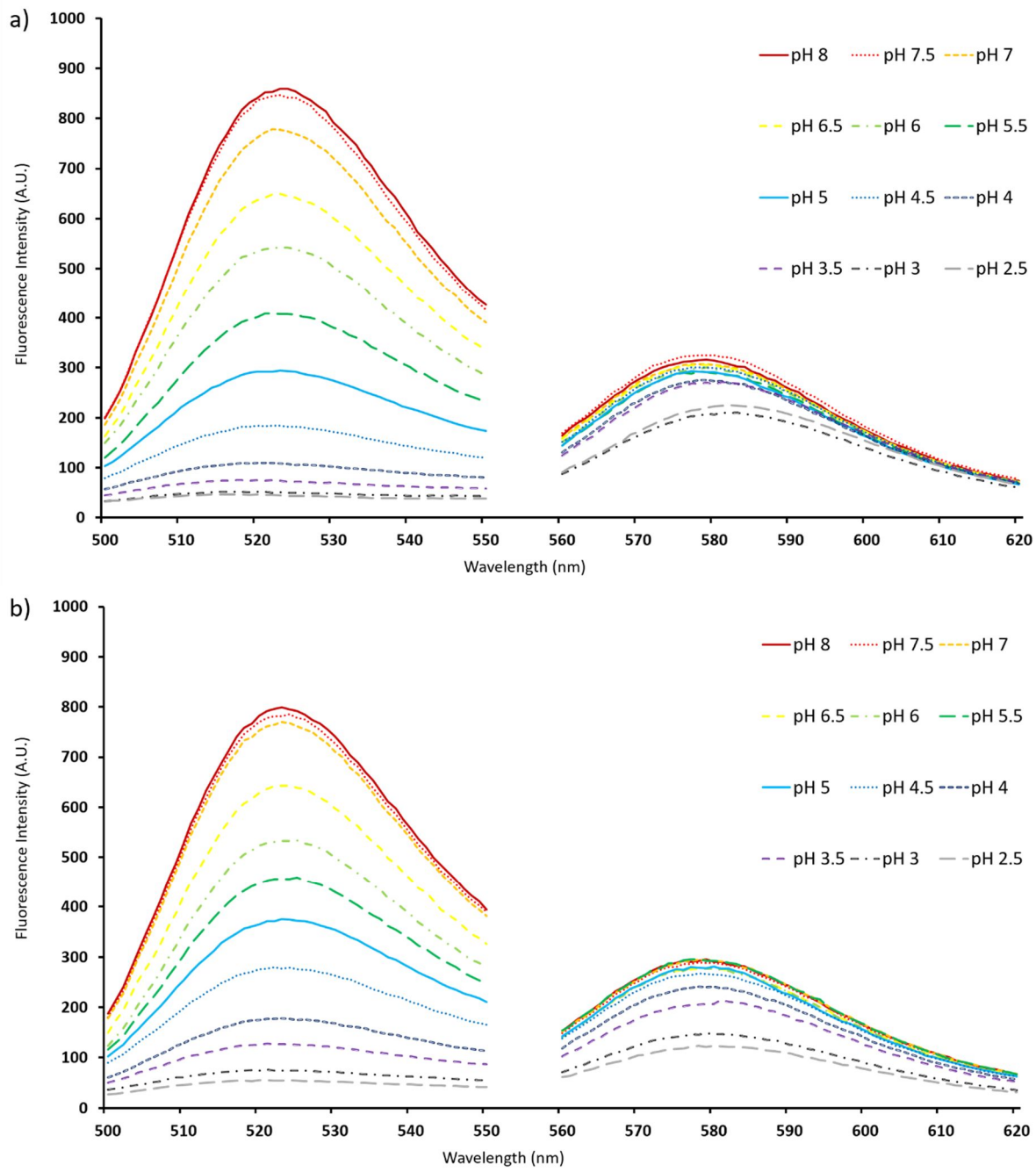

Figure 5.2.2-1: Comparable emission scans for neutral (a) and cationic (b) polyacrylamide nanosensors obtained from a fluorescence spectrometer – Both neutral and cationic pH-sensitive polyacrylamide nanosensors were diluted to a working concentration of 1 mg mL^{-1} in a range of pH buffers (pH 2.5-8). Two emission scans were performed to detect the fluorescence intensity peaks of OG/FAM and TAMRA in the buffered solutions. **Left-side**: ex:488 nm, em:500-550 nm to detect the fluorescence emissions of OG & FAM. **Right-side**: ex:540 nm, em:560-620 nm to detect the fluorescence emissions of TAMRA. n=3.

The first emission scan (left), from 500-600 nm, measured the response of the pH-sensitive fluorophores, OG & FAM. This shows a decrease in fluorescence intensity as the pH decreased (as described in **Figure *5.2.2-1***), with a peak at ~522 nm. The second emission scan (right), from 550-650 nm, shows an almost constant fluorescence intensity for the pH-insensitive fluorophore TAMRA. However, fluorescence intensity is reduced in pH buffers 2.5 & 3. This observation can be explained as TAMRA is known to become sensitive to pH at values at pH 3 and below, due to the eventual protonation of the lone electron pair on the nitrogen double bond (**Figure *5.1.2-1***a), leading to the reduced fluorescence intensity. To calibrate the pH from these results, a ratio can be calculated between OG/FAM and TAMRA, using the maximum fluorescence values (**Figure *5.2.2-2***).

A second method, described in **Table *4.2.2-2***, was used to corroborate results produced in the Fluorescence Spectrometer. The pH calibration was carried out using a TECAN microplate reader, with the results shown in **Figure *5.2.2-2***. Plotting the ratios calculated between OG/FAM and TAMRA; the representative pH calibration curves from the Fluorescence Spectrometer (**Figure *5.2.2-2***a & b) and the TECAN plate reader (**Figure *5.2.2-2***c & d) are comparable, whilst both show a linear increase between pH 3.5 – 7.5. The plateauing seen at both high (> pH 7.5) and low (≤ pH 3) pH indicate pH-insensitivity from OG/FAM and TAMRA, respectively.

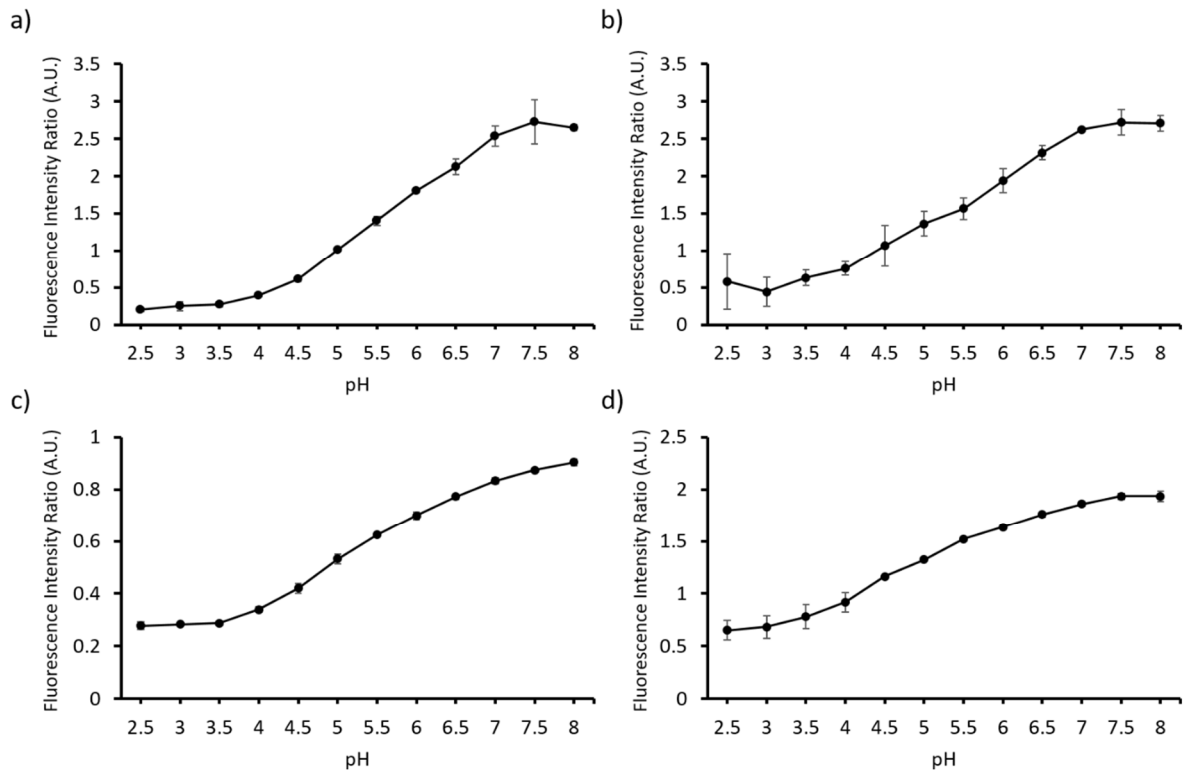

Figure 5.2.2-2: Comparable pH calibration curves of neutral (a&c) and cationic (b&d) polyacrylamide nanosensors using a fluorescence spectrometer (a&b) or a TECAN plate reader (c&d). – pH-sensitive polyacrylamide nanosensors at a working concentration of 1 mg mL^{-1} were added to a range of pH buffers (pH 2.5-8), before the fluorescence intensity of OG/FAM and TAMRA were measured (ex:488 nm, em:520 nm & ex:540 nm, em:580 nm), using either a fluorescence spectrometer **(a&b)** or a TECAN plate reader **(c&d)**. The fluorescence intensity ratio between OG/FAM and TAMRA was calculated and plotted. Error bars are ± 1 S.D. n=3 for spectrometer, n=1 for plate reader.

5.2.3. PAO1-N WT growth is unaffected by low concentrations of polyacrylamide nanosensors

In order to use the polyacrylamide nanosensors in further experiments, it was necessary to determine whether the nanosensors would be detrimental to the growth of bacteria when incubated together. The OD_{600} was taken every 15 min for 18 h with PAO1-N WT grown in LB media and either neutral or cationic polyacrylamide nanosensors ranging from 0.1 to 25 mg mL^{-1}. The resultant absorbance data was normalised, as described in 4.5.1, due to higher concentrations of nanosensors increasing the initial starting OD_{600} reading, causing the growth to be artificially increased. The Area Under to Curve (AUC) was also calculated as described in 4.5.1, and used in each result where AUC is displayed.

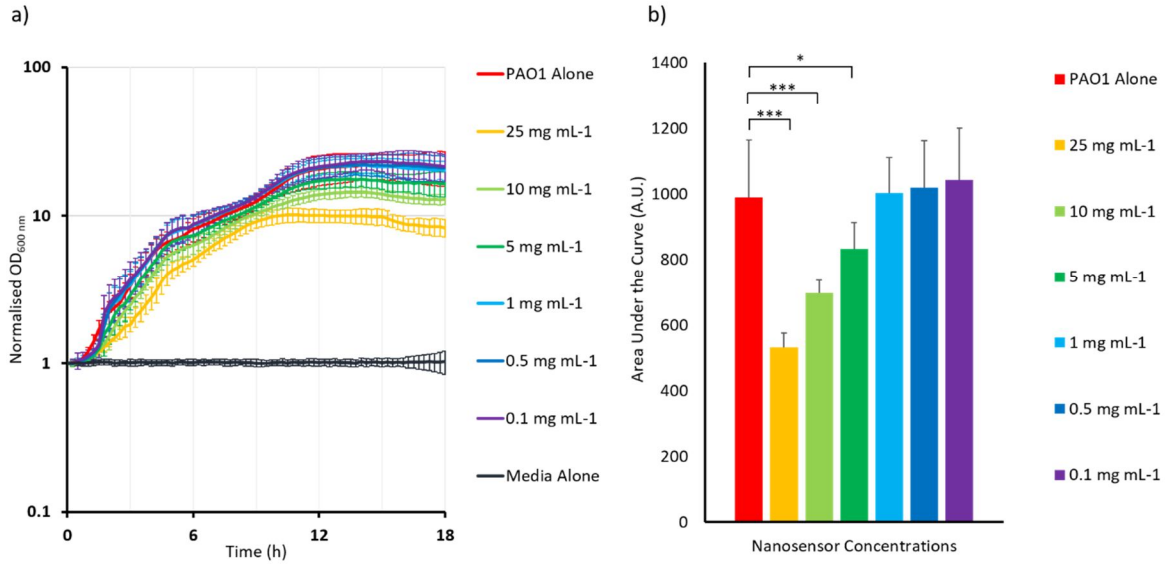

Figure 5.2.3-1: PAO1-N WT growth with neutral polyacrylamide nanosensor is uninhibited below 1 mg mL^{-1} – PAO1-N WT at OD_{600} of 0.05 was incubated in LB media and neutral polyacrylamide nanosensors ranging from 0.1 mg mL^{-1} to 25 mg mL^{-1} for 18 h. (**a**) OD_{600} was measured every 15 min, which was plotted on a log scale against time. (**b**) Area under the curve is represented in the bar chart. Error bars are ± 1 S.D. n=3x3 ***=P<0.001 & * = P<0.05

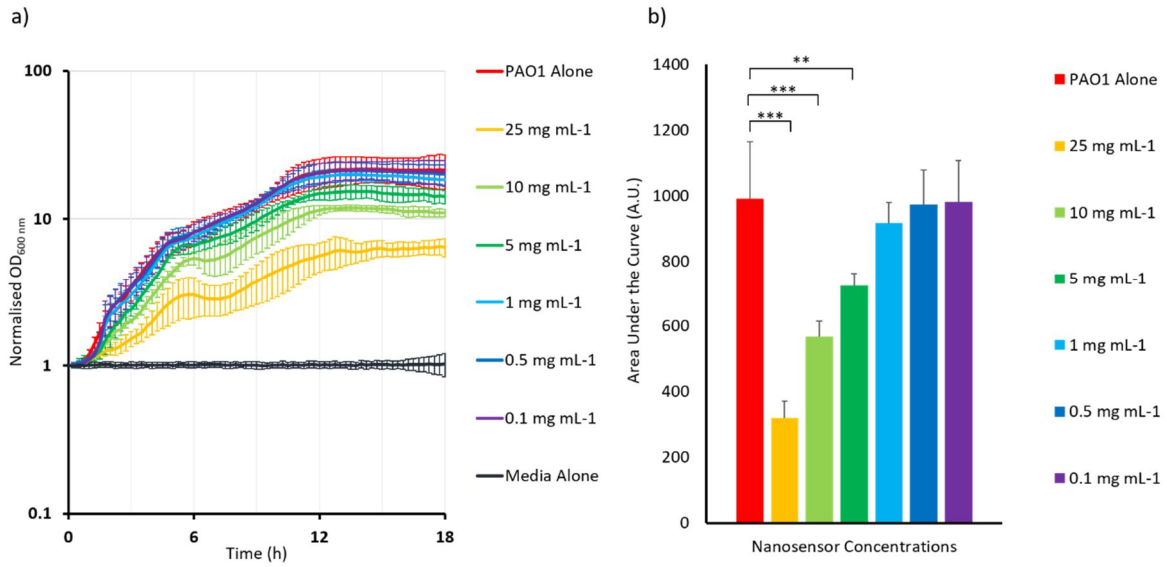

Figure 5.2.3-2: PAO1-N WT growth with cationic polyacrylamide nanosensor is uninhibited below 1 mg mL^{-1} – PAO1-N WT at OD_{600} of 0.05 was incubated in LB media and cationic polyacrylamide nanosensors ranging from 0.1 mg mL^{-1} to 25 mg mL^{-1} for 18 h. (**a**) OD_{600} was measured every 15 min, which was plotted on a log scale against time. (**b**) Area under the curve is represented in the bar chart. Error bars are ± 1 S.D. n=3x3 ***=P<0.001 & * = P<0.05

There is no significant effect in the growth of PAO1-N WT over 18 h when using either neutral or cationic polyacrylamide nanosensors at 1 mg mL^{-1} and below (**Figure *5.2.3-1*** & **Figure *5.2.3-2***). However, growth is significantly reduced when the concentration of the nanosensors was ≥5 mg mL^{-1} (P<0.001 for 25 mg mL^{-1} & 10 mg mL^{-1}, P<0.05 & P<0.005 for 5 mg mL^{-1} neutral and positive respectively).

5.2.4. Cationic polyacrylamide nanosensors interact and coat planktonic PAO1-N WT when incubated overnight

With the purpose of understanding the interaction between planktonic *P. aeruginosa* and polyacrylamide nanosensors, overnight cultures incorporating either neutral or cationic nanosensors were set up, as described in 4.4.

The question was whether the polyacrylamide nanosensors would become internalised during the overnight incubation, or would remain externally within the medium. Overnight cultures were either washed in LB or transferred directly onto 1% agarose before 0.1 µm TetraSpeck™ fluorescent microspheres were added in order to aid alignment of the images during processing. Cells were imaged using a Zeiss PS1 Super Resolution Microscope. Images for both washed and unwashed planktonic cultures with cationic polyacrylamide nanosensors are shown in ***Figure 5.2.4-1*** & ***Figure 5.2.4-2***.

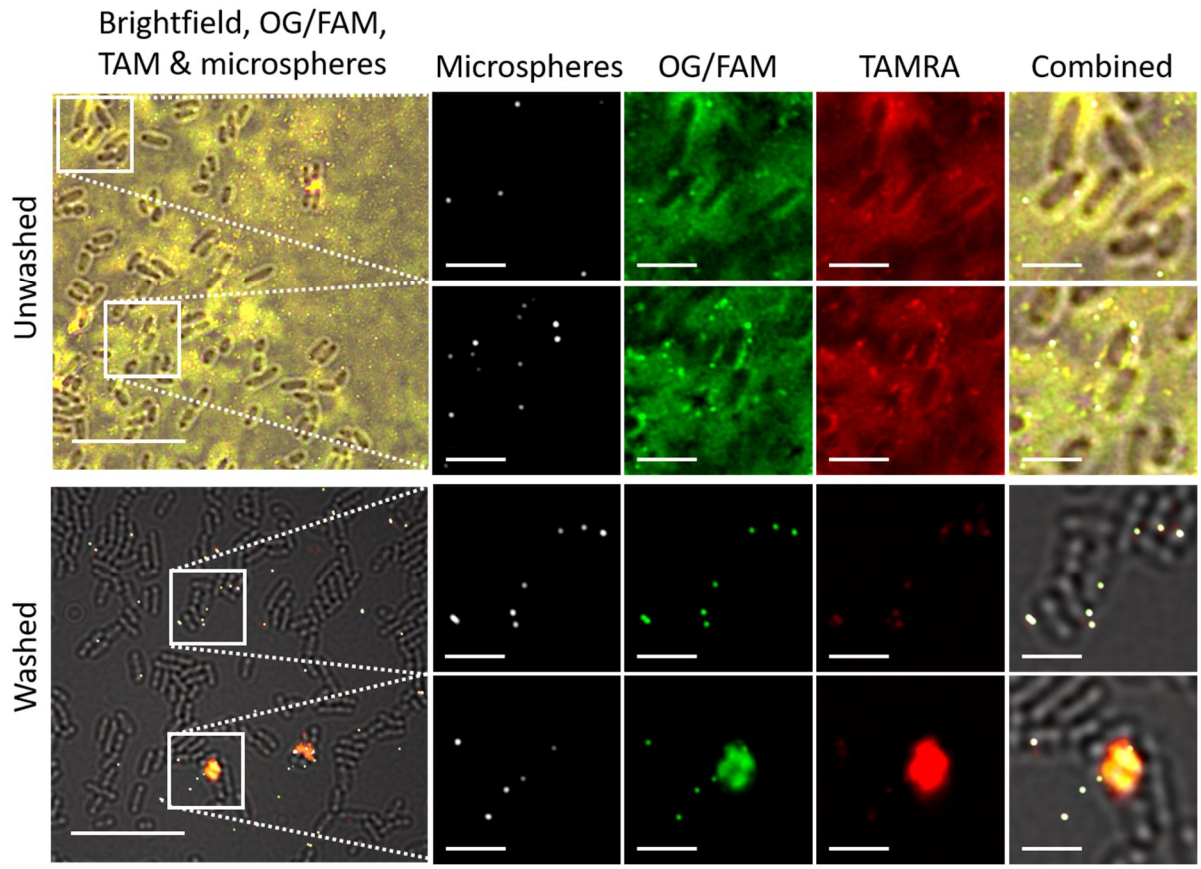

Figure 5.2.4-1: Cationic polyacrylamide nanosensors coat planktonic PAO1-N WT after overnight incubation – After incubation in 1 mg mL^{-1} cationic nanosensors, cells were either loaded onto agarose or washed with LB before loading. 0.1 µm TetraSpeck™ fluorescent microspheres were added before images were taken using a Zeiss PS1 Super Resolution microscope with 63x objective. **Top half**) represents an unwashed region of planktonic PAO1-N WT with two Regions of Interest (ROIs) expanded upon. **Bottom half**) represents a washed region of planktonic PAO1-N WT with two ROIs. PAO1-N WT are coated in the cationic polyacrylamide nanosensors, suggesting interaction. **Scale bar 10 µm** for large panels, 2 µm for small panels. n=1x3

Figure 5.2.4-1 (Top panels) shows PAO1-N WT taken directly from an overnight culture grown with cationic polyacrylamide nanosensors. The two expanded Regions of Interest (ROIs) shows fluorescence from both OG/FAM (ex:488 nm; em:520 nm) and TAMRA (ex:540 nm; em:580 nm) as well as the microspheres (at ex:660 nm; em:680 nm, ex:488 nm; em520 nm, and ex:540 nm; em:580 nm). The OG/FAM and TAMRA fluorescence was most intense surrounding the bacteria. Furthermore, the cationic nanosensors did not appear to have been

internalised by the cells. This is confirmed by the bottom panels of ***Figure 5.2.4-1***, which show PAO1-N WT after washing with LB. Fluorescence in OG/FAM and TAMRA channels were virtually removed with the wash and where regions of fluorescence can still be seen (bottom row of panels), it appears to line up with where larger clusters of cells had formed.

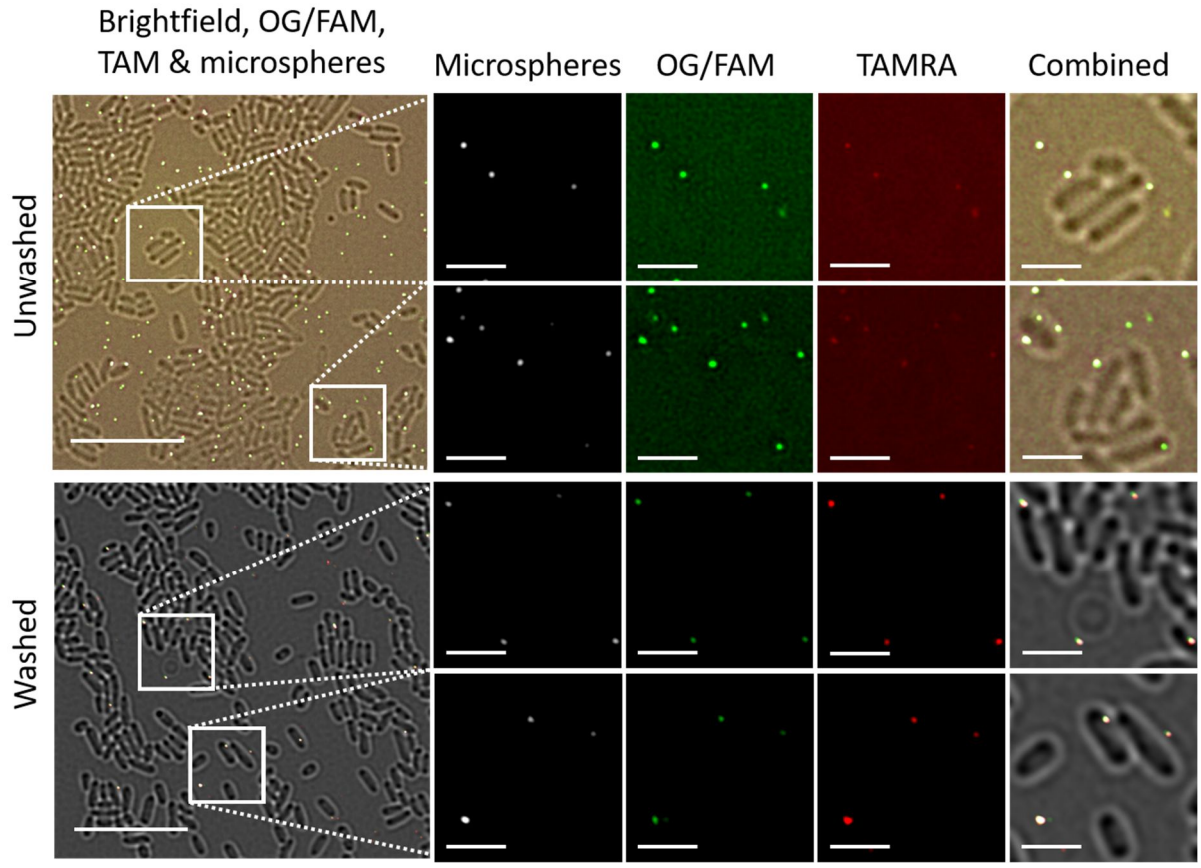

Figure 5.2.4-2: Neutral polyacrylamide nanosensors show no attachment to Planktonic PAO1-N WT overnight incubation – After incubation in 1 mg mL^{-1} neutral nanosensors, cells were either loaded onto agarose or washed with LB before loading. 0.1 µm TetraSpeck™ fluorescent microspheres were added before images were taken using a Zeiss PS1 Super Resolution microscope with 63x objective. **Top half)** represents an unwashed region of planktonic PAO1-N WT with two ROIs expanded upon. **Bottom half**) represents a washed region of planktonic PAO1-N WT with two ROIs. PAO1-N WT incubated overnight in neutral polyacrylamide nanosensors show no attachment to planktonic cells, but fluorescence in the medium; whilst all fluorescence is lost when washed with LB. **Scale bar 10 µm** for large panels, 2 µm for small panels. n=1x3

The interaction of neutral nanosensors (**Figure *5.2.4-2***) with PAO1-N WT is in contrast with cationic nanosensors. The top panels of ***Figure 5.2.4-2*** show PAO1-N WT taken directly from an overnight culture grown with neutral polyacrylamide nanosensors. Fluorescence in both OG/FAM and TAMRA channels is evenly dispersed across the plane of view, rather than interacting with PAO1-N WT, as seen with the cationic nanosensors in ***Figure 5.2.4-1***. Again, the bottom panels represent washed cells. After washing, the fluorescence from the neutral nanosensors is completely absent, matching controls where a culture was grown in absence of nanosensors (***Figure 5.2.4-3***).

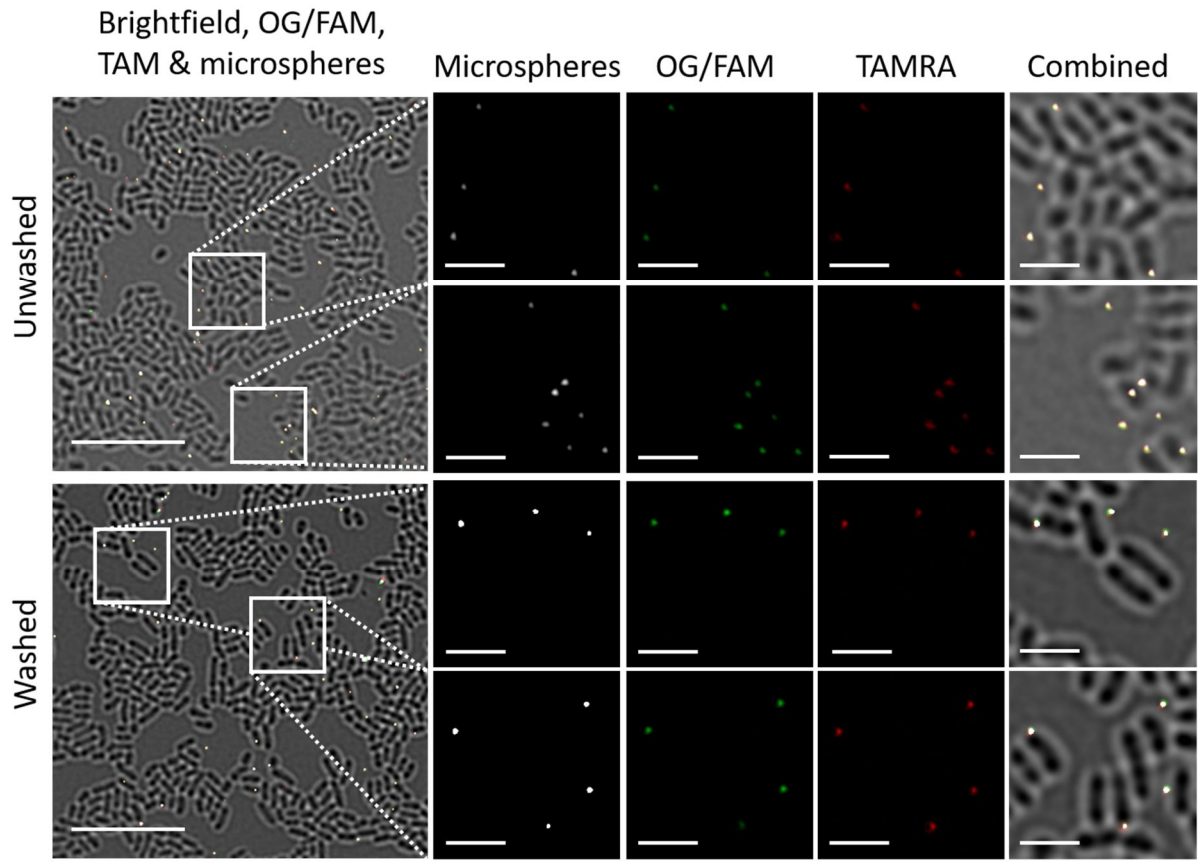

Figure 5.2.4-3: PAO1-N WT grown in absence of nanosensors highlights the absence of fluorescence – PAO1-N WT was either loaded onto agarose or washed with LB before loading. 0.1 µm TetraSpeck™ fluorescent microspheres were added before images were taken using a Zeiss PS1 Super Resolution microscope with 63x objective. **Top half**) represents an unwashed region of planktonic PAO1-N WT with two ROIs expanded upon. **Bottom half**) represents a washed region of planktonic PAO1-N WT with two ROIs. Images highlight the absence of fluorescence when nanosensors are absent from overnight cultures. Fluorescent microspheres were used to calibrate images across each channel. **Scale bar 10 µm** for large panels, 2 µm for small panels. n=1x3

5.2.5. TAMRA and Rhodamine Red-X are not photo stable over an extended period

To elucidate the photostability of each fluorophore used (OG, FAM, TAMRA & Rhodamine Red-X) in the cationic polyacrylamide nanosensors, fluorescence intensity was measured over time in a range of pH buffers (2.5-8), as described in 4.5.3.

Figure *5.2.5-1*a, c & e) shows the fluorescence intensity from the TAMRA-based cationic polyacrylamide nanosensors, whilst **Figure *5.2.5-1***b, d & f) shows the fluorescence intensity from the Rhodamine Red-X-based nanosensors.

Figure *5.2.5-1*a & b) shows the fluorescence intensity of OG & FAM (ex:488 nm, em:520 nm). The fluorescence intensity reduces as the pH reduces, as seen in **Figure *5.2.2-1***. The fluorescence intensity also remains stable over a 21 h period. However, **Figure *5.2.5-1***c & d) shows the fluorescence intensity (em:580 nm) of TAMRA (**c**) & Rhodamine Red-X (**d**) decrease over the same period when excited at 540 nm. The reduction in fluorescence intensity is most noticeable at a lower pH and for TAMRA-based versus Rhodamine Red-X-based nanosensors. Finally, **Figure *5.2.5-1***e & f) shows the fluorescence intensity of TAMRA & Rhodamine Red-X using an excitation wavelength of 570 nm and measuring the emission at 590 nm (as per the manufacturers instructions for Rhodamine Red-X). These results fluctuate between each 15 min reading.

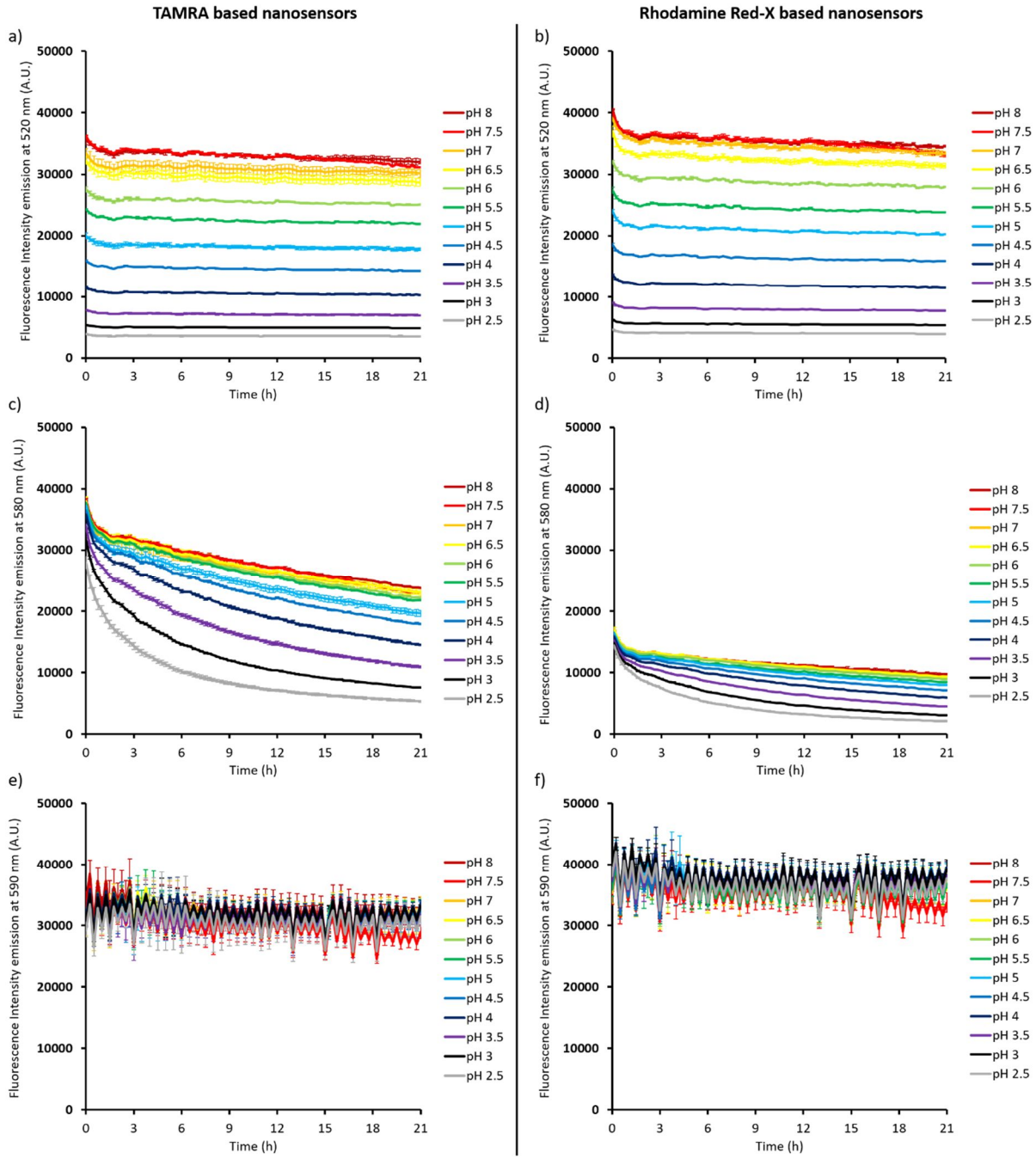

Figure 5.2.5-1: Comparison between TAMRA-based and Rhodamine Red-X-based cationic polyacrylamide nanosensors shows reduced fluorescence intensity (photobleaching) over time – 4 mg mL^{-1} cationic polyacrylamide nanosensors containing either TAMRA or Rhodamine Red-X as a reference dye were suspended 1:10 PBS and diluted to a working concentration of 1 mg mL^{-1} in a range of pH buffers (2.5-8). Fluorescence intensity was measured every 15 min for 21 h at 37^{o}C using: ex:488 nm, em:520 nm for **(a & b)**, ex:540 nm, em:580 nm for **(c & d)**, and ex:570 nm, em:590 nm for **(e & f)**. Error bars are ± 1 S.D n=3x3.

Reducing the number of reads from every 15 min to every 1 h did not improve the photostability of either TAMRA or Rhodamine Red-X (**Supplemental Figure *10-1***), whilst reducing the temperature from 37°C to 25°C, with reads every 15 min, caused fluctuations in the Rhodamine Red-X-based nanosensors (**Supplemental Figure *10-2***).

As Rhodamine Red-X fluorescence intensity decreased over time the least, (**Figure *5.2.5-1***d), further pH work requiring a microplate reader was carried forward using pH-sensitive nanosensors containing Rhodamine Red-X.

5.2.6. Extracellular pH decreases over time as PAO1-N WT metabolises available carbon sources

To reveal whether the pH-sensitive nanosensors could detect pH changes over time in planktonic culture, PAO1-N WT was grown in M9 minimal media with either glucose or succinate as a carbon source, as described in 4.5.4.

Figure *5.2.6-1*a) shows the normalised growth of PAO1-N WT in either M9 glucose or M9 succinate in the presence and absence of 1 mg mL^{-1} cationic nanosensors. There is no apparent difference between growth with and without nanosensors whilst initial growth with succinate as the carbon source appears slightly improved.

Figure *5.2.6-1*b) shows the resultant pH from PAO1-N WT over 21 h when grown in M9 glucose (blue line) or M9 succinate (orange line). The pH was calculated using measurements from pH 2.5-8 buffers with 1 mg mL^{-1} cationic polyacrylamide nanosensors, as shown in **Supplemental Figure *10-3***. A ratio between OG/FAM fluorescence intensity **(a)** and Rhodamine Red-X fluorescence

intensity (ex:540 nm; em:580 nm) **(b)** was created **(c)**. As the pH ratio gradually increases over time due to the fluorescence intensity of Rhodamine Red-X gradually decreasing, the resultant linear regression was calculated every 1 h (*i.e.* 22 are calculated for 0-21 h). The next step was to determine the fluorescence intensity emission from the wells containing PAO1-N WT, as shown in **Supplemental Figure *10-4***. Again, a ratio between OG/FAM fluorescence intensity **(a)** and Rhodamine Red-X fluorescence intensity **(b)** was created **(c)**, which can be converted to a pH value **(d)** using the 'rolling' linear regression calculated from **Supplemental Figure *10-3***c). The difference between pH values from M9 glucose & M9 succinate, with and without PAO1-N WT, were subtracted to produce the final pH values shown in **Figure *5.2.6-1***b).

The final pH values show a slight increase in pH initially for both M9 glucose (pH 7.1 to 7.5) and M9 succinate (pH 6.37 to 6.98) before gradually decreasing from ~7 h onwards to a final pH reading of pH 6.08 (M9 glucose) and pH 5.84 (M9 succinate).

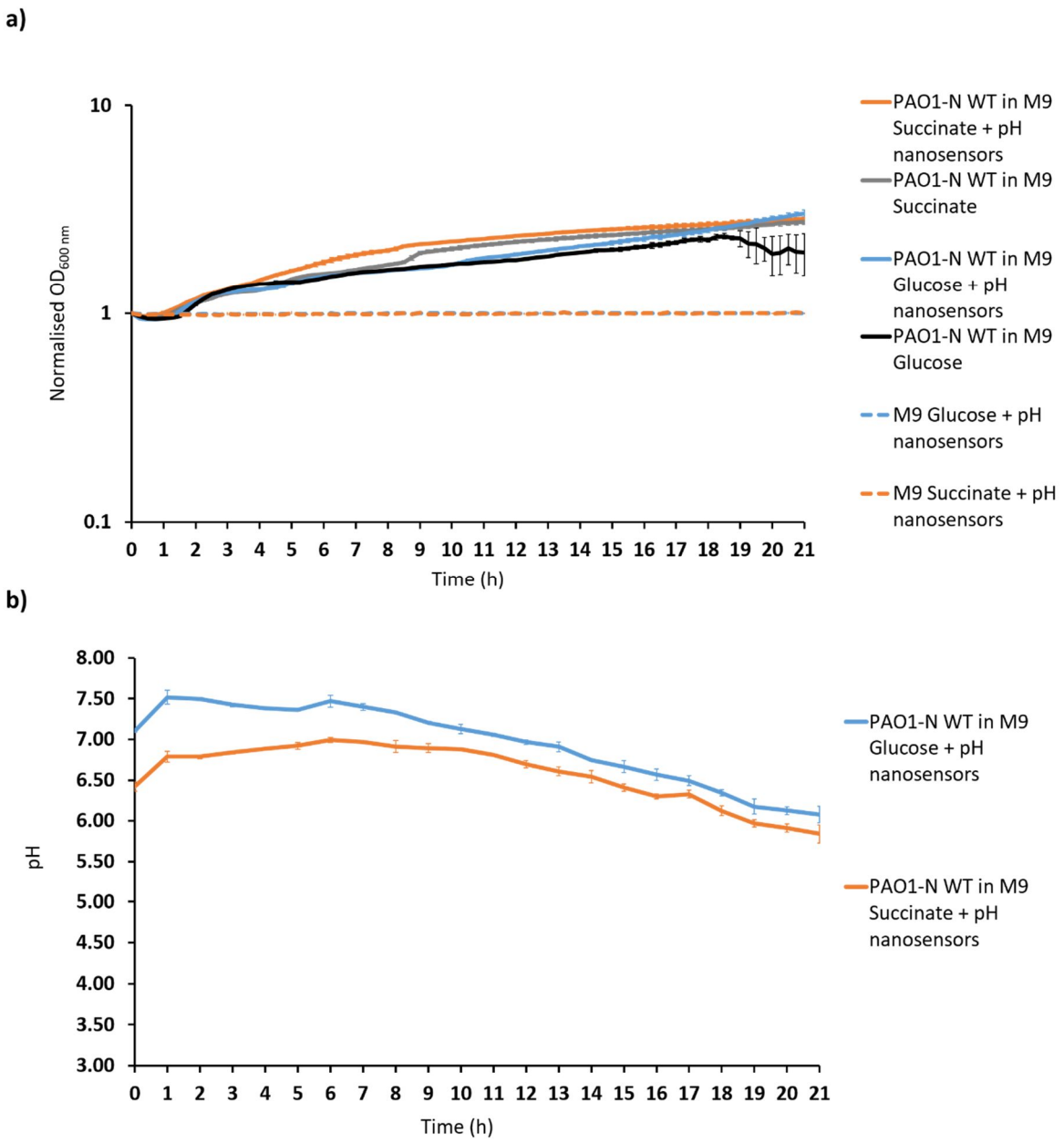

Figure 5.2.6-1: PAO1-N WT growth reduces the extracellular pH over time – 4 mg mL^{-1} cationic polyacrylamide nanosensors containing Rhodamine Red-X as a reference dye were suspended in either M9 glucose or M9 succinate and diluted to a working concentration of 1 mg mL^{-1}. Nanosensors were diluted in either PAO1-N WT at an OD_{600} of 0.05 (solid blue or orange) or M9 media alone (dashed blue or orange). PAO1-N WT was also measured in absence of nanosensors (black or grey line). **(a)** Absorbance at 600 nm was measured every 15 min for 21 h at 37°C. **(b)** Fluorescence intensity was measured using: ex:488 nm, em:520 nm and ex:540 nm, em:580 nm and a fluorescence intensity ratio was calculated. The resultant pH calculated from fluorescence intensity ratio and a 'rolling' linear regression from the fluorescence intensity ratio calculated using pH buffers (pH 2.5-8). Error bars are ± 1 S.D n=3x3.

5.2.7. Generation of static biofilm models of PAO1-N WT with polyacrylamide nanosensors highlight their effects on the biofilm formation and their dispersal throughout the biofilm

To determine the interaction of PAO1-N WT with both neutral and cationic polyacrylamide nanosensors within a biofilm, a static biofilm model was produced, as described in 4.8.1.

Both neutral and cationic nanosensors were added to separate PAO1-N WT suspensions in RPMI for a working concentration of 1 mg mL^{-1} with OD_{600} at 0.05. After 48 h incubation, the resultant biofilm was stained with DAPI (30 µg mL^{-1}) and imaged using a Zeiss confocal laser scanning microscope. In addition to the nanosensors, controls with PAO1-N WT alone were grown and imaged for comparison. The following images represent a biofilm with cationic polyacrylamide nanosensors (**Figure *5.2.7-2***), neutral nanosensors (**Figure *5.2.7-3***) and no nanosensors (**Figure *5.2.7-1***).

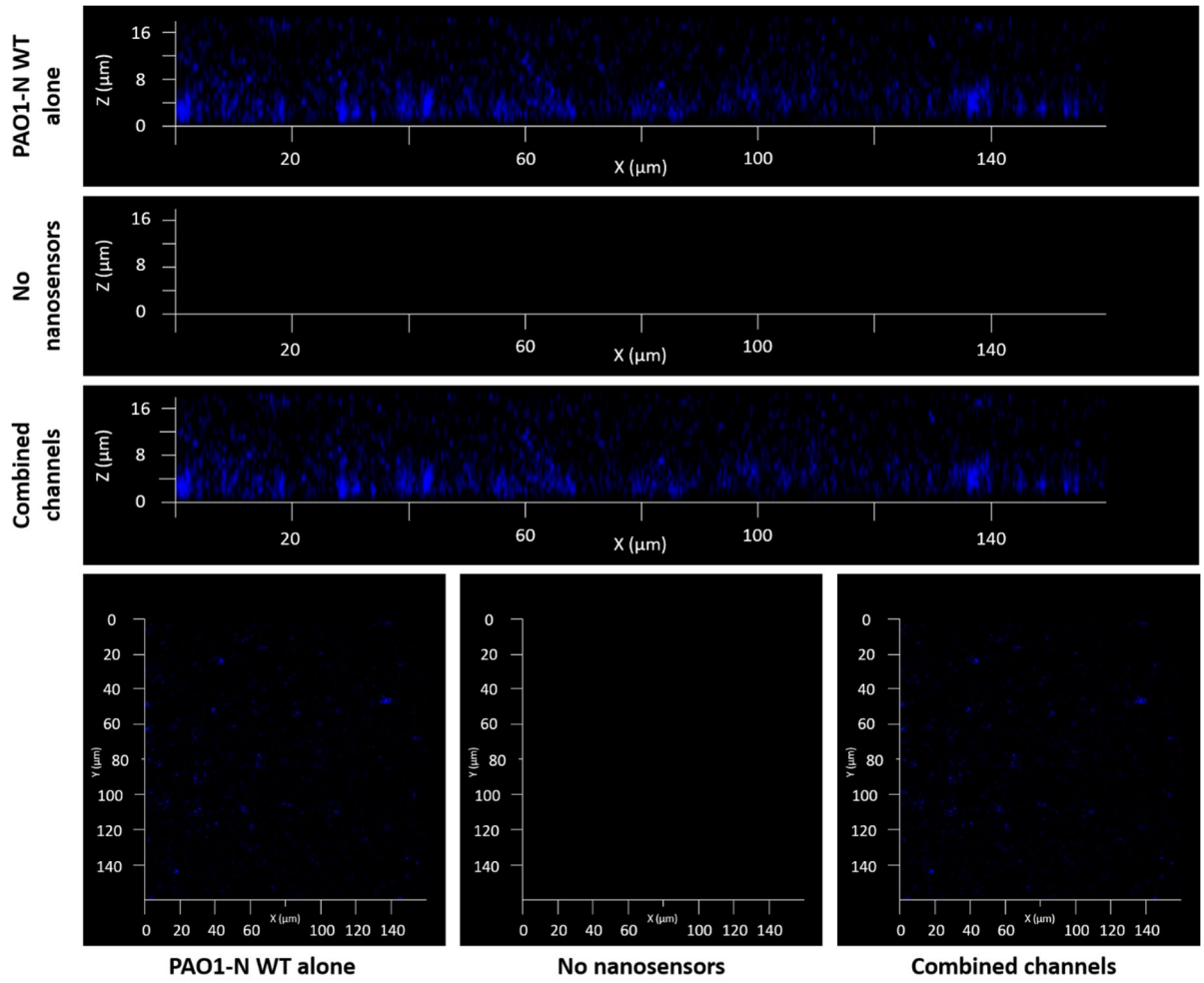

Figure 5.2.7-1: PAO1-N WT biofilm grown in the absence of nanosensors – Representative models of PAO1-N WT grown over 48 h in RPMI with no nanosensors. Images taken with a Zeiss confocal laser scanning microscope with a 40x/1.2na objective **First row**) Side 3D view of DAPI (405 nm excitation). **Second row**) Side 3D view of OG/FAM (488 nm excitation) & TAMRA (555 nm excitation). **Third row**) Side 3D view of overlay image. **Fourth row; left panel**) Top 3D of DAPI. **Fourth row; central panel**) Top 3D view of OG/FAM & TAMRA. **Fourth row; right panel**) Top 3D view of overlay image. No nanosensors (**right**) produce biofilms approximately 8 µm thick. n=3x3

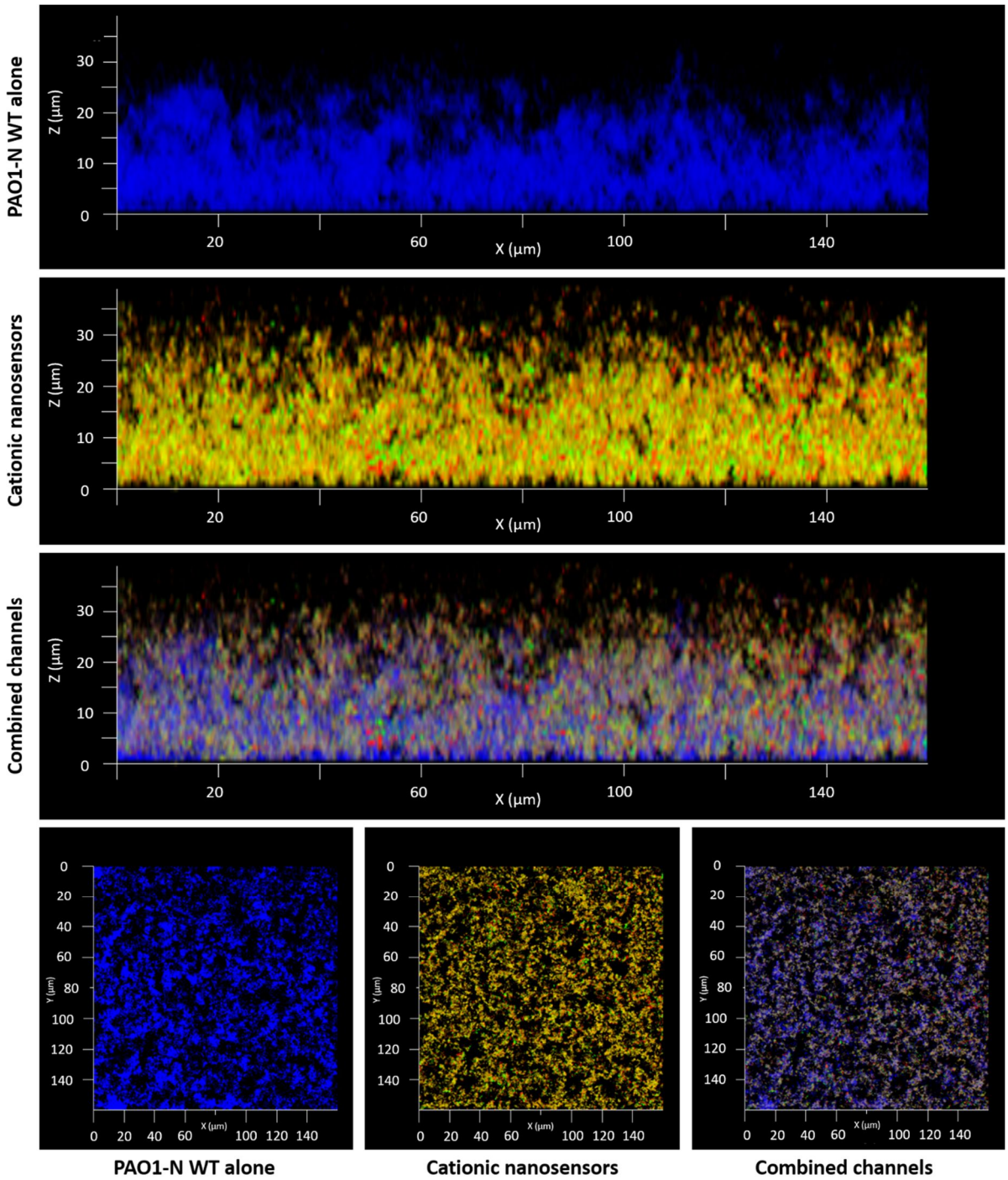

Figure 5.2.7-2: Cationic nanosensors increase the thickness of the PAO1-N WT biofilm – Representative models of PAO1-N WT grown over 48 h in RPMI with 1 mg mL^{-1} cationic nanosensors Images taken with a Zeiss confocal laser scanning microscope with a 40x/1.2na objective. **First row**) Side 3D view of DAPI (405 nm excitation). **Second row**) Side 3D view of OG/FAM (488 nm excitation) & TAMRA (555 nm excitation). **Third row**) Side 3D view of overlay image. **Fourth row; left panel**) Top 3D of DAPI. **Fourth row; central panel**) Top 3D view of OG/FAM & TAMRA. **Fourth row; right panel**) Top 3D view of overlay image. Cationic nanosensors produces a biofilm approximately 30 µm thick with co-localisation between nansensors and cells. n=3x3

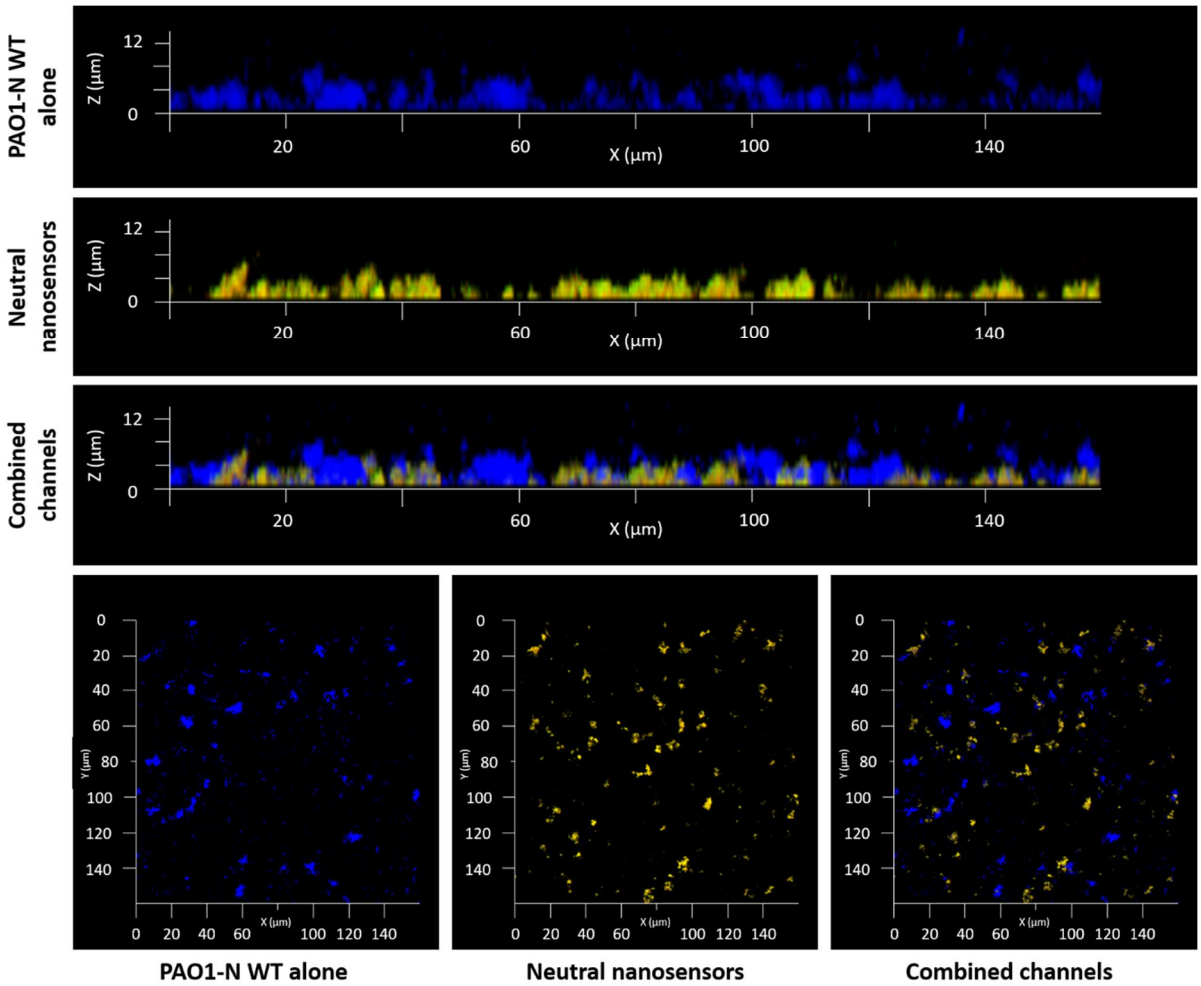

Figure 5.2.7-3: Neutral nanosensors form discrete regions of aggregation amongst the PAO1-N WT biofilm - Representative models of PAO1-N WT grown over 48 h in RPMI with 1 mg mL^{-1} neutral nanosensors. Images taken with a Zeiss confocal laser scanning microscope with a 40x/1.2na objective. **First row**) Side 3D view of DAPI (405 nm excitation). **Second row**) Side 3D view of OG/FAM (488 nm excitation) & TAMRA (555 nm excitation). **Third row**) Side 3D view of overlay image. **Fourth row; left panel**) Top 3D of DAPI. **Fourth row; central panel**) Top 3D view of OG/FAM & TAMRA. **Fourth row; right panel**) Top 3D view of overlay image. Neutral nanosensors produce biofilms approximately 8 µm thick. The neutral nanosensors form discrete regions of aggregation between the cells. n=3x3

A PAO1-N WT biofilm grown for 48 h in RPMI in the absence of nanosensors typically achieves a thickness ~8 μm with small microcolonies (~5 μm -10 μm), using a model representation produced via Confocal Laser Scanning Microscopy (CLSM) (**Figure *5.2.7-1***). The second and fourth row (central panel) shows an absence of fluorescence, as nanosensors were not added.

Both the thickness of the biofilm and the distribution of the nanosensors appears different when comparing a biofilm grown in the presence of cationic polyacrylamide nanosensors (**Figure *5.2.7-2***) and a biofilm grown in the presence of neutral polyacrylamide nanosensors (**Figure *5.2.7-3***). The thickness of the PAO1-N WT biofilm grown with neutral nanosensors biofilm (8- 10 μm) is comparable to PAO1-N WT grown alone. However, the thickness of the PAO1-N WT biofilm grown in the presence of cationic nanosensors is approximately 4x greater. The surface charge on the nanosensors also affects their distribution in a biofilm, as the neutral nanosensors appear to form distinct aggregates distributed between the cells within the biofilm. This is indicated by the yellow regions where OG/FAM and TAMRA are overlain whilst the blue fluorescence (cells stained with DAPI) are separate. In contrast, the cationic polyacrylamide nanosensors appear to co-localise with the bacteria within the biofilm.

5.2.8. Acetic acid treatment is readily detectable by embedded nanosensors in a PAO1-N WT biofilm

To test the nanosensors response to acid treatment, PAO1-N WT was grown with 1 mg mL^{-1} cationic nanosensors embedded within the biofilm, as described in 4.8.2.

After incubation, images were taken before the biofilm was treated with 3% acetic acid, as shown in ***Figure 5.2.8-1***. The fluorescence intensity is markedly changed (***Figure 5.2.8-1***b) by the introduction of an acidic product, shifting from yellow/orange to red, indicating the acidification of the nanosensors and hence the biofilm. This pH change can also be visualised in ***Figure 5.2.8-1***c). Incidentally the addition of the acetic acid also reduces the thickness of the biofilm from approximately 40-50 μm to 25-30 μm (***Figure 5.2.8-1***a).

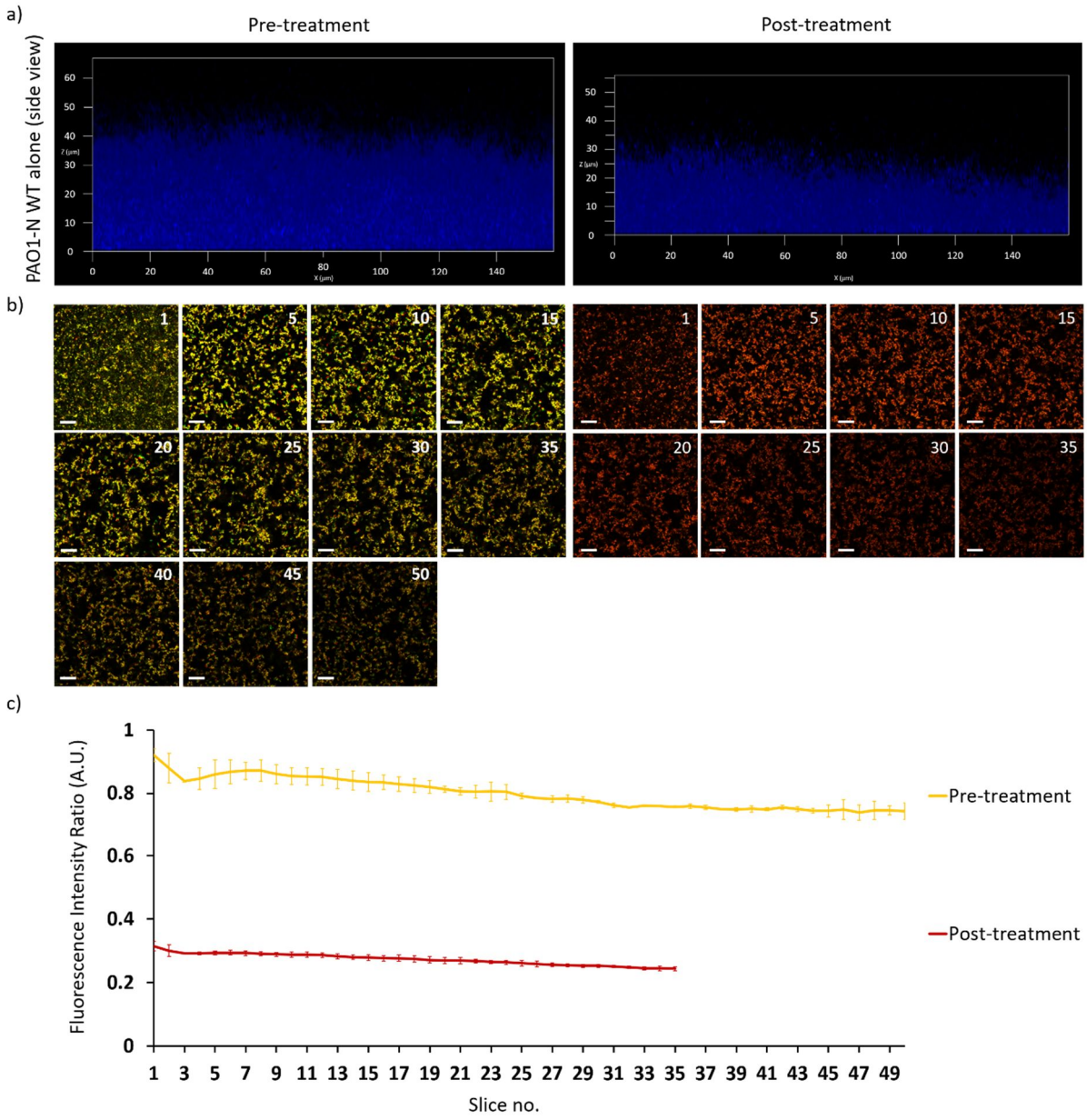

Figure 5.2.8-1: Cationic nanosensors are capable of responding to treatment with 3% acetic acid resulting in comprehensive changes in fluorescence intensity when compared to pre-treated – Representative models of PAO1-N WT grown over 48 h in RPMI with 1 mg mL^{-1} cationic nanosensors. Images were initially taken before 3% acetic acid was added to the medium and left for 30 min. Images were taken with a Zeiss confocal laser scanning microscope with a 40x/1.2na objective. **a)** Side 3D view of DAPI (405 nm excitation) before and after 3% acetic acid treatment. **b)** Slices show the top view of OG/FAM & TAMRA in increments of five. **Scale bar 20 µm**. **c)** Each slice from the subsequent z-stacks taken with CLSM were processed in ImageJ. Fluorescence intensity measurements were taken for both channels (OG/FAM & TAMRA) and a ratio calculated. Slices were taken from the base of the biofilm till the furthest point cells appear on the cross section. Error bars are ± 1 S.D n=2x2.

5.3. Discussion

Previous research has indicated the formation of physicochemical gradients within microbial biofilms (Hunter and Beveridge, 2005, Hidalgo et al., 2009, Fulaz et al., 2019), and the impact an acidic environment can have on treatment methods (Wilton et al., 2016). Therefore, there is a need for novel approaches to probe these microenvironments to determine their effect on biofilm-specific processes. In order to characterise these physicochemical gradients in biofilms, pH-sensitive nanosensors were used in this study.

The first objective was to detect any possible inhibition of growth the nanosensors had with our selected bacterial species. The results of the overnight growth of planktonic PAO1-N WT in increasing concentrations of both neutral and cationic polyacrylamide nanosensors indicate that concentrations up to 1 mg mL^{-1} had no effect on the growth (***Figure 5.2.3-1*** & ***Figure 5.2.3-2***). However, growth with nanosensors at 5 mg mL^{-1} and above was increasingly reduced. The inhibition of growth at ≥ 5 mg mL^{-1} for both neutral and cationic is likely due to an accumulation of the nanosensors on the surface, leading to compromised cellular permeability (Abbaszadegan et al., 2015). The impact on growth was most noticeable with the cationic nanosensors which is likely due to the addition of (3-acrylamidopropyl) trimethylammonium chloride, which has been commonly referred to as ACTA (Elsutohy et al., 2017), APTAC or AMPTMA (Zhou et al., 2017, Li et al., 2018). ACTA was used to introduce a net positive charge in the cationic nanosensors. It is likely the increased concentration of cationic charges led to the retardation in growth (Zhou et al., 2017). Therefore, the working concentration was chosen to be 1 mg mL^{-1}, as the growth of PAO1-N WT was unaffected at this concentration, whilst a balance was needed to be stuck between signal intensity and any potential inhibition in growth.

The second objective was to determine whether the nanosensors remained extracellular. Super-Resolution microscopy was used to determine the interaction of polyacrylamide nanosensors with planktonic PAO1-N WT after overnight incubation in culture; whilst CLSM was used to image and construct 3D representative models of biofilms to study the distribution and interaction of both neutral and cationic polyacrylamide nanosensors with PAO1-N WT in a biofilm. The most apparent difference in both planktonic and biofilm analysis was between the dispersal of neutral and cationic polyacrylamide nanosensors.

First looking at the planktonic data, the representative images taken with the Zeiss PS1 Super-Resolution microscope (***Figure 5.2.4-1*** & ***Figure 5.2.4-2***) show this difference clearly. In the unwashed samples, the cationic nanosensors were coating the rod-shaped cells of PAO1-N WT. Brighter regions were also present where cells were absent; indicating that the cationic nanosensors were likely interacting with excreted products such as eDNA, proteins and exopolysaccharides, as well as with the outer membrane of PAO1-N WT. In order to explain the extracellular clumping, the net charges of the constituent parts of the ECM should be considered. Three major EPS molecules for *P. aeruginosa* are excreted to aid establishment of biofilms. These are Psl, which is neutral (Byrd et al., 2009), Pel which is cationic (Jennings et al., 2015), and alginate which is anionic (Ghafoor et al., 2011). The anionic charge of alginate means that it could be considered as a potential ECM component that could interact with the cationic nanosensors; however, alginate production has been shown to be absent in PAO1 planktonic culture (Wozniak et al., 2003), therefore it is unlikely. Still, treatment with alginate lyase would confirm whether the interaction was in fact with alginate. Another excreted product is eDNA, which also has a anionic charge and is present at low basal levels of *P. aeruginosa* culture during initial and mid-log phase of

growth, before large quantities are released in the late-log phase of growth (Allesen-Holm et al., 2006). At these larger quantities, clumping between cells and eDNA have been shown, indicating eDNA may function to aid cell-to-cell interaction. It is therefore possible that the cationic nanosensors are interacting with the anionic eDNA, but this would require examination in the presence of DNase I to degrade the eDNA to confirm.

The coating of the cells can be explained by the observation that bacteria typically possess a net negative surface charge (Jucker et al., 1996, Gottenbos et al., 1999), due to the presence of carboxyl, phosphate and amino groups (vanderWal et al., 1997) and also lipopolysaccharides (LPS) (Langley and Beveridge, 1999). *P. aeruginosa* PAO1 produces two chemically and antigenically distinct types of O-antigen side chains as part of its LPS; termed A-band LPS and B-band LPS. The A-band LPS is neutral at physiological pH, whilst the B-band LPS is anionic at physiological pH due to the presence of carboxylate groups (Makin and Beveridge, 1996, Langley and Beveridge, 1999, Shephard et al., 2008). The expression of B-band LPS has been shown to increase in proportion to A-band LPS in planktonic culture (Shephard et al., 2010), providing a net anionic charge to the surface of PAO1-N. It is therefore likely that the cationic nanosensors are interacting with B-band LPS, amongst other molecules, causing the coating of the cells. However, this cannot be confirmed until isogenic LPS mutants are used (A^+B^+, A^+B^-, A^-B^+, A^-B^-). Although this would not provide a complete picture of what outer membrane molecules the cationic nanosensors are interacting with. The coating of bacteria by cationic nanoparticles can supported by previous publications, albeit with Gram-positive bacteria (Li et al., 2018). Using a range of Gram-positive bacteria treated with cationic (36-41 mV) block copolymer nanoparticles, a change in ζ potential from negative to positive was seen; indicating the binding of the cationic

nanoparticles to the bacterial surface. Cryo-transmission electron microscopy (cryo-TEM) also showed the accumulation of the nanoparticles around the surface of the *S. aureus* strain BAA40, with the cell wall remaining intact (Li et al., 2018). Conversely, the neutral polyacrylamide nanosensors used in this study were not seen to be interacting with the cells at all; rather, the neutral nanosensors were well dispersed throughout the culture, with no discernible regions of increased fluorescence that were present with the cationic nanosensors. The term neutral is a misnomer as the ζ potential is -3.09 mV (±2.25) (**Table *5.2.1-1***), inferring a slight negative charge. This would explain the dispersal of the nanosensors as a result of an electrostatic barrier between the nanosensors and the bacteria. Similar repulsion was reported in silver nanoparticles, with reduced antibacterial activity in neutral and, in particular, the anionic nanoparticles, as both were repulsive to Gram-positive and Gram-negative bacteria (Abbaszadegan et al., 2015).

Previous nanoparticle work has shown that the introduction of the net positive charge (via ACTA) aids spontaneous internalisation of the nanoparticle by eukaryotic cells (Sun et al., 2009). Super-resolution microscopy was therefore used to determine whether the polyacrylamide nanosensors remained external to bacterial cells. It can be concluded that neither the neutral nor the cationic nanosensors appear to enter the bacterial cells. This was highlighted by the 'washed' samples, as fluorescence was absent (***Figure 5.2.4-1*** & ***Figure 5.2.4-2***). The removal of cationic nanosensors suggests that the nanosensors were interacting weakly with anionic cell surface molecules such as LPS, as previously described. The clumping of fluorescence visualised in ***Figure 5.2.4-1*** (bottom row panel), reinforces the suggestion that the cationic nanosensors interact with extracellular products such as eDNA, as mentioned previously, as eDNA has been shown to cluster with *P. aeruginosa* cells in culture (Allesen-Holm

et al., 2006). The cationic nanosensors are likely to become trapped by the cell clusters that were not thoroughly broken up during washing steps. Whilst the absence of fluorescence in the washed neutral nanosensor images emphasise the idea that the neutral nanosensors remain evenly dispersed and are not interacting with cells and external material.

The third objective was to use the pH-sensitive nanosensors to measure real-time pH changes in PAO1-N WT when grown in two different carbon sources. The first issue to overcome was the photostability of the two pH-insensitive fluorophores, TAMRA and Rhodamine Red-X. **Figure *5.2.5-1***a & b) showed that OG/FAM fluorescence emission remained stable over 21 h in a range of pH buffers; however **Figure *5.2.5-1***c & d) showed the gradual decrease in fluorescence intensity emission at 580 nm for both TAMRA **(c)** and Rhodamine Red-X **(d)** based polyacrylamide nanosensors. This gradual decrease in fluorescence intensity is referred to as photobleaching and would affect resultant pH values, limiting the use of the pH-sensitive nanosensors. The change in the number of reads did not affect the photobleaching of the fluorescence intensity (**Supplemental Figure *10-1***), whilst a reduction in temperature was shown to have an impact on Rhodamine Red-X fluorescence (**Supplemental Figure *10-2***). The fluctuations seen in **Figure *5.2.5-1***e & f) are likely due to the emission bandwidth for the experiment being set at 20 nm, which causes an overlapping of the absorption (ex:570 nm) and emission (em:590 nm) spectra. This is likely to cause the rapidly changing fluorescence intensity emission at 590 nm as the initial excitation wavelength may potentially be detected during the emission measurements.

Rhodamine Red-X-based nanosensors were chosen for pH measurements over time as the photobleaching of fluorescence intensity at 580 nm was reduced, compared to TAMRA. This reduction in the fluorescence intensity emission at

580 nm could be overcome for the calibration step by using a new linear regression calculated from the fluorescence intensity ratio at every 1 h time point (**Supplemental Figure *10-3***c). This would compensate for the gradual increase in the fluorescence intensity ratio. The decrease in fluorescence intensity emission at 580 nm could also be seen in **Supplemental Figure *10-4***, where the fluorescence intensity was measured during PAO1-N WT growth in either M9 glucose or M9 succinate. The fluorescence intensity emission at 580 nm decreased slightly over 21 h for M9 glucose and M9 succinate alone, whilst for M9 Glucose and M9 Succinate with PAO1-N WT the fluorescence intensity emission at 580 nm decreased much more rapidly (**Supplemental Figure *10-4***b). This was in a similar fashion to the fluorescence intensity emission at 520 nm (OG/FAM) (**Supplemental Figure *10-4***a). The resultant fluorescence intensity ratio (FIR) was therefore skewed, due to the decrease in the fluorescence intensity emission at 580 nm, as seen in **Supplemental Figure *10-4***c. Another factor was the change in pH of the medium alone as the temperature increased. This was solved by the subtraction of the difference in pH between PAO1-N WT and the control (nanosensors alone).

The resultant pH calculations (**Figure *5.2.6-1***) showed the pH increasing slightly before decreasing over the 21 h period. The decrease in pH was likely due to the production of CO_2 as the bacterial cells metabolise the carbon sources present in the M9 medium.

The fourth objective was to determine the interaction of the polyacrylamide nanosensors in a biofilm. The observations between cationic and neutral nanosensor distribution in planktonic culture can also be seen during biofilm formation. For the neutral nanosensors, they appear to form distinct aggregates amongst the cells during biofilm formation (**Figure *5.2.7-3***, fourth row; right

panel), whilst the cationic nanosensors were well dispersed throughout the biofilm where they interact with the bacteria. This can be seen by the overlaying of the OG/FAM, TAMRA, and DAPI fluorescence across the images (**Figure *5.2.7-2***, fourth row; right panel). This co-localisation may also be a factor in the different thicknesses of the biofilms reported. The addition of neutral nanosensors led to the formation of biofilms with comparable thickness to biofilms without nanosensors (~8 to 10 μm), as seen in **Figure *5.2.7-1*** (first row). However, the addition of cationic nanosensors led to much thicker biofilms (~30-35 μm) as shown in **Figure *5.2.7-2*** (first row). The charge of the nanosensors may explain this observation, as the cationic nanosensors are interacting with the net negative surface charge of bacteria as previously described. For example, the presence of negatively charged, B-band LPS in planktonic culture likely aids in the reduction of aggregation through repulsion (Shephard et al., 2010). However, it is possible the B-band LPS acts to attract more cationic nanosensors, resulting in the reduction of the surface charge, which in turn may aid the initial aggregation and attachment to a surface. The neutral nanosensors, on the other hand, may potentially be repelled from the cells due to their lack of charge, or may not interact well with components of the ECM such as eDNA. The cationic nanosensors may therefore function to attract and even stick multiple cells together, hence the formation of a thicker biofilm. The combination of the results from the Super-Resolution microscopy and the CLSM lead to the theory that the charge is essential to aiding the formation of thicker biofilms by acting as a 'glue', through the interaction with both cells and external products. Finally, with the Super-resolution images indicating that the nanosensors do not seem enter PAO1-N WT during incubation in a planktonic culture, any pH variation that might be measured using the pH-sensitive polyacrylamide nanosensors would indicate external pH changes

within the biofilm rather than measuring any pH change inside of the cells. Altogether, these results suggest that the cationic nanosensors are more suitable than the neutral nanosensors for biofilm work as the cationic nanosensors are well distributed throughout the biofilm, providing the potential to detect subtle pH changes in the microenvironment.

The final objective was to measure pH changes in biofilms with an acetic acid challenge. The ability of the nanosensors to detect pH changes was demonstrated in the acetic acid assay. Before the biofilm was treated with acetic acid, the pH of the PAO1-N WT biofilm showed a variation as the FIR gradually increased through the biofilm from the top to the bottom (***Figure 5.2.8-1***b & c). This varies from a previous biofilm study using pH-sensitive nanosensors. *P. fluorescens* biofilms were shown to have a more acidic central base with the upper regions of the biofilm becoming more neutral (Fulaz et al., 2019). However, variations in the set-up of their biofilms, such as choice of species (*P. fluorescens* v. *P. aeruginosa*), length of incubation (72 h v. 48 h), and the inclusion of shaking (100 rpm), could influence the formation of acidic microenvironments within a biofilm. For instance, the metabolic activity of the cells and the resultant acidic by-products, including CO_2 and organic acids, as well as the distribution of metabolites are likely to be affected by the method of growth. This serves to highlight the complexities of biofilm research as biofilm growth can vary drastically between studies.

Once the acetic acid was added, the pH change was detected across the whole of the representative image (***Figure 5.2.8-1***). This indicates the nanosensors are capable of detecting pH changes within a biofilm irrigated with acid. Finally, the change in the thickness of the biofilm was likely caused by changes in the physical properties of the biofilm matrix. A similar observation was made when a

multispecies biofilm was irrigated with acidic media, leading to the contraction of the biofilm thickness (Stoodley et al., 1997).

To conclude, the pH-sensitive nanosensors were shown to behave differently when introduced to PAO1-N WT in both culture and biofilm; which is likely due to their charge. Additionally, by using the cationic nanosensors, pH changes could be detected in both bacterial culture and a biofilm, as evidenced during irrigation with acetic acid.

6. Optimisation of oxygen-sensitive, polyacrylamide nanosensor manufacture and their use with *Pseudomonas aeruginosa*

6.1. Introduction

6.1.1. The role of oxygen in microbial biofilms

Chemical gradients are produced as nutrients and oxygen diffuse into a biofilm, whilst metabolic by-products, such as CO_2 and organic acids, are excreted into the ECM encasing the biofilm (Dashper and Reynolds, 1996, McLean et al., 2008, Beyenal and Babauta, 2012). The formation of these gradients can influence the growth of bacteria across the three-dimensional structure, in both single and multispecies biofilm (Werner et al., 2004). For example, nutrient gradients in multispecies biofilms can create niche microenvironments suitable for the location of different microbial species, generated by the availability of nutrients and by-products produced by neighbouring species (Welch et al., 2016). Biofilms also typically form at the liquid-surface interface where oxygen can become a limited resource (Borriello et al., 2004); as the penetration of oxygen can be limited towards the core of microcolonies, creating anaerobic regions within a biofilm (Xu et al., 1998). These gradients help create a complex community that requires studying at the nanoscale.

6.1.1.1. Oxygen availability and biofilm formation

Whilst these chemical gradients are a product of the formation of biofilms, the initial availability of nutrients and oxygen can also influence the initial attachment and eventual formation of a biofilm. For instance, oxygen availability has been shown to influence microbial growth and the formation of biofilm. Uribe-Alvarez et al. (2016) demonstrated the role of oxygen availability on both planktonic

culture and biofilm growth for the facultative anaerobe, *S. epidermidis*. The stationary phase for planktonic growth under aerobic shaking conditions was reached within half the time (~12 h) it took under microaerobic (5% CO_2) and anaerobic conditions (~24-27 h). However, biofilm growth was significantly increased under both microaerobic and anaerobic conditions when compared to static and shaking aerobic conditions. This would suggest the depletion of oxygen may induce a protective state for *S. epidermidis* to enter. One such locus linked to this action is the intercellular adhesion (*ica*) operon. Under anaerobic conditions, *ica* gene expression is dramatically increased, leading to the production of polysaccharide intercellular adhesion (PIA), an extracellular polysaccharide that mediates the cell-cell adhesion of both *S. aureus* and *S. epidermidis*; increasing biofilm formation in both species under anaerobic conditions (Cramton et al., 2001, Arciola et al., 2015). Similar effects were seen as Gupta et al. (2016) used a range of oxygen conditions to highlight the effects oxygen availability had on planktonic growth and biofilm formation of laboratory and clinical strains of *S. aureus, P. aeruginosa* and *K. pneumoniae.* Under oxygen-limiting conditions (anoxic - 0%, hypoxic - 7-9% O_2 & 5% CO_2), the planktonic growth of *S. aureus* strains SH1000 and FPR3757 was restricted compared to normoxic oxygen levels (20.8% O_2), whilst growth under hyperoxic (95-99% O_2) was vastly improved. Conversely, *K. pneumoniae* strains AZ1169 and ATCC 33495 planktonic growth was only reduced under anaerobic conditions whilst unaffected under other conditions. Finally, *P. aeruginosa* strains PA14 and PaA planktonic growth only appeared affected under anoxic conditions whilst normoxic growth sharply decreased after 20 h. These results highlight the vast range of effects oxygen availability have on planktonic growth; however, given all three species are facultative anaerobes, each species preferentially uses aerobic respiration for

planktonic growth (Alvarez-Ortega and Harwood, 2007). Equally, oxygen concentration does not always significantly affect biofilm formation, as Gupta et al. (2016) highlighted. Biofilm mass was unaffected in four of the six strains when comparing normoxic oxygen levels to anoxic, hypoxic, and hyperoxic. However, SH1000 and PA14 both produced significantly greater biomass under hyperoxic conditions. This is where accurately measuring real-time oxygen availability may be beneficial to understand using oxygen availability as a preventative method to combat biofilm formation.

6.1.1.2. Oxygen availability and bacterial signalling

To understand why oxygen availability has an effect on biofilm formation, we must understand how bacteria have adapted to these extreme conditions and what molecular cell signalling is involved. QS, the interbacterial communication system, is influenced by oxygen availability. Similar to the action of pH on the structure of N-Acyl homoserine lactone (AHL), as discussed in 5.1.1, oxygen has been shown to be a key substrate in the synthesis of the *Pseudomonas* quinolone signal (PQS). PQS is a vital QS molecule that regulates virulence factors, as well as a separate arm of QS (*las* and *rhl*) and, more importantly, biofilm formation (Diggle et al., 2006). The role of PQS in biofilm formation can be linked to the release of eDNA, as PQS can induce autolysis of a sub-population of cells, leading to an increase in eDNA (D'Argenio et al., 2002, Allesen-Holm et al., 2006). The precursor to PQS, 2-heptyl-4-quinolone (HHQ), is hydroxylated by the FAD-dependent mono-oxygenase, PqsH, to generate PQS (Lin et al., 2018); in the absence of oxygen, PQS is not produced (Schertzer et al., 2010). Therefore, the implication is that biofilm formation in the absence of oxygen could be reduced due to the absence of PQS. PQS has also been demonstrated to inhibit the denitrification process in

P. aeruginosa, interfering with a mode of anaerobic respiration, suggesting a control mechanism when oxygen is present (Toyofuku et al., 2008).

Another quinolone, albeit one that is not active in QS, has a role in interfering with the respiratory system of *P. aeruginosa* (Thierbach et al., 2019). 2-n-heptyl-4-hydroxyquinoline-N-oxide (HQNO) inhibits the cytochrome bc_1 complex (Complex III in the electron transport chain), by binding to the Q_i site of the cytochrome bc_1 complex. This binding disrupts the flow of electrons from the cytochrome bc_1 complex to cytochrome *c,* causing the electrons to be donated to oxygen, which in turn produces reactive oxygen species (ROS) (Hazan et al., 2016). The production of ROS leads to autolysis of the bacterial cell and the release of key components of the ECM, such as eDNA (Turnbull et al., 2016). Therefore, the generation of HQNO by *P. aeruginosa* can induce cell lysis and promote biofilm formation (Hazan et al., 2016). Altogether, these are key examples of the influence oxygen can have on the signalling between bacterial cells, which can inform the response of bacteria to environmental changes.

6.1.2. Adaptation to oxygen stresses

Microbes are also capable of adapting under extreme oxygen environments, typically requiring oxygen-limiting conditions for biofilm development. The following adaptations are examples of *P. aeruginosa* in oxygen-limiting conditions. *P. aeruginosa* encodes all three ribonuclease reductase (RNR) classes (Ia, II and III). RNRs are a family of enzymes solely responsible for the *de novo* synthesis of deoxyribonucleotides (dNTP) and are therefore essential for DNA synthesis and repair (Crespo et al., 2016). RNR class Ia are oxygen dependent, class II are

oxygen independent and class III oxygen sensitive (Sjoberg and Torrents, 2011). The action of class II and III RNRs have been demonstrated to be essential for cell division in biofilm development and maturation, with biofilm formation drastically reduced when either class II or class III enzyme is knocked out (Crespo et al., 2016). Another example of *P. aeruginosa* adapting to oxygen-limitation is with aerobic terminal oxidases. *P. aeruginosa* encodes five aerobic terminal oxidases; the cyanide-insensitive cytochrome bd-like oxidase (CIO), the cytochrome bo_3 oxidase (CYO), the aa_3-type cytochrome *c* oxidase (aa_3), and two cbb_3-type cytochrome *c* oxidases, cbb_3 oxidase 1 (cbb_3-1) and cbb_3 oxidase 2 (cbb_3-2) (Jo et al., 2014, Arai et al., 2014, Liang et al., 2020). The role of the terminal oxidases is to catalyse the four-electron reduction of molecular oxygen to H_2O in the electron transport chain, which is the final step of aerobic respiration (Arai et al., 2014). CIO, CYO and aa_3 have low oxygen affinity, meaning they are ideally suited for respiration when oxygen is in abundance; whilst cbb_3-1 and cbb_3-2 have high oxygen affinity, meaning they function under oxygen-limited conditions (Jo et al., 2014). Incidentally, cbb_3-1 is expressed at high levels throughout growth at all concentrations of oxygen, meaning that *P. aeruginosa* is prepared for aerobic respiration when faced with oxygen-limitation without the need for a transcriptional response (Alvarez-Ortega and Harwood, 2007). These terminal oxidases play a role in the survival of *P. aeruginosa* in Cystic Fibrosis (CF) patients, where biofilms are established within the mucoidal airways of a CF patient. These mucoid regions contain steep hypoxic gradients due to an increase in epithelial oxygen consumption below the mucus masses (Worlitzsch et al., 2002). With the aid of the terminal oxidases, *P. aeruginosa* is able to transition from an oxygenated airway to infecting the built-up mucus, where it is able to establish a biofilm in oxygen-limited conditions. Here, *P. aeruginosa* has been demonstrated

to survive by microaerobic respiration, rather than solely on anaerobic nitrate respiration (Alvarez-Ortega and Harwood, 2007). However, it is likely both processes are used as *P. aeruginosa* is capable of using nitrate as an alternative electron acceptor; as nitrate is reduced to nitrogen oxides by denitrification enzymes, leading to these nitrogen oxides acting as an alternative election acceptor (Arai, 2011).

Another adaptation by *P. aeruginosa* to oxygen stress is the production of extracellular components that can generate oxygen limitation. This appears with the typically non-mucoid *P. aeruginosa* strain PAO1. Under oxygen rich conditions, Sabra et al. (2002) demonstrated a mucoid phenotype with the production of a exopolysaccharide coating (likely alginate) on the cell surface of PAO1. PAO1 was also shown to reduce the transfer rate of oxygen from the gas into the liquid phase, creating hypoxic conditions in the liquid culture. The exopolysaccharide, alginate, is a key component of mucoidal strains of *P. aeruginosa*, and is a contributing factor to biofilms established in CF patients (Pedersen et al., 1992). For example, the expression of alginate by *P. aeruginosa* has been shown to aid in the coinfection of *S. aureus* in CF patients by inhibiting the action of anti-*S. aureus* secreted factors (Limoli et al., 2017). In a biofilm, alginate has also been shown to limit oxygen transportation to cells below (Hassett, 1996); when alginate was layered on top of *Pseudomonas*, growth was limited compared to controls. However, when the *Pseudomonas* was supplemented with nitrate, growth was less limited due to nitrate being used as an alternative electron acceptor.

These adaptations by *P. aeruginosa* point towards a bacterial species that is capable of surviving in fluctuating oxygen conditions whilst being able to adjust the environment to best suit its survival.

6.1.3. Biogeography in biofilms

In vivo biofilms are often multispecies, with the potential to combine obligate anaerobes and aerobes with facultative anaerobes, microaerophiles and aerotolerant organisms (Welch et al., 2016). The demand for oxygen can therefore create strata and specialised architecture either to limit the presence of oxygen or to allow access (De Beer et al., 1994, Xu et al., 1998). For example, oral biofilms consist of a host of microbes, with a range of aerobic and anaerobic respiration. Biogeography studies have shown that distinct strata can form in *in vitro* oral biofilms (Welch et al., 2016). Aerobes, such as *Corynebacterium* were shown to form needle-like structures throughout an *in vitro* biofilm to provide stability; whilst facultative anaerobes, such as *S. mutans* were present towards the surface, covering the needle structures. Here, *S. mutans* could consume dietary sugars and oxygen, whilst producing CO_2 and organic acids such as acetate and lactate. These by-products provide nutrients for anaerobes, such as *Veillonella spp.,* and are protected from oxygen (Delwiche et al., 1985, Periasamy and Kolenbrander, 2010, Welch et al., 2016). The formation of strata can therefore explain how anaerobic bacteria are capable of surviving in a biofilm with aerated liquid constantly passing across the surface, through the process of oxygen limitation (Stewart and Franklin, 2008).

When studying single species biofilms, such as those of the facultative anaerobe *P. aeruginosa*, stratification is still present. Static *P. aeruginosa* has been shown to produce stratified biofilms with metabolically active cells towards the surface where oxygen could penetrate, and inactive cells below (Werner et al., 2004, Folsom et al., 2010). The inactivity shown in Werner et al. (2004), was due to the inability of *P. aeruginosa* to anaerobically metabolise the TSA media provided. However, if a nitrate substitute was used, the cells may not have become inactive

as *P. aeruginosa* is capable of using nitrate as an alternative electron acceptor, as mentioned above. Distinct structures have also been detected within aerobic biofilms; for example, horizontal channels and vertical voids have been shown surrounding dense cell clusters. These voids were demonstrated to facilitate the transport of oxygen from the bulk liquid through the biofilm itself (De Beer et al., 1994).

6.1.4. Potential effects of oxygen availability

Biofilms are less tolerant to antimicrobial treatment than planktonic cells, as discussed previously in 1.4. However, the limited action of certain antimicrobials is not just restricted to a lack of penetration and subsequent transportation through the biofilm; another factor affecting antimicrobial killing and increased tolerance is oxygen limitation (Walters et al., 2003, Borriello et al., 2004).

Certain antimicrobials used to treat bacterial infection require active cells for their internalisation. For example, aminoglycosides rely on proton motive force (PMF) for their uptake into the bacterial cell; with limited entry in non-respiring bacteria (Radlinski et al., 2019). As discussed above, anaerobic regions can form within biofilms, where cells can become metabolically inactive. These cells are typically referred to as persister cells (Wood et al., 2013). As the action of some antimicrobials require active cells using aerobic respiration, the susceptibility of bacteria to antimicrobials can change.

Gupta et al. (2016) demonstrated the effects of oxygen availability on the minimum inhibitory concentration (MIC) for a range of antimicrobials on both laboratory and clinical strains of *S. aureus, P. aeruginosa* and *K. pneumoniae.* For the *S. aureus* strain FPR 3757, increased MICs were apparent for a range of

antimicrobials when conducted under anoxic conditions; including the aminoglycosides (gentamicin, amikacin, tobramycin & kanamycin) and the β-lactams (Meropenem, doripenem, ampicillin & piperacillin/tazobactam). Similar increases in aminoglycoside MICs for *S. aureus* SH1000 were also seen. The reduced susceptibility of *S. aureus* to aminoglycosides is due to the antimicrobial's requirement for active electron transport, which enables uptake into the cell. In the absence of oxygen, aminoglycoside uptake is reduced (Krause et al., 2016). β-lactam susceptibility was also reduced in anoxic conditions for *S. aureus*. β-lactams bind to penicillin-binding proteins (PBPs) on the cell membrane where they inhibit bacterial cell wall synthesis (Zapun et al., 2008). Reduced oxygen may reduce PBP expression or the affinity of β-lactams (Gupta et al., 2016). For the *K. pneumoniae* strains AZ1169 and ATCC 33495, the macrolide azithromycin showed the most significant increase in MICs across all oxygen conditions (anoxic, hypoxic & hyperoxic) when compared to normoxic conditions. This reduced susceptibility in both oxygen-limiting and oxygen-rich environments may be due to the modification of azithromycin targets under different oxygen environments (Gupta et al., 2016). Finally, for *P. aeruginosa* strains PA14 and PaA*,* a reduction in the MICs to tetracyclines in anoxic, hypoxic and hyperoxic conditions were seen. This suggests both oxygen-limiting and oxygen-rich environments are playing a role in downregulating pathways protecting against tetracyclines (Gupta et al., 2016).

Similar results were shown by Walters et al. (2003) who treated *P. aeruginosa* biofilms with ciprofloxacin (a fluoroquinolone) and tobramycin. As mentioned above, tobramycin is an aminoglycoside, whose uptake is oxygen-dependent; whilst ciprofloxacin has been shown to be inactive against anaerobes (Appelbaum, 1999). Walters et al. (2003) demonstrated a reduction in the killing of

P. aeruginosa biofilms below a metabolically active region of cells close to the air interface. Susceptibility was returned once the *P. aeruginosa* was dispersed from their colony biofilms. This was also shown with *P. aeruginosa* biofilms when 48 h old biofilms were treated with carbenicillin, ceftazidime, chloramphenicol, or tetracycline as well as tobramycin and ciprofloxacin for 12 h (Borriello et al., 2004). Oxygen was present within the top layer where metabolic activity was occurring. However, below the metabolically active region, *P. aeruginosa* became less susceptible to antimicrobial killing.

As well as limiting the action of antimicrobials, oxygen limitation can influence the host immune response. Computer modelling has been used to determine the oxygen availability at the interface between a biofilm and neutrophil layer, mimicking three medically relevant geometries (a biofilm near an air interface replicating a dermal wound, a biofilm on an implant, and a biofilm aggregate in mucus) (Wu et al., 2018). Hypoxia was predicted at each interface under certain plausible parameters. This is significant, as oxygen limitation can reduce the killing ability of neutrophils due to the inability to generate ROS required for killing (Wu et al., 2018). Equally, oxygen availability has an impact on the expression of bacterial toxins. For instance, the expression of the *P. aeruginosa* exotoxin (ETA) gene *toxA* and its positive regulator *ptxR* is considerably higher when grown anaerobically under static conditions when compared to normoxic (20% O_2) under shaking conditions (Gaines et al., 2005).

Another implication of oxygen availability is the effect on competition between different bacterial species. Competition in co-culture between *P. aeruginosa* and *S. aureus* has been shown to be affected by the presence or absence of oxygen. In normoxic conditions, PAO1 and three CF isolates were shown to drastically reduce the colony forming units (CFU) of *S. aureus.* However, under anoxic

conditions, only one CF isolate could reduce the CFU of *S. aureus,* whilst *S. aureus* was unaffected by the other three *P. aeruginosa* strains (Pallett et al., 2019). Similar results were shown in mixed species biofilms, as three of the four *P. aeruginosa* strains could not outcompete *S. aureus* when grown under anoxia; whilst in normoxic conditions, *S. aureus* was reduced (Pallett et al., 2019). Conversely, oxygen availability generated by one bacterial species has been linked to increasing the virulence of another bacterial species during coinfection in oral biofilms. *S. gordonii* has been shown to enhance the bioavailability of oxygen during infection, allowing *Aggregatibacter actinomycetemcomitans* to shift from a primarily fermentative metabolism to a respiratory metabolism that enhances both its growth yields and persistence in abscesses (Stacy et al., 2016). This is likely due to the production of H_2O_2 by *S. gordonii* which *A. actinomycetemcomitans* utilises to produce oxygen (Stacy et al., 2014, Stacy et al., 2016).

Oxygen, therefore, plays an important role in aiding the removal of biofilms via both antimicrobials and the host immune response, whilst also influencing the virulence and cooperation of bacteria. Altogether, oxygen is a vital component to understand in order to improve treatment methods.

6.1.5. Current tools for oxygen detection

In order to study the oxygen gradients that can form within a microbial biofilm, adequate tools are required to prevent the disruption of these microenvironments in order to mimic *in vivo* conditions as closely as possible.

One such method is the utilisation of protein synthesis as oxygen availability is essential for this process. Therefore, protein expression or inactivity are good

markers for the presence of oxygen. For instance, localised gene expression within a biofilm has been examined using laser capture microdissection microscopy (LCMM) combined with quantitative real-time reverse transcriptase PCR (qRT-PCR) (Lenz et al., 2008). The expression of an apparent housekeeping gene, *acpP,* and a gene controlled by QS, *aprA*, was demonstrated to be higher within the top 30 μm of a *P. aeruginosa* biofilm. AcpP is required for the synthesis of fatty acids and new cell membranes; indicating the top 30 μm is most active in membrane synthesis. As the green fluorescent protein (GFP) is oxygen dependent, Lenz et al. (2008) also used IPTG-induced GFP in combination with LCMM and qRT-PCR, to show that *gfp* expression was significantly higher in the top 30 μm of the IPTG-induced biofilm than in the middle and lower regions. The lack of fluorescence signified a reduction in protein synthesis in the lower regions, rather than inactivity of expressed GFP. This reinforces the suggestion of reduced activity within the core of a biofilm. Similar protein synthesis at the surface of *P. aeruginosa* biofilms was seen in Folsom et al. (2010) and Xu et al. (1998). The former demonstrated that IPTG-induced GFP fluorescence was limited to the surface of the *P. aeruginosa* biofilm, whilst the latter used alkaline phosphatase activity to show that protein synthesis was limited to the upper 30 μm of *P. aeruginosa* biofilm due to oxygen availability.

As well as using protein synthesis as a biological marker, there is a varied collection of tools used to measure oxygen; one such tool are microelectrodes. De Beer et al. (1994) set up a flow-cell system consisting of an undefined mixture of detached bacteria from a mature biofilm and measured the formation of oxygen gradients in aerobic biofilms using CLSM and oxygen microelectrodes. Using the oxygen microelectrode, De Beer et al. (1994) probed vertical and horizontal voids formed in mature biofilms, where oxygen concentrations were higher than the

surrounding cell clusters. These voids may facilitate the transport of oxygen and nutrients from the bulk liquid interface into the biofilm. Central regions of cell clusters were also shown to be anaerobic, with oxygen only detected within the initial phase of clusters up to a depth of 30 μm. Similarly, Xu et al. (1998), using oxygen microelectrodes in conjunction with alkaline phosphatase activity, demonstrated the formation of anaerobic regions below metabolically active bands of *P. aeruginosa* approximately 30 μm deep, as mentioned above. However, the drawback of microelectrodes are the potential disruption to biofilm architecture whilst unable to provide horizontal readings of a biofilm. Microelectrodes have also been used more recently in the study biofilm-associated wound treatment. Kiamco et al. (2017) used microelectrodes to measure dissolved oxygen (DO) penetration and pH changes in *S. aureus* biofilms challenged with the antimicrobials vancomycin or ciprofloxacin in combination with medical-grade honey or cadexomer iodine.

Another tool currently utilised to detect changes in oxygen concentration are oxygen-sensitive fluorophores. Companies such as *PreSens* have moved towards manufacturing commercially available products capable of detecting either pH or oxygen gradients in both probe form and as microplates. The oxygen-sensitive microplates contain two fluorophores, one oxygen-sensitive and one insensitive, entrapped within a matrix at the bottom of each well, as described in **Figure *4.10.1-1***. These can provide real-time measurements of oxygen consumption in planktonic culture but are limited in their ability to measure absorbance. The separation of the fluorophores from the bacteria also limit the scope for measuring oxygen gradients within a biofilm.

Fluorescent particles, containing oxygen-sensitive fluorophores, have also been used to measure oxygen concentrations in bacterial biofilms. An early example of

oxygen-sensitive microparticles used two fluorophores immobilised to the surface of silica microparticles, 1.19 ± 0.23 μm in diameter (Acosta et al., 2012). The oxygen-sensitive fluorophore was tris (4,7-diphenyl-1,10-phenanthroline) ruthenium (II) dichloride; more commonly referred to as $Ru(Ph_2phen_3)Cl_2$, whilst Nile blue chloride was used as a reference. Acosta et al. (2012) incorporated oxygen-sensitive microparticles into a *S. aureus* biofilm in order to measure oxygen across the 3D structure. Each microparticle was slightly larger than an individual *S. aureus* bacterium (noted as 0.87 ± 0.01 μm). Their results showed a gradual decrease in oxygen concentration from the top to the bottom of the *S aureus* biofilm. The particle size was used to prevent endocytosis and universal distribution, however, work in 5.2.4 suggest our polyacrylamide nanosensors remain extracellular and appear dispersed throughout the biofilm (5.2.7).

Another more recent example of oxygen-sensitive particles is by Jewell et al. (2019) who encapsulated the oxygen-sensitive fluorophore platinum (II) meso-tetra(pentafluorophenyl)porphine (PtTFPP) and the oxygen-insensitive fluorophore 4-Di-16-ASP (4-[4-(dihexadecylamino)styryl]-*N*-methylpyridinium iodide) (DiA) within a PEG-lipid shell to produce oxygen-sensitive nanosensors at ~200 nm in diameter. Using these oxygen nanosensors Jewell et al. (2019) demonstrated that the nanosensors were capable of detecting a reduction in oxygen with the introduction of glucose and glucose oxidase to a chemically fixed biofilm, as well as a gradual increase in oxygen over time within a biofilm treated with the antimicrobial, colistin. Further work by Jewell et al. (2020b) used these oxygen nanosensors as an alternative method of determining the minimum biofilm inhibitory concentrations (MBICs) for a range of antimicrobials (tobramycin and colistin). By measuring oxygen availability, the metabolic activity of antimicrobial-treated *P. aeruginosa* biofilms could be inferred. Any change in metabolism could

then imply antimicrobial activity. This work relied on measuring changes in fluorescence intensity using a microplate reader; *P. aeruginosa* biofilms were grown on peg-lids with embedded nanosensors before being treated with increasing concentrations of tobramycin or colistin. The fluorescence intensity changes would therefore be reduced to a single measurement, lacking spatial distinction across a whole biofilm. In addition, as shown above, cells below a particular depth (~30 μm) are typically metabolically inactive. However, the thickness of these biofilms may not necessarily be >30 μm as they were grown on a peg-lid (biofilm dimensions were not given), meaning cells could potentially all be metabolically active. This may raise the question whether these biofilms were a suitable representation of *in vivo* biofilms. The use of controls would alleviate the issue of metabolic inactivity, as treatment with no antimicrobials should provide a baseline for fluorescence intensity and inferred oxygen availability/metabolic activity of the biofilm as a whole. In addition, there appears to be no way of confirming their oxygen nanosensors had in fact embedded into the biofilm forming on a peg-lid.

The final example of oxygen-sensitive particles have been produced by the Aylott Lab, where the pH-sensitive polyacrylamide nanosensors discussed in 5.1.2 (**Figure *5.1.2-1***) have been used to create a dual pH-oxygen nanosensor, by covalently attaching various porphyrin molecules to the surface of the polyacrylamide shell (Chauhan et al., 2016). Following on from this work, oxygen-sensitive nanosensors have been developed, as described in ***Figure 6.1.5-1***. ***Figure 6.1.5-1***a) shows the chemical structure of the oxygen-sensitive fluorophore platinum (II) porphyrin and its optimal excitation and emission wavelengths (ex:405 nm, em:650 nm). The schematic in ***Figure 6.1.5-1***b shows the structure of the oxygen-sensitive nanosensors. Here, the platinum (II)

porphyrin fluorophore (***Figure 6.1.5-1***a) is covalently linked, via the succinimidyl ester group, to the surface of an inert cross-linked matrix that contains free amine groups, provided by *N*-(3-Aminopropyl)methacrylamide hydrochloride (APMA). Encapsulated within the polyacrylamide shell is the oxygen-insensitive fluorophore, TAMRA, which provides a reference.

Altogether, this creates an oxygen-sensitive nanosensor that has the potential to provide real-time, ratiometric measurements of oxygen consumption during bacterial growth and the potential to map three-dimensional oxygen gradients within a biofilm. With this, research can be carried out to better understand the availability of a key chemical of bacterial survival and an essential component required in the action of antimicrobials and the host defences.

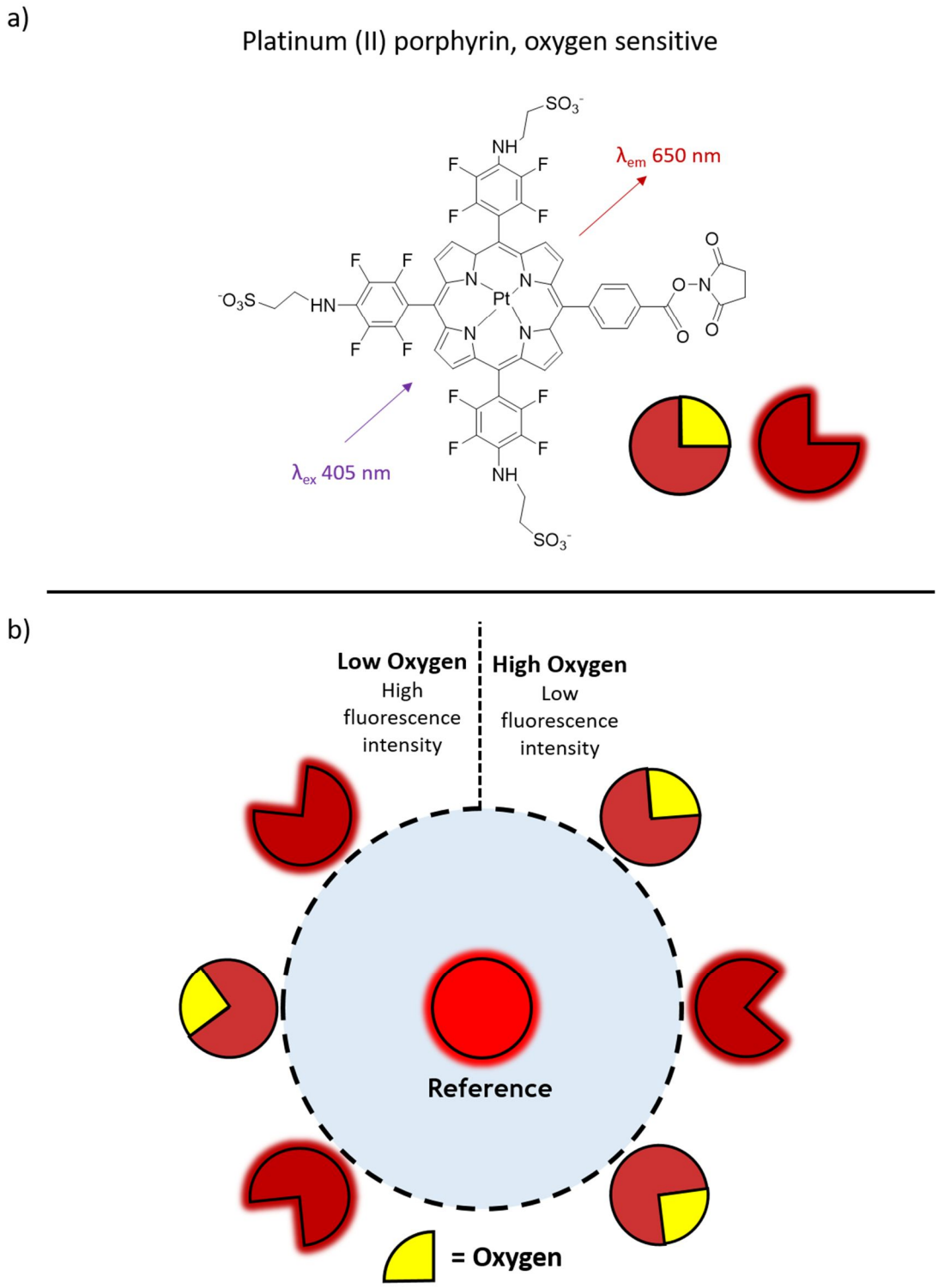

Figure 6.1.5-1: a) Chemical structure of platinum (II) porphyrin b) Representative diagram of nanosensors and their mode of action – The matrix contains the fluorophore TAMRA, whilst platinum (II) porphyrin covalently binds to the free amine group provided by matrix bound APMA. Oxygen quenches the fluorescence of platinum (II) porphyrin, whilst the fluorescence from TAMRA remains unaffected.

6.2. Results

6.2.1. Determining the particle size and charge of the oxygen-sensitive polyacrylamide nanosensors

To verify that the oxygen-sensitive polyacrylamide nanosensors were appropriately synthesised, each batch was prepared for post-production characterisation to determine the zeta potential and size, as described in 4.2.1. The average size, zeta potential and polydispersal index (PDI) is listed in **Table *6.2.1-1***.

Table 6.2.1-1: Average size, charge and PDI of oxygen-sensitive polyacrylamide nanosensors

Parameters	Oxygen nanosensors
Size (nm)	203.54 (±7.37)
PDI (A.U.)	0.21 (±0.01)
Zeta Potential (mV)	4.17 (±0.24)

6.2.2. The quenching of fluorescence from platinum (II) porphyrin by oxygen is reversible

For the oxygen calibration, the Agilent Fluorescence Spectrometer was used to generate an emission scan as described in 4.2.3. ***Figure 6.2.2-1*** shows an emission scan for oxygen nanosensors at 1 mg mL^{-1} in 1:10 PBS. The emission scan, from 550-700 nm, measures the response of the oxygen-sensitive fluorophore, platinum (II) porphyrin, as oxygen is gradually bubbled into the solution. The scan shows a decrease in fluorescence intensity as the oxygen gradually increased from the initial measurement at 4.1% of dissolved oxygen (DO). Once the concentration of DO reaches 60.2%, argon is introduced, displacing the oxygen and increasing the fluorescence intensity, as shown at

41.2%, 27.5% and 22.9%. A small peak is present at ~577 nm caused by the excitation of TAMRA.

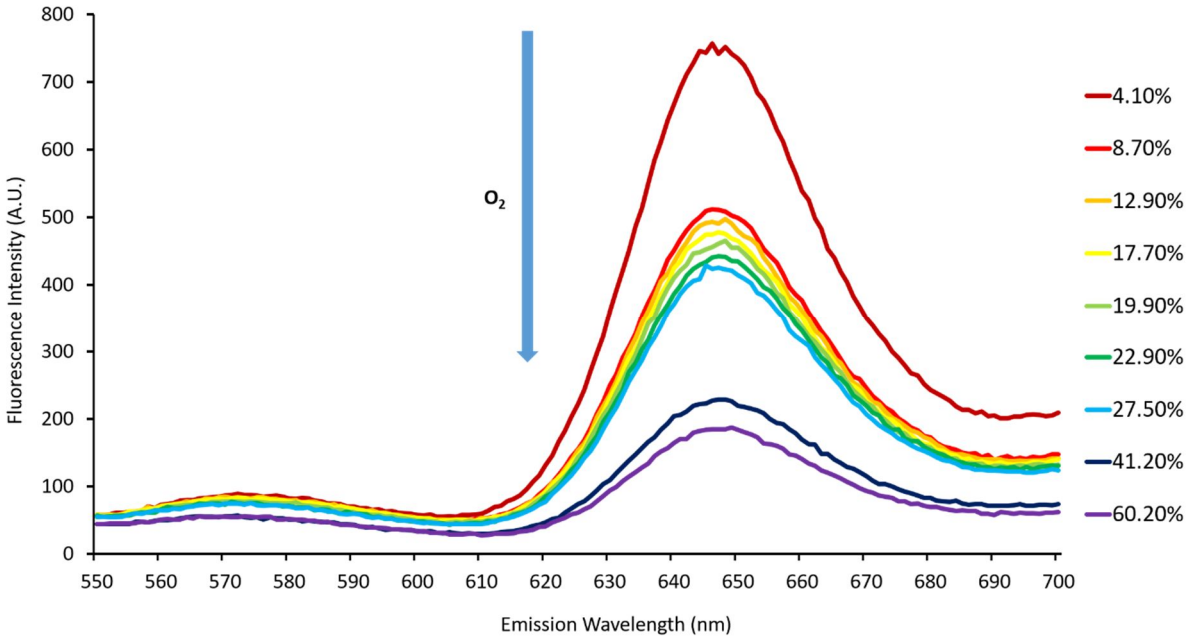

Figure 6.2.2-1: Platinum (II) porphyrin fluorescence intensity decreases as the concentraion of dissolved oxygen increases – The oxygen-sensitive polyacrylamide nanosensors were diluted to a working concentration of 1 mg mL^{-1} in 1:10 PBS. An emission scan was performed to detect the fluorescence intensity peaks of platinum (II) porphyrin and TAMRA. The emissions scan used an excitation of 405 nm, and detected emissions between 550-700 nm. Between measurements the oxygen nanosensor solution was 'bubbled' with argon and the oxygen concentraion was measured using an oxygen probe (*Ocean Insight*). To increase the oxygen concentration after the 60.2% measurement was taken, oxygen was 'bubbled' into the solution. n=1

6.2.3. Auto-fluorescence at 650 nm is present in PAO1 strains

In order to determine whether *P. aeruginosa* produced auto-fluorescence that may interfere with readings taken for the platinum (II) porphyrin emission, fluorescence intensity at 650 nm was measured using four PAO1 strains grown in the presence and absence of oxygen nanosensors, as described in 4.6.1.

In the presence of oxygen nanosensors, the fluorescence intensity at 650 nm steadily increases over time, as shown in ***Figure 6.2.3-1*** (solid lines). However, in the absence of oxygen nanosensors, emission at 650 nm also increases (dotted lines). Only growth in PAO1-L with the addition of 1mg mL^{-1} oxygen nanosensors was significantly reduced (**Supplemental Figure *10-5***).

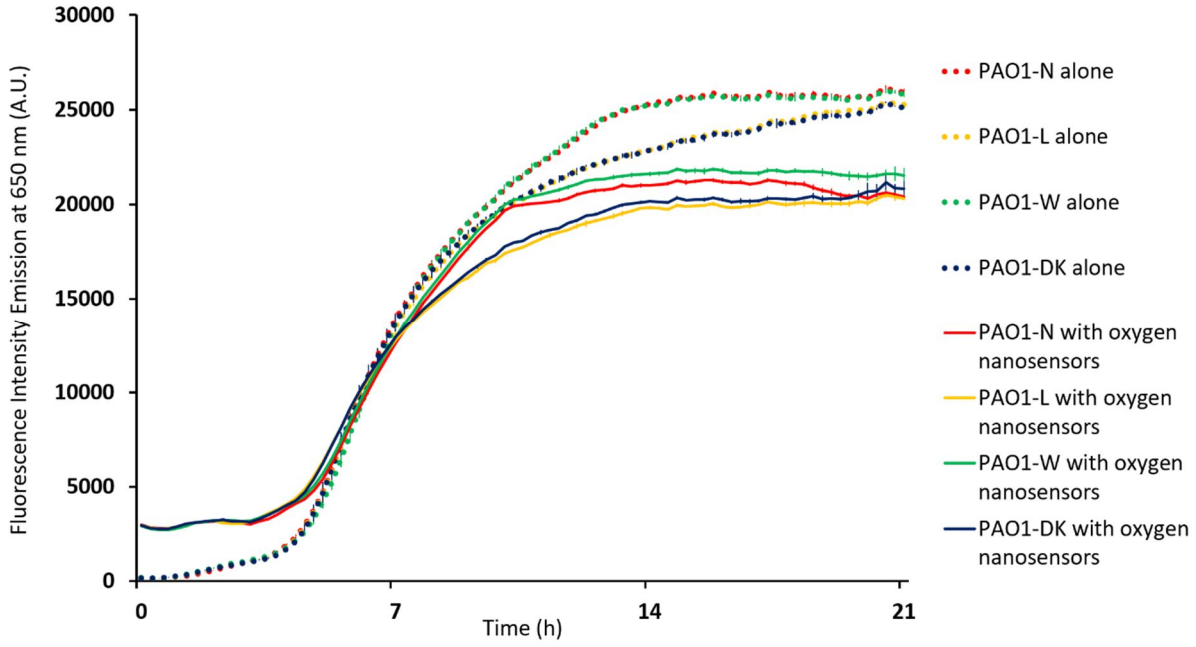

Figure 6.2.3-1: Fluorescence intensity emission at 650 nm increased over time in the presence and absence of oxygen nanosensors – PAO1 strains at OD_{600} of 0.05 were incubated in M9 succinate & 1% w/v casamino acids, with 1 mg mL^{-1} oxygen nanosensors as an additional condition. Emission at 650 nm was measured every 15 min. Fluorescence intensity increased in both the presence and absence of oxygen nanosensors. Error bars are ±1 S.D. n=2x3

6.2.4. Increase in fluorescence at 650 nm only seen in *P. aeruginosa*

To investigate whether other bacterial species also produced auto-fluorescence that may interfere with the platinum (II) porphyrin emission, fluorescence intensity at 650 nm was measured using the *E. coli* strain DH5α, the *S. aureus* strain SH1000 and PAO1-N, as described in 4.6.2.

Figure 6.2.4-1a) shows that only PAO1-N (red lines) increases in fluorescence intensity over time, whilst auto-fluorescence (dotted red line) only appears present in PAO1-N. Growth was not a contributing factor as all strains grew similarly in each condition (***Supplemental Figure 10-6****). **Figure 6.2.4-1***b) shows SH1000 and DH5α rescaled without PAO1-N; where there appears a slight increase in fluorescence intensity over time with the oxygen nanosensors present.

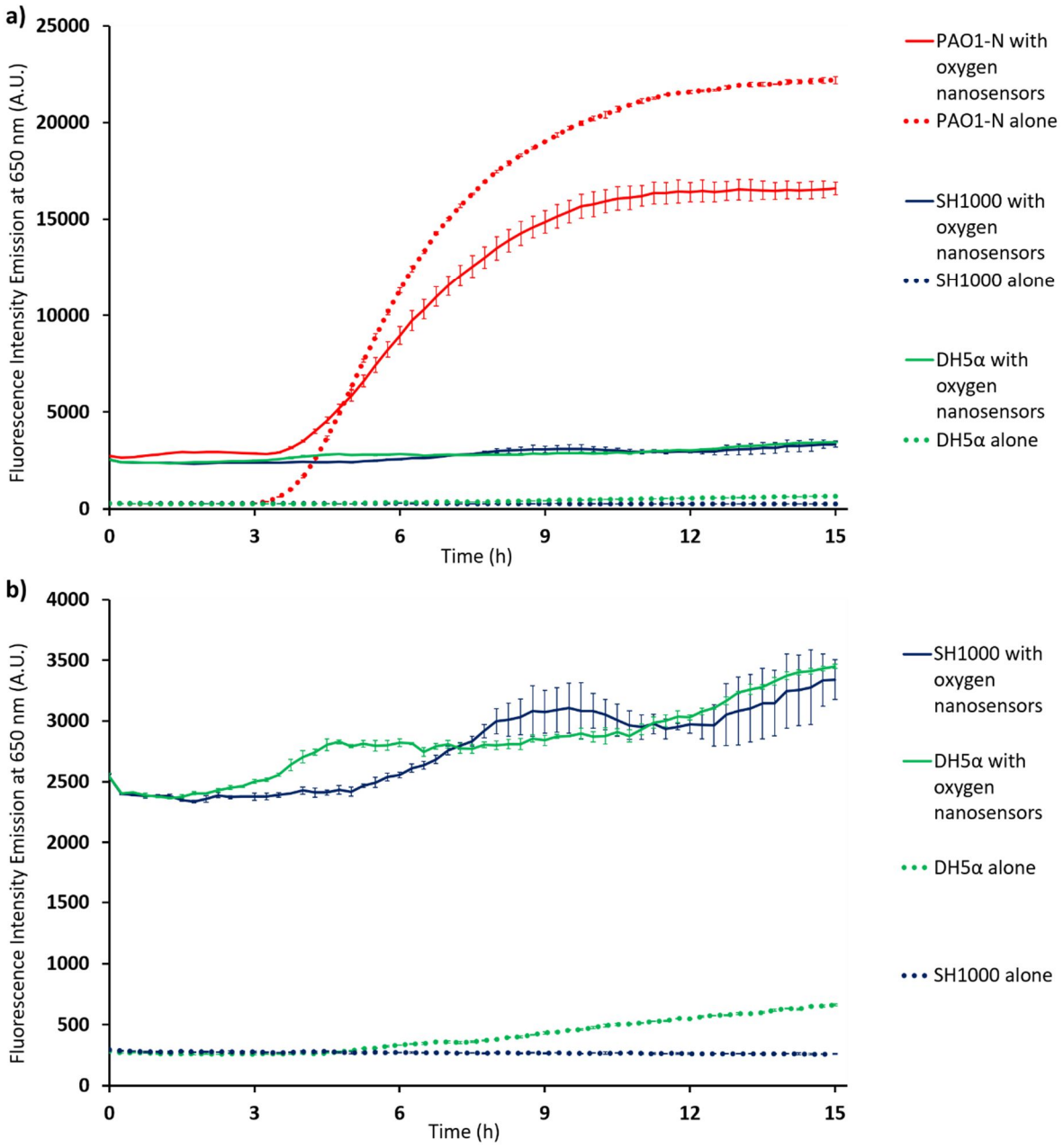

Figure 6.2.4-1: Fluorescence intensity emission at 650 nm only increased over time for PAO1-N when grown in the presence and absence of oxygen nanosensors – Strains at OD_{600} of 0.05 were incubated in M9 glucose, with 1 mg mL^{-1} oxygen nanosensors as an additional condition. Emission at 650 nm was measured every 15 min. **a)** Fluorescence intensity emission at 650 nm of each species grown with 1 mg mL^{-1} oxygen nanosensors (solid line) compared to the fluorescence intensity of each species alone (dotted line). **b)** Fluorescence intensity emission at 650 nm of SH1000 and DH5α grown with 1 mg mL^{-1} oxygen nanosensors (solid line) compared to the fluorescence intensity of SH1000 and DH5α species alone (dotted line), rescaled without PAO1-N. Error bars are ±1 S.D. n=2x3

6.2.5. Pyoverdine appears to cause auto-fluorescence

Continuing the investigation into auto-fluorescence, fluorescence intensity at 650 nm was measured using pyoverdine, pyochelin and pyocyanin mutants, as described in 4.6.3.

Figure 6.2.5-1a) shows that the fluorescence intensity at 650 nm increases over time for both wildtype strains of PAO1 (Nottingham and C++), as well as the pyochelin (PAO1-NΔ*pchEF*) and pyocyanin (CW4T1) mutants. Fluorescence intensity at 650 nm in PA14 is also present, albeit reduced in comparison to the PAO1 strains. However, the fluorescence intensity for the three mutants lacking pyoverdine is drastically reduced. Again, growth was not a contributing factor as all strains grew similarly in all conditions (**Supplemental Figure *10-7***). ***Figure 6.2.5-1***b) shows a slight increase in fluorescence intensity over time for PAO1-NΔ*pvdD*, PAO1 C++Δ*pvdD* and PAO1 C++Δ*pvdD*Δ*pchEF* when rescaled.

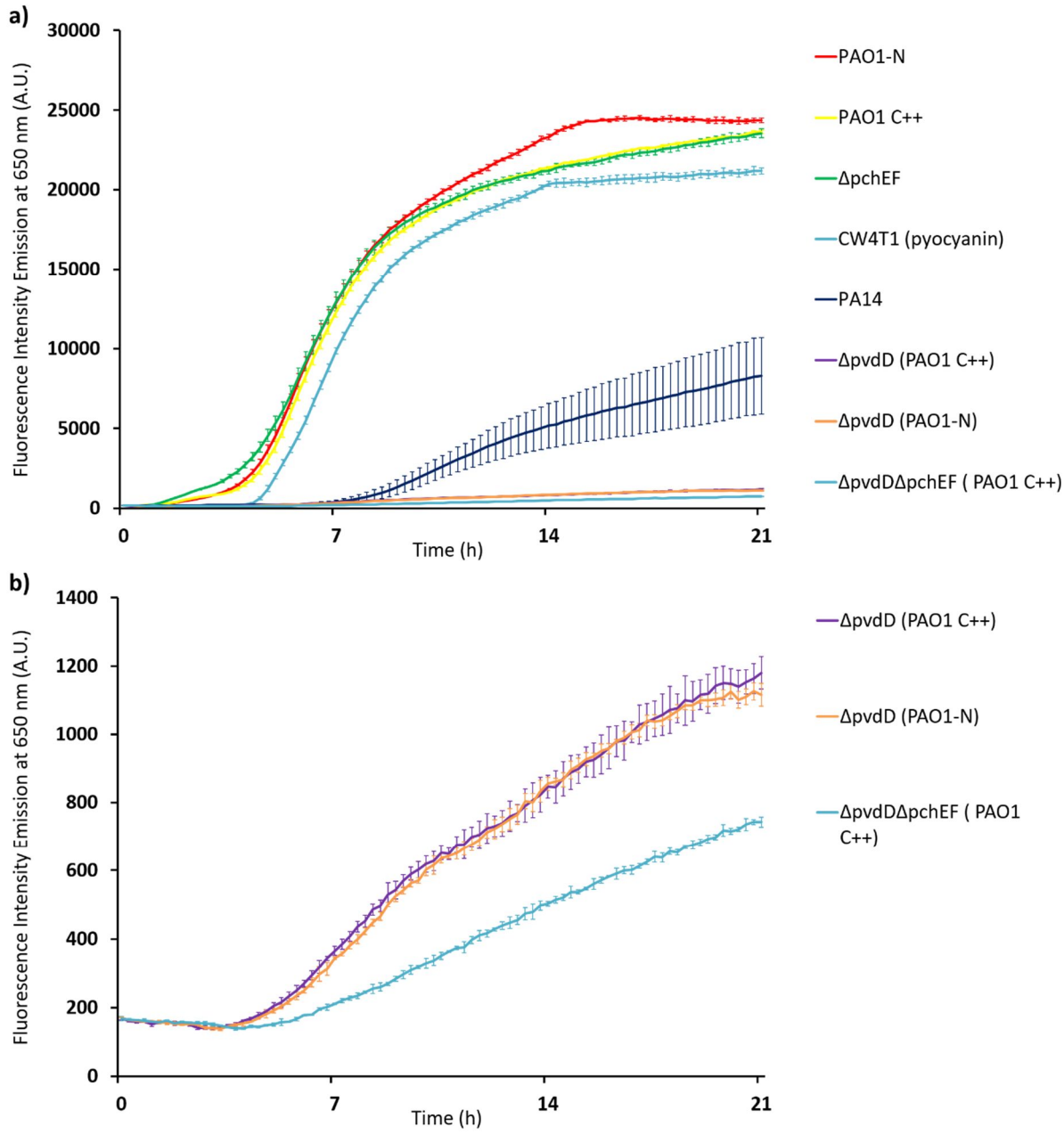

Figure 6.2.5-1: A pyoverdine mutation significantly reduces auto-fluorescence of *P. aeruginosa* at 650 nm – *P. aeruginosa* strains at OD_{600} of 0.05 were incubated in M9 succinate & casamino acids. Emission at 650 nm was measured every 15 min. **a)** Fluorescence intensity emission at 650 nm of each *P. aeruginosa* species over 21 h. **b)** Fluorescence intensity emission at 650 nm of PAO1-NΔ*pvdD*, PAO1-C++Δ*pvdD* and PAO1-C++Δ*pvdD*Δ*pchEF* after rescaling. Error bars are ±1 S.D. n=2x3

6.2.6. Oxygen consumption varies drastically between bacterial species

Having determined that pyoverdine caused auto-fluorescence, PAO1-NΔ*pvdD* (rather than PAO1-N) DH5α, SH1000 and were used to investigate whether the oxygen nanosensors could measure the real-time consumption of oxygen from different bacterial species, as described in 4.6.4.

Firstly, to confirm that a gas permeable membrane was a suitable additional control, half of a microplate was covered with a gas permeable membrane and fluorescence emission at 650 nm was measured, as shown ***Figure 6.2.6-1***a). The four conditions were atmospheric (~20% oxygen) and ~0% oxygen, either covered or uncovered. The 'Atmospheric' control was created by vortexing the oxygen nanosensor solution thoroughly before transferring to the microplate; whilst the '~0%' was created by adding sodium sulphite to the oxygen nanosensor solution where it can scavenge available oxygen. Both covered readings (yellow & blue lines) remain steady over 21 h, providing a minimum and maximum oxygen reading within physiological conditions. Conversely, both uncovered readings (grey & black lines) decrease over time. This was most apparent with the uncovered atmospheric measurements. Secondly, to confirm that no auto-fluorescence was present at 650 nm, measurements were taken in the absence of oxygen nanosensors, as shown in ***Figure 6.2.6-1***b). Here we see the fluorescence emission of all three bacteria is consistently low when compared to the two controls, atmospheric (~20% oxygen) and ~0% oxygen.

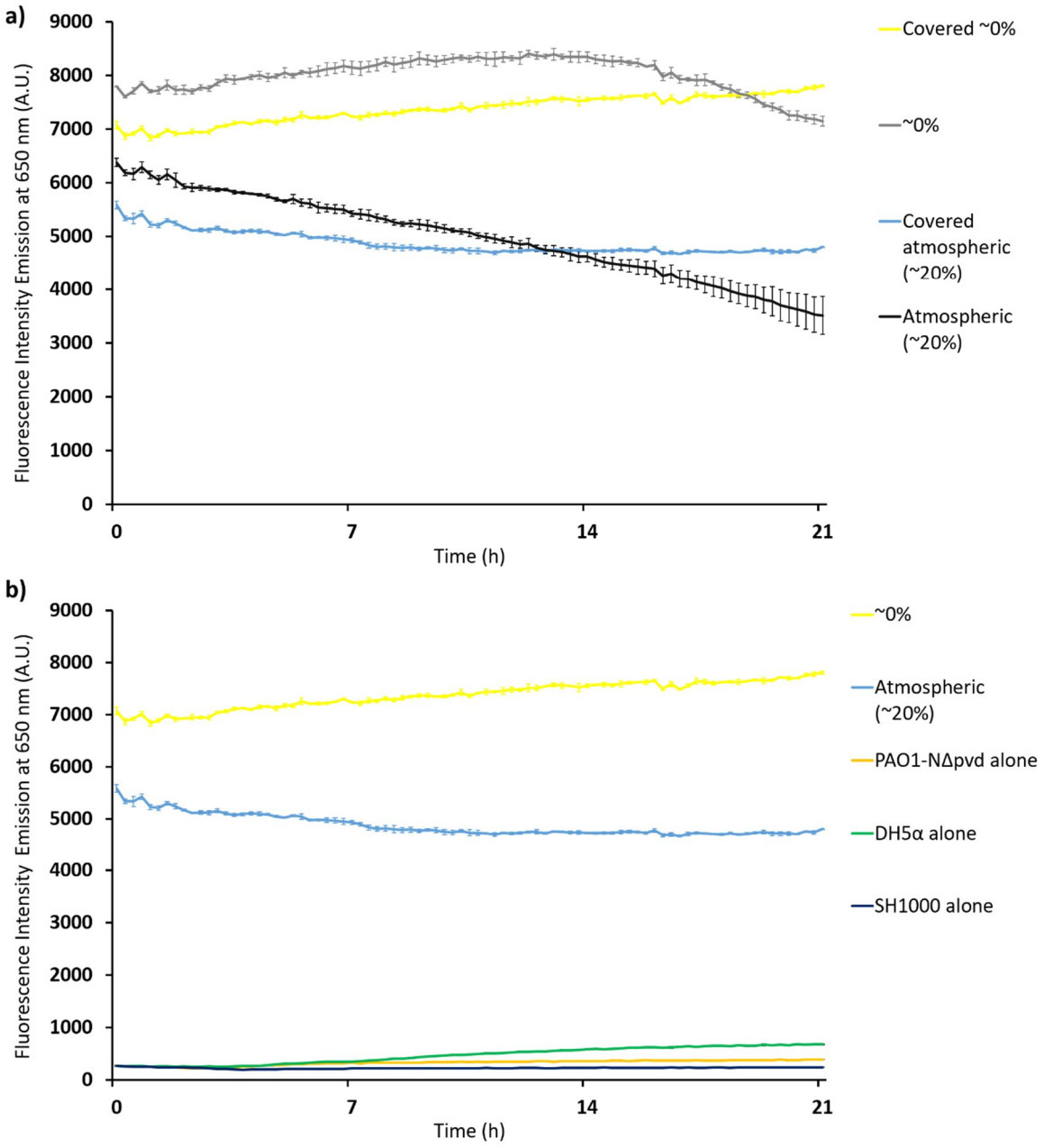

Figure 6.2.6-1: a) Determining the suitability of gas permeable membranes for microplate assays, b) measuring emission at 650 nm for DH5α, SH1000 and PAO1-NΔ*pvdD* grown in the absence of oxygen nanosensors – Strains at OD_{600} of 0.05 were incubated in M9 glucose and emission at 650 nm was measured every 15 min for 21 h. **a)** Half of the microplate was covered with a gas permeable membrane. Emission at 650 nm for atmospheric (blue) and ~0% (yellow) remained steady over 21 h when covered with the membrane. **b)** Fluorescence intensity for PAO1-NΔ*pvdD*, DH5α and SH1000 in the absence of the oxygen nanosensors, in comparison to the controls (~0% & atmospheric). Error bars are ±1 S.D. n=2x3

Thirdly, to confirm that the oxygen nanosensors could measure oxygen consumption over time, fluorescence emissions at 580 nm (ex:540 nm) and 650 nm (ex:405 nm) were measured, as well as absorbance (600 nm) to track growth. The resultant fluorescence intensity ratio was normalised, as discussed in 4.6.4, assuming that the initial oxygen concentration matched atmospheric conditions.

The growth varies between the three bacterial species, as shown in **Figure 6.2.6-2**a, with PAO1-NΔ*pvdD* reaching stationary phase first, followed by DH5α then SH1000; whilst oxygen consumption of the three bacterial species over 21 h can be seen in ***Figure 6.2.6-2***b. An increase in the fluorescence intensity ratio (FIR) indicates a reduction in oxygen in the wells, as platinum (II) porphyrin fluorescence intensity increases whilst TAMRA fluorescence intensity remains insensitive to changes in oxygen. This change in the FIR is most apparent in PAO1-NΔ*pvdD* (orange line) as the FIR increases rapidly, before the FIR initially plateaus after ~ 5 h. This plateauing mirrors the time where PAO1-NΔ*pvdD* reached stationary phase (***Figure 6.2.6-2***a – orange line). The FIR for PAO1-NΔ*pvdD* continues to increase between ~8-14 h before it plateaus again. PAO1-NΔ*pvdD* also reaches the highest FIR of the three species. FIR is slow to increase for both DH5α and SH1000 within the first 2 h, indicating a lag phase, before eventually increasing, albeit at different rates. The FIR for SH1000 increases in a shallow manner over 21 h, mirroring its growth, whereas the FIR for DH5α rapidly increases between hours 2-5 before plateauing. This varies from when DH5α reaches stationary phase after ~ 10 h.

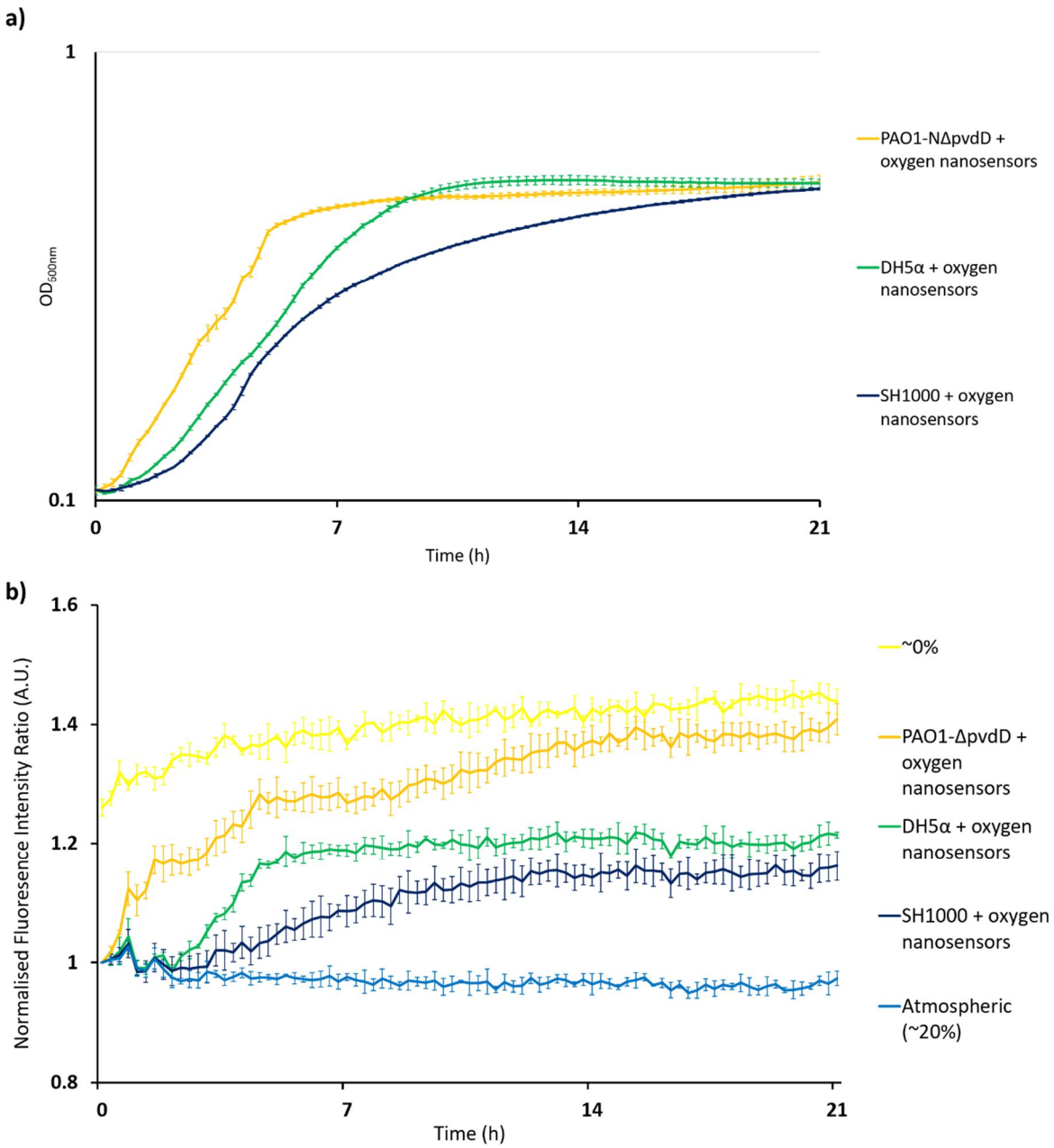

Figure 6.2.6-2: Oxygen consumption was detectable in three species – Strains at OD_{600} of 0.05 were incubated in M9 glucose, with 1 mg mL^{-1} oxygen nanosensors as an additional condition. Absorbance at 600 nm and emission at 580 nm & 650 nm were measured every 15 min. Wells were covered with a gas permeable membrane. Controls using vortexed oxygen nanosensor solution and 40 mg mL^{-1} sodium sulphite dissolved in the oxygen nanosensor solution were used as physiological ranges. **a**) Stationary phase was reached at varying times by DH5α, SH1000 and PAO1-NΔ*pvdD*. **b**) The fluorescence intensity ratio (FIR), varied drastically with PAO1-NΔ*pvdD* increasing the most, followed by DH5α then SH1000. Error bars are ±1 S.D. n=2x3

6.2.7. Oxygen consumption plateaus with increasing concentrations of potassium nitrate

For further testing to determine whether the oxygen nanosensors could detect changes in oxygen consumption in planktonic culture, PAO1-NΔ*pvdD* was grown in M9 minimal media with 1% w/v casamino acids either alone or with an increasing concentration of KNO_3 (5 mM, 10 mM or 20 mM), as described in 4.6.5. Additionally, the experiment was used to determine the excess of KNO_3 for PAO1-NΔ*pvdD* growth.

The results show that the addition of KNO_3 to the M9 minimal media significantly reduces the growth of PAO1-NΔ*pvdD* over 21 h for all conditions, as shown in ***Figure 6.2.7-1***a & b). The results also show that the FIR is significantly reduced over time with the addition of KNO_3, whilst there is also a significant reduction in FIR between 1% w/v casamino acids with 5 mM KNO_3 and both 10 mM & 20 mM KNO_3 (***Figure 6.2.7-1***c & d), inferring a reduction in oxygen consumption when KNO_3 is ≥ 10 mM.

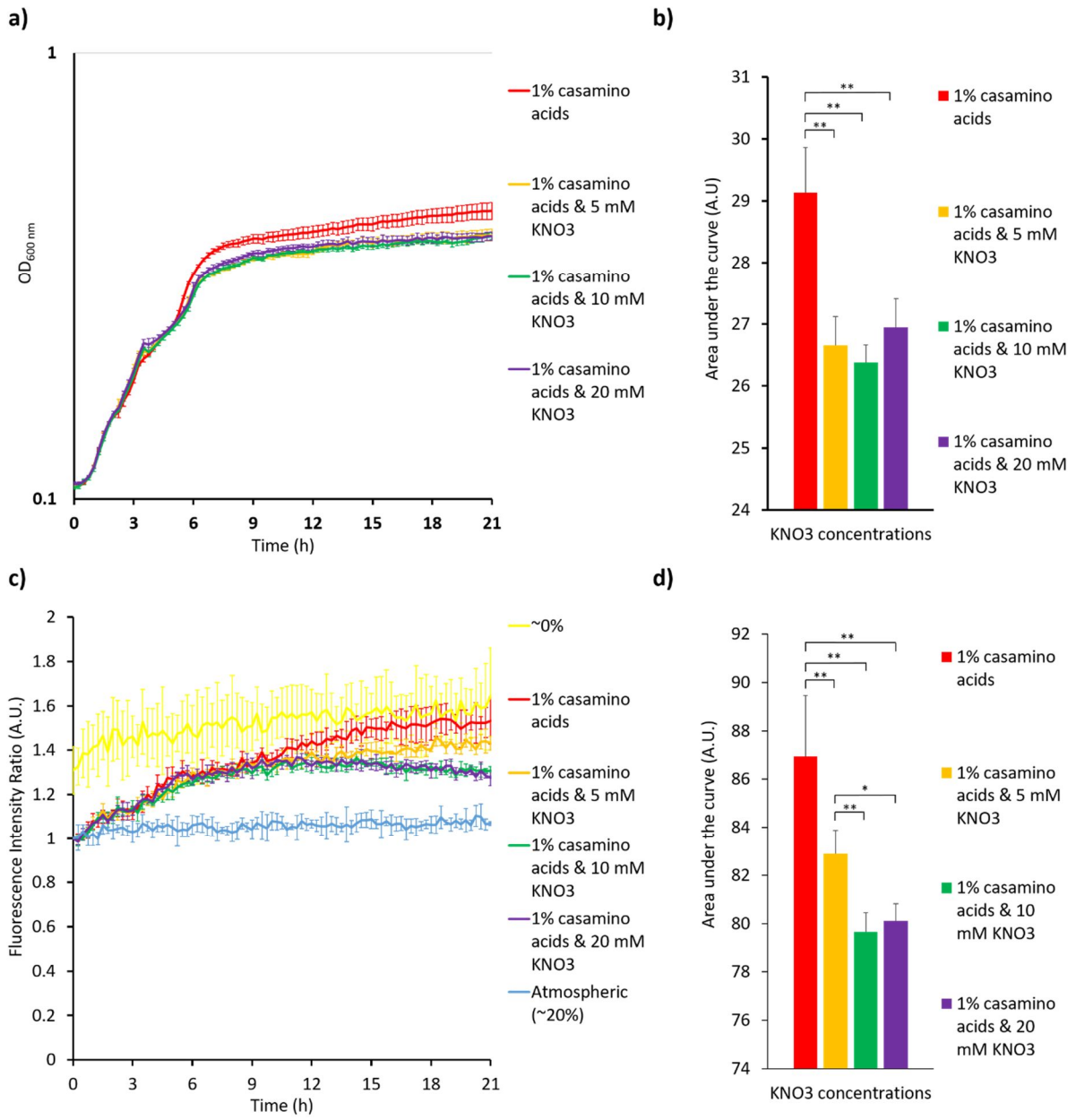

Figure 6.2.7-1: Oxygen consumption in PAO1-NΔ*pvdD* is significantly reduced when supplemented with ≥ 10 mM KNO_3 - PAO1-NΔ*pvdD* at OD_{600} of 0.05 was incubated in M9 minimal media with 1% w/v casamino acids either in the presence of increasing concentrations of KNO_3 (5 mM, 10 mM or 20 mM) or alone. 1 mg mL^{-1} oxygen nanosensors was added to measure the oxygen concentration. Absorbance at 600 nm and emission at 580 nm & 650 nm were measured every 15 min. Wells were covered with a gas permeable membrane. Controls using vortexed oxygen nanosensor solution and 40 mg mL^{-1} sodium sulphite dissolved in the oxygen nanosensor solution were used as physiological ranges. **a & b**) OD measured over 21 h showed significantly reduced growth with the addition of KNO_3 when compared to 1% w/v casamino acids alone. No significant difference was seen in growth between the KNO_3 conditions **c & d**) The fluorescence intensity ratio (FIR), was significantly reduced between 1% w/v casamino acids alone and when supplemented with KNO_3. FIR was also significantly reduced as KNO_3 increased in concentration. (*= P<0.05, **= P<0.005 & ***= P<0.001). Error bars are ±1 S.D. n=1x4

6.2.8. Oxygen nanosensors disrupt PAO1-N microcolony formation in biofilms

A comparison between PAO1-N and PAO1-NΔ*pvdD* was required to determine the effects of pyoverdine on biofilm growth and auto-fluorescence; therefore, PAO1-N and PAO1-NΔ*pvdD* biofilms were grown in the presence and absence of oxygen nanosensors, as described in 4.8.3.

Figure 6.2.8-1 shows a PAO1-N biofilm grown over 48 h in M9 succinate without oxygen nanosensors. The top panel shows a thin layer of PAO1-N cells ~ 6 μm thick whilst the second panel shows a few regions of fluorescence at 650 nm emission but none present at 580 nm. The final panels show clusters of PAO1-N cells, forming microcolonies throughout the biofilm. Less fluorescence at 650 nm is present from the top view.

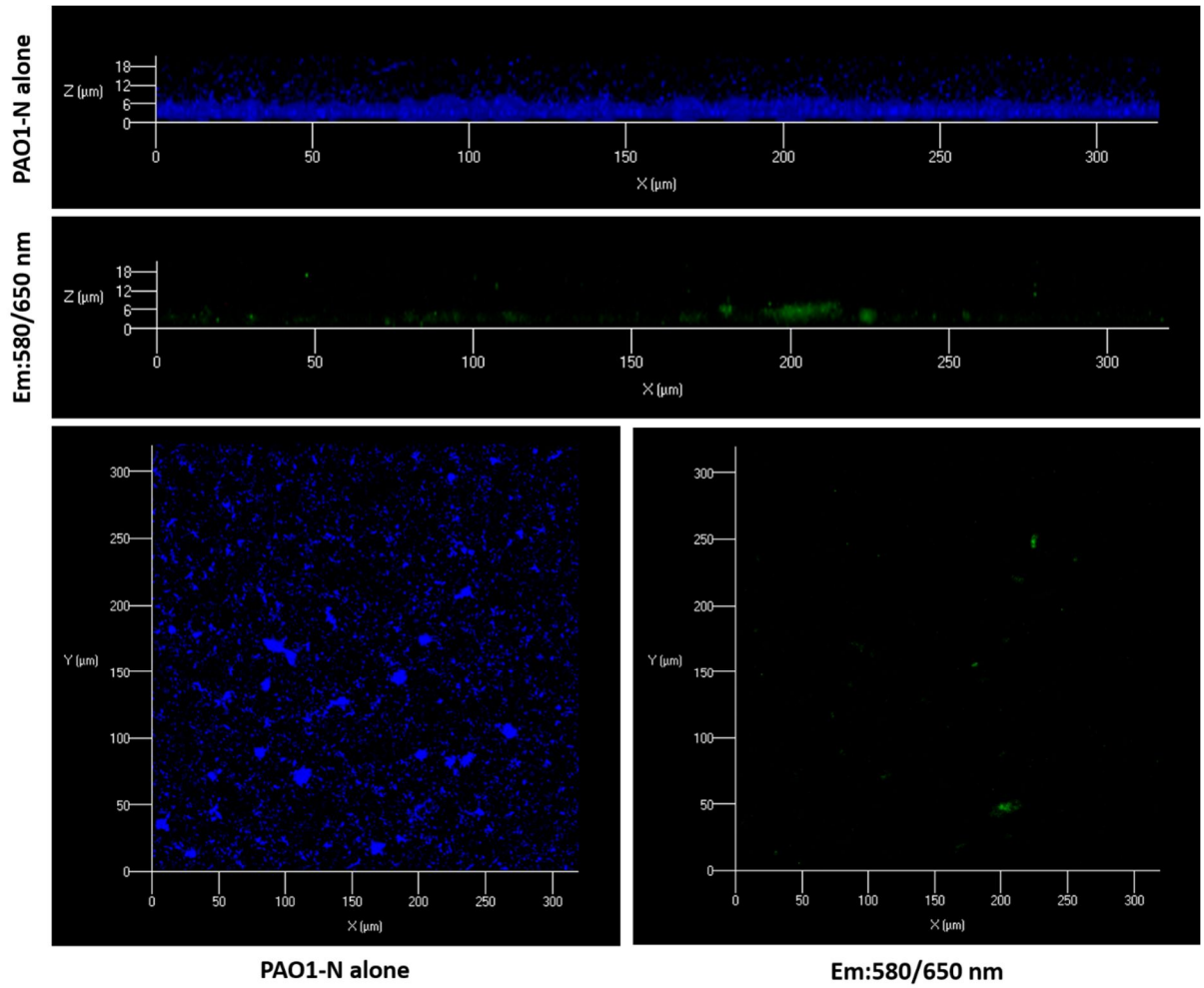

Figure 6.2.8-1: PAO1-N biofilm grown in absence of oxygen-sensitive nanosensors produces large microcolonies with reduced fluorescence intensity at 650 nm - Representative model of PAO1-N grown over 48 h in M9 succinate. Images taken with a Zeiss confocal laser scanning microscope with a 20x/0.8na objective. **First row**) Side 3D view of DAPI (405 nm excitation). **Second row**) Side 3D view of 580/650 nm emissions to detect autofluorescence (540 nm and 405 nm excitation respectively). **Third row; left image**) Top 3D view of DAPI (405 nm excitation). **Third row; right image**) Top 3D of 580/650 nm emission.

Figure 6.2.8-2 shows a PAO1-NΔ*pvdD* biofilm grown without oxygen nanosensors. The top panel shows a thicker biofilm than PAO1-N, with less clear regions of emission at 650 nm and still no fluorescence present at 580 nm. From the top view, the PAO1-NΔ*pvdD* appears less densely packed, with fewer microcolonies present. Fluorescence is also greatly reduced at 650 nm when viewed from the top.

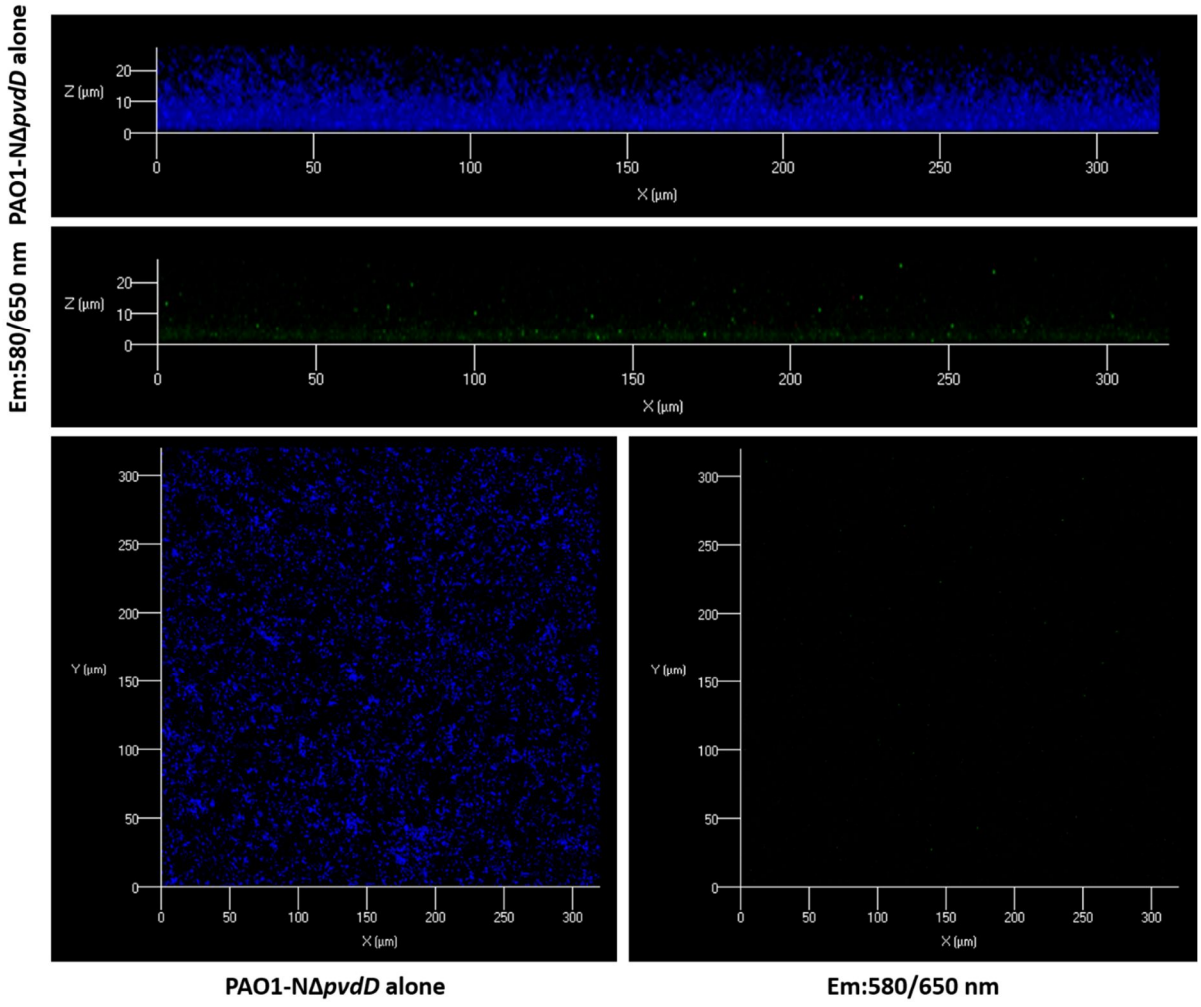

Figure 6.2.8-2: PAO1-NΔ*pvdD* biofilms grown in absence of oxygen-sensitive nanosensors produce reduced microcolonies - Representative model of PAO1-NΔ*pvdD* grown over 48 h in M9 succinate. Images taken with a Zeiss confocal laser scanning microscope with a 20x/0.8na objective. **First row**) Side 3D view of DAPI (405 nm excitation). **Second row**) Side 3D view of 580/650 nm emissions to detect auto-fluorescence (540 nm and 405 nm excitation respectively). **Third row; left image**) Top 3D view of DAPI (405 nm excitation). **Third row; right image**) Top 3D of 580/650 nm emission.

Figure 6.2.8-3 shows a PAO1-N biofilm grown with 1 mg mL^{-1} oxygen nanosensors. The thickness of the PAO1-N biofilm grown with oxygen nanosensors is similar to the thickness when the nanosensors are absent (***Figure 6.2.8-1***); however, fewer microcolonies are present, as shown in the top view (bottom left panel). Clear fluorescence emission is seen at both 580 nm and 650 nm, indicating the presence of the oxygen nanosensors. The nanosensors also appear fairly well dispersed throughout the biofilm, yet with clear clusters of nanosensors in regions.

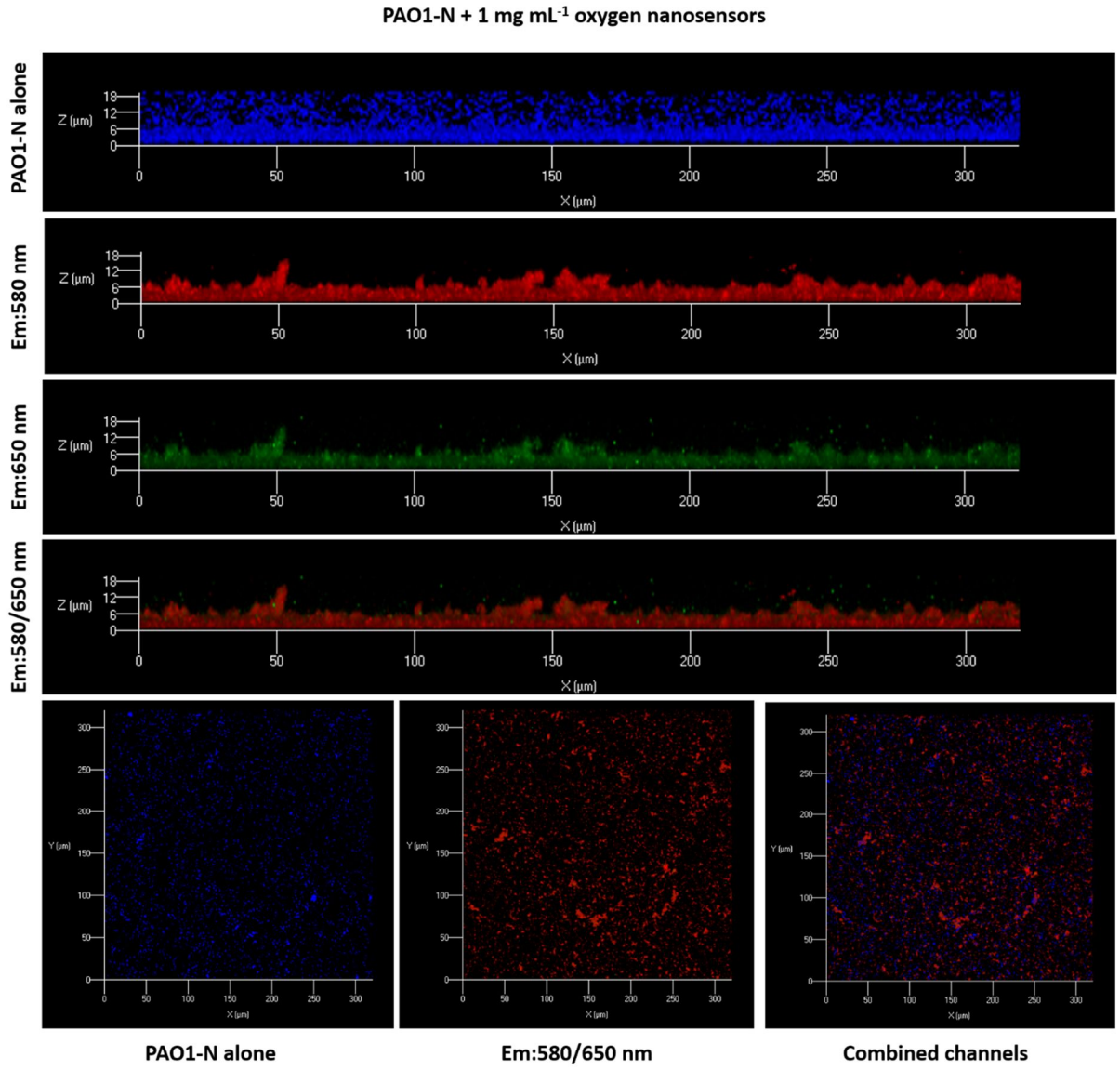

Figure 6.2.8-3: Oxygen-sensitive nanosensors form clusters within a PAO1-N biofilm - Representative model of PAO1-N grown over 48 hr in M9 succinate. Images taken with a Zeiss confocal laser scanning microscope with a 20x objective. **First row**) Side 3D view of DAPI (405 nm excitation). **Second row**) Side 3D view of TAMRA emission (540 nm excitation). **Third row**) Side 3D view of platinum (II) porphyrin emission (405 nm excitation). **Fourth row**) Side 3D view of 580/650 nm emission. **Fifth row; left image**) Top 3D view of DAPI (405 nm excitation). **Fifth row; centre image**) Top 3D view of 580/650 nm emission. **Fifth row; right image**) Top 3D view of DAPI and 580/650 nm emission.

Figure 6.2.8-4 shows a PAO1-NΔ*pvdD* biofilm grown with 1 mg mL^{-1} oxygen nanosensors. Again, the biofilm is thicker than the PAO1-N biofilm, yet the addition of the oxygen nanosensors disrupt the formation of the microcolonies (bottom left panel). Clear fluorescence emission is seen at both 580 nm and 650 nm, indicating the presence of the oxygen nanosensors. The nanosensors appear to form large clusters throughout the biofilm, at a higher concentration than seen in the PAO1-N + oxygen nanosensors condition. This is confirmed by the significant reduction in fluorescence intensity for both OG/FAM and TAMRA for PAO1-N + oxygen nanosensors condition, when compared to the OG/FAM and TAMRA measurements taken for the PAO1-NΔ*pvdD* + oxygen nanosensors condition (OG/FAM $P<0.001$ & TAMRA $P<0.005$) (**Supplemental Table *10-1***).

Fluorescence at 650 nm is also significantly higher across the section of biofilm when compared to ***Figure 6.2.8-3***, resulting in yellow/orange regions rather than darker red regions seen in the PAO1-N + oxygen nanosensors biofilm. This is shown by the maximum intensity z-projection (**Supplemental Figure *10-8***) where the average fluorescence intensity ratio for PAO1-N + oxygen nanosensors (0.42 ± 0.01 A.U.) is significantly lower than the average fluorescence intensity ratio for PAO1-NΔ*pvdD* + oxygen nanosensors (0.62 ±0.02 A.U.) ($P<0.005$) (**Supplemental Table *10-1***).

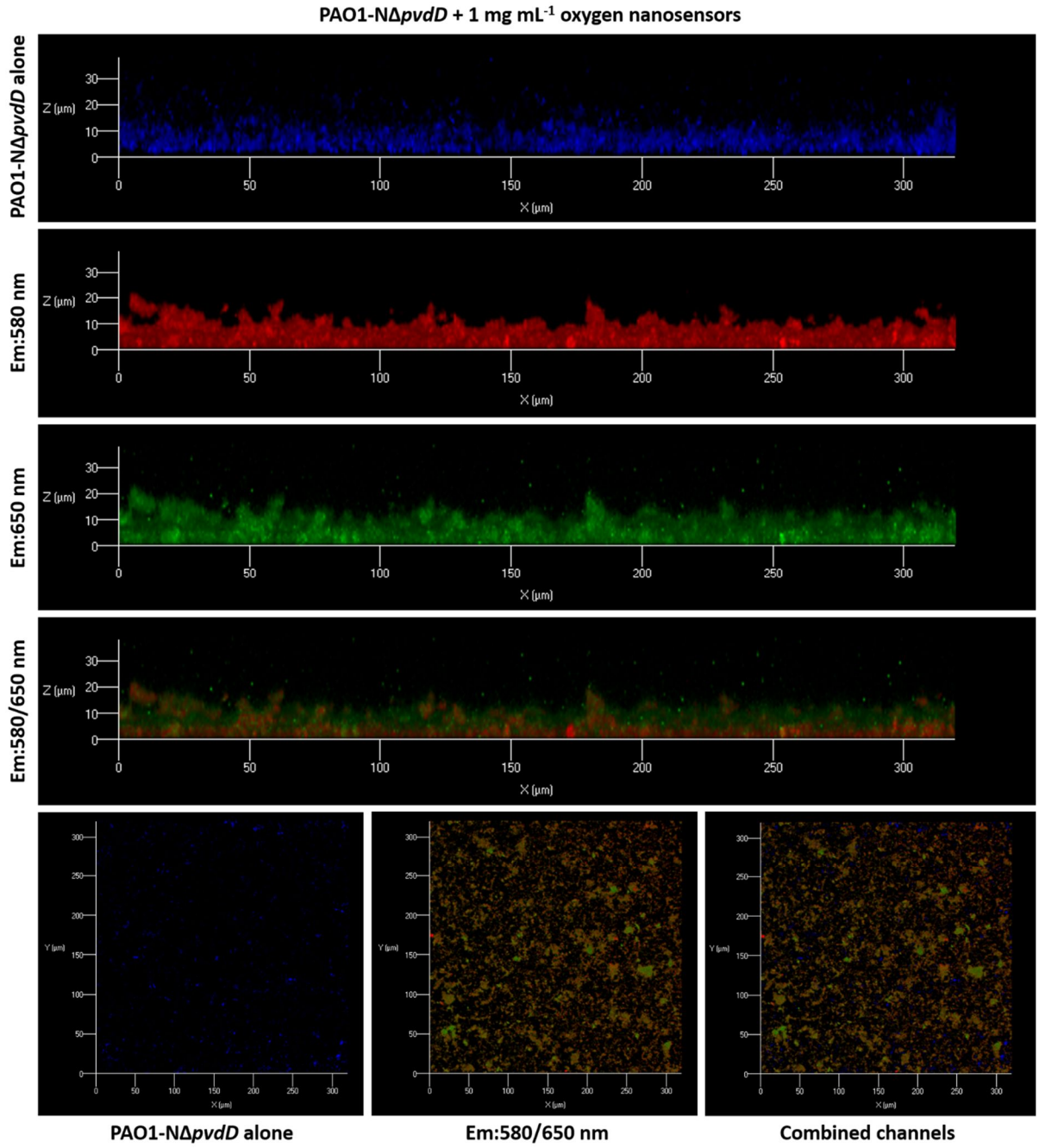

Figure 6.2.8-4: Oxygen-sensitive nanosensors disrupt the formation of microcolonies a PAO1-NΔ*pvdD* biofilm - Representative model of PAO1-NΔ*pvdD* grown over 48 h in M9 succinate. Images taken with a Zeiss confocal laser scanning microscope with a 20x/0.8na objective. **First row**) Side 3D view of DAPI (405 nm excitation). **Second row**) Side 3D view of TAMRA emission (540 nm excitation). **Third row**) Side 3D view of platinum (II) porphyrin emission (405 nm excitation). **Fourth row**) Side 3D view of 580/650 nm emission. **Fifth row; left image**) Top 3D view of DAPI (405 nm excitation). **Fifth row; centre image**) Top 3D view of 580/650 nm emission. **Fifth row; right image**) Top 3D view of DAPI and 580/650 nm emission.

6.2.9. Amphiphilic polymers significantly reduce bacterial attachment and biofilm formation

By using the Calgary Biofilm Device (CBD) Assay in combination with either OxoPlates or oxygen-sensitive nanosensors, the aim was to determine the effectiveness of anti-biofouling materials coating individual pegs of the CBD, as described in 4.10.1.

By measuring the fluorescence intensity changes of the oxygen-sensitive indicator dye contained in the base of an OxoPlate, oxygen consumption can be tracked over time. The assumption is that any variation in oxygen consumption is due to the presence of bacteria attached to the peg-lid after incubation in culture for 5 h. These measurements can then be compared to the uncoated peg used as a control. The cut off point for measurements is when the uncoated control peg (grey dashed line) first begins to plateau, with a similar value 30 min later, indicating metabolic inactivity. The Area under the Curve (AUC) can then be calculated as the sum of each measurement over a specific time series and plotted as a single value; this value is referred to the total fluorescence intensity ratio (total FIR) over this window of time. Any material that has a lower total FIR than the uncoated peg is likely to inhibit bacterial attachment, and any that has a higher total FIR is likely to promote bacterial attachment. All results were normalised as it was assumed that the initial readings matched atmospheric conditions, as described in 4.10.1. (Material 5 changed between experiments and so was discounted).

For PAO1-N, the cut-off point is 270 min, at which point the measurements from the uncoated peg begin to plateau (**Figure *6.2.9-1***a). The AUC is therefore between 0 min and 270 min (**Figure *6.2.9-1***b). The total FIR is only significantly reduced for Materials 3, 4 & 6 (*=P<0.05, **=P<0.005 & ***=P<0.001), whilst there is no significant difference in the total FIR for Materials 1, 2, 7 & 8.

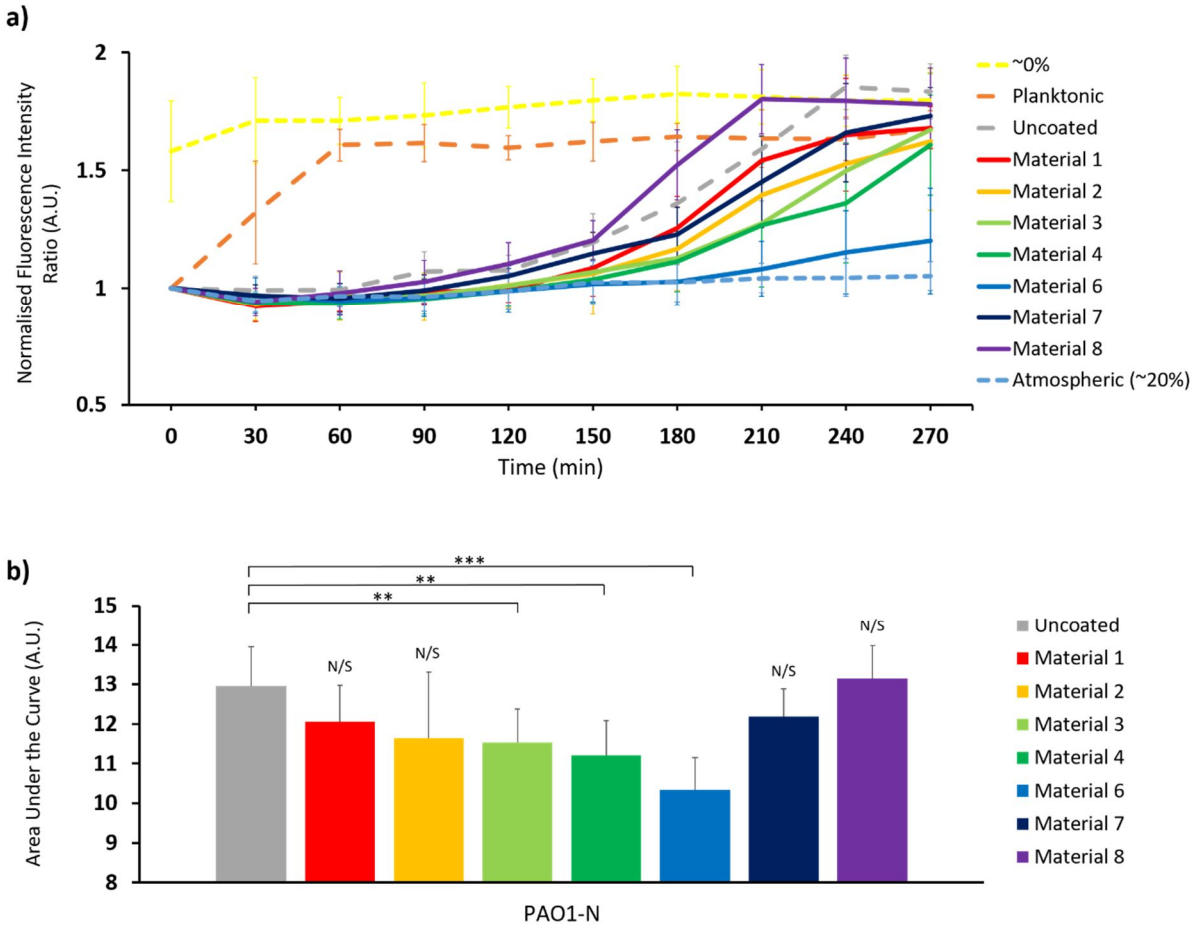

Figure 6.2.9-1: Oxygen consumption was significantly reduced for Materials 3, 4 and 6 indicating reduced attachment of PAO1-N to the coated peg-lids - Using a Calgary Biofilm Device (CBD) assay, peg-lids coated in a range of materials were incubated for 5 h in PAO1-N culture before being transferred to an OxoPlate with TSB media. Fluorescence intensity at ex:540 nm, em:650 nm for the indicator dye and ex:540 nm, em:590 nm for the reference dye was measured every 30 min for 20 h. **a)** the fluorescence intensity ratio (FIR) was plotted over time for each material until 'Uncoated' reached its plateau point (270 min). **b)** The Area Under the Curve (AUC) was calculated to determine total fluorescence intensity ratio (total FIR) over 270 min. (*=P<0.05, **=P<0.005 & ***=P<0.001). Error bars are ±1 S.D. n=1x9

For PA14, the uncoated peg only plateaus after 420 min (**Figure *6.2.9-1***a). The AUC is therefore between 0 min and 420 min (**Figure *6.2.9-1***b). The total FIR is significantly reduced for Materials 1-6, whilst there is no significant difference in the total FIR for Materials 7 & 8.

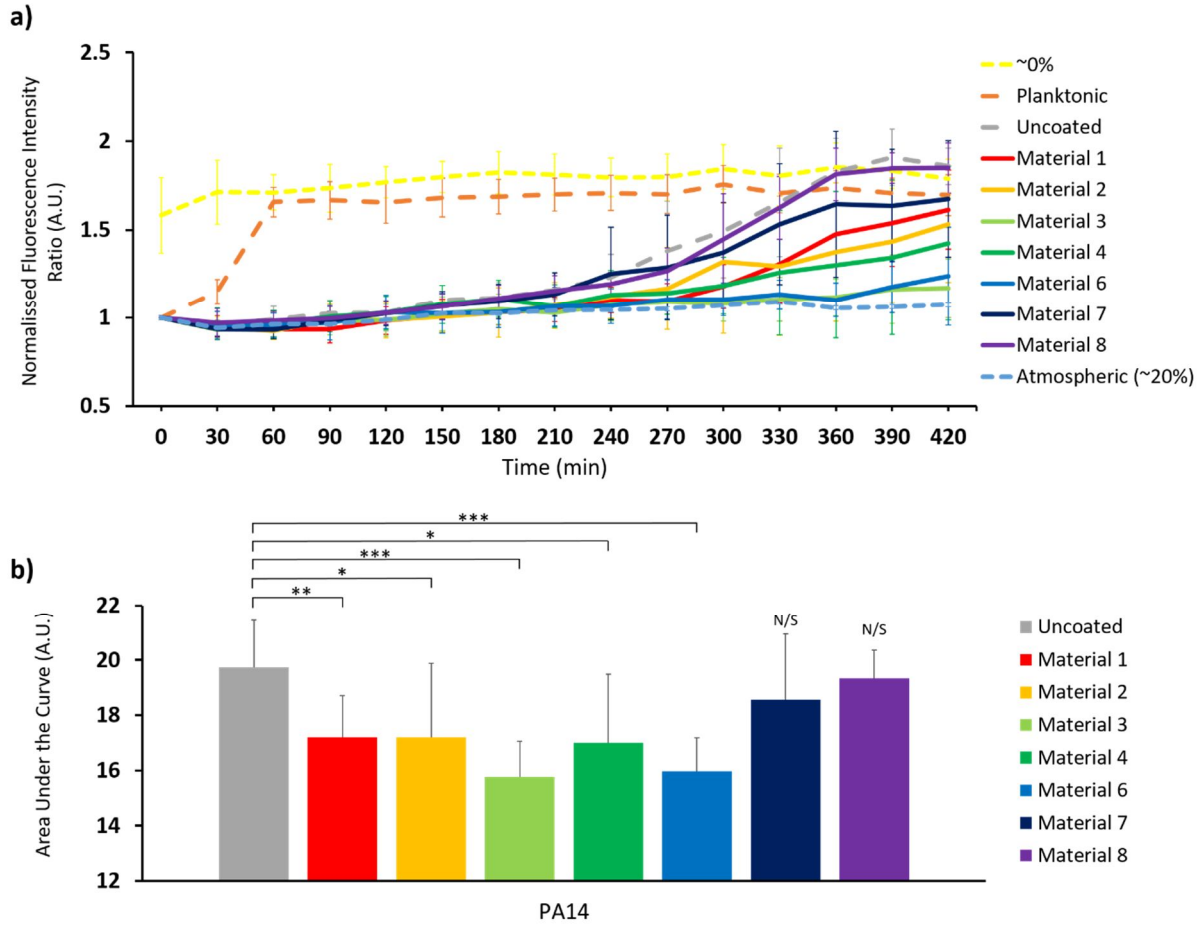

Figure 6.2.9-2: Oxygen consumption was significantly reduced for Materials 1-4 and 6 indicating reduced attachment of PA14 to the coated peg-lids - Using a Calgary Biofilm Device (CBD) assay, peg-lids coated in a range of materials were incubated for 5 h in PA14 culture before being transferred to an OxoPlate with TSB media. Fluorescence intensity at ex:540 nm, em:650 nm for the indicator dye and ex:540 nm, em:590 nm for the reference dye was measured every 30 min for 20 h. **a)** the FIR was plotted over time for each material until 'Uncoated' reached its plateau point (420 min). **b)** The AUC was calculated to determine total FIR over 420 min. (*=P<0.05, **=P<0.005 & ***=P<0.001). Error bars are ±1 S.D. n=1x9

For the *S. aureus* strain ATCC 6538, the uncoated peg again only plateaus after 420 min, as shown in **Figure *6.2.9-3***a). This means the AUC is between 0 min and 420 min (**Figure *6.2.9-3***b). This time the total FIR is only significantly reduced for Materials 2, 4 & 6, whilst there is no significant difference in the total FIR for Materials 1, 3, 7 & 8.

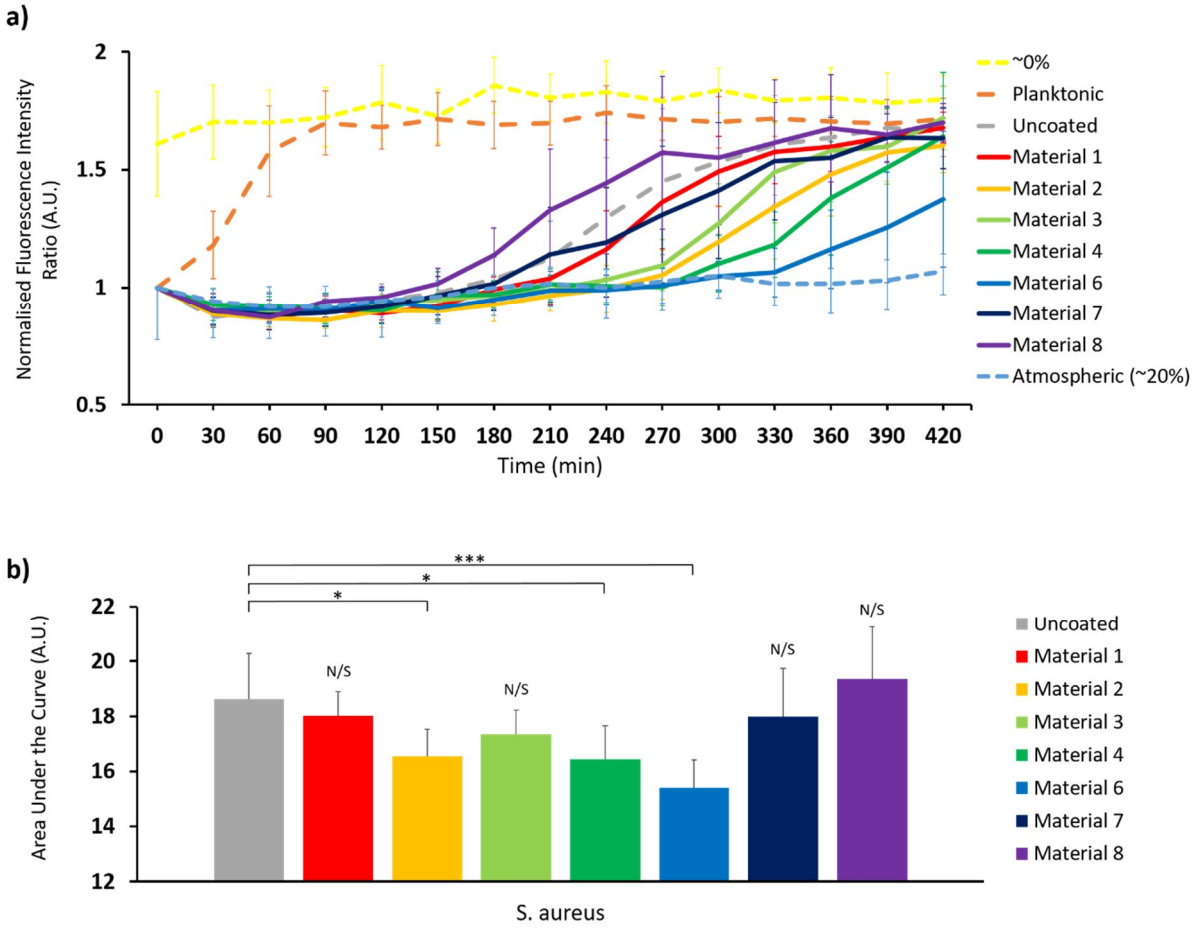

Figure 6.2.9-3: Oxygen consumption was significantly reduced for Materials 2, 4 and 6 indicating reduced attachment of *S. aureus* to the coated peg-lids - Using a Calgary Biofilm Device (CBD) assay, peg-lids coated in a range of materials were incubated for 5 h in *S. aureus* strain ATCC 6538 culture before being transferred to an OxoPlate with TSB media. Fluorescence intensity at ex:540 nm, em:650 nm for the indicator dye and ex:540 nm, em:590 nm for the reference dye was measured every 30 min for 20 h. **a)** the FIR was plotted over time for each material until 'Uncoated' reached its plateau point (420 min). **b)** The AUC was calculated to determine total FIR over 420 min. (*=P<0.05, **=P<0.005 & ***=P<0.001). Error bars are ±1 S.D. n=1x9

Finally, for the *E. coli* strain ATCC 10536 the cut-off point is 120 min, the quickest of the four bacterial species **Figure *6.2.9-4***a), meaning the AUC is calculated between 0 min and 120 min (**Figure *6.2.9-4***b). The total FIR is significantly reduced over 120 min for Materials 3-6, whilst there is no significant difference in the total FIR over 120 min for Material 1, 2 & 8. Oxygen consumption of planktonic *E. coli* is greatly reduced compared to the other three species, similar to the trend in oxygen consumption shown in **Figure *6.2.6-2***.

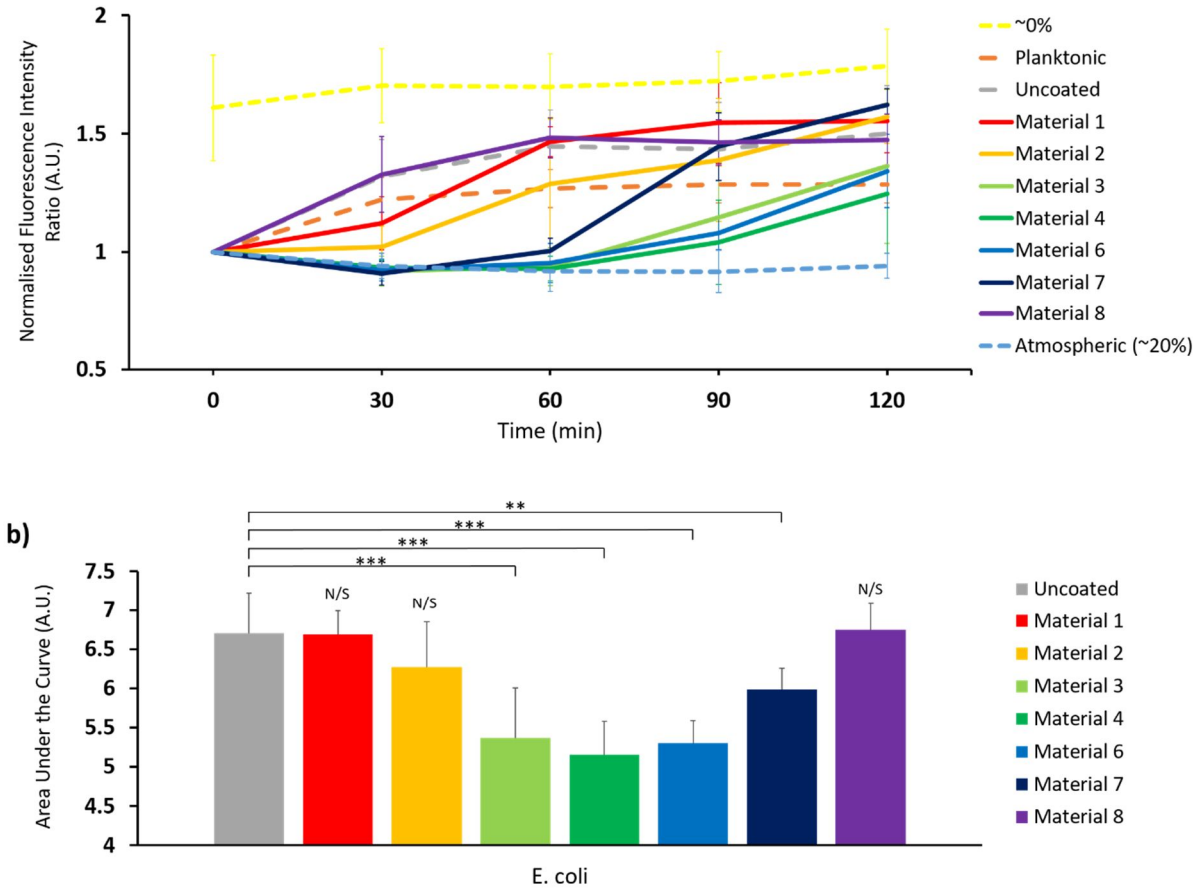

Figure 6.2.9-4: Oxygen consumption was significantly reduced for Materials 3, 4, 6 and 7 indicating reduced attachment of *E. coli* to the coated peg-lids – Using a Calgary Biofilm Device (CBD) assay, peg-lids coated in a range of materials were incubated for 5 h in *E. coli* strain ATCC 10536 culture before being transferred to an OxoPlate with TSB media. Fluorescence intensity at ex:540 nm, em:650 nm for the indicator dye and ex:540 nm, em:590 nm for the reference dye was measured every 30 min for 20 h. **a)** the FIR was plotted over time for each material until 'Uncoated' reached its plateau point (120 min). **b)** The AUC was calculated to determine total FIR over 120 min. (*=P<0.05, **=P<0.005 & ***=P<0.001). Error bars are ±1 S.D. n=1x9

By repeating the CBD assay using oxygen-sensitive nanosensors, a comparison between two oxygen-sensing products could be carried out.

The trends between bacterial species and material are similar to the reduction in total FIR shown in the OxoPlate data. However, there is no significant difference between uncoated and the test materials for three of the four bacterial species (**Figure *6.2.9-5***b, **Figure *6.2.9-6***b, **Figure *6.2.9-7***b & **Figure *6.2.9-8***b).

The response of the oxygen nanosensors appears to be generally more rapid than the OxoPlate, however the FIRs appear to fluctuate between each 30 min read as opposed to the constant increase in FIRs for the OxoPlate readings (all rescaled in **Supplemental Figure *10-9***). The FIR for the 'Atmospheric Control' using the oxygen nanosensors also gradually increases over time, whilst this control for the OxoPlates remains constant. Materials 3, 4 & 6 regularly dip below the Atmospheric control readings for all four bacterial species, whilst the only results that are significantly reduced are in **Figure *6.2.9-8***b, where Material 3 & 6 are significantly reduced compared to 'Uncoated'.

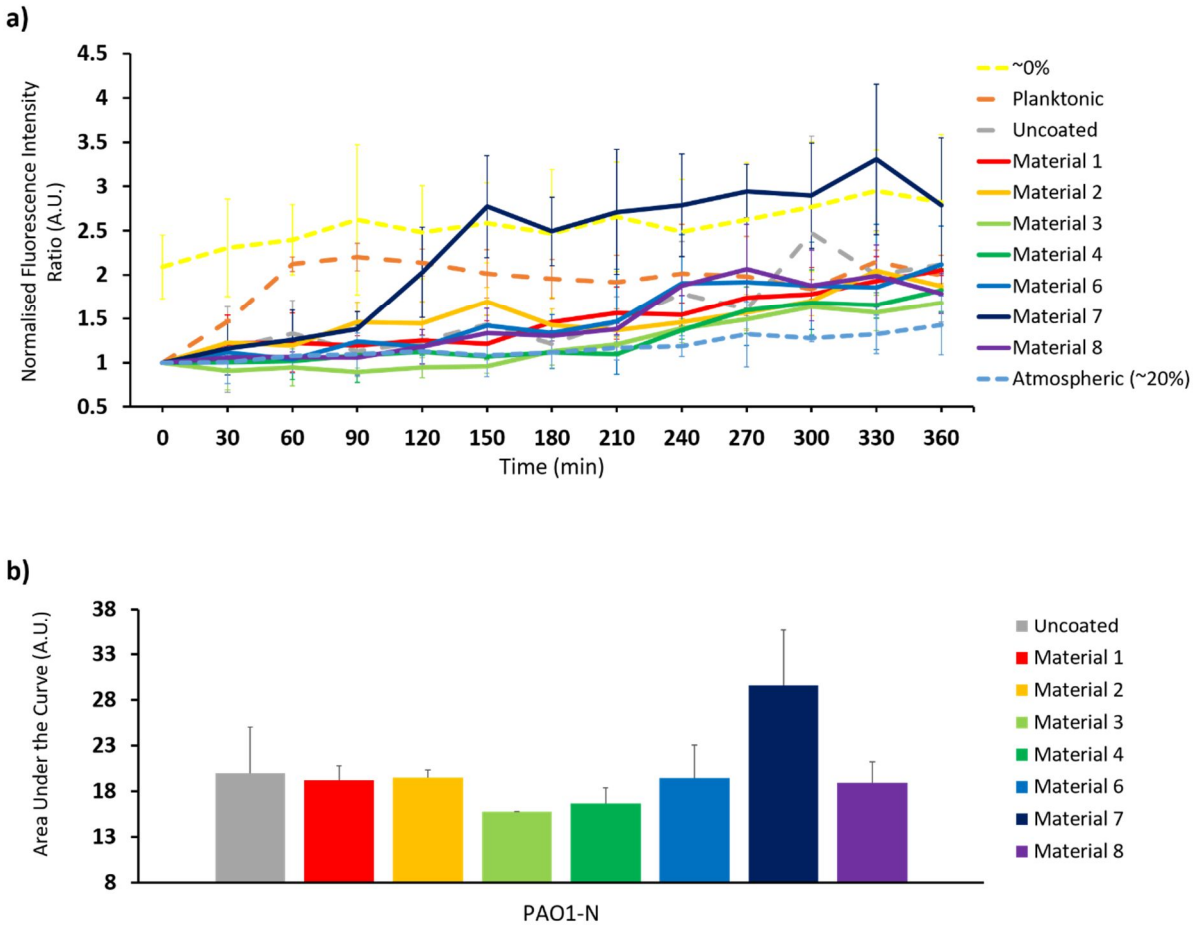

Figure 6.2.9-5: Oxygen-sensitive nanosensors could not detect significant reductions in oxygen consumption for PAO1-N attachment - Using a Calgary Biofilm Device (CBD) assay, peg-lids coated in a range of materials were incubated for 5 h in PAO1-N culture. The peg-lid was then transferred to an 96-well plate containing 0.5 mg mL^{-1} oxygen nanosensors suspended in TSB media. Fluorescence intensity at 580 nm and 650 nm was measured every 30 min for 20 h. **a)** the fluorescence intensity ratio (FIR) was plotted over time for each material until 'Uncoated' reached its plateau point (360 min). **b)** The Area Under the curve was calculated to determine total fluorescence intensity ratio (total FIR) over 360 min. (*=P<0.05, **=P<0.005 & ***=P<0.001). Error bars are ±1 S.D. n=1x2

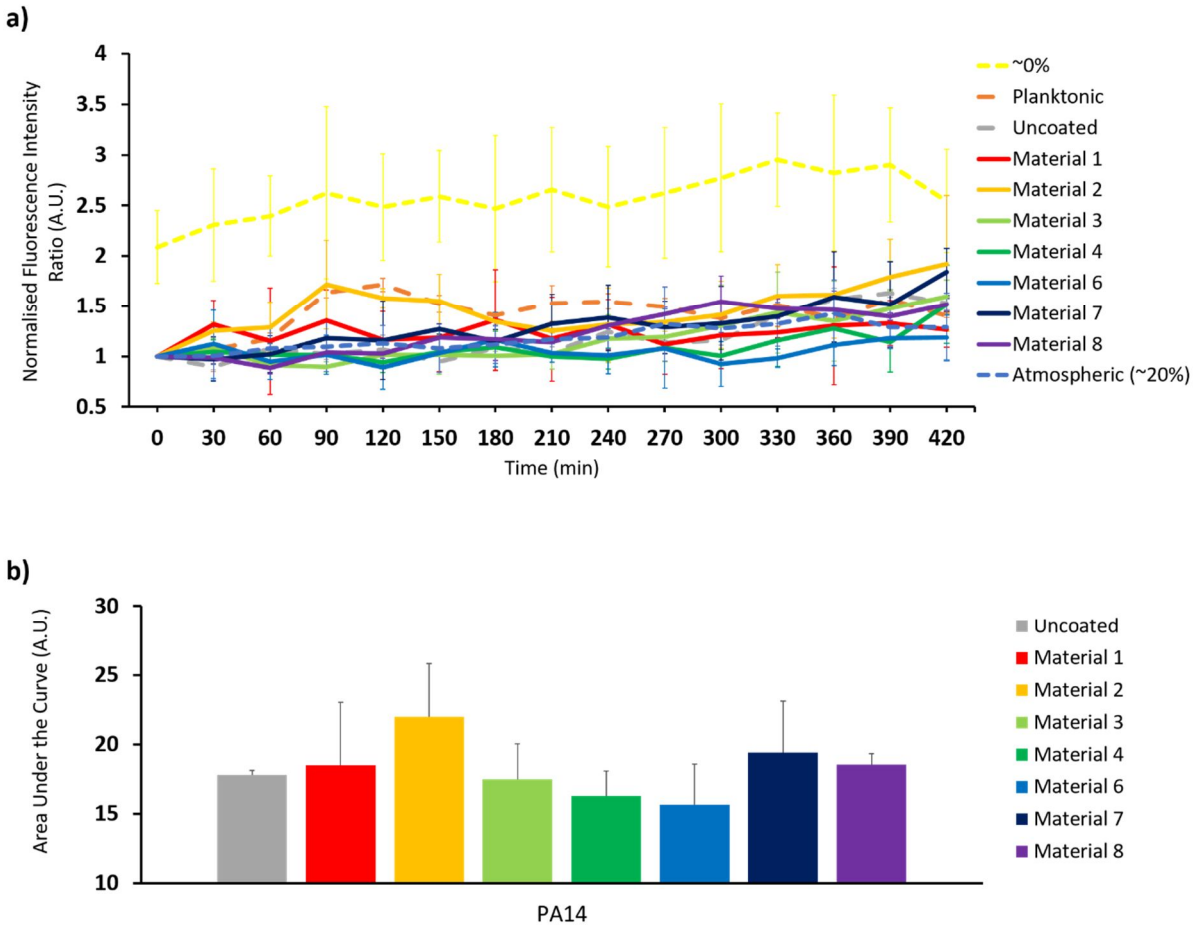

Figure 6.2.9-6: Oxygen-sensitive nanosensors could not detect significant reductions in oxygen consumption for PA14 attachment - Using a Calgary Biofilm Device (CBD) assay, peg-lids coated in a range of materials were incubated for 5 h in PA14 culture. The peg-lid was then transferred to an 96-well plate containing 0.5 mg mL^{-1} oxygen nanosensors suspended in TSB media. Fluorescence intensity at 580 nm and 650 nm was measured every 30 min for 20 h. **a)** the FIR was plotted over time for each material until 'Uncoated' reached its plateau point (420 min). **b)** The AUC was calculated to determine total FIR over 420 min. (*=P<0.05, **=P<0.005 & ***=P<0.001). Error bars are ±1 S.D. n=1x2

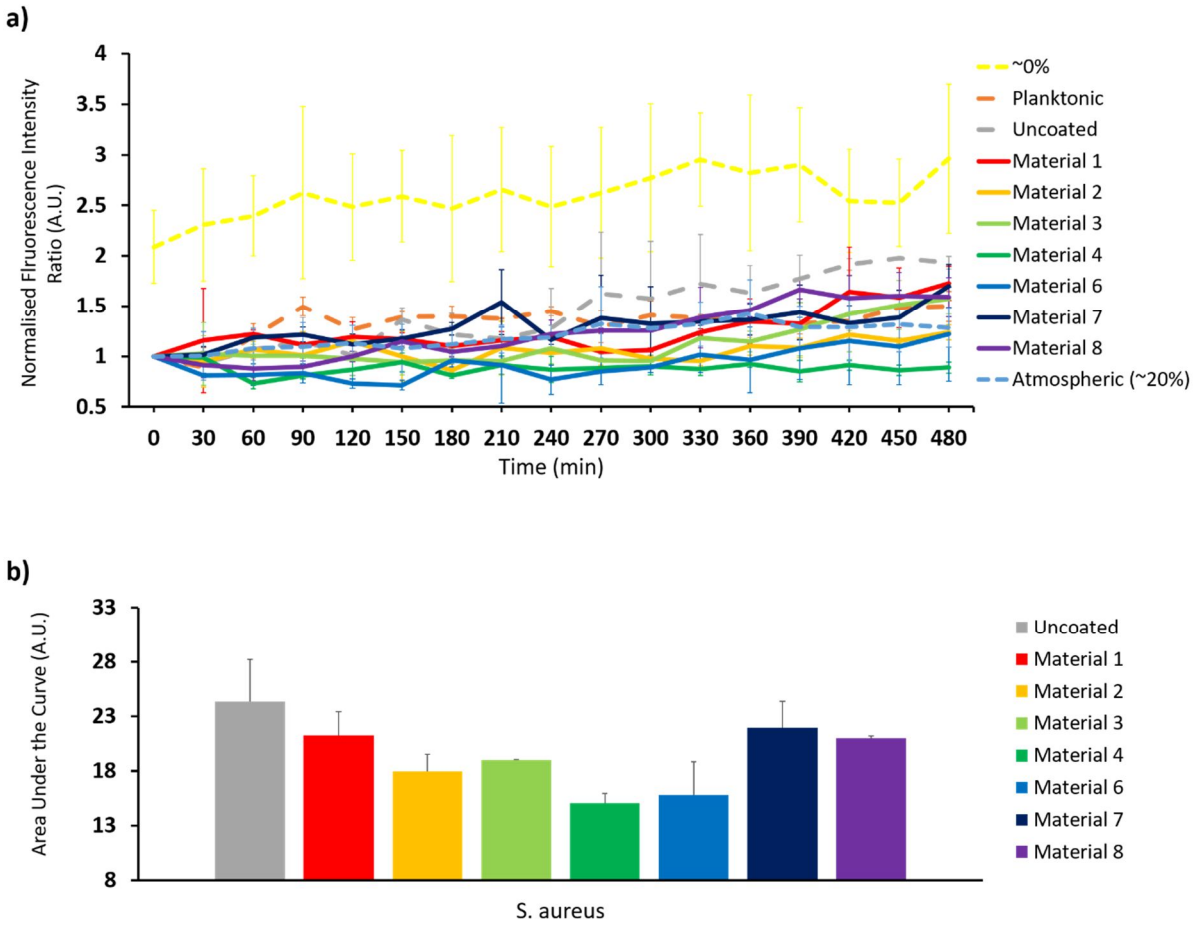

Figure 6.2.9-7: Oxygen-sensitive nanosensors could not detect significant reduction in oxygen consumption for *S. aureus* attachment - Using a Calgary Biofilm Device (CBD) assay, peg-lids coated in a range of materials were incubated for 5 h in *S. aureus* ATCC 6538 culture. The peg-lid was then transferred to an 96-well plate containing 0.5 mg mL^{-1} oxygen nanosensors suspended in TSB media. Fluorescence intensity at 580 nm and 650 nm was measured every 30 min for 20 h. **a)** the FIR was plotted over time for each material until 'Uncoated' reached its plateau point (480 min). **b)** The AUC was calculated to determine total FIR over 480 min. (*=P<0.05, **=P<0.005 & ***=P<0.001). Error bars are ±1 S.D. n=1x2

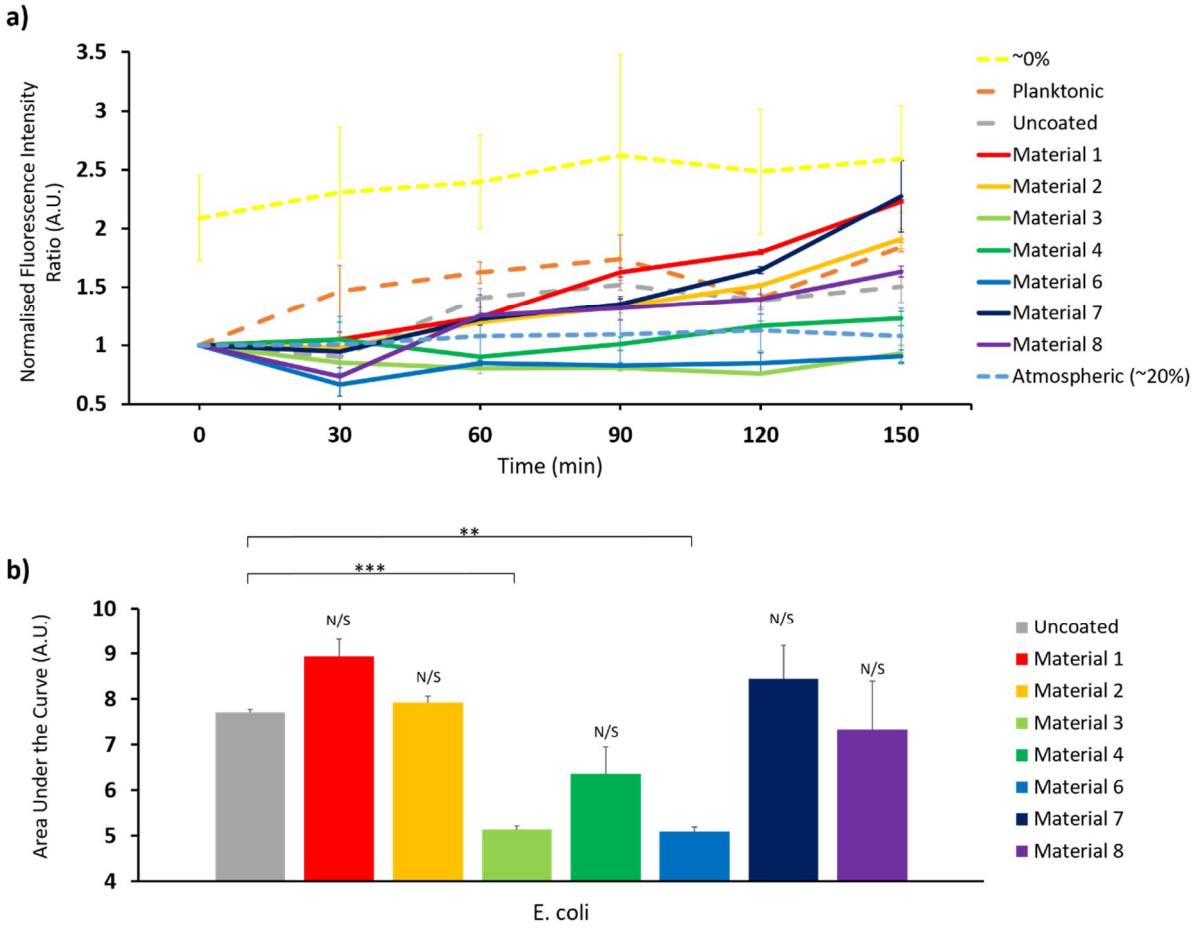

Figure 6.2.9-8: Oxygen-sensitive nanosensors detected a significant reduction in oxygen consumption for Materials 3 and 6 indicating reduced attachment of *E. coli* to the coated peg-lids - Using a Calgary Biofilm Device (CBD) assay, peg-lids coated in a range of materials were incubated for 5 h in *E. coli* ATCC 10536 culture. The peg-lid was then transferred to an 96-well plate containing 0.5 mg mL^{-1} oxygen nanosensors suspended in TSB media. Fluorescence intensity at 580 nm and 650 nm was measured every 30 min for 20 h. **a)** the FIR was plotted over time for each material until 'Uncoated' reached its plateau point (150 min). **b)** The AUC was calculated to determine total FIR over 150 min. (*=P<0.05, **=P<0.005 & ***=P<0.001). Error bars are ±1 S.D. n=1x2

Using oxygen nanosensors rather than an OxoPlate does provide the opportunity to measure any potential fluorescence produced by the bacteria in the absence of oxygen-sensitive and reference fluorophores. For PAO1-N and PA14, auto-fluorescence is present towards the end of the 20 h measurements, as seen in **Figure *6.2.9-9***a & b). The increase in fluorescence intensity is most noticeable in PAO1-N in both planktonic (black lines) and biofilm (brown lines) wells, whilst fluorescence intensity only subtly increases for PA14.

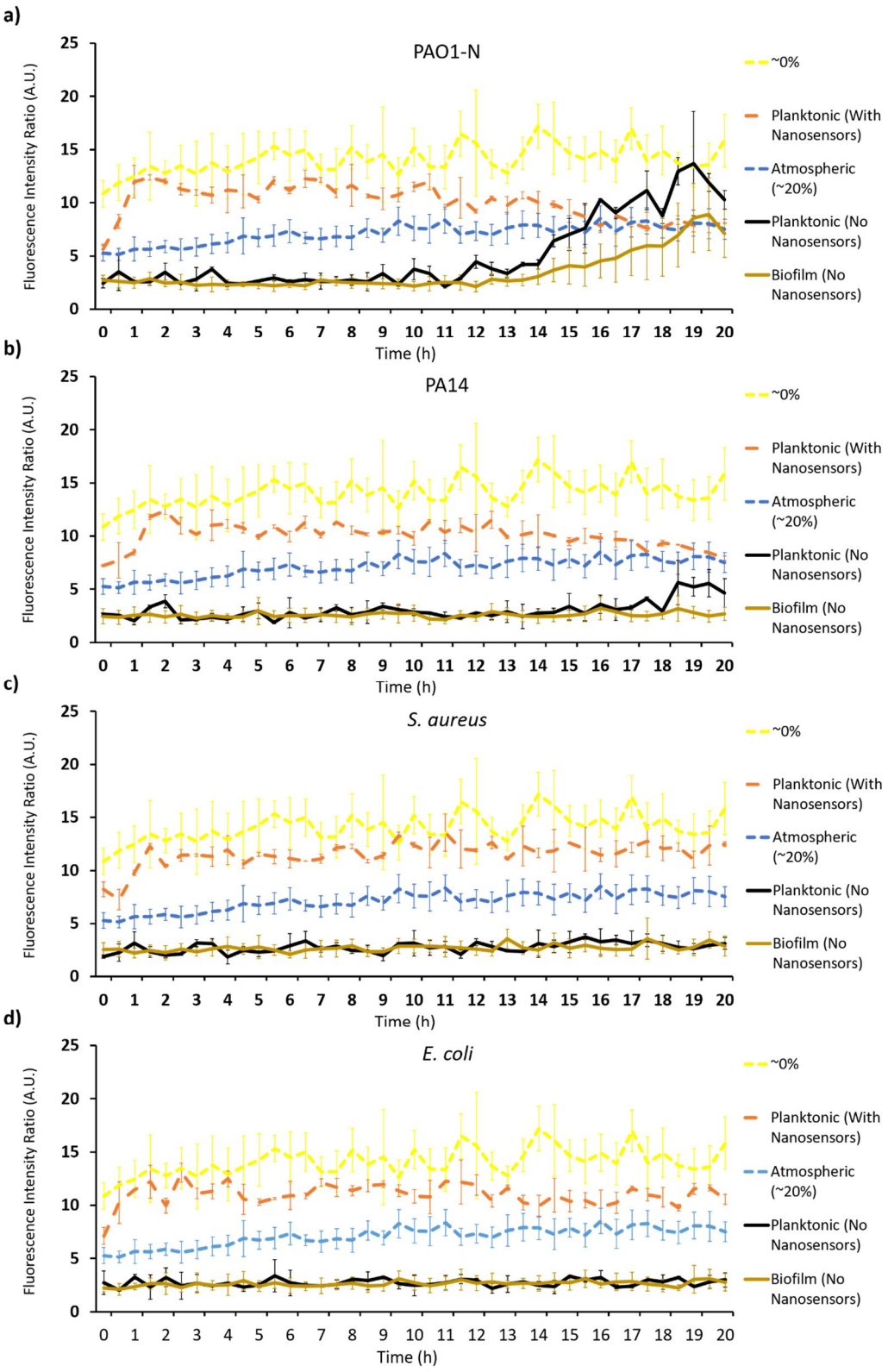

Figure 6.2.9-9: PAO1-N produced auto-fluorescence during CBD-oxygen nanosensor experiments - The fluorescence intensity in the wells absent of oxygen nanosensors was measured at 580 nm and 650 nm every 30 min for 20 h, to detect any auto-fluorescence during the experiment. **a)** shows the fluorescence intensity ratio (FIR) for PAO1-N over 20 h. **b)** shows the FIR for PA14, **c)** shows the FIR for *S. aureus* and **d)** shows the FIR for *E. coli.* Error bars are ±1 S.D. n=1x2

The final biofilm mass of each peg-lid was quantified using crystal violet staining. After 20 h incubation for fluorescence intensity measurements, each peg-lid was stained using the crystal violet method in 4.10.2.

By staining a material-treated peg-lid that had not been incubated in bacteria, background crystal violet absorption can be subtracted from the crystal violet readings generated by bacterial staining. The results can then be compared to the 'Uncoated' samples. **Figure *6.2.9-10*** shows both a simplified version of the above data and the crystal violet staining after 20 h incubation. Green panels indicate reduced attachment compared to uncoated, whilst red panels indicate increased attachment, and yellow panels indicate no significant effect on attachment. A variation between fluorescence intensity ratio and crystal violet results are due to different processes being measured; fluorescence intensity is inferred bacterial attachment whilst crystal violet is measuring final biofilm mass.

Crystal violet staining between the OxoPlate and nanosensor results again shows similar trends for reduced biofilm formation with *E. coli* (Materials 1-7) and PA14 (Materials 1-6), whilst PAO1-N biofilm formation appears to be increased in most materials for both assays. Finally Material 8 appears to increase biofilm formation across most species for OxoPlate work (Material 8 is a positive control – PDMS) whilst Material 7 appears to increase biofilm formation across most species for oxygen nanosensor work.

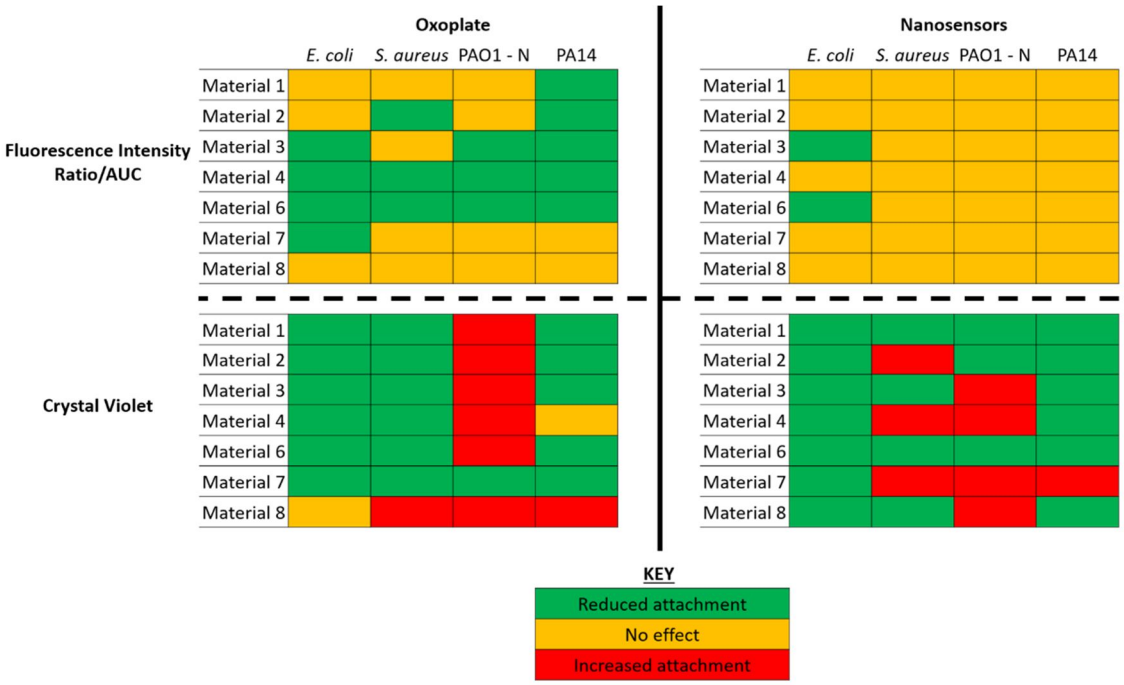

Figure 6.2.9-10: Materials 3, 4 and 6 reduced bacterial attachment and biofilm formation most significantly of the seven materials used – (**Top Panels**) Comparison of oxygen consumption between bacterial species and materials for OxoPlate and oxygen nanosensor results. (**Bottom Panels**) Comparison of Crystal Violet measurements taken from the peg-lids post 20 h incubation. Peg-lids were stained with 0.05% crystal violet before two washing steps with H_2O. Crystal violet was removed using 95% ethanol and the resultant crystal violet was measured for absorption at 590 nm. Final results were subtracted from crystal violet values taken from material treated peg-lid not incubated in bacteria.

6.3. Discussion

Oxygen availability plays an essential role in the establishment of microbial biofilms, whilst oxygen gradients can both inform organisational structure (where multiple species are present) and form as a result of a mature biofilm. One such result of the formation of oxygen gradients is the impact low oxygen concentrations can have on the action of certain antimicrobials. Therefore, there is a need for novel approaches to probe these oxygen gradients to determine their effect on biofilm-specific processes. In order to characterise these physicochemical gradients in biofilms, oxygen-sensitive nanosensors were used in this study.

The first objective was to confirm the suitability of the platinum (II) porphyrin based oxygen-sensitive nanosensors as a functional analytical tool; and to confirm whether the *P. aeruginosa* strain PAO1-N was a suitable model organism to test the oxygen-sensitive nanosensors. The initial experiment using an Agilent Fluorescence Spectrometer, concurrently with an oxygen probe, showed that the oxygen nanosensors themselves were suitable for measuring changes in varying oxygen concentrations (***Figure 6.2.2-1***). As oxygen decreased, the fluorescence intensity at 650 nm decreased. The quenching effect of oxygen was also reversible as the bubbling of argon into the oxygen nanosensor mixture resulted in the increase of fluorescence intensity; this was due to the density of the argon, which can displace the oxygen, allowing an increase in fluorescence intensity. The sensitivity of platinum (II) porphyrin to oxygen, paired with the insensitivity of TAMRA could therefore provide the ratiometric measurements required to track oxygen consumption in planktonic culture and oxygen availability in microbial biofilms.

The additional experiments to determine the suitability of PAO1-N as a model organism highlighted the issues with auto-fluorescence in biological samples, especially with *Pseudomonas* species. Wide ranging work measuring the fluorescence spectra of *P. aeruginosa* often plot the maximum emission reading at ≤600 nm when using an excitation wavelength of 400 nm (Sosnin et al., 2014, Folschweiller et al., 2002). Additionally, previous work to determine the site of synthesis and exportation of the virulence factor pyoverdine in *P. aeruginosa* only measured fluorescence emission at 450 nm (Yeterian et al., 2010). However, none expands the emission range up to 650 nm in order to detect auto-fluorescence that is shown in this work.

By measuring emission at 650 nm, using an excitation of 405 nm, auto-fluorescence was detected in PAO1 growth assays, even when the oxygen-sensitive nanosensors were absent, as shown in ***Figure 6.2.3-1***. Four strains of PAO1 were used (Nottingham, Lausanne, Washington and Denmark) in an effort to determine the source of auto-fluorescence as sublines of the laboratory strain PAO1 have emerged, leading to genome diversity between the strains (Klockgether et al., 2010). These results suggested that all four PAO1 strains used produce a pigment that fits within the fluorescence spectra used to measure platinum (II) porphyrin fluorescence. This auto-fluorescence was not present in either *S. aureus* strain SH1000 or *E. coli* strain DH5α (***Figure 6.2.4-1***), indicating an isolated issue to *Pseudomonas spp*. So, what was causing the auto-fluorescence in planktonic culture? *Pseudomonas spp.* produce a variety of extracellular pigments that can act as virulence factors and provide distinct colour changes in planktonic culture. *Pseudomonas spp.* are capable of producing one or more of these pigments, including pyocyanin, pyoverdine and pyochelin. Pyocyanin is a blue pigment and a redox-active phenazine that acts as a virulence

factor for *P. aeruginosa* (Lau et al., 2004, Huang et al., 2012) (**Figure *6.3-1***a). For example, pyocyanin can act on other bacteria, such as *S. aureus*, where it can both inhibit respiration and generate ROS to kill non-respiring *S. aureus* (Noto et al., 2017). Both pyoverdine and pyochelin are siderophores; a secreted molecule which binds and transports iron in iron limited conditions. Pyoverdine is a yellow-green pigment that is comprised of three distinct structural parts; a dihydroxyquinoline chromophore that is responsible for its fluorescence, a peptide chain of 6-12 amino acids bound to the carboxyl group, and a small dicarboxylic acid bound to the NH_2 group of the chromophore (Budzikiewicz et al., 2007) (**Figure *6.3-1***b). Finally, pyochelin is a simpler molecule lacking the chromophore (Hoegy et al., 2014) (**Figure *6.3-1***c). Pyochelin can be detected with a fluorescence emission peak at 432 nm when excited at 320 nm (Brandel et al., 2012), whereas pyoverdine fluorescence emission peak can differ depending on the *P. aeruginosa* strain used. For example, Folschweiller et al. (2002) reported pyoverdine emission peaked at 447 nm when excited at 400 nm, whilst Sosnin et al. (2014) reported peaks at 435-445 nm and 455-470 nm for two different stains.

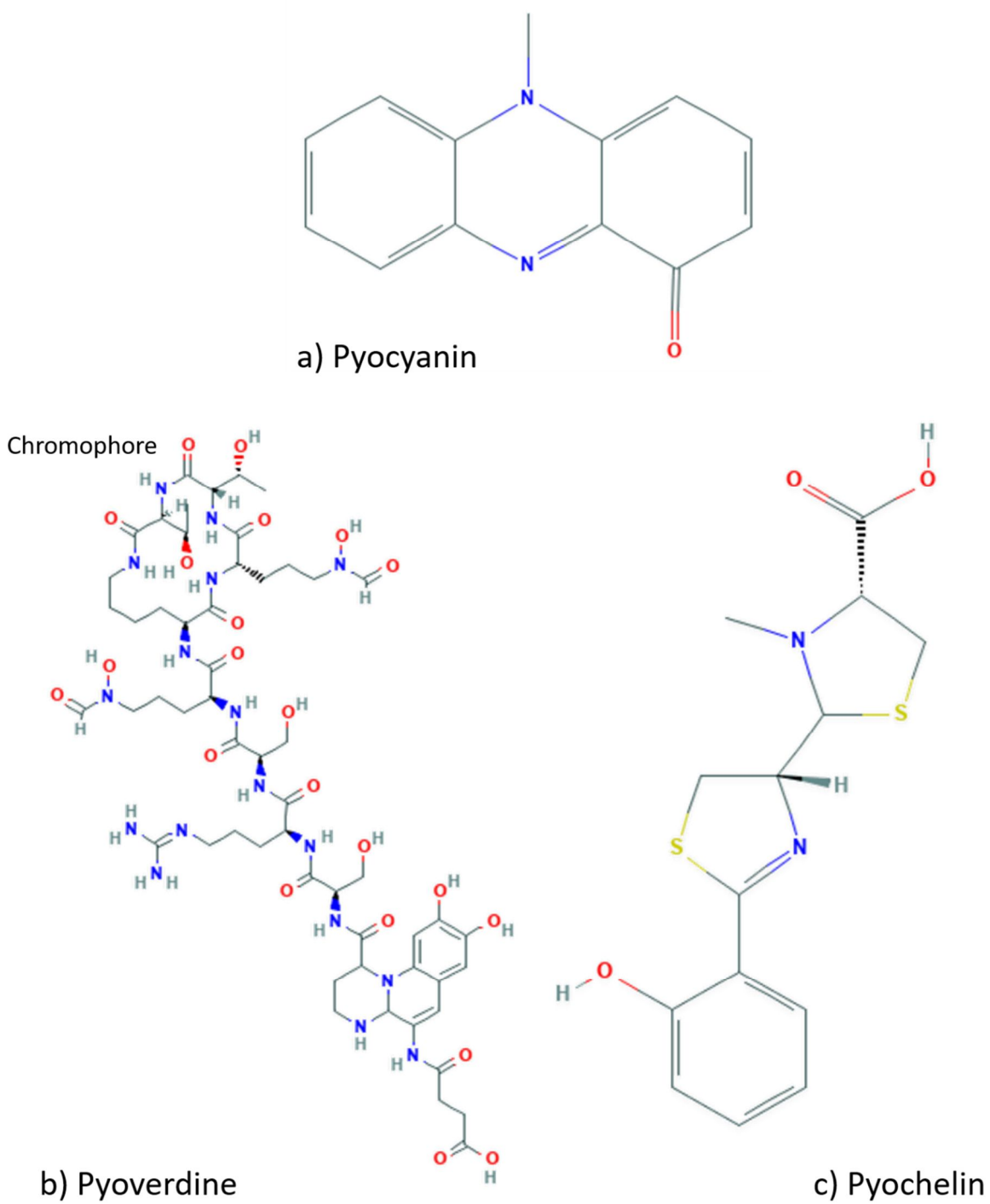

Figure 6.3-1: The chemical structures of the three *P. aeruginosa* virulence factors (a) pyocyanin, (b) pyochelin and (c) pyoverdine – Sourced from PubChem *https://pubchem.ncbi.nlm.nih.gov*

As seen in ***Figure 6.2.5-1***, the fluorescence intensity at 650 nm was greatly reduced in PAO1 C++Δ*pvdD*, PAO1-NΔ*pvdD* and PAO1 C++Δ*pvdD*Δpch*EF* mutants, whilst the auto-fluorescence was unaffected in the wildtype strains PA14, PAO1-N and PAO1 C++, as well as the pyochelin (PAO1-NΔ*pchEF*) and pyocyanin (CW4T1) mutants. This suggested that pyoverdine, or a precursor, was causing the auto-fluorescence present in previous experiments. This may also explain the absence of fluorescence seen in DH5α and SH1000, as neither strain produces fluorescent pigmentation such as pyoverdine.

The second objective was to detect variations in oxygen consumption in planktonic culture. Initial experiments were required to confirm that a gas permeable membrane was an essential addition to the experimental design. As shown in ***Figure 6.2.6-1***a, fluorescence intensity of the two physiological standards were measured over time, with and without coverage. The addition of the gas permeable membrane maintained stable measurements for the atmospheric and ~0% controls, whilst the measurements from the controls without the membrane decreased over time. This suggested that without a gas permeable membrane, oxygen could permeate into the wells causing the '~0%' control to gradually decrease in fluorescence intensity at 650 nm (a decrease in fluorescence intensity at 650 nm indicates an increase in oxygen). The reduction in fluorescence intensity for 'atmospheric' may also be due to the quenching effect of oxygen causing gradual photobleaching (Kim et al., 2015). ***Figure 6.2.6-1***b also confirmed that PAO1-NΔ*pvdD*, DH5α and SH1000 were reliable strains for measuring emission at 650 nm as only negligible fluorescence was present at 650 nm when each strain was grown in the absence of the oxygen-sensitive nanosensors.

Progressing forward using PAO1-NΔ*pvdD* as a reliable *Pseudomonas* strain, alongside DH5α and SH1000, both growth (in M9 glucose) and oxygen consumption was measured over 21 h, as shown in **Figure *6.2.6-2***. Growth varied significantly between the three species, with PAO1-NΔ*pvdD* reaching stationary phase first, followed by DH5α then SH1000 (**Figure *6.2.6-2***a). The effect of glucose supplementation on *Staphylococci species* growth has been previously shown to be significantly decreased, whilst *E. coli* and *P. aeruginosa* remained unaffected (Luo et al., 2020).

Initially looking at **Figure *6.2.6-2***c, the atmospheric control remained stable over time; this would indicate oxygen levels remained consistent across all control wells, which would infer any fluorescence intensity change to the porphyrin would be due to oxygen being consumed by the cell. **Figure *6.2.6-1***b also confirmed that bacterial cells were not the contributing factor to any fluorescence intensity changes *i.e.* by the production of auto-fluorescent molecules. The fluorescence intensity ratio (FIR) for '~0%' did increase slightly over 21 h; however, this may be explained by excess sodium sulphite still scavenging oxygen during that period of time.

Looking next at the FIR for each bacterial species, the FIR varied greatly over 21 h, suggesting oxygen consumption was different between each species. PAO1-NΔ*pvdD* consumed oxygen at a greater rate and to a greater extent. The initial increase in FIR matched the increase in Optical Density (OD) as it appeared PAO1-NΔ*pvdD* lacked any lag phase in growth. This rapid change in FIR mirrored the PAO1-NΔ*pvdD* growth rate, where the FIR plateaued at a similar time as PAO1-NΔ*pvdD* reached stationary phase. There also appeared to be a second phase to the FIR increase between ~8-15 h, which indicates oxygen was still

required to maintain stationary phase. Whilst *P. aeruginosa* is versatile metabolically (Arai, 2011), the initial rapid increase in FIR would suggest that PAO1-NΔ*pvdD* was preferentially using oxygen during the exponential phase of growth. The FIR of SH1000 appeared to follow a similar trend as PAO1-NΔ*pvdD* did, with the increase in the FIR mirroring the growth rate. The initial plateau matched the growth, indicating SH1000 was in lag phase, before the FIR slowly increased in line with the growth curve without a clear plateau stage, as SH1000 did not reach stationary phase. Again, this would suggest oxygen consumption matching cell replication. For DH5α the initial plateau indicated a lag phase, which was confirmed by the growth curve. However, DH5α varied from the other two species (where a gradual increase in the FIR was followed by a plateau). For DH5α the plateau in the FIR (~5 h) was much earlier than the plateau seen in the growth rate (~10 h). This would indicate that DH5α, a facultative anaerobe, switched to fermentation during planktonic growth. Further work would be required to confirm whether these results highlight the efficiency of bacteria to consume oxygen, as both *E. coli* and *P. aeruginosa* reached similar cell density yet *P. aeruginosa* consumed significantly more oxygen. This could be achieved by performing MTT cell viability assay to confirm endpoint cell viability. It must also be taken into consideration that the terms used to describe the growth of planktonic cells in these experiments (*i.e.* lag and stationary phase) are not so easily defined for bacterial growth *in vivo*. Microbes in nature most likely exist in a biofilm rather than in a planktonic form. This would lead to the overlapping of cell growth, dormancy, and cell death.

The effect of efficiency and metabolic flexibility can provide a competitive advantage when infecting various sites. This is shown in the ability of *E. coli* to infect streptomycin-treated mouse intestine (Jones et al., 2007); where oxygen

was shown to be key for the colonisation of mouse intestine. *E. coli* has a metabolic hierarchy where aerobic respiration is the highest level in the hierarchy, followed by nitrate respiration and finally anaerobic respiration (Unden et al., 1994). This provides an initial advantage to grow and exhaust carbohydrates present. Once resources are depleted, *E. coli* can switch to anaerobic respiration to continue growth. This action would overwhelm their competitors and improve colonisation.

The above results showed that the nanosensors could measure oxygen consumption for a range of bacterial species, the next step was to see whether variations in oxygen consumption could be seen when *P. aeruginosa* was supplied with nitrate. *Pseudomonas* also has a hierarchical metabolism where it will preferentially metabolise amino acids before moving to hydrocarbons (Rojo, 2010). *P. aeruginosa* is also capable of using nitrate as an alternative electron acceptor, as mentioned above (Arai, 2011). Using PAO1-N∆*pvdD* with and without potassium nitrate (0, 5, 10 & 20 mM), supplemented by casamino acids (1% w/v), the objective was to detect any difference in oxygen consumption when nitrate was added. Planktonic growth was reduced when PAO1-N∆*pvdD* was supplemented with KNO_3 (***Figure 6.2.7-1***); this may be the case as nitrate can act as an environmental cue to transition from planktonic growth to biofilm development. The two-component nitrate sensor-response regulator pair NarX/NarL can detect exogenous nitrate and initiate both swimming and swarming of PAO1, leading to the development of a biofilm (Van Alst et al., 2007). However, the possible presence of a biofilm was not confirmed during this assay. Oxygen consumption also increased between 1% w/v casamino acid alone and the KNO_3 supplemented conditions (***Figure 6.2.7-1***c &d). This was likely due to PAO1-N∆*pvdD* using the nitrate as an alternative electron acceptor. There was also a significant difference between 1% w/v casamino acids with 5 mM KNO_3 and

the 10 mM/20 mM conditions. As the KNO_3 increased in concentration, the FIR flattened for 10 mM and 20 mM, whilst the FIR for 5 mM continued to increase. This suggested that 10 mM KNO_3 was an adequate concentration to provide an alternative to oxygen for *P. aeruginosa*.

The third objective was to determine the interaction of the oxygen nanosensors in a *P. aeruginosa* biofilm. The initial question was whether to proceed with PAO1-N WT or PAO1-NΔ*pvdD* to limit the impact pyoverdine may have an auto-fluorescence during imaging. The fluorescence intensity (em:580/650 nm) in **Figure *6.2.8-1*** (PAO1-N WT alone), was absent at 580 nm and negligible at 650 nm, indicating little to no auto-fluorescence that may interfere with the fluorescence of the oxygen nanosensors when embedded in a biofilm. Similar results were shown when PAO1-NΔ*pvdD* was grown in the absence of nanosensors (**Figure *6.2.8-2***) as the fluorescence intensity of the 650 nm was also negligible. It was likely that any auto-fluorescent pigment was substantially removed during the biofilm set-up for imaging, as part of the preparation process was the removal and replacement of the growth media with saline. Pyoverdine is secreted into the media in order to scavenge available iron; as the growth media was removed, it was likely that the secreted pyoverdine was removed, reducing the potential for auto-fluorescence with PAO1-N WT. Additionally, the structure of the biofilm varied between the two biofilms grown in the absence of nanosensors. PAO1-N WT produced a thinner biofilm (~6 μm) than PAO1-NΔ*pvdD* (~10 μm) but with more microcolonies. The reduction in microcolonies was likely caused by the absence of pyoverdine, as it is an important factor for biofilm formation due to intracellular iron acting as a signal for biofilm establishment (Banin et al., 2005, Kang et al., 2018). PAO1-N WT thus appeared to be the most suitable stain for follow-on oxygen nanosensor work.

Figure *6.2.8-3* and **Figure *6.2.8-4*** showed representative images of PAO1-N WT and PAO1-NΔ*pvdD*, respectively, with 1 mg mL^{-1} oxygen nanosensors. However, further optimisation of the protocols used to incorporate the oxygen-sensitive nanosensors is required, as it is not yet fully reproducible. As a general theme, there were occasions where the oxygen nanosensors disrupted microcolony formation or were not uniformly dispersed throughout the biofilm; this did not appear to be limited to a particular batch of oxygen nanosensors. These results may hinder the use of the oxygen nanosensors for static biofilm work in the future. The aspects of the protocol that could be optimised to improve the incorporation of the oxygen nanosensors would include using a nutrient rich medium such as Luria Broth (LB), rather than a minimal media, whilst longer incubation times (>48 h) may also allow for improved biofilm formation. Finally, a change from a glass surface to polystyrene may improve bacterial attachment and encourage improved microcolony formation.

Understanding what may have disrupted the microcolony formation is also important. Planktonic growth appeared unaffected by the nanosensors (**Supplemental Figure *10-5***); which would suggest the surface attached platinum (II) porphyrin was not inhibiting the growth of PAO1-N WT. The charge of the oxygen nanosensors was reduced, when compared to the pH-sensitive nanosensors (4.17 ±0.24 mV vs. 18.18 ±2.359 mV), yet the oxygen nanosensors still possessed a positive charge which, as discussed above, can improve biofilm thickness in PAO1-N WT. The only remaining difference is particle size. The oxygen nanosensors were 203.54 nm (±7.37), a similar size to the oxygen nanosensors produced by Jewell et al. (2019) (163.4 ±1.5 nm), yet much larger than the pH-sensitive nanosensors used in this thesis (44.61 ±2.35 nm). It is unclear whether the oxygen nanosensors used by Jewell et al. (2019) disrupted *P. aeruginosa*

biofilm formation, however it appeared that their nanosensors clustered in a similar fashion as our nanosensors. It is therefore possible that the size of the nanosensors prevented the formation of microcolonies in PAO1-N WT biofilms.

The final objective was to elucidate the anti-biofilm properties of a range of polymer materials. Preventing bacterial attachment was of interest to Unilever as their aim is to develop a treatment method that could limit bacterial attachment to clothes during washing and to the washing machine itself. To test these materials, a commercially available oxygen-sensing product (*PreSens* OxoPlate OP96U) was used to measure oxygen availability as a proxy for bacterial attachment. The second part of the objective was to compare this commercial product to our oxygen-sensitive polyacrylamide nanosensors.

Peg-lids coated with a range of materials were incubated for 5 h in bacterial culture, before being incubated in media either aliquoted into an OxoPlate or a 96-well plate containing oxygen nanosensors; where fluorescence intensity readings were taken every 30 min for 20 h. The more cells attached after the initial 5 h incubation, the more oxygen that would, theoretically, be consumed during the second 20 h incubation step. Materials that were significantly below the uncoated, polystyrene control could be considered an inhibitor of attachment whilst any result significantly above the uncoated control could be considered a promoter. The final biofilm mass was also quantified using Crystal Violet staining to determine whether the attached cells could form a biofilm. A similar method of measuring oxygen consumption to infer growth has been used by Jewell et al. (2020b), incorporating their oxygen nanosensors in the biofilm during initial incubation for cell attachment, rather than in the media during biofilm formation. This method would not have been conducive for this work as we were focused on

bacterial attachment and biofilm formation between materials rather than treatment to uniform biofilms.

Of the seven materials tested for their anti-biofouling potential, Material 8 (Polydimethylsiloxane – PDMS) was used as an additional, positive control. Both PDMS and polystyrene aid attachment due to the hydrophobic interactions between bacteria and the surface material (Fletcher and Loeb, 1979); thermodynamics dictates the binding of bacteria to surfaces; attachment is more extensive to hydrophilic surfaces when the surface tension of the bacteria is larger than the solution used to suspend the bacteria. However, if the surface tension of the suspending solution is larger than that of the bacteria, attachment to hydrophobic surfaces is increased (Absolom et al., 1983); therefore, this made PDMS and polystyrene excellent controls. Comparing PDMS to the 'Uncoated' polystyrene control, showed no significant difference in the fluorescence intensity ratio; this would indicate PDMS had no impact in the reduction of attachment.

For the other materials, significant differences between oxygen consumption was seen for all four bacterial species compared to the 'Uncoated' polystyrene control. (**Figure *6.2.9-1***, **Figure *6.2.9-2***, **Figure *6.2.9-3*** & **Figure *6.2.9-4***). ***Developing Anti-biofouling Materials*** (1.2.1) explained why each material was chosen, whilst **Error! Reference source not found.** shows the materials used. To summarise; Materials 1 & 2 were PEOX 200 kDa and PEOX 500 kDa respectively. These were Poly(2-ethyl-2-oxazoline) with PEOX 500 kDa having an increased number of repeat units. Both were hydrophilic with PEOX 500 kDa being less water soluble compared to lower the molecular weight PEOX 200 kDa.

Materials 3 & 4 were the Poloxamers, F127 and P123, respectively. These were PEO-PPO-PEO block copolymers where the end tail PEO regions were hydrophilic

and the central PPO region was hydrophobic, creating an amphiphilic polymer. The first two numbers (12) define the proportion of the PPO region (multiplied by 300), whilst the final number defines the proportion of the PEO region as a percentage of the total molecular weight. Therefore, both had the same chain length hydrophobic region whilst F127 had more hydrophilic character compared to P123. Once coated on the peg-lid, the hydrophobic central region absorbs into the hydrophobic polystyrene of the peg-lid while the hydrophilic portions extend to form a linear brush layer (O'Connor et al., 1999, Razatos et al., 2000).

Finally, Materials 6 & 7 were P20 and P26 respectively. P20 was a copolymer of Poly(ethylene glycol) methacrylate, Lauryl Methacrylate, and Poly(ethylene glycol), forming a PEGMA:LMA:PEG monomer with a molar ratio of 9:4:1; whilst P26 was a copolymer using Poly(glycerol methacrylate) forming a PGMA:LMA:PEG monomer with a molar ratio of 67:5:1. Similar to the PEO regions of the Poloxamer materials, the PEG region of these copolymers form a linear brush layer, whilst the PEGMA region forms a bottlebrush structure **Figure *1.2.1-1***.

As mentioned previously, bacterial adhesion and bacterial attachment are subtly different; non-motile bacteria adhere to surfaces at low and moderate velocities, whilst at higher velocities non-motile bacteria are simply transported away. For motile bacteria, attachment can occur at any fluid velocity (Tuson and Weibel, 2013). I will proceed with the term attachment for this section henceforth.

Using the composite data from **Figure *6.2.9-10*** (top left panel), F127 (Material 3), P123 (Material 4) and P20 (material 6) were the most successful at reducing bacterial attachment, with *S. aureus* attachment to F127 the only species unaffected. All three materials were amphiphilic, containing either poly(ethylene glycol) (PEG) or poly(ethylene oxide) (PEO) brush layers, which have been most

commonly used as anti-biofouling materials. (O'Connor et al., 1999, Razatos et al., 2000, Marsh et al., 2002, Harris et al., 2004, Cheng et al., 2005, Cheng et al., 2007, Nejadnik et al., 2008, Gunkel et al., 2011, Perez-Roldan et al., 2014, Ozcelik et al., 2017, Stirpe et al., 2020).

So with these results, which factors play a role in the prevention of bacterial attachment? Bacterial cells deal with both hydrodynamic and phyisocochemical effects when interacting with a surface, however it is not believed that electrostatic and van der Waals forces between a bacterial cell and a surface (DLVO theory) are strong enough to aid in the reversible adhesion of bacteria to a surface (Vigeant et al., 2002). Hydrodynamic effects can lead to bacteria swimming closely to a surface where they undergo torque from the surface as well as torque from their shape ("form drag"). This hydrodynamic effect causes bacteria to become entrapped against a surface as their orientation sees them constantly swim into a surface (Vigeant et al., 2002). This effect is likely to aid attachment for hydrophobic materials but is unlikely to aid attachment to the hydrophilic materials discussed. As mentioned above, thermodynamics influence bacterial attachment; when faced with a hydrophilic brush layer, as seen with F127, P123 and P20, bacterial attachment is hindered (Absolom et al., 1983). The brush-like layer can also prevent bacterial attachment by blocking the strong interaction forces between the bacteria and the polystyrene surface below. For example, Kolewe et al. (2018) demonstrated, through the use of PEG hydrogels, that the thickness, as well as softness, has an effect on bacterial attachment to surfaces; concluding that thicker, softer hydrogels reduced attachment the most. Finally, steric repulsion may also prevent attachment in F127, P123, and P20 (Razatos et al., 2000, Chen et al., 2010). Steric repulsion occurs as bacterial proteins approach the hydrophilic PEG/PEO chains that make up the brush layer; the

compression of these chains can increase surface tension, leading to the shift in the thermodynamic properties, which discourage bacterial attachment (Jeon et al., 1991).

Interestingly, for the OxoPlate work (data not shown), Material 5 was P21 (Poly(PEGMA2000/LMA/PEG500), A:B P21). Attachment was only reduced for *E. coli* and *S. aureus* whilst there was no significant difference for PAO1-N and PA14. This is interesting when compared to P20, which significantly reduced the bacterial attachment for all four species. The difference between P20 and P21 was increased molecular weight of PEGMA. This suggests that an increase in PEGMA reduces the effectiveness of the PEGMA:LMA:PEG random copolymer. P26 (material 7) material is also amphiphilic yet bacterial attachment was uninhibited. It is believed that the PEGMA in P20 provides an additional, secondary layer of a brush-like structure, commonly referred to as a bottlebrush structure (as described in **Figure *1.2.1-1***), that is lacking in P26, due to the substitution of PEGMA for PGMA (Cheng et al., 2005, Maan et al., 2020). Finally, PEOX 200 kDa (Material 1) and PEOX 500 kDa (Material 2) had varying effects on bacterial attachment. Both reduced the attachment of PA14 but had no significant effect on either *E. coli* or PAO1-N. These two materials are forming simple, self-assembled monolayers (SAMs) over the polystyrene, rather than forming a brush layer that is seen with the Poloxamers and the PEGMA:LMA:PEG copolymers. This lessens the 'physical' barrier, or steric hindrance, that would prevent the strong attraction between the bacteria and the hydrophobic polystyrene.

The Crystal Violet results (**Figure *6.2.9-10*** - bottom left panel) showed that over the 20 h incubation period, Materials 1-6 reduced biofilm formation for three of the four bacterial species. However, across the 20 h period, PAO1-N biofilm formation was significantly increased (compared to the 'Uncoated' polystyrene

control). This is most interesting for Materials 3-6 as these significantly reduced bacterial attachments. This would indicate that even though the material discouraged the attachment of PAO1-N, it had no effect on the formation of a biofilm. Similar results were shown in Nejadnik et al. (2008) as bacterial attachment was reduced using F127 as an anti-biofouling material yet biofilm formation was still present, albeit at a slower rate. For P26 (Material 7) Crystal Violet bound more readily for the control peg-lid (no attached bacterial cells). It is likely that this skewed the P26 results for the Crystal Violet assay as the resultant absorption at 590 nm was a negative value. To conclude the first part of the objective, the OxoPlate data and resultant Crystal Violet results suggested that Materials 3, 4 & 6 were the most effective in limiting bacterial attachment (oxygen consumption data) and inhibiting biofilm formation (crystal violet data).

The second part of the objective was to compare the commercial product (OxoPlate) to our oxygen nanosensors. By comparing these two methods, significant limitations could be seen with the oxygen nanosensors in this system. One major factor was that the experiment required large quantities of oxygen nanosensors; for example, the OxoPlate work used 12 replicates for each condition/material. Even with a large number of replicates, final error bars for the OxoPlate results were relatively large, indicating variation between repeats. This could be due simply to variation in metabolism between repeats; or that the oxygen was slow to permeate out of the matrix at the bottom of the well creating a slower response of the fluorophores trapped within the matrix. However, the response time of the *PreSens* OxoPlate system is noted as < 30 secs at 37^{o}C (*PresSens* OxoPlate manual). Owing to the limited yield of oxygen nanosensors, fewer repeats were carried out in comparison to the OxoPlate results. There are, nevertheless, two possible benefits of using the oxygen nanosensors; 1) faster

response to oxygen changes as nanosensors would be in closer proximity to the peg-lids and cells; and 2) the nanosensors provide the option of producing additional controls that are capable of detecting auto-fluorescence as part of the experiment. Although this could feasibly be addressed with the OxoPlate assay by including two separate control plates using 'empty' 96-well plates rather than OxoPlates. Additionally, the Crystal Violet assay produced dissimilar results between the two experiments. It is likely the number of repeats could have produced more confidence in the Crystal Violet results from the oxygen nanosensor work; however, the results for both the bacterial attachment and the Crystal Violet are unclear and more work is required to be confident the oxygen nanosensors could replicate the results produced by the OxoPlates.

Overall, the system in place has been designed for OxoPlate use and a high number of repeats are required to produce significant results. Using the Oxygen nanosensors can provide a more rapid response to oxygen consumption; however, there are limitations of reliably scaling up the experiment using oxygen nanosensors.

7. Proof of Principle – Mapping pH changes in *Streptococcus mutans* biofilms using fluorescent, ratiometric, pH-sensitive polyacrylamide nanosensors

7.1. Introduction

7.1.1. The importance of chemical gradients in biofilms

Chemical gradients produced by the diffusion of nutrients, metabolites and signalling molecules play a crucial role in the establishment and maintenance of microbial biofilms (Hunter and Beveridge, 2005, Hidalgo et al., 2009). Of particular importance is the formation of dynamic pH gradients, which can be produced within various regions of a biofilm; generating individual microenvironments as part of a biofilm (Vroom et al., 1999, Horev et al., 2015). These pH gradients typically result from the accumulation of metabolic byproducts-, such as lactic and acetic acid, within the biofilm and can contribute to the pathology of a biofilm-related disease. These include the development of dental caries, (Schlafer et al., 2015, Klein et al., 2015) the reduction of the antimicrobial activity of aminoglycosides (Wilton et al., 2016), or influencing the complex communication within a biofilm. For example, the QS molecule N-Acyl homoserine lactone (AHL) is stable below pH 5 whilst hydrolysis begins to occur between pH 6 to 8 (Yates et al., 2002).

7.1.2. Oral biofilms and *Streptococcus mutans*

Oral biofilms play a crucial role in the aetiology of oral diseases, such as dental caries, gingivitis and periodontitis, which can lead to increased economic burden and reduced quality of life (Flemmig and Beikler, 2011, Decker et al., 2014).

Oral biofilms are characterised by a bacterial shift from early colonisers of the tooth towards increasingly acid-producing (acidogenic) and acid tolerant (aciduric) species (Schlafer et al., 2011). On a cleaned tooth surface, the acquired enamel pellicle (AEP), composed of host derived salivary components (lysozyme, amylase, mucin and agglutinins), as well as bacterial components (glucosyltransferases, fructosyltransferases and lipoteichoic acid (LTA)) initially covers both hard and soft oral tissue. This AEP covering provides the basis for bacterial attachment to the enamel of the tooth surface (Kolenbrander, 1993, Hannig et al., 2005, Krzysciak et al., 2014). In the early stages of colonisation, *Actinomyces* species, including *A. naeslundii* and *A. oris,* are predominant colonisers; proceeded by the mitis-group streptococci, *Streptococcus oralis, Streptococcus mitis, Streptococcus gordonii* and *Streptococcus sanguinis* (Dige et al., 2009, Li et al., 2004, Schlafer et al., 2011). The adherence of the mitis-group of streptococci to the enamel is enhanced by host-derived amylase, present in the AEP coating the tooth surface, which selectively binds to this group of bacteria (Scannapieco, 1994, Scannapieco et al., 1995). By establishing microcolonies and altering physiological conditions, these pioneer species help to develop conditions for further bacterial involvement. Other bacterial species are encouraged to proliferate, adhere and aggregate to the tooth surface or established microcolonies, leading to the formation of mutualistic, multispecies communities (Kolenbrander, 1993, Colby and Russell, 1997). Middle colonisers, such as *Fusobacterium nucleatum,* require specific species to be present before colonising

(Periasamy et al., 2009), whilst late colonisers, such as the periodontopathogen *A. actinomycetemcomitans*, show an ability to grow in the presence of commensal bacteria such as *Veillonella* species (Periasamy and Kolenbrander, 2009). As the multispecies community expands, acidogenic species such as the mutans streptococci (MS) group and Lactobacilli begin to colonise. However, as pathogenic microbes become predominant in this mutualistic community, dysbiosis of the microbiome can occur, which can lead to the elevation of cariogenic bacteria such as the Gram-positive bacterium *S. mutans* (Zhan, 2018, Mieher et al., 2018).

S. mutans is both an aciduric and acidogenic bacterium, and a pre-dominant species in late stage oral biofilms (Takahashi and Nyvad, 2011, Klein et al., 2015). The interest in oral bacteria, such as *S. mutans,* lies in their participation in dental caries, the most common infection affecting humans. (Balakrishnan et al., 2000). The transition of *S. mutans* from planktonic cells to sessile, biofilm-forming cells occurs through either a sucrose-independent or sucrose-dependent mechanism (Scharnow et al., 2019).

For sucrose-independent attachment, the AEP provides receptors to initiate bacterial attachment to the tooth surface (Gong, 2000), *e.g.* amylase adherence to mitis-group streptococci, as previously described. For *S. mutans*, the agglutinins play a key role in their adhesion and aggregation. The agglutinins interact with AgI/II, a major surface protein anchored in the cell wall of *S. mutans* that acts as an adhesin (Brady et al., 2010, Krzysciak et al., 2014). This interaction leads to the continued promotion of biofilm formation.

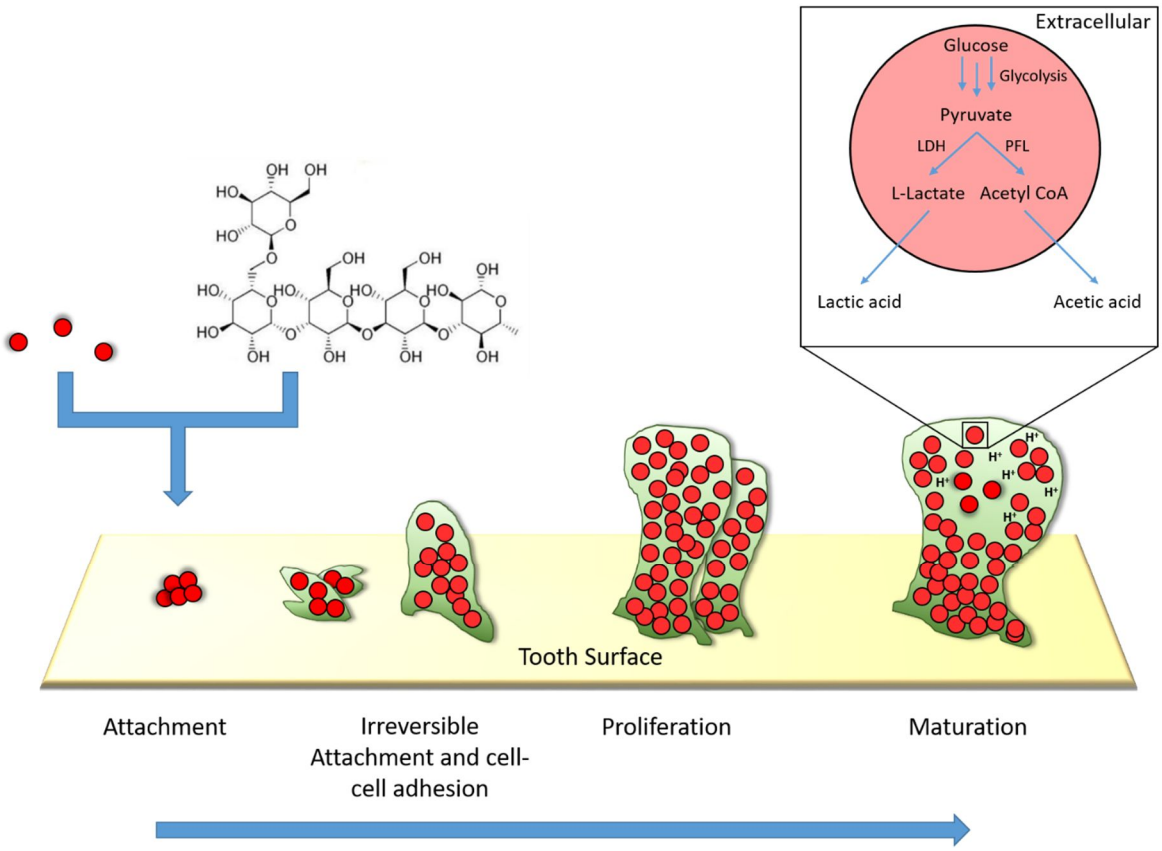

Figure 7.1.2-1: Sucrose –dependent biofilm formation of *S. mutans* – *S.* mutans biofilm formation begins with the attachment of a single cell, promoted by the presence of glucans generated by glucosyltransferases (α-1,6 linkage shown). Increased acid production occurs as the biofilm matures.

For sucrose-dependent attachment (**Figure *7.1.2-1***), *S. mutans* expresses a range of streptococcal glucosyltransferases (GtfB, GtfC & GtfD), that are extracellular or cell-associated exoenzymes. These Gtfs hydrolyse sucrose and use the resultant glucose to synthesise various glucan polymers (Vacca-Smith et al., 1996, Bowen and Koo, 2011, Souza et al., 2020) These glucan polymers then provide anchoring sites on the tooth surface and aid aggregation of bacteria. GtfB is surface-associated, binding to the surface of both *S. mutans* and other bacterial species (*e.g. Actinomyces* spp.) that do not express Gtfs, where it synthesises primarily insoluble glucans (α-1,3 glycosidic linkages), aiding the aggregation and

cohesion of the multispecies community. GtfD produces metabolisable polysaccharides that can also act as a primer for GtfB. Finally, GtfC is present in the AEP where it is adsorbed into the enamel and produces a mixture of insoluble and soluble glucans (α-1,6 glycosidic linkages) that aids adherence to the tooth surface (Bowen and Koo, 2011, Krzysciak et al., 2014, Scharnow et al., 2019).

S. mutans also produce proteins, referred to as to as Glucan-binding proteins (Gbps - GbpA, GbsB, GbpC & GbpD), that mediate the interaction of glucans with bacteria. Incidentally, Gtfs can also bind glucan, however Gbps are non-glucosyltransferases (Lynch et al., 2007). GbpA is secreted and has been shown to contribute to biofilm architecture, promoting taller microcolonies via binding to α-1,6 glycosidic linkages within glucan (Banas et al., 2007, Lynch et al., 2007). GbpB appears to lack a role in adhesion or aggregation, rather GbpB is likely to have a role in cell-wall construction and cell maintenance (Fujita et al., 2007). GbpC appears to be the most vital Gbps, and is associated with the bacterial cell wall, where it acts as a receptor for glucan (Krzysciak et al., 2014). GbpC also shares structural similarities with AgI/II and can adhere to agglutinin present in the AEP, providing an overlapping system to aid *S. mutans* adhesion in both a sucrose dependent and independent manner (Mieher et al., 2018). Finally, GbpD is another secreted Gbp which appears to play a similar role as GbpA, contributing to the structure and cohesiveness of the biofilm through glucan interactions (Lynch et al., 2007). These interactions enable *S. mutans* and other oral bacteria to continue to colonise and establish more biofilm (Klein et al., 2009, Koo et al., 2010, Bowen and Koo, 2011, Scharnow et al., 2019).

Once established on the tooth surface, *S. mutans* ferments available carbohydrates, readily found in a sugar-laden diet, via glycolysis; resulting in the production of pyruvate (Takahashi and Nyvad, 2011). The resultant pyruvate can

be metabolised to produce lactate, which is then secreted in the form of lactic acid (Dashper and Reynolds, 1996, Krzysciak et al., 2014). In the absence of oxygen, *S. mutans* can also produce formate, acetate and ethanol (Abbe et al., 1982). Under strict anaerobic conditions, pyruvate formate lyase (PFL) can convert pyruvate to formate and acetyl CoA, resulting in the secretion in the form of acetic acid (Yamada et al., 1985). These short-chain organic acids can provide an energy source for other bacteria present in the oral biofilm; for example, the early colonising *Veillonella* species are unable to utilise glucose to support growth, instead *Veillonella* spp. ferments available lactic acid (Delwiche et al., 1985, Periasamy and Kolenbrander, 2010). As well as providing an energy source for other microbes, these acids also promote the demineralisation of the tooth's enamel via the shift in solubility of hydroxyapatite, a key component of enamel (see **Figure *7.1.2-2***). Therefore, the acidification of the biofilm at the tooth surface leads to the formation of dental caries (Selwitz et al., 2007, Salli and Ouwehand, 2015, Xiao et al., 2017).

$$Ca_{10}(PO_4)_6(OH)_{2(s)} \rightleftharpoons 10\ Ca^{2+}_{(aq)} + 6\ PO_4^{3-}{}_{(aq)} + 2\ OH^-_{(aq)}$$

Figure 7.1.2-2: The equation for the solubility of hydroxyapatite (HA) – Hydroxyapatite is the main component of enamel. As the local acidity decreases, the solubility equation shifts towards the right. This results in the demineralisation of the enamel and the formation of dental caries.

Oral biofilms are inherently multispecies; however, the introduction of pathogenic species, such as *S. mutans,* is a key component to caries formation (Li et al., 2010, Laitala et al., 2012). *S. mutans* has become the target of research as the reduction or elimination of *S. mutans* has shown to lessen caries (Zhan et al., 2006, Laitala et al., 2013). Therefore, *S. mutans* is a perfect model organism to determine the efficacy of an analytical tool that is capable of tracking pH changes *in situ*.

7.1.3. Nanosensors in oral biofilm studies

In order to accurately detect and map pH microenvironments within oral biofilms, a system capable of providing real-time pH measurements at a single cell level is required. Previous research has used pH-sensitive fluorophores or proteins as tools to detect these pH gradients within *S. mutans* biofilms. These include using the cell surface displayed pH-sensitive green fluorescent protein, pH-luorin, fused to the *S. mutans* cell surface protein SpaP (Guo et al., 2013a), or the pH-sensitive fluorophores lysosensor yellow/blue conjugated with dextran (Xiao et al., 2012, Xiao et al., 2017), and C-SNARF-4 (Schlafer et al., 2015, Dige et al., 2016, Schlafer and Dige, 2016); to investigate acid production in *S. mutans.* pHluorin comes in two forms, ratiometric and elliptical, providing a limited physiological pH range between pH 5.5 – 7.5 (Miesenbock et al., 1998). Ratiometric pHluorin displays a bimodal excitation spectrum with peaks at 395 and 475 nm, and an emission maximum at 509 nm (Miesenbock et al., 1998, Mahon, 2011, Reifenrath and Boles, 2018). During protonation, ratiometric pHluorin excitation at 395 nm decreases with a corresponding increase in excitation at 475 nm (Mahon, 2011). However, an elliptical pHluorin was used by Guo et al. (2013a), which gradually loses fluorescence as the pH is decreased. At < pH 6, the excitation at 475 nm is completely quenched, whilst at 390 nm the excitation is weak (Miesenbock et al., 1998). Lysosensor yellow/blue exhibits a dual-emission spectral peak with emission maxima at 452 and 521 nm that is pH dependent, providing a pH range between 3.5 – 7 (DePedro and Urayama, 2009, Xiao et al., 2017). C-SNARF-4 also exhibits a dual-emission spectral peak with emission maxima at 580 and 640 nm, providing a pH range between 4 – 8 (Hunter and Beveridge, 2005, Schlafer et al., 2015). Each technique has its drawbacks, due in part to limited physiological range (pH 5.5 – 7.5 for pHluorin) and exposure to cellular components (as discussed in

1.6.2). To avoid these pitfalls, our ratiometric, fluorescent pH-sensitive nanosensors, consisting of a combination of fluorophores encapsulated within an inert polyacrylamide matrix were used in this study (see **Figure *5.1.2-1***).

7.2. Results

7.2.1. *S. mutans* growth is uninhibited by polyacrylamide nanosensors at low concentrations

In order to use the pH-sensitive polyacrylamide nanosensors in further experiments with *S. mutans*, it was necessary to determine whether the nanosensors would be detrimental to the growth of bacteria when incubated together. 21 h growth assays were therefore performed, as described in 4.5.2.

The OD_{600} was taken every 15 min with *S. mutans* NCTC 10449 grown in BHI media and either neutral or cationic polyacrylamide nanosensors ranging from 0.1 to 10 mg mL^{-1}.

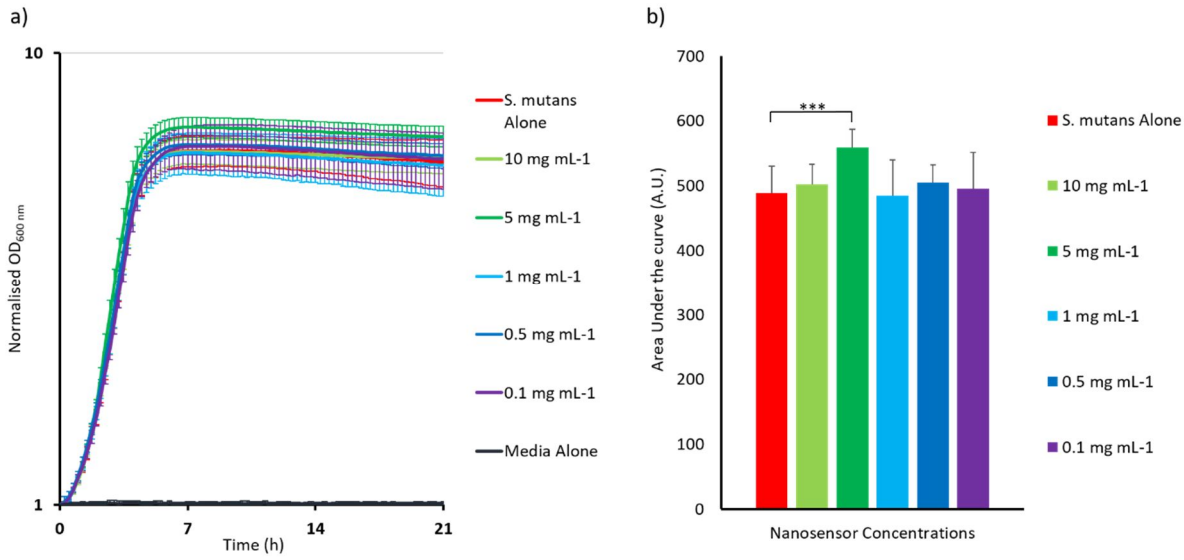

Figure 7.2.1-1: *S. mutans* growth is uninhibited by neutral polyacrylamide nanosensors – *S. mutans* NCTC 10449 at OD_{600} of 0.05 was incubated in BHI media and nanosensors for 21 h. (**a**) OD_{600} was measured every 15 min, which was plotted on a log scale against time. (**b**) Area under the curve is represented in the bar chart. Error bars are ±1 S.D. n=2x3 ***=P<0.001

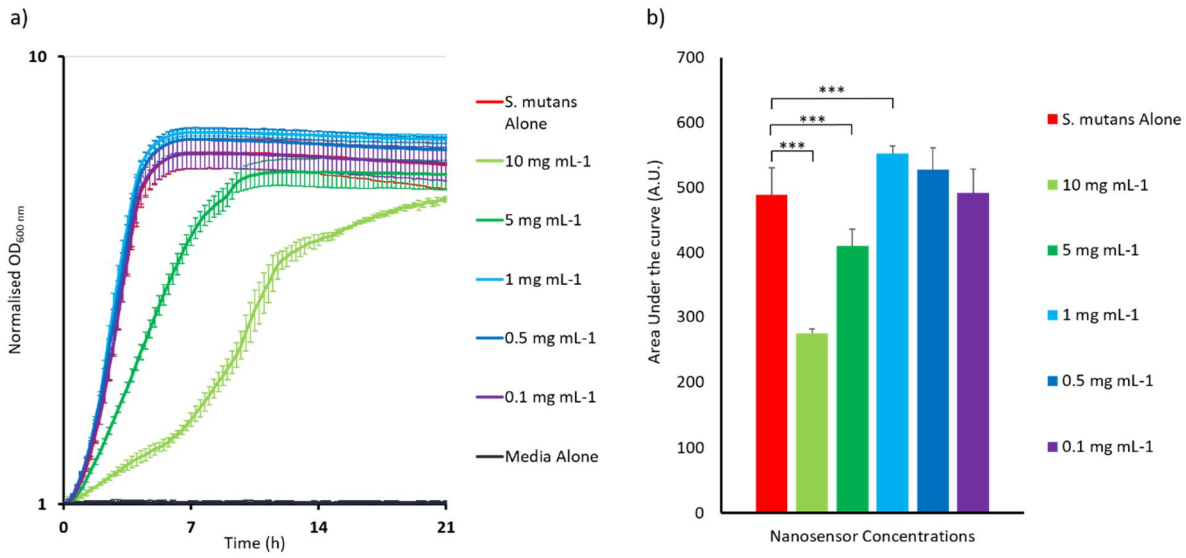

Figure 7.2.1-2: *S. mutans* growth with cationic polyacrylamide nanosensor is uninhibited below 0.5 mg mL^{-1} – *S. mutans* NCTC 10449 at OD_{600} of 0.05 was incubated in BHI media and nanosensors for 21 h. (**a**) OD_{600} was measured every 15 min, which was plotted on a log scale against time. (**b**) Area under the curve is represented in the bar chart. Error bars are ±1 S.D. n=2x3 ***=P<0.001

For the neutral polyacrylamide nanosensors, there was no significant effect on the growth of *S. mutans* NCTC 10449 over 21 h, except for 5 mg mL^{-1}, where growth was significantly improved (P<0.001) (**Figure *7.2.1-1***). However, for the cationic polyacrylamide nanosensors, growth was reduced at 10 & 5 mg mL^{-1} (***=P<0.001) and only improved (over *S. mutans* grown alone) at 1 mg mL^{-1} (***=P<0.001) (**Figure *7.2.1-2***). Measuring the fluorescence intensity at ex:488 nm; em:520 & ex:540, em:580 nm also confirmed that NCTC 10499 did not produce auto-fluorescence when grown in a planktonic culture (**Supplemental Figure *10-10***).

7.2.2. The introduction of glucose and sucrose drastically reduces the pH of the medium when added to starved, planktonic *S. mutans*

In order to determine the response of starved planktonic *S. mutans* to the introduction of a fermentable carbon source (glucose & sucrose) versus a non-fermentable carbon source (xylose & xylitol), the pH-sensitive nanosensors were used to measure potential pH changes in the medium as an indirect indication of the fermentation of a carbon source, as described in 4.7.

Fluorescence microscopy revealed that the addition of either glucose or sucrose to the starved NCTC 10449 leads to a change in fluorescence intensity during a 30 min period (***Figure 7.2.2-1***a). This is in comparison to xylose, xylitol, and saline (control) which remains unchanged over the same period. Further imaging using pH buffers (pH 3 – 8) with 1 mg mL^{-1} cationic nanosensors was taken to determine fluorescence intensity ratios from known pH values. Using these values, the linear regression was applied to the fluorescence intensity ratios calculated from each condition, providing a pH value for each time-point. These results show a drastic reduction in pH from ~ pH 5.3 to ~ pH 3.8 when either glucose or sucrose is added (***Figure 7.2.2-1***b), whilst the pH remained constant for the other conditions. Further controls show that the addition of the carbon sources to saline, in absence of cells, produced no pH change themselves (***Supplemental Figure 10-11***).

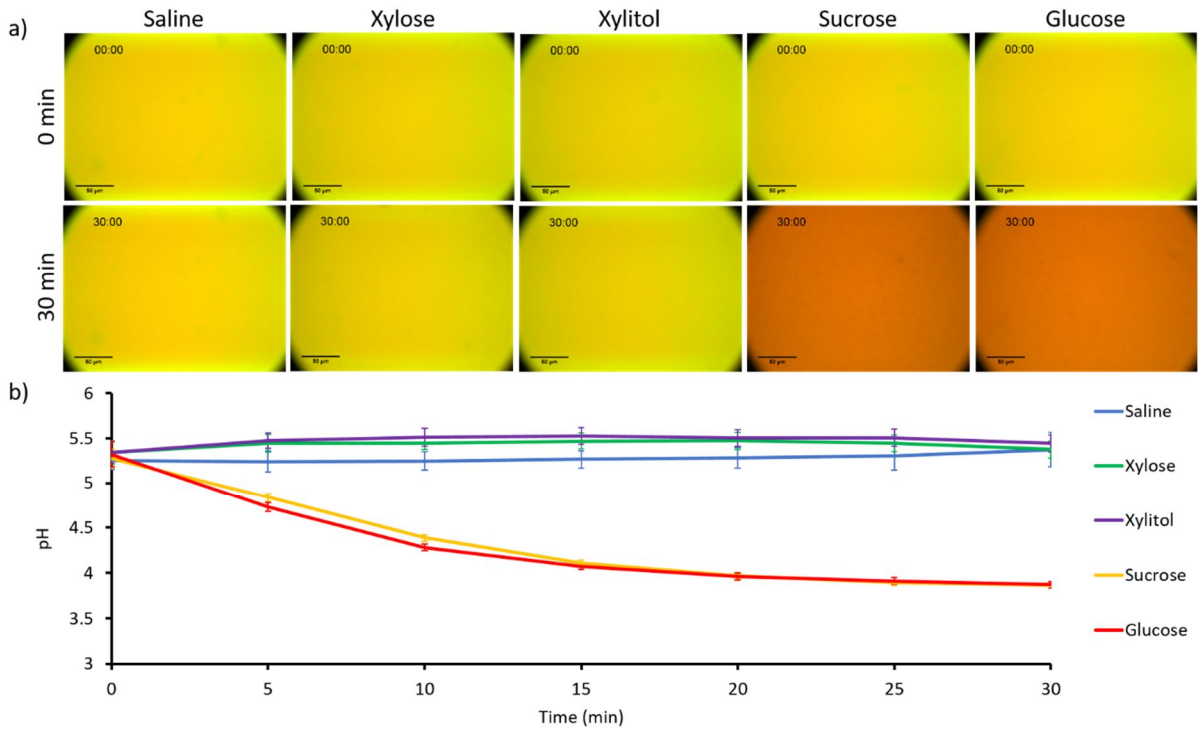

Figure 7.2.2-1: The addition of either glucose or sucrose to starved *S. mutans* results in a reduction of the extracellular pH – Changes in fluorescence intensity were measured using fluorescent images of starved planktonic *S. mutans* NCTC 10449 in culture with 1 mg mL^{-1} cationic, pH-sensitive nanosensors. An initial image was taken at time point 0 min before either 1% w/v glucose, 1% w/v sucrose, 1% w/v xylose, 1% w/v xylitol or saline was added. Further images were then taken every 5 min for the remaining 30 min. All images were taken using a Nikon inverted fluorescence microscope. **Scale bar 50 µm.** Error bars are ±1 S.D. n=3x2

7.2.3. Sucrose supplementation improves microcolony formation in a *S. mutans* biofilm

In order to optimise the generation of a robust and reproducible biofilm, *S. mutans* strain D282 was grown in the presence or absence of a 1% w/v sucrose supplement, as described in 4.9.1.

Additionally, the establishment and growth of the biofilm was tested both with and without the cationic polyacrylamide nanosensors. Both conditions were evaluated using CLSM. *S. mutans* strain NCTC 10449 was not used for biofilm work as there appeared to be auto-fluorescence at ex:488 nm, em:520 nm (**Supplemental Figure *10-12***); which would interfere with the fluorescence emission of OG and FAM.

The addition of sucrose supplementation at 1% w/v results in the formation of microcolonies within the biofilm as seen in ***Figure 7.2.3-1***a; whilst in the absence of sucrose, smaller aggregates of cells form (***Figure 7.2.3-1***b). The thickness of the biofilm remains similar between each condition; with sucrose supplementation producing a biofilm 15-20 µm thick and without supplementation 16-20 µm thick (see ***Figure 7.2.3-1***c **iii-iv**). The introduction of nanosensors at the beginning of incubation does not appear to restrict the establishment of a biofilm in the presence or absence of the sucrose supplement (see ***Figure 7.2.3-2*** a**i** & b**i**); as both microcolonies and small aggregates are still present. However, the thickness of the biofilm appears slightly reduced for both supplemented (8-16 µm) and un-supplemented cultures (10-15 µm) (see ***Figure 7.2.3-2*** a**iv** & b**iv**).

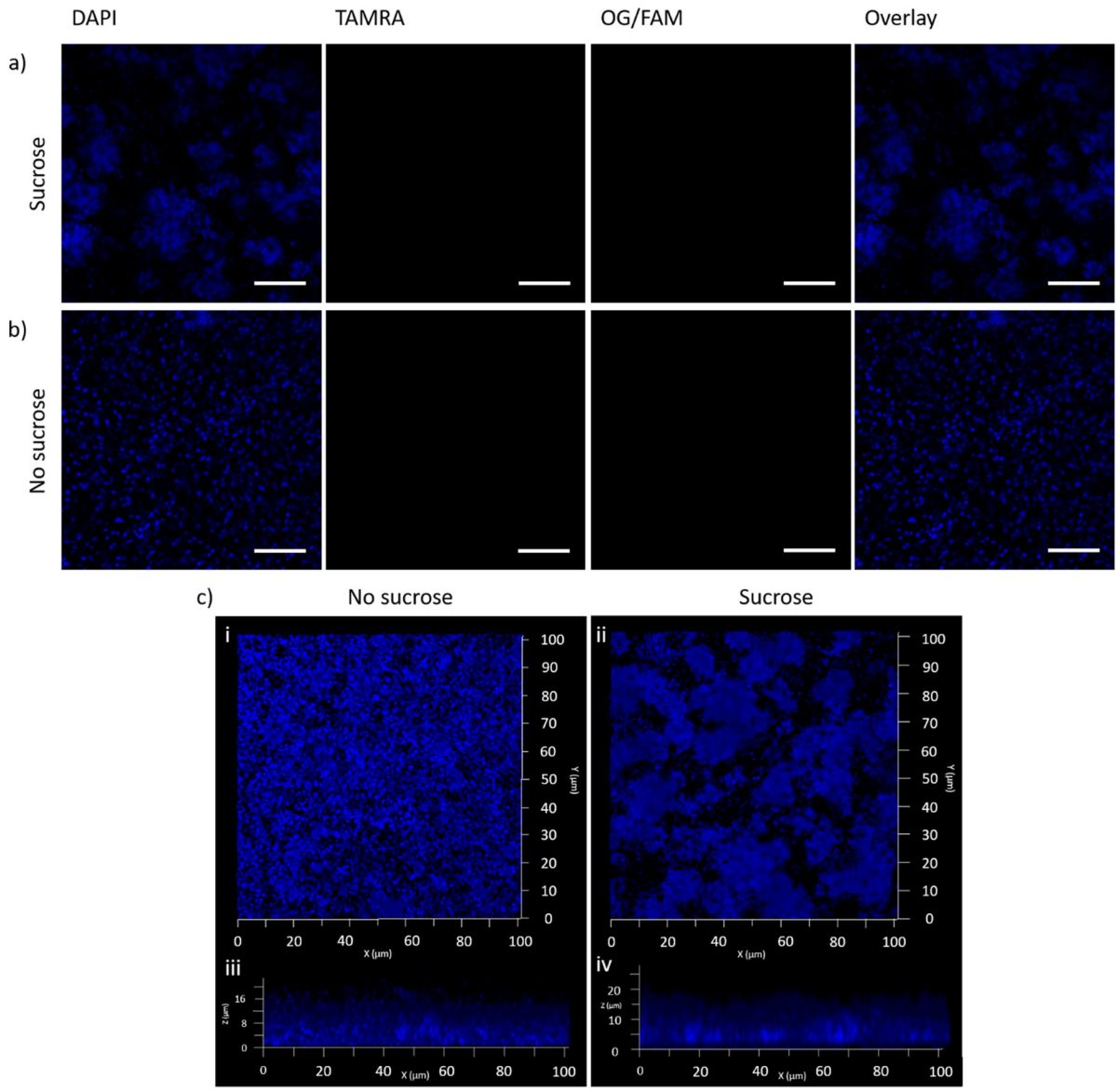

Figure 7.2.3-1: Microcolony formation in *S. mutans* biofilm formation is improved with 1% w/v sucrose supplementation– Representative images taken with a Zeiss confocal laser scanning microscope using a 63x/1.46na objective. *S. mutans* was grown in Todd Hewitt media with a 1% w/v sucrose supplement **(a)** or Todd Hewitt alone **(b)** for 48 h at 37^0C, 5% CO_2. The media was removed and replaced with Todd Hewitt alone for both **(a)** & **(b)** for a further 24 h. Prior to imaging the media was replaced with saline and the cells were stained with DAPI. **c)** are 3D representative models of **(a)** and **(b)** with **i)** & **ii)** representing the top view and **iii)** & **iv)** representing the side view. **Scale bar 20 µm.** n=2x2

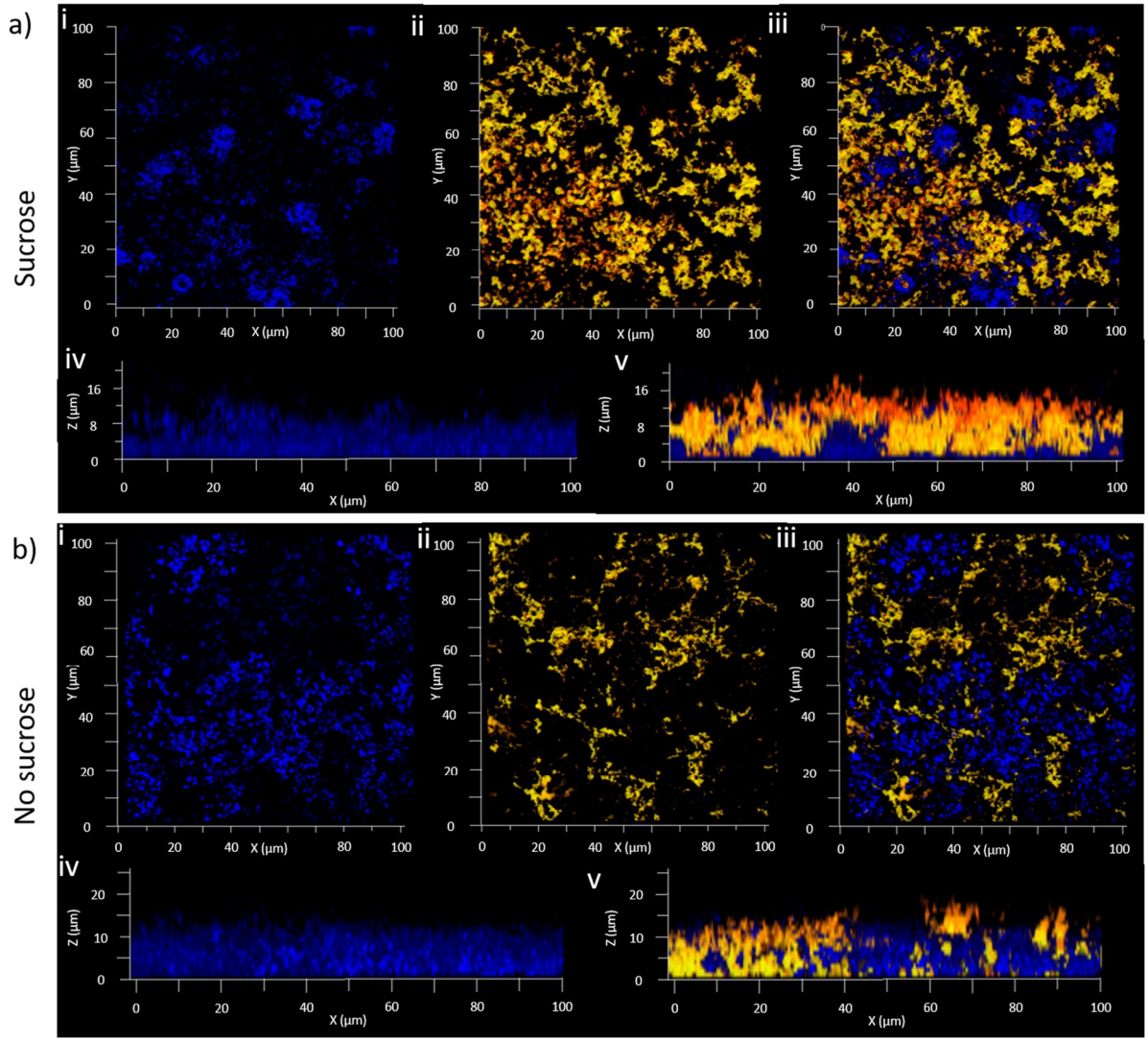

Figure 7.2.3-2: Altered distribution of cationic polyacrylamide nanosensors in a *S. mutans* biofilm dependent on sucrose – 3D representative models taken using Zeiss confocal microscopy. *S. mutans* was grown with 1 mg mL^{-1} cationic, pH-sensitive, polyacrylamide nanosensors- in Todd Hewitt media with a 1% w/v sucrose supplement **(a)** or Todd Hewitt alone **(b)** for 48 h at 37^0C, 5% CO_2. The media was removed and replaced with Todd Hewitt alone for both **(a)** & **(b)** for a further 24 h. Prior to imaging the media was replaced with saline and the cells were stained with DAPI. **i)** DAPI alone, **ii)** OG/FAM & TAMRA alone, **iii)** Overlay of i) & ii), **iv)** side view of DAPI alone, **v)** side view of overlaid channels. n=2x2

7.2.4. The addition of cationic, polyacrylamide nanosensors with the inoculum results in the formation of distinct structures within the biofilm

To analyse the penetration of the cationic polyacrylamide nanosensors to an established biofilm, 1 mg mL^{-1} was added to an *S. mutans* biofilm. This was compared to an *S. mutans* biofilm grown with nanosensors present at the point of inoculation onto the substratum, as described in 4.9.2**.**

The cationic nanosensors appear to associate in distinct regions within the biofilm when introduced to the inoculum from the initial set up (0 h), as seen in ***Figure 7.2.4-1***. These structures are able to remain as the media was replaced twice, once after an initial 48 h incubation and again before imaging (***Figure 7.2.4-1***a). These nanosensor structures appear to form separate from the *S. mutans* microcolonies (stained with DAPI) of the biofilm itself. When the nanosensors are applied to an established biofilm (after 48 h), fewer pockets of nanosensors can be detected (compare ***Figure 7.2.4-1***a. to ***Figure 7.2.4-1***b); instead, small aggregates of nanosensors form.

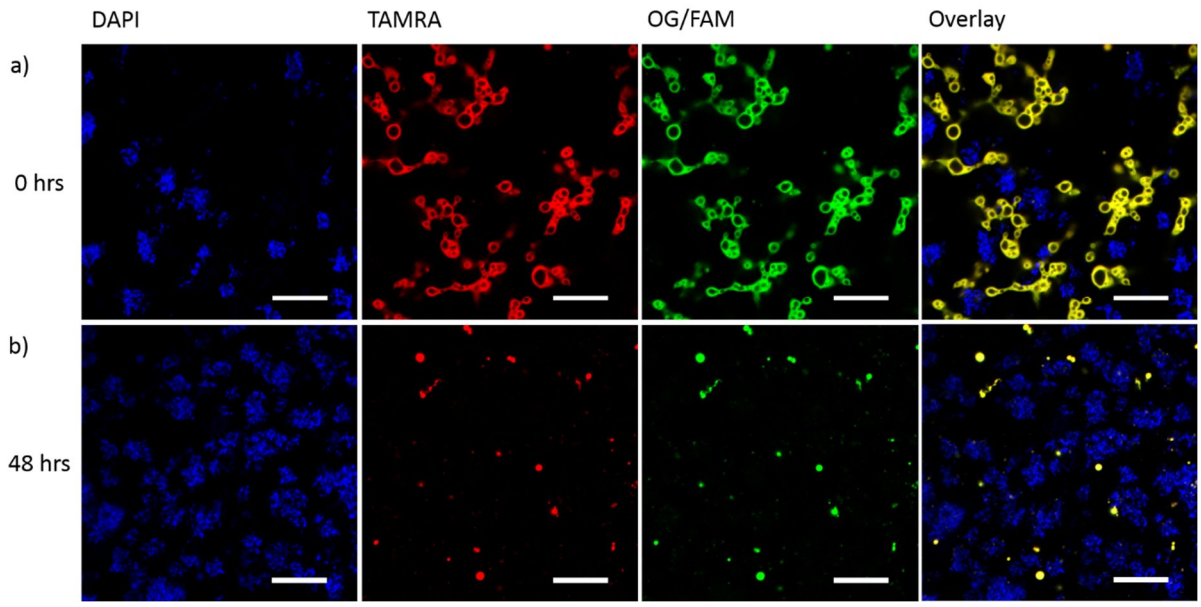

Figure 7.2.4-1: The addition of cationic nanosensors to an established *S. mutans* biofilm led to limited penetration of the nanosensors – Representative images taken with a Zeiss confocal laser scanning microscope of *S. mutans* strain D282 stained with DAPI. D282 was incubated for 48 h at 37°C, 5% CO_2 with 1 mg mL^{-1} pH-sensitive polyacrylamide nanosensors from the initial inoculation of the substratum **(a)** or after 48 h incubation **(b)**. After 48 h incubation the media was removed and replaced with Todd Hewitt alone **(a)** or 1 mg mL^{-1} nanosensors suspended in Todd Hewitt media **(b)** for a further 24 h. Prior to imaging, the media was removed and replaced with H_2O. **Scale bar 20 µm.** n=1x2

7.2.5. Cationic nanosensors show responsiveness to various pH solutions

To investigate the responsiveness of the cationic, pH-sensitive polyacrylamide nanosensors when grown within a *S. mutans* biofilm, the nanosensors were challenged with a range of pH solutions and the change in fluorescence intensity was measured, as described in 4.9.3.

Figure 7.2.5-1a shows an initial reduction in the fluorescence intensity ratio (FIR), with it plateauing after 2 min, as the pH first decreases using a pH 4 solution. An almost instant increase in the ratio then occurs with the addition of a pH 7 solution. The FIR then reduces with the addition of gradually lower pH solutions with plateauing requiring approximately 2 min with each solution. ***Figure 7.2.5-1***b provides similar results as the FIR changes almost instantly with the addition of the pH solutions.

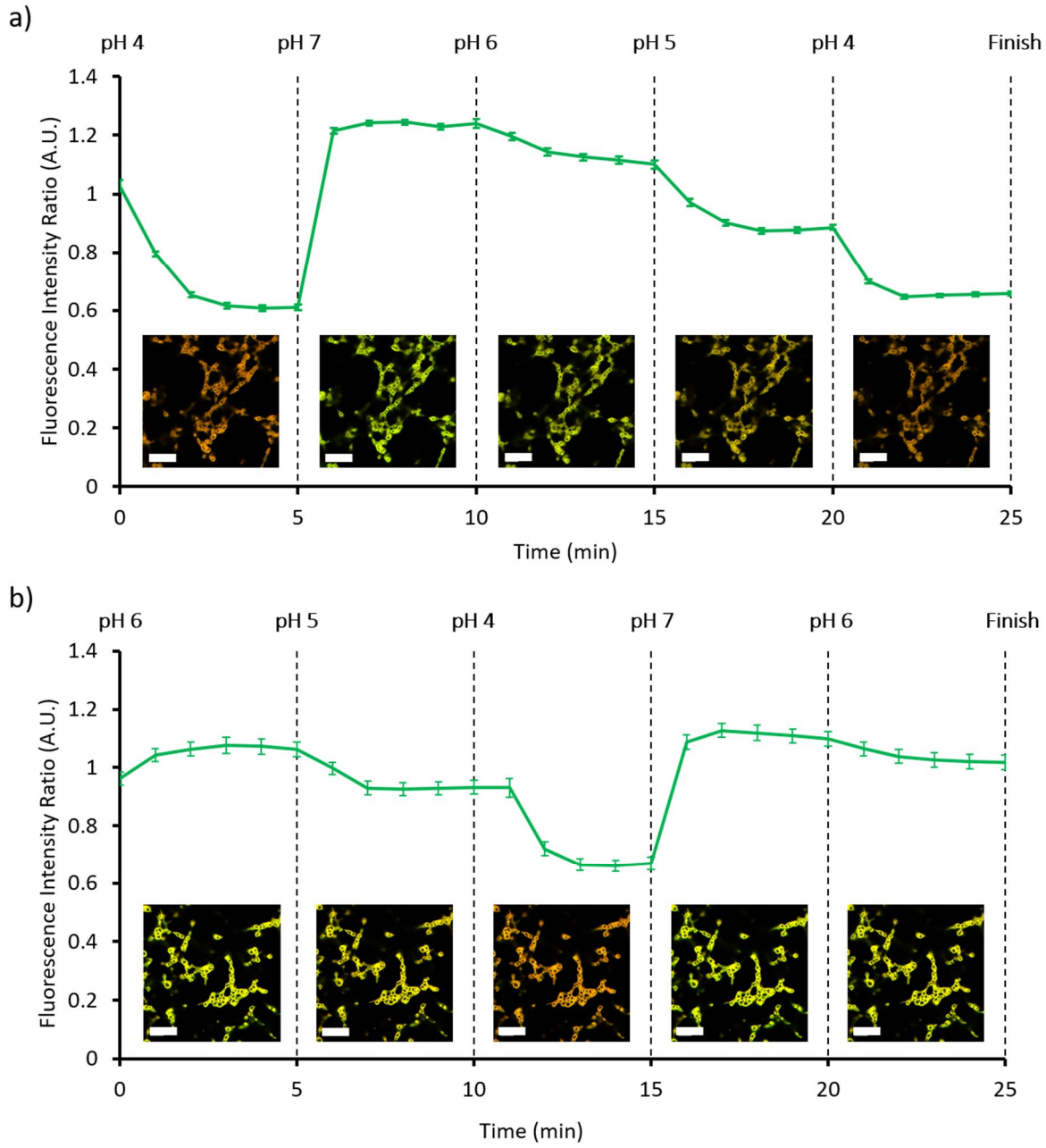

Figure 7.2.5-1: Embedded pH-sensitive nanosensors responded to various pH buffers – Snapshot images taken every minute for 25 minutes with a Zeiss confocal scanning microscope using a 63x/1.46na objective. **a)** After an initial image was taken (time point 0 min) a pH 4 solution was added; followed by the addition of a pH 7 solution at 5 min, pH 6 solution at 10 min, pH 5 solution of 15 min and finally a pH 4 solution at 20 min. **b)** A second example of nanosensor responsiveness to changing pH, using a different order of addition. After an initial image was taken (time point 0 min) a pH 6 solution was added; followed by the addition of a pH 5 solution at 5 min, pH 4 solution at 10 min, pH 7 solution of 15 min and finally a pH 6 solution at 20 min. Images shown were taken at 5 min, 10 min, 15 min, 20 min and 25 min respectively. **Scale bar 20 µm.** Error bars are ±1 S.D. n=1x3

7.2.6. The glucose challenge resulted in a significant reduction in fluorescence intensity when introduced to an *S. mutans* biofilm

The response of an *S. mutans* biofilm to a glucose challenge was examined by introducing 1% w/v glucose into the medium hydrating the biofilm, as described in 4.9.4.

Measuring fluorescence intensity using CLSM reveals a reduction in the FIR when the *S. mutans* biofilm is challenged with 1% w/v glucose, as seen in ***Figure 7.2.6-1***a; whilst there is only a slight reduction in the FIR when distilled water is added. These changes in fluorescence intensity can be visualised in the time-lapse panel (***Figure 7.2.6-1***b) as the assigned colour changes from yellow to orange, caused by the reduction in fluorescence from the pH-sensitive fluorophores, OG & FAM. The decrease in fluorescence intensity with the addition of a 4.5 pH buffer also confirms that the nanosensors are responsive to induced pH changes.

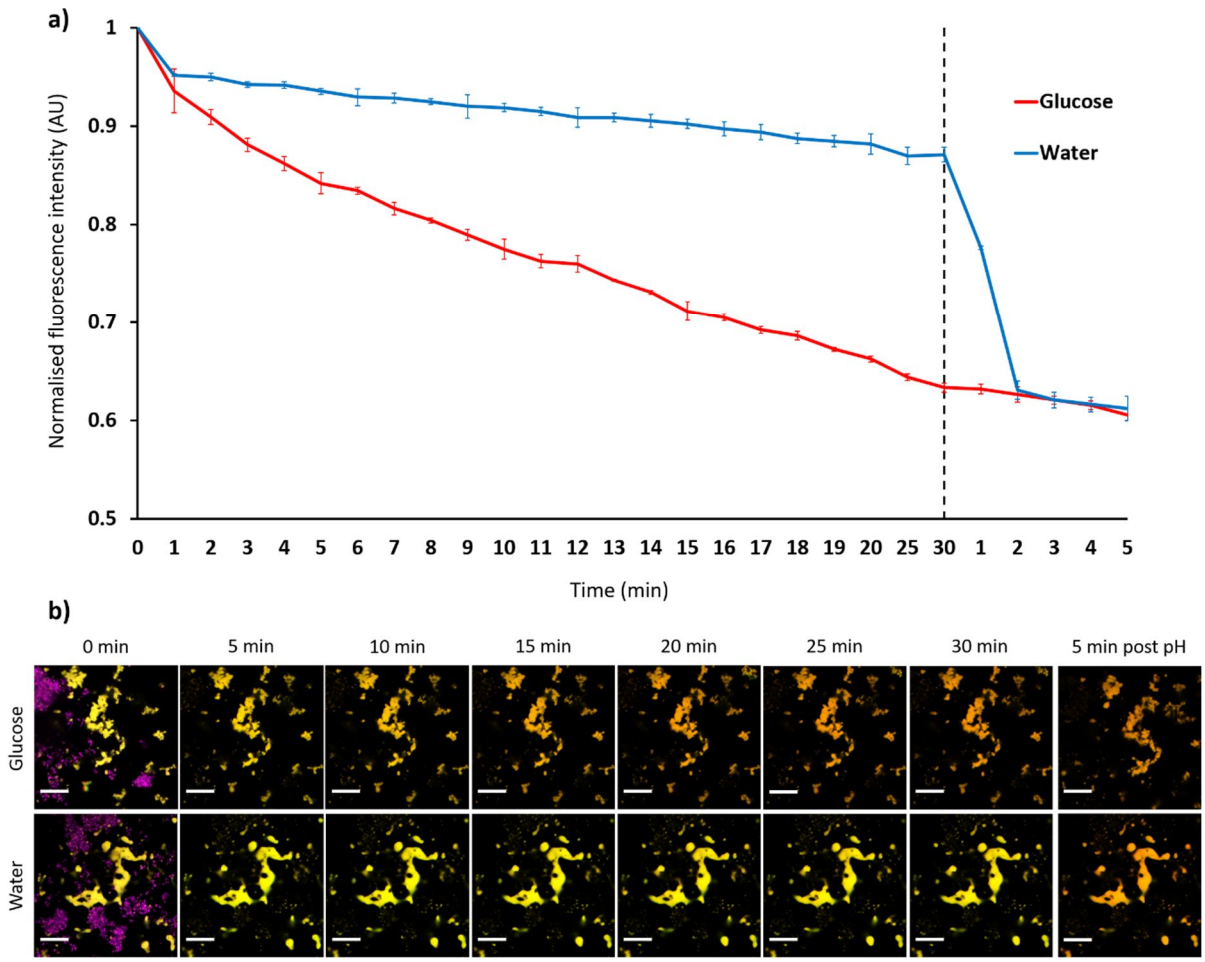

Figure 7.2.6-1: pH changes were brought on by the addition of glucose to a mature *S. mutans* biofilm with embedded pH-sensitive nanosensors – Snapshot images taken with a Zeiss confocal scanning microscope with a 63x/1.46na objective. After an initial image was taken for time point 0 min, either 1% w/v glucose or water was added to the biofilm. Further images were taken every minute for 20 min then at 25 and 30 min. After 30 min, a 4.5 pH buffer was added and further images were taken every minute for 5 min **a)** Represents the fluorescence intensity ratio changes over time after the glucose challenge and **b)** The panel shows visual representation of the fluorescence intensity changes seen in **a**). The images represent the combination of the OG/FAM (ex:488 nm, em:520 nm) and TAMRA (ex:540 nm, em:580 nm) channels which depict the change in fluorescence when glucose had been added, compared to when water had been added. Duplicate images at 0 min and 5 min post pH treatment were taken to visualise DAPI stained *S. mutans* (magenta) **Scale bar 20 µm.** Error bars are ±1 S.D. n=1x3

7.3. Discussion

Oral biofilms inhabited by pathogens such as *S. mutans* are the most prevalent bacterial disease in developed countries, contributing to a decline in the standard of living and creating an economic burden (Colby and Russell, 1997). *S. mutans* has to adapt to the shifting availability of carbohydrates caused by changes in host behaviours. These can be brought on through the fluctuation of diets, as well as through host secretions of glycoproteins and those carbohydrates produced by the oral microbiome itself (Moye et al., 2014). *S. mutans* is therefore versatile in the carbohydrates it can utilise (Colby and Russell, 1997). *S. mutans* is a pre-dominant species found in oral biofilms and participates in the production of dental caries. These dental caries are formed by secreted organic acids, which are a result of the fermentation of carbohydrates present in a typical human diet (Featherstone, 2000). As the acidity of an oral biofilm decreases, the solubility of hydroxyapatite (a key component of enamel) shifts, leading to chemical dissolution of the hydroxyapatite and the demineralisation of the enamel of a tooth (**Figure *7.1.2-2***) (Abou Neel et al., 2016). In order to design a suitable treatment strategy for the prevention of dental caries, we must understand the response of oral biofilms to the introduction of a variety of dietary carbohydrates.

Before using the polyacrylamide nanosensors with *S. mutans*, growth assays were required to determine whether the nanosensors would inhibit growth. For neutral polyacrylamide nanosensors, growth was unaffected, for the exception of 5 mg mL^{-1}, which improved the growth of *S. mutans* over 21 h. For the cationic polyacrylamide nanosensors, growth was significantly reduced at the higher concentrations (10 & 5 mg mL^{-1}) whilst growth was significantly improved at 1 mg mL^{-1}. As *S. mutans* required 5% CO_2 for planktonic growth, it can be

speculated that improved growth in the presence of the cationic nanosensors was due to the likely coating of cells, where it may have reduced access of oxygen.

The first objective was to use the pH-sensitive, polyacrylamide nanosensors to detect pH changes generated by *S. mutans* in planktonic culture, when treated with a range of carbohydrates. By using pH-sensitive nanosensors dispersed within the medium of starved planktonic *S. mutans*, changes in fluorescence intensity were measured and the resultant external pH changes calculated (***Figure 7.2.2-1***). With the addition of simple mono- and disaccharides such as glucose or sucrose, a reduction in the pH was observed, as *S. mutans* is capable of the metabolism of both glucose and sucrose via glycolysis to produce pyruvate (Takahashi and Nyvad, 2011). The resultant pyruvate is metabolised to form lactate which would be secreted in the form of lactic acid, leading to the reduction of the pH of the medium (Dashper and Reynolds, 1996). Interestingly, the presence of oxygen in the medium would inhibit the action of pyruvate formate lyase (PFL), preventing the pyruvate from being converted to formate and acetyl CoA (Yamada et al., 1985).

However, with the addition of xylose or its derivative, xylitol, the external pH was unchanged throughout the experiment. This was a result of both xylose and xylitol being non-fermentable by *S. mutans* (Paulino et al., 2003). Xylose is initially taken up and reduced to xylitol, which is then phosphorylated to xylitol-5-phosphate (X5P). As *S. mutans* is unable to metabolise X5P further, X5P is accumulated intracellularly (Kakuta et al., 2003). This accumulation of X5P has been attributed to the inhibition of glycolytic enzymes; leading to the repression of acid production (Miyasawa et al., 2003, Kakuta et al., 2003). However, Takahashi and Washio (2011) demonstrated that the presence of X5P had no effect on acid production when supragingival plaques were rinsed with glucose after an initial application of

xylitol. This would imply that xylitol is simply a non-fermentative sugar alcohol rather than an inhibitor.

The second objective was to generate a reproducible and robust model for the growth of an *S. mutans* biofilm, incorporating the pH-sensitive, cationic, polyacrylamide nanosensors. Glass surfaces have been shown to be suitable surfaces for *S. mutans* biofilm formation as an alternative to hydroxyapatite (HA) discs or polystyrene, albeit with a reduction in adhesiveness (Yoshida and Kuramitsu, 2002, Kreth et al., 2004). However, for the purposes of this work, Ibidi glass chambers are suitable as dense biofilms with microcolonies were formed.

The mechanism underlying the influence of sucrose upon the production of glucans via glucosyltransferases and the establishment of biofilms on an enamel surface with glucan-binding proteins (Gbps) has been discussed in the literature (Fujita et al., 2007, Koo et al., 2010), and was summarised in 7.1.2. In order to determine the effectiveness of sucrose on the attachment and development of an *S. mutans* biofilm, sucrose was added exogenously. The addition of 1% w/v sucrose vastly improved the formation of microcolonies (***Figure 7.2.3-1***a) in comparison to the absence of any sucrose supplementation (***Figure 7.2.3-1*** b). Kreth et al. (2004) described similar results, when comparing 0%, 0.1% and 1% sucrose supplementation. In the absence of sucrose, *S. mutans* attached in small aggregates to form a thin biofilm; whilst with 1% sucrose, *S. mutans* formed a thick biofilm with dense microcolonies (Kreth et al., 2004). Salli et al. (2016) also showed a significant increase in *S. mutans* colonisation of a hydroxyapatite (HA) surface with the addition of 1% sucrose to artificial saliva, whilst xylitol supplementation limited the ability of certain *S. mutans* strains from adhering to HA. The generation of microcolonies in ***Figure 7.2.3-1***a) is likely a result of glucan synthesis, which not only provides sites for adhesion to the enamel of a tooth, but

also adhesion to other microorganisms (Bowen and Koo, 2011, Krzysciak et al., 2014, Scharnow et al., 2019). This explains the absence of microcolonies when sucrose is not present, as the sucrose independent pathway will not play a role in the formation of these biofilms as AEP was not present; therefore, agglutinins would not be able to aid the adhesion of *S. mutans* to the surface. Previous research has also shown that the addition of a sucrose supplement to a *S. mutans* biofilm leads to the up-regulation of many genes involved with adhesion (*gbpB* as a glucan-binding protein) and biofilm formation (*atlA*, *vicR* &, *wapA*), in comparison to growth medium containing glucose (Decker et al., 2014). The base medium used in the experiments by Decker et al. (2014) is comparable to Todd Hewitt media used for this study, which contains D--glucose at 0.2%. This would explain the formation of a biofilm with the absence of sucrose, as seen in ***Figure 7.2.3-1***, as adhesion and biofilm formation genes are still expressed without sucrose, as shown in Decker et al. (2014). Incidentally, the use of sucrose as a supplement for future experimentation was further reinforced by Decker et al. (2014) who showed an up-regulation in carbohydrate uptake genes (*SMU.104*, *SMU.105* and *sorA)* which would improve the response of *S. mutans* to a fermentable carbon source such as glucose.

The *S. mutans* biofilm in the presence of nanosensors, both with and without sucrose, appeared generally unaffected as the pattern of formation remains the same; microcolonies were present with sucrose supplementation, whilst only small aggregates were present without sucrose (***Figure 7.2.3-2***). However, the effect on the dispersal of the cationic nanosensors between different bacterial species is noticeable. As described in 5.2.7, the cationic nanosensors promoted the formation of thicker *P. aeruginosa* biofilms, whilst the nanosensors themselves were well distributed. However, when grown with the Gram-positive *S. mutans*,

the thickness of the biofilm appeared slightly reduced and the nanosensors appeared to form distinct structures, separated from the *S. mutans* microcolonies. It is not clear why the nanosensors did not promote a thicker biofilm with *S. mutans* and why the nanosensors formed clusters around the microcolonies. However, it is likely that the clustering of nanosensors around the *S. mutans* microcolonies is influencing the thickness of *S. mutans* biofilms. As mentioned above, cationic (36-41 mV) block copolymer nanoparticles have been shown to coat a range of Gram-positive bacteria as the ζ potential of the bacterial cells changed from negative to positive (Li et al., 2018). Therefore, it is reasonable to believe the cationic nanosensors used in the current study would interact with *S. mutans* in a similar fashion, as shown in 5.2.4. However, as the nanosensors appear to form clusters separate to the *S. mutans* microcolonies; it is likely the cationic nanosensors are interacting with negatively charged, extracellular polymeric substances within the ECM of the biofilm rather than the cells themselves. One such extracellular polymeric substance could be eDNA, which is speculated to be the most likely candidate that the cationic nanosensors are interacting with in *P aeruginosa* cultures and biofilms (as discussed in 5.3). In contrast, eDNA may not play as crucial a role in the formation of an *S. mutans* biofilm when supplemented with sucrose alone. For example, when treated with DNase I, an *S. mutans* biofilm supplemented with sucrose showed no significant reduction in biomass when compared to untreated. However, when *S. mutans* was grown with sucrose and starch, the DNase I treatment showed a significant reduction in biomass (Klein et al., 2010). This would suggest eDNA is not vital for biofilm formation, however it is still present in the ECM (Klein et al., 2015). A second candidate would be the glucan structures that *S. mutans* generate in the presence of sucrose. Yet it would be unlikely that charge is the determining factor

for any interaction between the glucan structures and the cationic nanosensors, as *in vitro* glucan is uncharged (Bowen and Koo, 2011). Furthermore, the clustering of the nanosensors in the biofilm grown in absence of sucrose ***Figure 7.2.3-2***b) would suggest that glucan is not the key component in the interaction of the cationic nanosensors with the ECM, as glucan production will be limited under this condition. A third candidate would be lipoteichoic acid (LTA) which is produced in significant amounts by *S. mutans* (Rolla et al., 1980). Due to its negative charge, LTA can confer this negative charge to the ECM (Klein et al., 2015, Pedraza et al., 2017) which will aid the interaction with the cationic nanosensors.

To conclude, the thicker biofilm in PAO1-N WT was likely caused by a combination of cell coating and the interaction with ECM components such as eDNA, acting as a glue to promote greater aggregation; whilst the effect on an *S. mutans* biofilm differs due to the distinct ECM formation. Xiao and Koo (2010) perfectly summarises the development of distinct ECM domains during *S. mutans* biofilm formation, providing spatial distribution of *S. mutans* microcolonies. These distinct ECM domains can be seen in ***Figure 7.2.3-2***, ***Figure 7.2.4-1***, ***Figure 7.2.5-1*** and ***Figure 7.2.6-1***, where the nanosensors are clustered. It is likely that the cationic nanosensors are interacting with a negative component, such as LTA and eDNA, where these components are embedded within the ECM that typically forms pockets in and around the *S. mutans* microcolonies, limiting the effect of the cationic nanosensors on the thickness of the biofilm. It is worth noting that the sequestration of the nanosensors to the ECM should not be a limitation as the ECM facilitates the creation of highly acidic microenvironments (Klein et al., 2015).

Additionally, part of the second objective was to determine whether the cationic nanosensors could be introduced to a mature biofilm. Previous work measuring pH changes in microbial biofilms have introduced pH-sensitive fluorophores to a mature, established biofilm (Hunter and Beveridge, 2005, Schlafer et al., 2015, Dige et al., 2016). Previous results show that the cationic, polyacrylamide nanosensors used in our lab can be introduced along with *S. mutans* at the initial stage of inoculation of the substratum (***Figure 7.2.4-1***). When added to the inoculum, the nanosensors form distinct structures close to the microcolonies of *S. mutans*, as discussed previously. However, with the addition of the nanosensors to an established biofilm, the nanosensors were unable to penetrate the biofilm completely. This could be due to either particle size or the charge. Focusing on the particle charge; biofilms generally have an overall negative charge due to components of the extracellular matrix (Zhang et al., 2011), which can impact the penetration and dispersal of nanoparticles through a biofilm (Javanbakht et al., 2016). Prior research may explain why our cationic nanosensors could not fully diffuse into the biofilm and were instead sequestered into small clusters. Tseng et al. (2013) showed that the penetration of the positively charged antimicrobial tobramycin was limited in *P. aeruginosa* biofilms, as it was sequestered in the periphery; whilst the penetration of a neutral antimicrobial ciprofloxacin was not restricted. Meanwhile, Peulen and Wilkinson (2011) were able to show that the self-diffusion of anionic silver nanoparticles into a *P. fluorescens* biofilm was reduced due to charge as well as increasing size. Finally, Javanbakht et al. (2016) showed that the zeta potential (mV) of cationic nanoparticles drastically shifted to a negative reading after the nanoparticles were incubated in a *S. mutans* biofilm (22.mV ± 0.3 before incubation and -15mV ± 0.5 after incubation). This would infer that cationic nanosensors are attracted to the negatively charged

components of the biofilm, leading to the coating and the potential sequestration of nanoparticles. This may explain why our cationic nanosensors added after 48 h were not penetrating the biofilm due to their inability to diffuse sufficiently into the biofilm.

The third objective in this study was to determine the responsiveness of pH-sensitive, polyacrylamide nanosensors to a variety of pH solutions. The results, as seen in ***Figure 7.2.5-1***, showed a change in the fluorescence intensity ratio between the pH-sensitive fluorophores OG and FAM, and the pH-insensitive fluorophore TAMRA. Guo et al. (2013a) demonstrated similar changes in fluorescence intensity by treating a biofilm of *S. mutans,* tagged with surface expressed pHluorin, initially with a pH 5.5 buffer followed by a pH 7.5 buffer. Our pH-sensitive nanosensors were able to detect pH changes rapidly with the fluorescence intensity changing almost immediately and plateauing within a maximum of 2 min with each addition. The speed of response is important as previous research has detected pH changes in *S. mutans* biofilms within 5 min of treatment with glucose (Schlafer et al., 2015). This would suggest that the polyacrylamide nanosensors were suitable for detecting and measuring rapid pH changes within a biofilm when treated with a carbon source. Furthermore, the nanosensors were capable of responding to various pH changes, from a reduction to an acidic environment up to a neutral environment and vice versa. This proved the pH nanosensors could provide a flexible system to measure various pH changes.

The final objective was to detect potential pH changes generated by an *S. mutans* biofilm when treated with a fermentable sugar. The negligible change in the fluorescence intensity ratio when water was added may be caused by residual carbon still present in the biofilm. Nevertheless, with the addition of 1% w/v

glucose to an established biofilm containing cationic, pH-sensitive polyacrylamide nanosensors, a reduction in the FIR over a period of 30 min was observed. The FIR was calculated by dividing the fluorescence intensity emitted at 520 nm (OG & FAM) by the fluorescence intensity emitted at 580 nm (TAMRA). As the fluorescence intensity at 580 nm stays unchanged due to TAMRA being insensitive to pH, the ratio will only change as the fluorescence at 520 nm changes. A fluorescence intensity ratio decreasing over time indicates a reduction in fluorescence at 520 nm caused by the reduction in the pH. Therefore, this result inferred a pH decrease as the *S. mutans* fermented the glucose added, resulting in the production of acidic by-products that could be secreted into the extracellular matrix and detected by the nanosensors. However, until a suitable calibration method is developed, a pH value for the individual time points cannot be assigned.

The response of our cationic, pH-sensitive polyacrylamide nanosensors can be compared to other systems used to measure real-time pH changes. Guo et al. (2013a) showed a decrease in pH over a 60 min period when introducing 2% sucrose to an *S. mutans* biofilm with surface expressed pHluorin. The medium of the *S. mutans* biofilm was initially increased to pH 7.5 before adding 2% sucrose. This may have been carried out to maximise the range of the pH-sensitive protein (pHluorin pH range is 5.5-7.5). Similarly, the *S. mutans* biofilms in ***Figure 7.2.6-1*** were initially incubated in a saline solution, before being treated with 1% w/v glucose. This provides a suitable starting point to detect pH changes created by an *S. mutans* biofilm. Due to surface expression of the pHluorin, changes in fluorescence intensity could be detected closer to the cell surface as well as the surrounding medium. Guo et al. (2013b) demonstrated a greater pH decrease within the microcolonies (pH 7.5 to pH 5.5) than within the medium (pH 7.5 to pH 7). This may be a limiting factor for our nanosensors as they are isolated within

the ECM rather than dispersed within the microcolonies themselves. However, acidic by-products from fermentation remain within the ECM, creating localised acidic regions, rather than diffuse out into the medium, as shown by Xiao et al. (2012), Xiao et al. (2017), suggesting our nanosensors should still be capable of detecting changes in acidity within the ECM. Another comparison can be made with Schlafer et al. (2011), who used C-SNARF-4 to measure pH changes in five early oral colonisers; *A. naeslundii, S. oralis, S. mitis, S. gordonii* and *S. sanguinis.* Rapid pH changes were seen in certain fields of view, as saliva containing either 0.4% glucose or 10% glucose was added. The pH decreased from 7.5 to 5.5 over an hour in some regions, whilst in other regions it required >6 h to reduce to pH 5.5. This may explain the issues with reproducibility with our biofilm work, as the field of view was reduced to focus on fewer microcolonies in greater detail.

8. Conclusions and Future Work

8.1. Conclusions

Accurately measuring and mapping chemical gradients that form within the extracellular matrix of a biofilm is of great importance to the improvement of treatment methods to combat microbial biofilms. Biofilms are associated with life-threatening infections in Cystic Fibrosis patients and lowering the quality of life and health of an affected host through dental caries and periodontitis, whilst biofouling has been linked to hospital-associated infections through catheters. The generation of chemical microenvironments, such as pH gradients are an important factor for bacterial survival as well as contributing to biofilm-associated diseases such as dental caries and periodontitis, whilst the availability of oxygen plays a crucial role in the survival of bacteria in both planktonic states and biofilms. The formation of these gradients aids in the protection of bacteria from host immune responses and antimicrobial agents; by developing tools either to use these microenvironments to our advantage or to bypass these protective mechanisms and eradicate the cells could lead to better treatment methods to combat microbial biofilms.

As discussed in the Aims and Objectives (2), this work was aimed at characterising the interaction of both pH-sensitive and oxygen-sensitive polyacrylamide nanosensors in a range of different bacteria, as well as elucidating their suitability for measuring changes in pH and oxygen gradients produced by these bacteria.

This work began by confirming whether the neutral or cationic pH-sensitive, polyacrylamide nanosensors would inhibit the growth of our chosen bacterial candidate, the well-studied *P. aeruginosa* laboratory strain, PAO1-N WT. The pH

nanosensors were shown to have no inhibitory effect on the growth of PAO1-N WT at concentrations ≤ 1 mg mL^{-1} when introduced to a bacterial culture. 1 mg mL^{-1} was therefore chosen for a working concentration to strike a balance between adequate signal-to-noise ratio and the potential inhibitory effects of the nanosensors on the growth of PAO1-N WT.

When the pH nanosensors were added to both planktonic cultures and biofilms, the cationic polyacrylamide nanosensors were shown to co-localise with PAO1-N WT, where they were likely interacting with extracellular components, such as LPS, coating the bacterial cells. In a biofilm, this co-localisation led to a thicker biofilm formation over 48 h. Conversely, the neutral polyacrylamide nanosensors became dispersed within a planktonic culture; whilst in a biofilm the neutral nanosensors formed distinct regions amongst the cells. Both nanosensors also appeared to remain outside of the cell so that any pH measurement was made in the extracellular environment. Once the cationic nanosensors were embedded in a PAO1-N WT biofilm, the nanosensors were capable of detecting pH changes in a biofilm as evidenced during irrigation with acetic acid. However, by using the pH nanosensors to measure pH changes in real-time during planktonic growth, a particular limitation came to light. The photostability of both pH-insensitive dyes, TAMRA and Rhodamine Red-X, led to photobleaching over time, whilst increasing temperature caused a change in the pH of the medium used.

The work continued by using oxygen-sensitive polyacrylamide nanosensors to measure oxygen consumption in planktonic culture and oxygen availability in microbial biofilms. Work was required to optimise the manufacturing of oxygen-sensitive nanosensors; initial methods produced nanosensors lacking fluorescence intensity suitably high enough for detection, whilst cationic nanoparticles functionalised with platinum (II) porphyrin led to the nanosensors forming

precipitates in the media during both planktonic growth and biofilm assays. Using neutral nanoparticles for functionalisation proved to produce oxygen-sensitive nanosensors suitable for measuring oxygen consumption in planktonic culture.

Planktonic growth using PAO1 strains highlighted an issue with *Pseudomonas spp.,* as *Pseudomonas spp.* produce an auto-fluorescent virulence factor called pyoverdine. Pyoverdine contains the dihydroxyquinoline chromophore that when excited at 405 nm caused the pyoverdine to emit at 650 nm. By using PAO1-N∆*pvdD* as an alternative to limit auto-fluorescence at 650 nm, the oxygen nanosensors were able to measure real-time consumption of oxygen across different bacterial species, while the introduction of an additional supplement, potassium nitrate, was capable of altering oxygen consumption.

By comparing the biofilm formation of PAO1-N WT against PAO1-N∆*pvdD*, work showed that PAO1-N WT was the most suitable strain for biofilm analysis as long as growth media was removed and replaced with saline before imaging. This limited auto-fluorescence at 650 nm as pyoverdine was likely removed during preparation. However, further issues arose with the oxygen-sensitive nanosensors when used in biofilm analysis. The inclusion of the oxygen nanosensors into a PAO1-N WT biofilm led to the disruption of microcolonies, which was likely due to the size of the nanosensors (203.54 ±7.37 nm).

By adapting the Calgary Biofilm Device (CBD) to use a commercially available, oxygen-sensing microplate (*PreSens* – OxoPlate), a range of biocompatible, non-toxic polymers were tested to determine which had the potential as an anti-biofouling material. The Polaxamers F127 and P123 as well as the PEGMA:LMA:PEG polymer, P20, were able to significantly reduce bacterial attachment and biofilm formation when compared to a polystyrene control.

Expanding this work, the oxygen nanosensors were used as a comparison to the OxoPlate; however, more limitations arose with the oxygen nanosensors. Although the oxygen nanosensors appeared more sensitive than the OxoPlates, and provided the option to include additional controls, the limited yield of nanosensors impacted the number of repeats meaning more data would be needed to be collected before a direct comparison with the OxoPlate assay can be made.

The work finished by utilising the well-studied biological system, *S. mutans*; where carbohydrate supplementation induces a pH response. This biological system provided an opportunity to test the range and potential of the pH sensitive, polyacrylamide nanosensors as a real-time analytical tool capable of accurately determining pH changes in extracellular media. By using the pH nanosensors in planktonic culture, the pH nanosensors responded to a range of carbon sources when added to starved *S. mutans*. The pH decreased as both glucose and sucrose were added, whilst the pH remained unchanged as xylose and xylitol were introduced into the medium. Similar results were also seen when glucose was added to a *S. mutans* biofilm with embedded pH nanosensors.

Practically speaking, the pH nanosensor system would have uses in the testing of oral hygiene products or sweetener alternatives soft drink production, in order to determine the impact on pH production. The nanosensors can provide flexibility, as a screening tool measuring pH changes in large-scale fluorescence assays; or as a more focused tool, tracking changes in the pH microenvironment of established oral biofilms over time, providing potential 4D analysis. The oxygen nanosensors have great potential to provide an insight into real-time oxygen consumption in planktonic culture; however, their current particle size is likely to limit their use in biofilm analysis.

8.2. Future Work

COVID-19 had an impact on the final months of this work. Due to the lockdown at the end of March, until access in August, lab work was halted completely. A three-month extension to my funding was granted and lab work restarted at the end of August; however, restrictions put in place to maintain a COVID secure facility meant that the scope of experiments had to be scaled back, whilst particular facilities became difficult to access. Before this, time was spent organising the connection of a Gas Control Module to a TECAN, which would have provided the opportunity to measure a range of oxygen concentrations in order to produce an oxygen calibration curve. This would have then meant an oxygen value (%) could have been assigned to the fluorescence intensity ratios calculated.

Without the impact of COVID-19, there would have be certain experiments required to finalise the findings reported in the thesis. Further work with Super-Resolution Microscopy would have been performed to delve further into the interaction between PAO1-N WT and the cationic pH nanosensors; including the addition of DNase I to confirm the hypothesis that the cationic nanosensors are forming clusters with eDNA. Further Super-Res work to determine the interaction of both the neutral and the cationic pH-sensitive, polyacrylamide nanosensors with *S. mutans* would have also been carried out.

Another experiment to confirm the hypothesis that pyoverdine was causing the auto-fluorescence would have been performed by including iron as a supplement during planktonic growth. This is due to the addition of iron sequestering the fluorescence of pyoverdine (Rong and Kisaalita, 1998); therefore, the addition to a growth assay may have prevented the increase in auto-fluorescence.

Moving forward with the project, there is scope for the continued use of both the pH-sensitive and oxygen-sensitive nanosensors.

8.2.1. A biological system for oxygen nanosensors

The susceptibility of a biofilm to antimicrobial treatment is calculated as either the minimal biofilm eradication concentration (MBEC), or the minimal biofilm inhibitory concentration (MBIC). These values provide the concentration of an antimicrobial required for the subsequent treatment of a biofilm-associated infection. Currently the Calgary Biofilm Device (CBD) is used to determine the MBIC of antimicrobials, where biofilms are grown on peg-lids and submerged in varying concentrations of antimicrobial before being stained with Crystal Violet. This method can be time-consuming and may not produce accurate concentrations for effective treatment.

An alternative could be to use the oxygen nanosensors as an analytical tool in the CBD, whereby the oxygen nanosensors measure oxygen availability within the well. As the antimicrobial halts the metabolism of the treated biofilm, an accurate MBIC for the antimicrobial can be calculated. As highlighted by Jewell et al. (2020b), measuring metabolic activity of bacteria to determine the effectiveness of antimicrobials is limited only to respiring cells, which would rule out anaerobic bacteria. This also limits the antimicrobial that could be used *i.e.* only antimicrobials that target metabolism directly, such as aminoglycosides, fluoroquinolones and polymyxins. Another factor to consider is the production of ROS during antimicrobial treatment. Stress-induced ROS production can lead to 'self-destruction', resulting in the release of ROS into the extracellular matrix (Zhao and Drlica, 2014, McBee et al., 2017, Hong et al., 2019). This stress-induced ROS production and release is only likely at concentrations above the

MBEC; therefore, it could provide a more accurate MBEC calculation as well as detect real-time cell death by measuring the release of ROS. More detailed work could be carried out once the nanosensors have been refined enough to embed within a static biofilm. Time-lapse biofilm assays of established, static biofilms treated with a range of antimicrobials could exploit the oxygen nanosensors as a tracking tool to detect the penetration of antimicrobials. Additionally, flow-cell systems such as BioFlux could be used to create antimicrobial gradients within the channel to match antimicrobial concentration, whilst using the emission from the nanosensors to calculate the MBIC and MBEC. For instance, a BioFlux 24-well plate allows the user to generate a concentration gradient across the channel; therefore, oxygen availability within microcolonies could be measured in real-time as an antimicrobial, at varying concentrations, is flowed through the channel.

The oxygen nanosensors could also augment our CF lung infection models, in particular as a tool to measure oxygen gradients that may be generated within microbial biofilms forming on lung epithelial cells, as well as a method to detect ROS production. ROS is of particular interest in lung infection models as intracellular ROS production by lung epithelial cells has been shown to increase when treated with PQS (Abdalla et al., 2017). The platinum (II) porphyrin based oxygen-sensitive nanosensors used in this work have the potential to detect intracellular ROS production, as similar zinc (II) porphyrin functionalised nanoparticles have been demonstrated to be internalised by human mesenchymal stem cells (hMSCs), whereby they act as photosensitizers in the intracellular production of ROS after stimulation with visible light (Lavado et al., 2015). However, intracellular ROS production can also be detected using fluorescent dyes, for example; (4,4,5,5-tetramethyl-1,3,2-dioxaborolan-2-yl)-4-(trifluoromethyl)-2H-chromen-2-one (BPTFMC) is transformed in the presence of

hydrogen peroxide (H_2O_2) to the fluorescent entity7-hydroxy-4-trifluoromethyl-coumarin (HTFMC) (Lavado et al., 2015) whilst dichlorodihydrofluorescein (DCF), dihydroethidium(DHE), and MitoSOX Red have been used to as oxidant-sensitive probes (Abdalla et al., 2017). So rather than internalise the oxygen nanosensors within epithelial cells, the oxygen nanosensors could be embedded into an *in vitro* lung infection model to measure extracellular release of ROS or to measure oxygen gradients at the interface between an established microbial biofilm and an lung epithelial layer. However, a consideration for the inclusion of the oxygen nanosensors in a biofilm model such as this must be made, as the internalisation of oxygen nanosensors by the eukaryotic cell should be avoided to prevent internal ROS measurements occurring. This could be achieved by embedding the oxygen nanosensors into compressed collagen sheets that can used to construct 3D matrices, as described by Giuntini et al. (2014). The generation of potential anaerobic regions within the biofilm could then be combined with detecting the expression of genes involved in the denitrification process or the oxygen-dependent production of PQS by PqsH, as discussed in 6.1.1.2, via the use of fluorescent tagging.

Similar work could be translated into chronic wound infection models where both hypoxia and ROS production are present (Sen, 2009, Dunnill et al., 2017). Here oxygen nanosensors could be used to measure and map hypoxic regions that may form in chronic wound infections, as well as to detect ROS production. Another aspect of interest in wound infection would be the detection of virulence factors such as **A**rginine-specific **A**minopeptidase of *Pseudomonas aeruginos**A*** (AaaA - PA0328). Previous work has highlighted the importance of AaaA in wound infection models. AaaA acts as a cell-surface tethered auto-transporter which cleaves N-terminal arginine-peptide/protein from an unknown substrate (Luckett et al.,

2012). Scavenged arginine can then serve as an alternative nutrient source in oxygen-limiting environments (Vanderwauven et al., 1984). PAO1Δ*aaaA* has been shown to grow equally well as PAO1 WT when fed solely arginine; however, when supplied with peptides with amino terminal arginine, PAO1 Δ*aaaA* was unable to grow (Luckett et al., 2012). Under low oxygen conditions, arginine catabolism occurs via the arginine deiminase (ADI) pathway. A transcriptional regulator of the ADI pathway is the anaerobic nitrate regular (ANR) (Lu et al., 1999). The induction of ANR is enhanced by exogenous arginine, through another regulatory protein called ArgR. Expression of *aaaA* is positively regulated by ArgR, with a 3.7 fold increase in *aaaA* expression under aerobic conditions when supplemented with L-arginine (Lu et al., 2004). The expression of *aaaA* is therefore linked to the availability of oxygen.

By using the oxygen nanosensors as an analytical tool, AaaA production could be tracked as oxygen availability becomes limited. By using a transcriptional reporter, such as the bacterial Lux reporter, inserted into the PAO1-NΔ*pvdD* mutant, *aaaA* expression could be measured via luminescence, whilst oxygen availability is measured by the oxygen nanosensors. This could determine the concentration of oxygen required to detect the induced expression of *aaaA* as an arginine scavenger in planktonic culture. A similar assay could be performed using a flow-cell system to simultaneously detect the formation of anaerobic/microaerophilic regions of microcolonies and the potential production of AaaA through fluorescent labelling.

8.2.2. Oral care and pH

For the pH nanosensors, there are a few avenues of interest that could be explored. Initially, it would be beneficial to produce an *S. mutans* biofilm that is

more biologically relevant, by adopting a growth medium more representative of the oral cavity. This could be achieved by using an artificial saliva medium that is similar to the AEP *i.e.* supplemented with mucin and agglutinins. This would aid in the attachment of *S. mutans* without the need for sucrose. The addition of a fluorescent metabolic indicator dye, such as 5-Cyano-2,3-ditolyl tetrazolium chloride (CTC) (ex:488 nm, em:630 nm), could also be used to simultaneously track metabolism during sucrose/glucose treatment (Guo et al., 2013b).

By using the pH nanosensors embedded within an oral biofilm, the nanosensors also could provide an analytical tool in measuring pH changes induced by a range of oral products. Of particular interest as a treatment method, is the addition of arginine. A collection of oral bacteria, including *S. gordonii* and *S. sanguinis*, are capable of catabolising arginine to produce ornithine, which in the process generates ATP and ammonium (Burne and Marquis, 2000, Berto et al., 2019). These species perform this catabolism through the use the arginine deiminase system (ADS), which is absent in *S. mutans*. ADS functions to protect the bacterial cells from low pH environments created by microbial species such as *S. mutans* and Lactobacilli, through the production of ammonium (Casiano-colon and Marquis, 1988, Griswold et al., 2004). The metabolism of arginine has been shown to have a two-fold affect; firstly, it has been shown by Bijle et al. (2020) to reduce the viable count and biofilm mass of *S. mutan*s, as arginine supplementation improved the growth of *Lactobacillus rhamnosus GG*, a common probiotic bacterial species. The enhanced growth caused a significant reduction in *S. mutans* biofilm development and a reduction in lactic acid production. Secondly, arginine supplementation has been shown to increase the pH of the bulk medium and protect *S. sanguinis* from acid damage (Casiano-colon and Marquis, 1988). This would suggest that the addition of arginine could both limit *S. mutans* involvement

in dental plaque but also raise the net pH to prevent the demineralisation of the tooth's enamel.

The work shown in this thesis could therefore be built-upon by the introduction of additional oral bacteria that contain ADS such as *S. gordonii S. sanguinis*, to test oral care products. As oral biofilms are inherently multispecies, the response of *S. mutans* in a single species biofilm may be drastically different to its response when in a biofilm with other species. The limiting factor with the introduction of additional microbial species is that the pH-sensitive nanosensors occupy both the green and red channels in fluorescent microscopy. This would limit fluorescent labelling of bacteria to either ends of the spectrum. The introduction of a flow-cell system, such as BioFlux, to test the oral care products could also have some interest to determine the effects of concentration across a mature *S. mutans* or polymicrobial biofilm as the BioFlux system can create concentration gradients.

9. References

ABBASZADEGAN, A., GHAHRAMANI, Y., GHOLAMI, A., HEMMATEENEJAD, B., DOROSTKAR, S., NABAVIZADEH, M. & SHARGHI, H. 2015. The effect of charge at the surface of silver nanoparticles on antimicrobial activity against Gram-positive and Gram-negative bacteria: A preliminary study. *Journal of Nanomaterials,* 16**,** 1-8.

ABBE, K., TAKAHASHI, S. & YAMADA, T. 1982. Involvement of oxygen-sensitive pyruvate formate-lyase in mixed-acid fermentation by *Streptococcus mutans* under strictly anaerobic conditions. *Journal of Bacteriology,* 152**,** 175-182.

ABDALLA, M. Y., HOKE, T., SERAVALLI, J., SWITZER, B. L., BAVITZ, M., FLIEGE, J. D., MURPHY, P. J. & BRITIGAN, B. E. 2017. Pseudomonas Quinolone Signal induces oxidative stress and inhibits heme oxygenase-1 expression in lung epithelial cells. *Infection and Immunity,* 85**,** 176-190.

ABDULKAREEM, E. H., MEMARZADEH, K., ALLAKER, R. P., HUANG, J., PRATTEN, J. & SPRATT, D. 2015. Anti-biofilm activity of zinc oxide and hydroxyapatite nanoparticles as dental implant coating materials. *Journal of Dentistry,* 43**,** 1462-1469.

ABOU NEEL, E. A., ALJABO, A., STRANGE, A., IBRAHIM, S., COATHUP, M., YOUNG, A. M., BOZEC, L. & MUDERA, V. 2016. Demineralization-remineralization dynamics in teeth and bone. *International Journal of Nanomedicine,* 11**,** 4743-4763.

ABSOLOM, D. R., LAMBERTI, F. V., POLICOVA, Z., ZINGG, W., VANOSS, C. J. & NEUMANN, A. W. 1983. Surface thermodynamics of bacterial adhesion. *Applied and Environmental Microbiology,* 46**,** 90-97.

ACOSTA, M. A., VELASQUEZ, M., WILLIAMS, K., ROSS, J. M. & LEACH, J. B. 2012. Fluorescent silica particles for monitoring oxygen levels in three-dimensional heterogeneous cellular structures. *Biotechnology and Bioengineering,* 109**,** 2663-2670.

ALLAN, V. J. M., MACASKIE, L. E. & CALLOW, M. E. 1999. Development of a pH gradient within a biofilm is dependent upon the limiting nutrient. *Biotechnology Letters,* 21**,** 407-413.

ALLESEN-HOLM, M., BARKEN, K. B., YANG, L., KLAUSEN, M., WEBB, J. S., KJELLEBERG, S., MOLIN, S., GIVSKOV, M. & TOLKER-NIELSEN, T. 2006. A characterization of DNA release in *Pseudomonas aeruginosa* cultures and biofilms. *Molecular Microbiology,* 59**,** 1114-1128.

ALVAREZ-ORTEGA, C. & HARWOOD, C. S. 2007. Responses of *Pseudomonas aeruginosa* to low oxygen indicate that growth in the cystic fibrosis lung is by aerobic respiration. *Molecular Microbiology,* 65**,** 153-165.

ALVAREZ, G., GONZALEZ, M., ISABAL, S., BLANC, V. & LEON, R. 2013. Method to quantify live and dead cells in multi-species oral biofilm by real-time PCR with propidium monoazide. *Amb Express,* 3**,** 1-8.

APPELBAUM, P. C. 1999. Quinolone activity against anaerobes. *Drugs,* 58**,** 60-64.

ARAI, H. 2011. Regulation and function of versatile aerobic and anaerobic respiratory metabolism in *Pseudomonas aeruginosa*. *Frontiers in Microbiology,* 2**,** 1-13.

ARAI, H., KAWAKAMI, T., OSAMURA, T., HIRAI, T., SAKAI, Y. & ISHII, M. 2014. Enzymatic characterization and *in vivo* function of five terminal oxidases in *Pseudomonas aeruginosa*. *Journal of Bacteriology,* 196**,** 4206-4215.

ARCIOLA, C. R., CAMPOCCIA, D., RAVAIOLI, S. & MONTANARO, L. 2015. Polysaccharide intercellular adhesin in biofilm: structural and regulatory aspects. *Frontiers in Cellular and Infection Microbiology,* 5**,** 1-10.

BALAKRISHNAN, M., SIMMONDS, R. S. & TAGG, J. R. 2000. Dental caries is a preventable infectious disease. *Australian Dental Journal,* 45**,** 235-245.

BANAS, J. A., FOUNTAIN, T. L., MAZURKIEWICZ, J. E., SUN, K. & VICKERMAN, M. M. 2007. *Streptococcus mutans* glucan-binding protein-A affects *Streptococcus gordonii* biofilm architecture. *FEMS Microbiology Letters,* 267**,** 80-88.

BANIN, E., VASIL, M. L. & GREENBERG, E. P. 2005. Iron and *Pseudomonas aeruginosa* biofilm formation. *Proceedings of the National Academy of Sciences of the United States of America,* 102**,** 11076-11081.

BAZAKA, K., JACOB, M. V., CRAWFORD, R. J. & IVANOVA, E. P. 2012. Efficient surface modification of biomaterial to prevent biofilm formation and the attachment of microorganisms. *Applied Microbiology and Biotechnology,* 95**,** 299-311.

BERTO, L. A., LAUENER, A., CARVALHO, T. S., LUSSI, A. & EICK, S. 2019. *In vitro* effects of arginine-containing toothpastes on cariogenic biofilms. *Oral Health & Preventive Dentistry,* 17**,** 375-383.

BEYENAL, H. & BABAUTA, J. T. 2012. Microscale gradients and their role in electron-transfer mechanisms in biofilms. *Biochemical Society Transactions,* 40**,** 1315-1318.

BIJLE, M. N., NEELAKANTAN, P., EKAMBARAM, M., LO, E. C. M. & YIU, C. K. Y. 2020. Effect of a novel synbiotic on *Streptococcus mutans*. *Scientific Reports,* 10**,** 1-9.

BILLINGS, N., BIRJINIUK, A., SAMAD, T. S., DOYLE, P. S. & RIBBECK, K. 2015. Material properties of biofilms-a review of methods for understanding permeability and mechanics. *Reports on Progress in Physics,* 78**,** 1-33.

BLASER, J. & LUTHY, R. 1988. Comparative-study on antagonistic effects of low pH and cation supplementation on *in vitro* activity of quinolones and aminoglycosides against *Pseudomonas aeruginosa*. *Journal of Antimicrobial Chemotherapy,* 22**,** 15-22.

BODELON, G., MONTES-GARCIA, V., LOPEZ-PUENTE, V., HILL, E. H., HAMON, C., SANZ-ORTIZ, M. N., RODAL-CEDEIRA, S., COSTAS, C., CELIKSOY, S., PEREZ-JUSTE, I., SCARABELLI, L., LA PORTA, A., PEREZ-JUSTE, J., PASTORIZA-SANTOS, I. & LIZ-MARZAN, L. M. 2016. Detection and imaging of quorum sensing in *Pseudomonas aeruginosa* biofilm communities by surface-enhanced resonance Raman scattering. *Nature Materials,* 15**,** 1203-1211.

BORLEE, B. R., GOLDMAN, A. D., MURAKAMI, K., SAMUDRALA, R., WOZNIAK, D. J. & PARSEK, M. R. 2010. *Pseudomonas aeruginosa* uses a cyclic-di-GMP-regulated adhesin to reinforce the biofilm extracellular matrix. *Molecular Microbiology,* 75**,** 827-842.

BORRIELLO, G., WERNER, E., ROE, F., KIM, A. M., EHRLICH, G. D. & STEWART, P. S. 2004. Oxygen limitation contributes to antibiotic tolerance of *Pseudomonas aeruginosa* in biofilms. *Antimicrobial Agents and Chemotherapy,* 48**,** 2659-2664.

BOWEN, W. H. & KOO, H. 2011. Biology of *Streptococcus mutans*-derived glucosyltransferases: Role in extracellular matrix formation of cariogenic biofilms. *Caries Research,* 45**,** 69-86.

BRADY, L. J., MADDOCKS, S. E., LARSON, M. R., FORSGREN, N., PERSSON, K., DEIVANAYAGAM, C. C. & JENKINSON, H. F. 2010. The changing faces of *Streptococcus* antigen I/II polypeptide family adhesins. *Molecular Microbiology,* 77**,** 276-286.

BRANDEL, J., HUMBERT, N., ELHABIRI, M., SCHALK, I. J., MISLIN, G. L. A. & ALBRECHT-GARY, A. M. 2012. Pyochelin, a siderophore of *Pseudomonas aeruginosa*: Physicochemical characterization of the iron(III), copper(II) and zinc(II) complexes. *Dalton Transactions,* 41**,** 2820-2834.

BUDZIKIEWICZ, H., SCHAFER, M., FERNANDEZ, D. U., MATTHIJS, S. & CORNELIS, P. 2007. Characterization of the chromophores of pyoverdins and related siderophores by electrospray tandem mass spectrometry. *Biometals,* 20**,** 135-144.

BURDIKOVA, Z., SVINDRYCH, Z., PALA, J., HICKEY, C. D., WILKINSON, M. G., PANEK, J., AUTY, M. A. E., PERIASAMY, A. & SHEEHAN, J. J. 2015. Measurement of pH micro-heterogeneity in natural cheese matrices by fluorescence lifetime imaging. *Frontiers in Microbiology,* 6**,** 1-10.

BURNE, R. A. & MARQUIS, R. E. 2000. Alkali production by oral bacteria and protection against dental caries. *FEMS Microbiology Letters,* 193**,** 1-6.

BYRD, M. S., SADOVSKAYA, I., VINOGRADOV, E., LU, H. P., SPRINKLE, A. B., RICHARDSON, S. H., MA, L. Y., RALSTON, B., PARSEK, M. R., ANDERSON, E. M., LAM, J. S. & WOZNIAK, D. J. 2009. Genetic and biochemical analyses of the *Pseudomonas aeruginosa* Psl exopolysaccharide reveal overlapping roles for polysaccharide synthesis enzymes in Psl and LPS production. *Molecular Microbiology,* 73**,** 622-638.

CAIAZZA, N. C. & O'TOOLE, G. A. 2004. SadB is required for the transition from reversible to irreversible attachment during biofilm formation by *Pseudomonas aeruginosa* PA14. *Journal of Bacteriology,* 186**,** 4476-4485.
CASIANO-COLON, A. & MARQUIS, R. E. 1988. Role of the arginine deiminase system in protecting oral bacteria and an enzymatic basis for acid tolerance. *Applied and Environmental Microbiology,* 54**,** 1318-1324.
CHAUHAN, V. M., GIUNTINI, F. & AYLOTT, J. W. 2016. Quadruple labelled dual oxygen and pH-sensitive ratiometric nanosensors. *Sensing and Bio-Sensing Research,* 8**,** 36-42.
CHAUHAN, V. M., ORSI, G., BROWN, A., PRITCHARD, D. I. & AYLOTT, J. W. 2013. Mapping the pharyngeal and intestinal pH of *Caenorhabditis elegans* and real-time luminal pH oscillations using extended dynamic range pH-sensitive nanosensors. *ACS Nano,* 7**,** 5577-5587.
CHEN, S. F., LI, L. Y., ZHAO, C. & ZHENG, J. 2010. Surface hydration: Principles and applications toward low-fouling/nonfouling biomaterials. *Polymer,* 51**,** 5283-5293.
CHENG, G., ZHANG, Z., CHEN, S. F., BRYERS, J. D. & JIANG, S. Y. 2007. Inhibition of bacterial adhesion and biofilm formation on zwitterionic surfaces. *Biomaterials,* 28**,** 4192-4199.
CHENG, Z. P., ZHU, X. L., KANG, E. T. & NEOH, K. G. 2005. Brush-type amphiphilic diblock copolymers from "living"/controlled radical polymerizations and their aggregation behavior. *Langmuir,* 21**,** 7180-7185.
COLBY, S. M. & RUSSELL, R. R. B. 1997. Sugar metabolism by *mutans streptococci*. *Journal of Applied Microbiology,* 83**,** S80-S88.
COLVIN, K. M., IRIE, Y., TART, C. S., URBANO, R., WHITNEY, J. C., RYDER, C., HOWELL, P. L., WOZNIAK, D. J. & PARSEK, M. R. 2012. The Pel and Psl polysaccharides provide *Pseudomonas aeruginosa* structural redundancy within the biofilm matrix. *Environmental Microbiology,* 14**,** 1913-1928.
COSTERTON, J. W. 1995. Overview of microbial biofilms. *Journal of Industrial Microbiology,* 15**,** 137-140.
COSTERTON, J. W., STEWART, P. S. & GREENBERG, E. P. 1999. Bacterial biofilms: A common cause of persistent infections. *Science,* 284**,** 1318-1322.
CRAMTON, S. E., ULRICH, M., GOTZ, F. & DORING, G. 2001. Anaerobic conditions induce expression of polysaccharide intercellular adhesin in *Staphylococcus aureus* and *Staphylococcus epidermidis*. *Infection and Immunity,* 69**,** 4079-4085.
CRESPO, A., PEDRAZ, L., ASTOLA, J. & TORRENTS, E. 2016. *Pseudomonas aeruginosa* exhibits deficient biofilm formation in the absence of class II and III ribonucleotide reductases due to hindered anaerobic growth. *Frontiers in Microbiology,* 7**,** 1-14.
D'ARGENIO, D. A., CALFEE, M. W., RAINEY, P. B. & PESCI, E. C. 2002. Autolysis and autoaggregation in *Pseudomonas aeruginosa* colony morphology mutants. *Journal of Bacteriology,* 184**,** 6481-6489.
DAI, X. M., GUO, Q. Q., ZHAO, Y., ZHANG, P., ZHANG, T. Q., ZHANG, X. G. & LI, C. X. 2016. Functional silver nanoparticle as a benign antimicrobial agent that eradicates antibiotic-resistant bacteria and promotes wound healing. *ACS Applied Materials & Interfaces,* 8**,** 25798-25807.
DAS, T. & MANEFIELD, M. 2012. Pyocyanin promotes extracellular DNA release in *Pseudomonas aeruginosa*. *PLOS One,* 7.
DASHPER, S. G. & REYNOLDS, E. C. 1996. Lactic acid excretion by *Streptococcus mutans*. *Microbiology-Uk,* 142**,** 33-39.
DAVIES, D. G., PARSEK, M. R., PEARSON, J. P., IGLEWSKI, B. H., COSTERTON, J. W. & GREENBERG, E. P. 1998. The involvement of cell-to-cell signals in the development of a bacterial biofilm. *Science,* 280**,** 295-298.
DE BEER, D., STOODLEY, P., ROE, F. & LEWANDOWSKI, Z. 1994. Effects of biofilm structures on oxygen distribution and mass-transport. *Biotechnology and Bioengineering,* 43**,** 1131-1138.
DE RIENZO, M. A. D., STEVENSON, P. S., MARCHANT, R. & BANAT, I. M. 2016. Effect of biosurfactants on *Pseudomonas aeruginosa* and *Staphylococcus aureus* biofilms in a BioFlux channel. *Applied Microbiology and Biotechnology,* 100**,** 5773-5779.

DECKER, E. M., KLEIN, C., SCHWINDT, D. & VON OHLE, C. 2014. Metabolic activity of *Streptococcus mutans* biofilms and gene expression during exposure to xylitol and sucrose. *International Journal of Oral Science,* 6**,** 195-204.
DELWICHE, E. A., PESTKA, J. J. & TORTORELLO, M. L. 1985. The *Veillonellae* - Gram-negative cocci with a unique physiology. *Annual Review of Microbiology,* 39**,** 175-193.
DEPEDRO, H. M. & URAYAMA, P. 2009. Using LysoSensor Yellow/Blue DND-160 to sense acidic pH under high hydrostatic pressures. *Analytical Biochemistry,* 384**,** 359-361.
DIGE, I., BAELUM, V., NYVAD, B. & SCHLAFER, S. 2016. Monitoring of extracellular pH in young dental biofilms grown in vivo in the presence and absence of sucrose. *Journal of Oral Microbiology,* 8**,** 1-8.
DIGE, I., RAARUP, M. K., NYENGAARD, J. R., KILIAN, M. & NYVAD, B. 2009. *Actinomyces naeslundii* in initial dental biofilm formation. *Microbiology-Sgm,* 155**,** 2116-2126.
DIGGLE, S. P., CORNELIS, P., WILLIAMS, P. & CAMARA, M. 2006. 4-Quinolone signalling in *Pseudomonas aeruginosa*: Old molecules, new perspectives. *International Journal of Medical Microbiology,* 296**,** 83-91.
DONLAN, R. M. 2002. Biofilms: Microbial life on surfaces. *Emerging Infectious Diseases,* 8**,** 881-890.
DRISCOLL, J. A., BRODY, S. L. & KOLLEF, M. H. 2007. The epidemiology, pathogenesis and treatment of *Pseudomonas aeruginosa* infections. *Drugs,* 67**,** 351-368.
DUNNILL, C., PATTON, T., BRENNAN, J., BARRETT, J., DRYDEN, M., COOKE, J., LEAPER, D. & GEORGOPOULOS, N. T. 2017. Reactive oxygen species (ROS) and wound healing: the functional role of ROS and emerging ROS-modulating technologies for augmentation of the healing process. *International Wound Journal,* 14**,** 89-96.
ELIAS, S. & BANIN, E. 2012. Multi-species biofilms: living with friendly neighbors. *FEMS Microbiology Reviews,* 36**,** 990-1004.
ELSUTOHY, M. M., CHAUHAN, V. M., MARKUS, R., KYYALY, M. A., TENDLER, S. J. B. & AYLOTT, J. W. 2017. Real-time measurement of the intracellular pH of yeast cells during glucose metabolism using ratiometric fluorescent nanosensors. *Nanoscale,* 9**,** 5904-5911.
FEATHERSTONE, J. D. B. 2000. The science and practice of caries prevention. *Journal of the American Dental Association,* 131**,** 887-899.
FILKINS, L. M. & O'TOOLE, G. A. 2015. Cystic fibrosis lung infections: Polymicrobial, complex, and hard to treat. *PLOS Pathogens,* 11**,** 1-8.
FLEMMIG, T. F. & BEIKLER, T. 2011. Control of oral biofilms. *Periodontology 2000,* 55**,** 9-15.
FLEMMING, H. C. 2002. Biofouling in water systems - cases, causes and countermeasures. *Applied Microbiology and Biotechnology,* 59**,** 629-640.
FLEMMING, H. C. & WINGENDER, J. 2001. Relevance of microbial extracellular polymeric substances (EPSs) - Part I: Structural and ecological aspects. *Water Science and Technology,* 43**,** 1-8.
FLEMMING, H. C. & WINGENDER, J. 2010. The biofilm matrix. *Nature Reviews Microbiology,* 8**,** 623-633.
FLETCHER, M. & LOEB, G. I. 1979. Influence of substratum characteristics on the attachment of a marine *Pseudomonad* to solid-surfaces. *Applied and Environmental Microbiology,* 37**,** 67-72.
FOLSCHWEILLER, N., GALLAY, J., VINCENT, M., ABDALLAH, M. A., PATTUS, F. & SCHALK, I. J. 2002. The interaction between pyoverdin and its outer membrane receptor in *Pseudomonas aeruginosa* leads to different conformers: A time-resolved fluorescence study. *Biochemistry,* 41**,** 14591-14601.
FOLSOM, J. P., RICHARDS, L., PITTS, B., ROE, F., EHRLICH, G. D., PARKER, A., MAZURIE, A. & STEWART, P. S. 2010. Physiology of *Pseudomonas aeruginosa* in biofilms as revealed by transcriptome analysis. *BMC Microbiology,* 10**,** 1-17.
FRIEDMAN, L. & KOLTER, R. 2004. Genes involved in matrix formation in *Pseudomonas aeruginosa* PA14 biofilms. *Molecular Microbiology,* 51**,** 675-690.

FUJITA, K., MATSUMOTO-NAKANO, M., INAGAKI, S. & OOSHIMA, T. 2007. Biological functions of glucan-binding protein B of *Streptococcus mutans*. *Oral Microbiology and Immunology,* 22**,** 289-292.
FULAZ, S., HIEBNER, D., BARROS, C. H. N., DEVLIN, H., VITALE, S., QUINN, L. & CASEY, E. 2019. Ratiometric imaging of the in situ pH distribution of biofilms by use of fluorescent mesoporous silica nanosensors. *ACS Applied Materials & Interfaces,* 11**,** 32679-32688.
GAINES, J. M., CARTY, N. L., COLMER-HAMOOD, J. A. & HAMOOD, A. N. 2005. Effect of static growth and different levels of environmental oxygen on toxA and ptxR expression in the *Pseudomonas aeruginosa* strain PAO1. *Microbiology-Sgm,* 151**,** 2263-2275.
GALYEAN, A. A., BEHR, M. R. & CASH, K. J. 2018. Ionophore-based optical nanosensors incorporating hydrophobic carbon dots and a pH-sensitive quencher dye for sodium detection. *Analyst,* 143**,** 458-465.
GATTLEN, J., AMBERG, C., ZINN, M. & MAUCLAIRE, L. 2010. Biofilms isolated from washing machines from three continents and their tolerance to a standard detergent. *Biofouling,* 26**,** 873-882.
GEESEY, G. G., RICHARDSON, W. T., YEOMANS, H. G., IRVIN, R. T. & COSTERTON, J. W. 1977. Microscopic examination of natural sessile bacterial populations from an alpine stream. *Canadian Journal of Microbiology,* 23**,** 1733-1736.
GEILICH, B. M., GELFAT, I., SRIDHAR, S., VAN DE VEN, A. L. & WEBSTER, T. J. 2017. Superparamagnetic iron oxide-encapsulating polymersome nanocarriers for biofilm eradication. *Biomaterials,* 119**,** 78-85.
GHAFOOR, A., HAY, I. D. & REHM, B. H. A. 2011. Role of exopolysaccharides in *Pseudomonas aeruginosa* biofilm formation and architecture. *Applied and Environmental Microbiology,* 77**,** 5238-5246.
GIUNTINI, F., CHAUHAN, V. M., AYLOTT, J. W., ROSSER, G. A., ATHANASIADIS, A., BEEBY, A., MACROBERT, A. J., BROWN, R. A. & BOYLE, R. W. 2014. Conjugatable water-soluble Pt(II) and Pd(II) porphyrin complexes: novel nano-and molecular probes for optical oxygen tension measurement in tissue engineering. *Photochemical & Photobiological Sciences,* 13**,** 1039-1051.
GONG, K. 2000. Salivary film expresses a complex, macromolecular binding site for *Streptococcus sanguis*. *Journal of Biological Chemistry,* 275**,** 8970-8974.
GOTTENBOS, B., VAN DER MEI, H. C., BUSSCHER, H. J., GRIJPMA, D. W. & FEIJEN, J. 1999. Initial adhesion and surface growth of *Pseudomonas aeruginosa* on negatively and positively charged poly(methacrylates). *Journal of Materials Science-Materials in Medicine,* 10**,** 853-855.
GOVAN, J. R. W. & DERETIC, V. 1996. Microbial pathogenesis in cystic fibrosis: Mucoid *Pseudomonas aeruginosa* and *Burkholderia cepacia*. *Microbiological Reviews,* 60**,** 539-574.
GRABER, M. L., DILILLO, D. C., FRIEDMAN, B. L. & PASTORIZA-MUNOZ, E. 1986. Characteristics of fluoroprobes for measuring intracellular pH. *Analytical Biochemistry,* 156**,** 202-12.
GRAHAM, M. V., MOSIER, A. P., KIEHL, T. R., KALOYEROS, A. E. & CADY, N. C. 2013. Development of antifouling surfaces to reduce bacterial attachment. *Soft Matter,* 9**,** 6235-6244.
GRISWOLD, A., CHEN, Y. Y. M., SNYDER, J. A. & BURNE, R. A. 2004. Characterization of the arginine deiminase operon of *Streptococcus rattus* FA-1. *Applied and Environmental Microbiology,* 70**,** 1321-1327.
GUNKEL, G., WEINHART, M., BECHERER, T., HAAG, R. & HUCK, W. T. S. 2011. Effect of polymer brush architecture on antibiofouling properties. *Biomacromolecules,* 12**,** 4169-4172.
GUO, L. H., HU, W., HE, X. S., LUX, R., MCLEAN, J. & SHI, W. Y. 2013a. Investigating acid production by *Streptococcus mutans* with a surface-displayed pH-sensitive green fluorescent protein. *PLOS One,* 8.

GUO, L. H., HU, W., HE, X. S., LUX, R., MCLEAN, J. & SHI, W. Y. 2013b. Investigating acid production by *Streptococcus mutans* with a surface-displayed pH-sensitive green fluorescent protein. *PLOS One,* 8**,** 1-10.

GUPTA, S., LASKAR, N. & KADOURI, D. 2016. Evaluating the effect of oxygen concentrations on antibiotic sensitivity, growth, and biofilm formation of human pathogens. *Micobiology Insights,* 9**,** 37-46.

HAMAD, M. A., DI LORENZO, F., MOLINARO, A. & VALVANO, M. A. 2012. Aminoarabinose is essential for lipopolysaccharide export and intrinsic antimicrobial peptide resistance in *Burkholderia cenocepacia*. *Molecular Microbiology,* 85**,** 962-974.

HANNIG, C., HANNIG, M. & ATTIN, T. 2005. Enzymes in the acquired enamel pellicle. *European Journal of Oral Sciences,* 113**,** 2-13.

HARIMAWAN, A. & TING, Y. P. 2016. Investigation of extracellular polymeric substances (EPS) properties of *Pseudomonas aeruginosa* and *Bacillus subtillis* and their role in bacterial adhesion. *Colloids and Surfaces B: Biointerfaces,* 146**,** 459-467.

HARRIS, L. G., TOSATTI, S., WIELAND, M., TEXTOR, M. & RICHARDS, R. G. 2004. *Staphylococcus aureus* adhesion to titanium oxide surfaces coated with non-functionalized and peptide-functionalized poly(L-lysine)-grafted-poly(ethylene glycol) copolymers. *Biomaterials,* 25**,** 4135-4148.

HARRISON, F. 2007. Microbial ecology of the cystic fibrosis lung. *Microbiology-Sgm,* 153**,** 917-923.

HASSETT, D. J. 1996. Anaerobic production of alginate by *Pseudomonas aeruginosa*: Alginate restricts diffusion of oxygen. *Journal of Bacteriology,* 178**,** 7322-7325.

HAZAN, R., QUE, Y. A., MAURA, D., STROBEL, B., MAJCHERCZYK, P. A., HOPPER, L. R., WILBUR, D. J., HREHA, T. N., BARQUERA, B. & RAHME, L. G. 2016. Auto poisoning of the respiratory chain by a quorum-sensing-regulated molecule favors biofilm formation and antibiotic tolerance. *Current Biology,* 26**,** 195-206.

HENTZER, M., TEITZEL, G. M., BALZER, G. J., HEYDORN, A., MOLIN, S., GIVSKOV, M. & PARSEK, M. R. 2001. Alginate overproduction affects *Pseudomonas aeruginosa* biofilm structure and function. *Journal of Bacteriology,* 183**,** 5395-5401.

HIDALGO, G., BURNS, A., HERZ, E., HAY, A. G., HOUSTON, P. L., WIESNER, U. & LION, L. W. 2009. Functional tomographic fluorescence imaging of pH microenvironments in microbial biofilms by use of silica nanoparticle sensors. *Applied and Environmental Microbiology,* 75**,** 7426-7435.

HO, Y. R., LI, C. M., YU, C. H., LIN, Y. J., WU, C. M., HARN, I. C., TANG, M. J., CHEN, Y. T., SHEN, F. C., LU, C. Y., TSAI, T. C. & WU, J. J. 2013. The enhancement of biofilm formation in Group B streptococcal isolates at vaginal pH. *Medical Microbiology and Immunology,* 202**,** 105-115.

HOEGY, F., MISLIN, G. L. A. & SCHALK, I. J. 2014. Pyoverdine and pyochelin measurements. *In:* FILLOUX, A. & RAMOS, J. L. (eds.) *Pseudomonas: Methods and Protocols.*

HONG, Y. Z., ZENG, J., WANG, X. H., DRLICA, K. & ZHAO, X. L. 2019. Post-stress bacterial cell death mediated by reactive oxygen species. *Proceedings of the National Academy of Sciences of the United States of America,* 116**,** 10064-10071.

HOREV, B., KLEIN, M. I., HWANG, G., LI, Y., KIM, D., KOO, H. & BENOIT, D. S. W. 2015. pH-activated nanoparticles for controlled topical delivery of farnesol to disrupt oral biofilm virulence. *ACS Nano,* 9**,** 2390-2404.

HOTTERBEEKX, A., KUMAR-SINGH, S., GOOSSENS, H. & MALHOTRA-KUMAR, S. 2017. *In vivo* and *in vitro* Interactions between *Pseudomonas aeruginosa* and *Staphylococcus spp*. *Frontiers in Cellular and Infection Microbiology,* 7**,** 1-13.

HU, D. F., LI, H., WANG, B. L., YE, Z., LEI, W. X., JIA, F., JIN, Q., REN, K. F. & JI, J. 2017. Surface-adaptive gold nanoparticles with effective adherence and enhanced photothermal ablation of methicillin-resistant *Staphylococcus aureus* biofilm. *ACS Nano,* 11**,** 9330-9339.

HUA, X., MARSHALL, M. J., XIONG, Y. J., MA, X., ZHOU, Y. F., TUCKER, A. E., ZHU, Z. H., LIU, S. Q. & YU, X. Y. 2015. Two-dimensional and three-dimensional dynamic imaging of live biofilms in a microchannel by time-of-flight secondary ion mass spectrometry. *Biomicrofluidics,* 9**,** 1-5.

HUANG, J. F., SONNLEITNER, E., REN, B., XU, Y. Q. & HAAS, D. 2012. Catabolite repression control of pyocyanin biosynthesis at an intersection of primary and secondary metabolism in *Pseudomonas aeruginosa*. *Applied and Environmental Microbiology,* 78**,** 5016-5020.

HUNTER, R. C. & BEVERIDGE, T. J. 2005. Application of a pH-sensitive fluoroprobe (C-SNARF-4) for pH microenvironment analysis in *Pseudomonas aeruginosa* biofilms. *Applied and Environmental Microbiology,* 71**,** 2501-2510.

JACKSON, K. D., STARKEY, M., KREMER, S., PARSEK, M. R. & WOZNIAK, D. J. 2004. Identification of *psl*, a locus encoding a potential exopolysaccharide that is essential for *Pseudomonas aeruginosa* PAO1 biofilm formation. *Journal of Bacteriology,* 186**,** 4466-4475.

JAMES, G. A., ZHAO, A. G., USUI, M., UNDERWOOD, R. A., NGUYEN, H., BEYENAL, H., PULCINI, E. D., HUNT, A. A., BERNSTEIN, H. C., FLECKMAN, P., OLERUD, J., WILLIAMSON, K. S., FRANKLIN, M. J. & STEWART, P. S. 2016. Microsensor and transcriptomic signatures of oxygen depletion in biofilms associated with chronic wounds. *Wound Repair and Regeneration,* 24**,** 373-383.

JAVANBAKHT, T., LAURENT, S., STANICKI, D. & WILKINSON, K. J. 2016. Relating the surface properties of superparamagnetic iron oxide nanoparticles (SPIONs) to their bactericidal effect towards a biofilm of *Streptococcus mutans*. *PLOS One,* 11**,** 1-13.

JENNINGS, L. K., STOREK, K. M., LEDVINA, H. E., COULON, C., MARMONT, L. S., SADOVSKAYA, I., SECOR, P. R., TSENG, B. S., SCIAN, M., FILLOUX, A., WOZNIAK, D. J., HOWELL, P. L. & PARSEK, M. R. 2015. Pel is a cationic exopolysaccharide that cross-links extracellular DNA in the *Pseudomonas aeruginosa* biofilm matrix. *Proceedings of the National Academy of Sciences of the United States of America,* 112**,** 11353-11358.

JEON, S. I., LEE, J. H., ANDRADE, J. D. & DE GENNES, P. G. 1991. Protein—surface interactions in the presence of polyethylene oxide. *Journal of Colloid and Interface Science,* 142**,** 149-158.

JEWELL, M. P., GALYEAN, A. A., HARRIS, J. K., ZEMANICK, E. T. & CASH, K. J. 2019. Luminescent nanosensors for ratiometric monitoring of three-dimensional oxygen gradients in laboratory and clinical *Pseudomonas aeruginosa* biofilms. *Applied and Environmental Microbiology,* 85**,** 1-12.

JEWELL, M. P., GREER, M. D., DAILEY, A. L. & CASH, K. J. 2020a. Triplet-triplet annihilation upconversion based nanosensors for fluorescence detection of potassium. *ACS Sensors,* 5**,** 474-480.

JEWELL, M. P., SACCOMANO, S. C., DAVID, A. A., HARRIS, J. K., ZEMANICK, E. T. & CASH, K. J. 2020b. Nanodiagnostics to monitor biofilm oxygen metabolism for antibiotic susceptibility testing. *Analyst,* 145**,** 3996-4003.

JO, J. Y., PRICE-WHELAN, A. & DIETRICH, L. E. P. 2014. An aerobic exercise: Defining the roles of *Pseudomonas aeruginosa* terminal oxidases. *Journal of Bacteriology,* 196**,** 4203-4205.

JONES, S. A., CHOWDHURY, F. Z., FABICH, A. J., ANDERSON, A., SCHREINER, D. M., HOUSE, A. L., AUTIERI, S. M., LEATHAM, M. P., LINS, J. J., JORGENSEN, M., COHEN, P. S. & CONWAY, T. 2007. Respiration of *Escherichia coli* in the mouse intestine. *Infection and Immunity,* 75**,** 4891-4899.

JUCKER, B. A., HARMS, H. & ZEHNDER, A. J. B. 1996. Adhesion of the positively charged bacterium *Stenotrophomonas* (*Xanthomonas*) *maltophilia* 70401 to glass and teflon. *Journal of Bacteriology,* 178**,** 5472-5479.

KAKUTA, H., IWAMI, Y., MAYANAGI, H. & TAKAHASHI, N. 2003. Xylitol inhibition of acid production and growth of *mutans streptococci* in the presence of various dietary sugars under strictly anaerobic conditions. *Caries Research,* 37**,** 404-409.

KANG, D., TURNER, K. E. & KIRIENKO, N. V. 2018. PqsA promotes pyoverdine production via biofilm formation. *Pathogens,* 7**,** 1-15.

KARATAN, E. & WATNICK, P. 2009. Signals, regulatory networks, and materials that build and break bacterial biofilms. *Microbiology and Molecular Biology Reviews,* 73**,** 310-347.

KARYGIANNI, L., HELLWIG, E. & AL-AHMAD, A. 2014. Multiplex fluorescence in situ hybridization (M-FISH) and confocal laser scanning microscopy (CLSM) to analyze multispecies oral biofilms. *Microbial Biofilms: Methods and Protocols,* 1147**,** 65-72.
KEAN, R., RAJENDRAN, R., HAGGARTY, J., TOWNSEND, E. M., SHORT, B., BURGESS, K. E., LANG, S., MILLINGTON, O., MACKAY, W. G., WILLIAMS, C. & RAMAGE, G. 2017. *Candida albicans* mycofilms support *Staphylococcus aureus* colonization and enhances miconazole resistance in dual-species interactions. *Frontiers in Microbiology,* 8**,** 1-11.
KIAMCO, M. M., ATCI, E., MOHAMED, A., CALL, D. R. & BEYENAL, H. 2017. Hyperosmotic agents and antibiotics affect dissolved oxygen and pH concentration gradients in *Staphylococcus aureus* biofilms. *Applied and Environmental Microbiology,* 83**,** 1-13.
KIM, H. D., YI, S. J. & KIM, K. C. 2015. Photo-bleaching characteristics of oxygen-sensitive particles. *Journal of Visualization,* 18**,** 321-333.
KIM, S. K. & LEE, J. H. 2016. Biofilm dispersion in *Pseudomonas aeruginosa*. *Journal of Microbiology,* 54**,** 71-85.
KLAUSEN, M., HEYDORN, A., RAGAS, P., LAMBERTSEN, L., AAES-JORGENSEN, A., MOLIN, S. & TOLKER-NIELSEN, T. 2003. Biofilm formation by *Pseudomonas aeruginosa* wild type, flagella and type IV pili mutants. *Molecular Microbiology,* 48**,** 1511-1524.
KLEIN, M. I., DEBAZ, L., AGIDI, S., LEE, H., XIE, G., LIN, A. H. M., HAMAKER, B. R., LEMOS, J. A. & KOO, H. 2010. Dynamics of *Streptococcus mutans* transcriptome in response to starch and sucrose during biofilm development. *PLOS One,* 5**,** 1-13.
KLEIN, M. I., DUARTE, S., XIAO, J., MITRA, S., FOSTER, T. H. & KOO, H. 2009. Structural and molecular basis of the role of starch and sucrose in *Streptococcus mutans* biofilm development. *Applied and Environmental Microbiology,* 75**,** 837-841.
KLEIN, M. I., HWANG, G., SANTOS, P. H. S., CAMPANELLA, O. H. & KOO, H. 2015. *Streptococcus mutans* derived extracellular matrix in cariogenic oral biofilms. *Frontiers in Cellular and Infection Microbiology,* 5.
KLOCKGETHER, J., MUNDER, A., NEUGEBAUER, J., DAVENPORT, C. F., STANKE, F., LARBIG, K. D., HEEB, S., SCHOCK, U., POHL, T. M., WIEHLMANN, L. & TUMMLER, B. 2010. Genome diversity of *Pseudomonas aeruginosa* PAO1 laboratory strains. *Journal of Bacteriology,* 192**,** 1113-1121.
KOLENBRANDER, P. E. 1993. Coaggregation of human oral bacteria - potential role in the accretion of dental plaque. *Journal of Applied Bacteriology,* 74**,** S79-S86.
KOLEWE, K. W., ZHU, J. X., MAKO, N. R., NONNENMANN, S. S. & SCHIFFMAN, J. D. 2018. Bacterial adhesion is affected by the thickness and stiffness of poly(ethylene glycol) hydrogels. *ACS Applied Materials & Interfaces,* 10**,** 2275-2281.
KOO, H., XIAO, J., KLEIN, M. I. & JEON, J. G. 2010. Exopolysaccharides produced by *Streptococcus mutans* glucosyltransferases modulate the establishment of microcolonies within multispecies biofilms. *Journal of Bacteriology,* 192**,** 3024-3032.
KOSTAKIOTI, M., HADJIFRANGISKOU, M. & HULTGREN, S. J. 2013. Bacterial biofilms: Development, dispersal, and therapeutic strategies in the dawn of the post-antibiotic era. *Cold Spring Harbor Perspectives in Medicine,* 3**,** 1-24.
KRAUSE, K. M., SERIO, A. W., KANE, T. R. & CONNOLLY, L. E. 2016. Aminoglycosides: An overview. *Cold Spring Harbor Perspectives in Medicine,* 6**,** 1-19.
KRETH, J., HAGERMAN, E., TAM, K., MERRITT, J., WONG, D., WU, B. & QI, F. 2004. Quantitative analyses of *Streptococcus mutans* biofilms with quartz crystal microbalance, microjet impingement and confocal microscopy. *Biofilms,* 1**,** 277-284.
KRZYSCIAK, W., JURCZAK, A., KOSCIELNIAK, D., BYSTROWSKA, B. & SKALNIAK, A. 2014. The virulence of *Streptococcus mutans* and the ability to form biofilms. *European Journal of Clinical Microbiology & Infectious Diseases,* 33**,** 499-515.
KUMAR, C. G. & ANAND, S. K. 1998. Significance of microbial biofilms in food industry: A review. *International Journal of Food Microbiology,* 42**,** 9-27.
LAITALA, M., ALANEN, P., ISOKANGAS, P., SODERLING, E. & PIENIHAKKINEN, K. 2012. A cohort study on the association of early *mutans streptococci* colonisation and dental decay. *Caries Research,* 46**,** 228-233.

LAITALA, M. L., ALANEN, P., ISOKANGAS, P., SODERLING, E. & PIENIHAKKINEN, K. 2013. Long-term effects of maternal prevention on children's dental decay and need for restorative treatment. *Community Dentistry and Oral Epidemiology,* 41**,** 534-540.

LANGLEY, S. & BEVERIDGE, T. J. 1999. Effect of O-side-chain-lipopolysaccharide chemistry on metal binding. *Applied and Environmental Microbiology,* 65**,** 489-498.

LAU, G. W., HASSETT, D. J., RAN, H. M. & KONG, F. S. 2004. The role of pyocyanin in *Pseudomonas aeruginosa* infection. *Trends in Molecular Medicine,* 10**,** 599-606.

LAVADO, A. S., CHAUHAN, V. M., ZEN, A. A., GIUNTINI, F., JONES, D. R. E., BOYLE, R. W., BEEBY, A., CHAN, W. C. & AYLOTT, J. W. 2015. Controlled intracellular generation of reactive oxygen species in human mesenchymal stem cells using porphyrin conjugated nanoparticles. *Nanoscale,* 7**,** 14525-14531.

LENZ, A. P., WILLIAMSON, K. S., PITTS, B., STEWART, P. S. & FRANKLIN, M. J. 2008. Localized gene expression in *Pseudomonas aeruginosa* Biofilms. *Applied and Environmental Microbiology,* 74**,** 4463-4471.

LI, J., HELMERHORST, E. J., LEONE, C. W., TROXLER, R. F., YASKELL, T., HAFFAJEE, A. D., SOCRANSKY, S. S. & OPPENHEIM, F. G. 2004. Identification of early microbial colonizers in human dental biofilm. *Journal of Applied Microbiology,* 97**,** 1311-1318.

LI, J. H., ZHANG, K. X., RUAN, L., CHIN, S. F., WICKRAMASINGHE, N., LIU, H. B., RAVIKUMAR, V., REN, J. H., DUAN, H. W., YANG, L. & CHAN-PARK, M. B. 2018. Block copolymer nanoparticles remove biofilms of drug-resistant Gram-positive bacteria by nanoscale bacterial debridement. *Nano Letters,* 18**,** 4180-4187.

LI, L. N., GUO, L. H., LUX, R., ECKERT, R., YARBROUGH, D., HE, J. A., ANDERSON, M. & SHI, W. Y. 2010. Targeted antimicrobial therapy against *Streptococcus mutans* establishes protective non-cariogenic oral biofilms and reduces subsequent infection. *International Journal of Oral Science,* 2**,** 66-73.

LIANG, P. D., FANG, X., HU, Y. Y., YUAN, M., RABA, D. A., DING, J., BUNN, D. C., SANJANA, K., YANG, J., ROSAS-LEMUS, M., HASE, C. C., TUZ, K. & JUAREZ, O. 2020. The aerobic respiratory chain of *Pseudomonas aeruginosa* cultured in artificial urine media: Role of NQR and terminal oxidases. *PLOS One,* 15**,** 1-20.

LIMOLI, D. H., WHITFIELD, G. B., KITAO, T., IVEY, M. L., DAVIS, M. R., GRAHL, N., HOGAN, D. A., RAHME, L. G., HOWELL, P. L., O'TOOLE, G. A. & GOLDBERG, J. B. 2017. *Pseudomonas aeruginosa* alginate overproduction promotes coexistence with *Staphylococcus aureus* in a model of cystic fibrosis respiratory infection. *mBio,* 8**,** 1-18.

LIN, J. S., CHENG, J. L., WANG, Y. & SHEN, X. H. 2018. The Pseudomonas Quinolone Signal (PQS): Not just for quorum sensing anymore. *Frontiers in Cellular and Infection Microbiology,* 8**,** 1-9.

LINGSTROM, P., IMFELD, T. & BIRKHED, D. 1993. Comparison of three different methods for measurement of plaque-pH in humans after consumption of soft bread and potato chips. *Journal of Dental Research,* 72**,** 865-70.

LU, C. D., WINTELER, H., ABDELAL, A. & HAAS, D. 1999. The ArgR regulatory protein, a helper to the anaerobic regulator ANR during transcriptional activation of the arcD promoter in *Pseudomonas aeruginosa*. *Journal of Bacteriology,* 181**,** 2459-2464.

LU, C. D., YANG, Z. & LI, W. 2004. Transcriptome analysis of the ArgR regulon in *Pseudomonas aeruginosa*. *Journal of Bacteriology,* 186**,** 3855-3861.

LUCKETT, J. C. A., DARCH, O., WATTERS, C., ABUOUN, M., WRIGHT, V., PAREDES-OSSES, E., WARD, J., GOTO, H., HEEB, S., POMMIER, S., RUMBAUGH, K. P., CAMARA, M. & HARDIE, K. R. 2012. A novel virulence strategy for *Pseudomonas aeruginosa* mediated by an autotransporter with arginine-specific aminopeptidase activity. *PLOS Pathogens,* 8**,** 1-21.

LUO, Z., YUE, S., CHEN, T., SHE, P. F. & WU, Y. 2020. Reduced growth of *Staphylococcus aureus* under high glucose conditions is associated with decreased pentaglycine expression. *Frontiers in Microbiology,* 11**,** 1-11.

LYNCH, D. J., FOUNTAIN, T. L., MAZURKIEWICZ, J. E. & BANAS, J. A. 2007. Glucan-binding proteins are essential for shaping *Streptococcus mutans* biofilm architecture. *FEMS Microbiology Letters* 268**,** 158-165.

MAAN, A. M. C., HOFMAN, A. H., DE VOS, W. M. & KAMPERMAN, M. 2020. Recent developments and practical feasibility of polymer-based antifouling coatings. *Advanced Functional Materials,* 30**,** 1-30.
MAHON, M. J. 2011. pHluorin2: an enhanced, ratiometric, pH-sensitive green florescent protein. *Advances in Bioscience and Biotechnology,* 02**,** 132-137.
MAKIN, S. A. & BEVERIDGE, T. J. 1996. The influence of A-band and B-band lipopolysaccharide on the surface characteristics and adhesion of *Pseudomonas aeruginosa* to surfaces. *Microbiology-Uk,* 142**,** 299-307.
MANIA-PRAMANIK, J., KERKAR, S. C., MEHTA, P. B., POTDAR, S. & SALVI, V. S. 2008. Use of vaginal pH in diagnosis of infections and its association with reproductive manifestations. *Journal of Clinical Laboratory Analysis,* 22**,** 375-379.
MARSH, L. H., COKE, M., DETTMAR, P. W., EWEN, R. J., HAVLER, M., NEVELL, T. G., SMART, J. D., SMITH, J. R., TIMMINS, B., TSIBOUKLIS, J. & ALEXANDER, C. 2002. Adsorbed poly(ethyleneoxide)-poly(propyleneoxide) copolymers on synthetic surfaces: Spectroscopy and microscopy of polymer structures and effects on adhesion of skin-borne bacteria. *Journal of Biomedical Materials Research,* 61**,** 641-652.
MASYUKO, R. N., LANNI, E. J., DRISCOLL, C. M., SHROUT, J. D., SWEEDLER, J. V. & BOHN, P. W. 2014. Spatial organization of *Pseudomonas aeruginosa* biofilms probed by combined matrix-assisted Laser desorption ionization mass spectrometry and confocal Raman microscopy. *Analyst,* 139**,** 5700-5708.
MAULINE, L., GRESSIER, M., ROQUES, C., HAMMER, P., RIBEIRO, S. J. L., CAIUT, J. M. A. & MENU, M. J. 2013. Bifunctional silica nanoparticles for the exploration of biofilms of *Pseudomonas aeruginosa*. *Biofouling,* 29**,** 775-788.
MCBEE, M. E., CHIONH, Y. H., SHARAF, M. L., HO, P. Y., CAI, M. W. L. & DEDON, P. C. 2017. Production of superoxide in bacteria is stress- and cell state-dependent: A gating-optimized flow cytometry method that minimizes ROS measurement artifacts with fluorescent dyes. *Frontiers in Microbiology,* 8**,** 1-17.
MCLEAN, J. S., MAJORS, P. D., REARDON, C. L., BILSKIS, C. L., REED, S. B., ROMINE, M. F. & FREDRICKSON, J. K. 2008. Investigations of structure and metabolism within *Shewanella oneidensis* MR-1 biofilms. *Journal of Microbiological Methods,* 74**,** 47-56.
MIEHER, J. L., LARSON, M. R., SCHORMANN, N., PURUSHOTHAM, S., WU, R., RAJASHANKAR, K. R., WU, H. & DEIVANAYAGAM, C. 2018. Glucan Binding Protein C of *Streptococcus mutans* mediates both sucrose-independent and sucrose-dependent adherence. *Infection and Immunity,* 86**,** 1-18.
MIESENBOCK, G., DE ANGELIS, D. A. & ROTHMAN, J. E. 1998. Visualizing secretion and synaptic transmission with pH-sensitive green fluorescent proteins. *Nature,* 394**,** 192-195.
MIKKELSEN, H., SIVANESON, M. & FILLOUX, A. 2011. Key two-component regulatory systems that control biofilm formation in *Pseudomonas aeruginosa*. *Environmental Microbiology,* 13**,** 1666-1681.
MIYASAWA, H., IWAMI, Y., MAYANAGI, H. & TAKAHASHI, N. 2003. Xylitol inhibition of anaerobic acid production by *Streptococcus mutans* at various pH levels. *Oral Microbiology and Immunology,* 18**,** 215-219.
MOREAU-MARQUIS, S., STANTON, B. A. & O'TOOLE, G. A. 2008. *Pseudomonas aeruginosa* biofilm formation in the cystic fibrosis airway. *Pulmonary Pharmacology & Therapeutics,* 21**,** 595-599.
MORIARTY, T. F., ELBORN, J. S. & TUNNEY, M. M. 2007. Effect of pH on the antimicrobial susceptibility of planktonic and biofilm-grown clinical *Pseudomonas aeruginosa* isolates. *British Journal of Biomedical Science,* 64**,** 101-104.
MOYE, Z. D., ZENG, L. & BURNE, R. A. 2014. Fueling the caries process: carbohydrate metabolism and gene regulation by *Streptococcus mutans*. *Journal of Oral Microbiology,* 6**,** 1-15.
MULCAHY, H., CHARRON-MAZENOD, L. & LEWENZA, S. 2008. Extracellular DNA chelates cations and induces antibiotic resistance in *Pseudomonas aeruginosa* biofilms. *PLOS Pathogens,* 4**,** 1-12.

MUNK, S., JOHANSEN, C., STAHNKE, L. H. & ADLER-NISSEN, J. 2001. Microbial survival and odor in laundry. *Journal of Surfactants and Detergents,* 4**,** 385-394.
MURAS, A., MALLO, N., OTERO-CASAL, P., POSE-RODRIGUEZ, J. M. & OTERO, A. 2020. Quorum sensing systems as a new target to prevent biofilm-related oral diseases. *Oral Diseases***,** 1-7.
MURPHY, K., PARK, A. J., HAO, Y., BREWER, D., LAM, J. S. & KHURSIGARA, C. M. 2014. Influence of O polysaccharides on biofilm development and outer membrane vesicle biogenesis in *Pseudomonas aeruginosa* PAO1. *Journal of Bacteriology,* 196**,** 1306-1317.
NEJADNIK, M. R., VAN DER MEI, H. C., NORDE, W. & BUSSCHER, H. J. 2008. Bacterial adhesion and growth on a polymer brush-coating. *Biomaterials,* 29**,** 4117-4121.
NIELSEN, A. T., TOLKER-NIELSEN, T., BARKEN, K. B. & MOLIN, S. 2000. Role of commensal relationships on the spatial structure of a surface-attached microbial consortium. *Environmental Microbiology,* 2**,** 59-68.
NOTO, M. J., BURNS, W. J., BEAVERS, W. N. & SKAAR, E. P. 2017. Mechanisms of pyocyanin toxicity and genetic determinants of resistance in *Staphylococcus aureus*. *Journal of Bacteriology,* 199**,** 1-13.
O'CONNOR, S. M., GEHRKE, S. H. & RETZINGER, G. S. 1999. Ordering of poly(ethylene oxide)/poly(propylene oxide) triblock copolymers in condensed films. *Langmuir,* 15**,** 2580-2585.
O'TOOLE, G. A., GIBBS, K. A., HAGER, P. W., PHIBBS, P. V. & KOLTER, R. 2000. The global carbon metabolism regulator Crc is a component of a signal transduction pathway required for biofilm development by *Pseudomonas aeruginosa*. *Journal of Bacteriology,* 182**,** 425-431.
O'TOOLE, G. A. & KOLTER, R. 1998. Flagellar and twitching motility are necessary for *Pseudomonas aeruginosa* biofilm development. *Molecular Microbiology,* 30**,** 295-304.
ORGAD, O., OREN, Y., WALKER, S. L. & HERZBERG, M. 2011. The role of alginate in *Pseudomonas aeruginosa* EPS adherence, viscoelastic properties and cell attachment. *Biofouling,* 27**,** 787-798.
OZCELIK, B., HO, K. K. K., GLATTAUER, V., WILLCOX, M., KUMAR, N. & THISSEN, H. 2017. Poly(ethylene glycol)-based coatings combining low-biofouling and quorum-sensing inhibiting properties to reduce bacterial colonization. *ACS Biomaterials Science & Engineering,* 3**,** 78-87.
PALLETT, R., LESLIE, L. J., LAMBERT, P. A., MILIC, I., DEVITT, A. & MARSHALL, L. J. 2019. Anaerobiosis influences virulence properties of *Pseudomonas aeruginosa* cystic fibrosis isolates and the interaction with *Staphylococcus aureus*. *Scientific Reports,* 9**,** 1-18.
PARKINS, M. D., CERI, H. & STOREY, D. G. 2001. *Pseudomonas aeruginosa* GacA, a factor in multihost virulence, is also essential for biofilm formation. *Molecular Microbiology,* 40**,** 1215-1226.
PARSEK, M. R. & TOLKER-NIELSEN, T. 2008. Pattern formation in *Pseudomonas aeruginosa* biofilms. *Current Opinion in Microbiology,* 11**,** 560-566.
PASSERINI, L., LAM, K., COSTERTON, J. W. & KING, E. G. 1992. Biofilms on indwelling vascular catheters. *Critical Care Medicine,* 20**,** 665-73.
PAULINO, T. P., CARDOSO, M., BRUSCHI-THEDEI, G. C. M., CIANCAGLINI, P. & THEDEI, G. 2003. Fermentable and non-fermentable sugars - A simple experiment of anaerobic metabolism. *Biochemistry and Molecular Biology Education,* 31**,** 180-184.
PEDERSEN, S. S., HOIBY, N., ESPERSEN, F. & KOCH, C. 1992. Role of alginate in infection with mucoid *Pseudomonas aeruginos*a in cystic-fibrosis. *Thorax,* 47**,** 6-13.
PEDRAZA, M. C. C., NOVAIS, T. F., FAUSTOFERRI, R. C., QUIVEY, R. G., TEREKHOV, A., HAMAKER, B. R. & KLEIN, M. I. 2017. Extracellular DNA and lipoteichoic acids interact with exopolysaccharides in the extracellular matrix of *Streptococcus mutans* biofilms. *Biofouling,* 33**,** 722-740.
PEREZ-ROLDAN, M. J., DEBARNOT, D. & PONCIN-EPAILLARD, F. 2014. Surface chemistry of PET for enhancing its antifouling properties. *RSC Advances,* 4**,** 64006-64013.

PERIASAMY, S., CHALMERS, N. I., DU-THUMM, L. & KOLENBRANDER, P. E. 2009. *Fusobacterium nucleatum* ATCC 10953 requires *Actinomyces naeslundii* ATCC 43146 for growth on saliva in a three-species community that includes *Streptococcus oralis* 34. *Applied and Environmental Microbiology,* 75**,** 3250-3257.

PERIASAMY, S. & KOLENBRANDER, P. E. 2009. *Aggregatibacter actinomycetemcomitans* builds mutualistic biofilm communities with *Fusobacterium nucleatum* and *Veillonella* species in saliva. *Infection and Immunity,* 77**,** 3542-3551.

PERIASAMY, S. & KOLENBRANDER, P. E. 2010. Central role of the early colonizer *Veillonella spp.* in establishing multispecies biofilm communities with initial, middle, and late colonizers of enamel. *Journal of Bacteriology,* 192**,** 2965-2972.

PEULEN, T. O. & WILKINSON, K. J. 2011. Diffusion of nanoparticles in a biofilm. *Environmental Science & Technology,* 45**,** 3367-3373.

PRIME, K. L. & WHITESIDES, G. M. 1991. Self-assembled organic monolayers - model systems for studying adsorption of proteins at surfaces. *Science,* 252**,** 1164-1167.

PRIME, K. L. & WHITESIDES, G. M. 1993. Adsorption of proteins onto surfaces containing end-attached oligo(ethylene oxide) - a model system using self-assembled monolayers. *Journal of the American Chemical Society,* 115**,** 10714-10721.

RADLINSKI, L. C., ROWE, S. E., BRZOZOWSKI, R., WILKINSON, A. D., HUANG, R., ESWARA, P. & CONLON, B. P. 2019. Chemical induction of aminoglycoside uptake overcomes antibiotic tolerance and resistance in *Staphylococcus aureus*. *Cell Chemical Biology,* 26**,** 1355-1364.

RAMSEY, M. M. & WHITELEY, M. 2004. *Pseudomonas aeruginosa* attachment and biofilm development in dynamic environments. *Molecular Microbiology,* 53**,** 1075-1087.

RAZATOS, A., ONG, Y. L., BOULAY, F., ELBERT, D. L., HUBBELL, J. A., SHARMA, M. M. & GEORGIOU, G. 2000. Force measurements between bacteria and poly(ethylene glycol)-coated surfaces. *Langmuir,* 16**,** 9155-9158.

REICHHARDT, C., WONG, C., DA SILVA, D. P., WOZNIAK, D. J. & PARSEK, M. R. 2018. CdrA interactions within the *Pseudomonas aeruginos*a biofilm matrix safeguard it from proteolysis and promote cellular packing. *mBio,* 9**,** 1-12.

REIFENRATH, M. & BOLES, E. 2018. A superfolder variant of pH-sensitive pHluorin for i*n vivo* pH measurements in the endoplasmic reticulum. *Scientific Reports,* 8**,** 1-8.

REVSBECH, N. P. 2005. Analysis of microbial communities with electrochemical microsensors and microscale biosensors. *Environmental Microbiology,* 397**,** 147-166.

ROJO, F. 2010. Carbon catabolite repression in *Pseudomonas*: optimizing metabolic versatility and interactions with the environment. *FEMS Microbiology Reviews,* 34**,** 658-684.

ROLLA, G., OPPERMANN, R. V., BOWEN, W. H., CIARDI, J. E. & KNOX, K. W. 1980. High amounts of lipoteichoic acid in sucrose-induced plaque *in vivo*. *Caries Research,* 14**,** 235-238.

RONG, X. & KISAALITA, W. S. 1998. Fluorescent *Pseudomonad* pyoverdines bind and oxidize ferrous ion. *Applied and Environmental Microbiology,* 64**,** 1472-1476.

ROOSJEN, A., VAN DER MEI, H. C., BUSSCHER, H. J. & NORDE, W. 2004. Microbial adhesion to poly(ethylene oxide) brushes: Influence of polymer chain length and temperature. *Langmuir,* 20**,** 10949-10955.

RUHAL, R., ANTTI, H., RZHEPISHEVSKA, O., BOULANGER, N., BARBERO, D. R., WAI, S. N., UHLIN, B. E. & RAMSTEDT, M. 2015. A multivariate approach to correlate bacterial surface properties to biofilm formation by lipopolysaccharide mutants of *Pseudomonas aeruginosa*. *Colloids and Surfaces B: Biointerfaces,* 127**,** 182-191.

RUMBAUGH, K. P. & SAUER, K. 2020. Biofilm dispersion. *Nature Reviews Microbiology,* 18**,** 571-586.

RYBTKE, M., HULTQVIST, L. D., GIVSKOV, M. & TOLKER-NIELSEN, T. 2015. *Pseudomonas aeruginosa* biofilm infections: Community structure, antimicrobial tolerance and immune response. *Journal of Molecular Biology,* 427**,** 3628-3645.

RYDER, C., BYRD, M. & WOZNIAK, D. J. 2007. Role of polysaccharides in *Pseudomonas aeruginosa* biofilm development. *Current Opinion in Microbiology,* 10**,** 644-648.

SABRA, W., KIM, E. J. & ZENG, A. P. 2002. Physiological responses of *Pseudomonas aeruginosa* PAO1 to oxidative stress in controlled microaerobic and aerobic cultures. *Microbiology-Sgm,* 148**,** 3195-3202.
SALLI, K. M., FORSSTEN, S. D., LAHTINEN, S. J. & OUWEHAND, A. C. 2016. Influence of sucrose and xylitol on an early *Streptococcus mutans* biofilm in a dental simulator. *Archives of Oral Biology,* 70**,** 39-46.
SALLI, K. M. & OUWEHAND, A. C. 2015. The use of *in vitro* model systems to study dental biofilms associated with caries: a short review. *Journal of Oral Microbiology,* 7**,** 1-7.
SAUER, K., CAMPER, A. K., EHRLICH, G. D., COSTERTON, J. W. & DAVIES, D. G. 2002. *Pseudomonas aeruginosa* displays multiple phenotypes during development as a biofilm. *Journal of Bacteriology,* 184**,** 1140-1154.
SCANNAPIECO, F. A. 1994. Saliva-bacterium interactions in oral microbial ecology. *Critical Reviews in Oral Biology & Medicine,* 5**,** 203-248.
SCANNAPIECO, F. A., TORRES, G. I. & LEVINE, M. J. 1995. Salivary amylase promotes adhesion of oral *Streptococci* to hydroxyapatite. *Journal of Dental Research,* 74**,** 1360-1366.
SCHACHTELE, C. F. & JENSEN, M. E. 1982. Comparison of methods for monitoring changes in the pH of human dental plaque. *Journal of Dental Research,* 61**,** 1117-25.
SCHARNOW, A. M., SOLINSKI, A. E. & WUEST, W. M. 2019. Targeting *Streptococcus mutans* biofilms: a perspective on preventing dental caries. *MedChemComm,* 10**,** 1057-1067.
SCHERTZER, J. W., BROWN, S. A. & WHITELEY, M. 2010. Oxygen levels rapidly modulate *Pseudomonas aeruginosa* social behaviours via substrate limitation of PqsH. *Molecular Microbiology,* 77**,** 1527-1538.
SCHLAFER, S. & DIGE, I. 2016. Ratiometric imaging of extracellular pH in dental biofilms. *Jove-Journal of Visualized Experiments***,** 1-7.
SCHLAFER, S., GARCIA, J. E., GREVE, M., RAARUP, M. K., NYVAD, B. & DIGE, I. 2015. Ratiometric imaging of extracellular pH in bacterial biofilms with C-SNARF-4. *Applied and Environmental Microbiology,* 81**,** 1267-1273.
SCHLAFER, S., RAARUP, M. K., MEYER, R. L., SUTHERLAND, D. S., DIGE, I., NYENGAARD, J. R. & NYVAD, B. 2011. pH landscapes in a novel five-species model of early dental biofilm. *PLOS One,* 6**,** 1-11.
SELWITZ, R. H., ISMAIL, A. I. & PITTS, N. B. 2007. Dental caries. *Lancet,* 369**,** 51-59.
SEN, C. K. 2009. Wound healing essentials: Let there be oxygen. *Wound Repair and Regeneration,* 17**,** 1-18.
SHARMA, G., RAO, S., BANSAL, A., DANG, S., GUPTA, S. & GABRANI, R. 2014. *Pseudomonas aeruginosa* biofilm: Potential therapeutic targets. *Biologicals,* 42**,** 1-7.
SHEPHARD, J., MCQUILLAN, A. J. & BREMER, P. J. 2008. Mechanisms of cation exchange by *Pseudomonas aeruginosa* PAO1 and PAO1 wbpL, a strain with a truncated lipopolysaccharide. *Applied and Environmental Microbiology,* 74**,** 6980-6986.
SHEPHARD, J. J., SAVORY, D. M., BREMER, P. J. & MCQUILLAN, A. J. 2010. Salt modulates bacterial hydrophobicity and charge properties influencing adhesion of *Pseudomonas aeruginosa* (PA01) in aqueous suspensions. *Langmuir,* 26**,** 8659-8665.
SINGH, N., ROMERO, M., TRAVANUT, A., MONTEIRO, P. F., JORDANA-LLUCH, E., HARDIE, K. R., WILLIAMS, P., ALEXANDER, M. R. & ALEXANDER, C. 2019. Dual bioresponsive antibiotic and quorum sensing inhibitor combination nanoparticles for treatment of *Pseudomonas aeruginosa* biofilms *in vitro* and *ex vivo*. *Biomaterials Science,* 7**,** 4099-4111.
SJOBERG, B. M. & TORRENTS, E. 2011. Shift in ribonucleotide reductase gene expression in *Pseudomonas aeruginosa* during Infection. *Infection and Immunity,* 79**,** 2663-2669.
SOSNIN, E. A., ZHDANOVA, O. S., KASHAPOVA, E. R. & ARTYUKHOV, V. Y. 2014. Pyoverdine as a fluorescent marker of antibiotic sensitivity of *Pseudomonas aeruginosa*. *Optics and Spectroscopy,* 117**,** 1018-1024.

SOUZA, J. G. S., BERTOLINI, M., THOMPSON, A., MANSFIELD, J. M., GRASSMANN, A. A., MAAS, K., CAIMANO, M. J., BARAO, V. A. R., VICKERMAN, M. M. & DONGARI-BAGTZOGLOU, A. 2020. Role of glucosyltransferase R in biofilm interactions between *Streptococcus oralis* and *Candida albicans*. *Isme Journal,* 14**,** 1207-1222.

STACY, A., EVERETT, J., JORTH, P., TRIVEDI, U., RUMBAUGH, K. P. & WHITELEY, M. 2014. Bacterial fight-and-flight responses enhance virulence in a polymicrobial infection. *Proceedings of the National Academy of Sciences of the United States of America,* 111**,** 7819-7824.

STACY, A., FLEMING, D., LAMONT, R. J., RUMBAUGH, K. P. & WHITELEY, M. 2016. A commensal bacterium promotes virulence of an opportunistic pathogen via cross-respiration. *mBio,* 7**,** 1-10.

STEWART, P. S. & FRANKLIN, M. J. 2008. Physiological heterogeneity in biofilms. *Nature Reviews Microbiology,* 6**,** 199-210.

STIRPE, M., BRUGNOLI, B., DONELLI, G., FRANCOLINI, I. & VUOTTO, C. 2020. Poloxamer 338 affects cell adhesion and biofilm formation in *Escherichia coli*: Potential applications in the management of catheter-associated urinary tract infections. *Pathogens,* 9**,** 1-16.

STOODLEY, P., DEBEER, D. & LAPPINSCOTT, H. M. 1997. Influence of electric fields and pH on biofilm structure as related to the bioelectric effect. *Antimicrobial Agents and Chemotherapy,* 41**,** 1876-1879.

STOVER, C. K., PHAM, X. Q., ERWIN, A. L., MIZOGUCHI, S. D., WARRENER, P., HICKEY, M. J., BRINKMAN, F. S. L., HUFNAGLE, W. O., KOWALIK, D. J., LAGROU, M., GARBER, R. L., GOLTRY, L., TOLENTINO, E., WESTBROCK-WADMAN, S., YUAN, Y., BRODY, L. L., COULTER, S. N., FOLGER, K. R., KAS, A., LARBIG, K., LIM, R., SMITH, K., SPENCER, D., WONG, G. K. S., WU, Z., PAULSEN, I. T., REIZER, J., SAIER, M. H., HANCOCK, R. E. W., LORY, S. & OLSON, M. V. 2000. Complete genome sequence of *Pseudomonas aeruginosa* PAO1, an opportunistic pathogen. *Nature,* 406**,** 959-964.

SUN, H. H., ANDRESEN, T. L., BENJAMINSEN, R. V. & ALMDAL, K. 2009. Polymeric nanosensors for measuring the full dynamic pH range of endosomes and lysosomes in mammalian cells. *Journal of Biomedical Nanotechnology,* 5**,** 676-682.

SUN, W. C., GEE, K. R., KLAUBERT, D. H. & HAUGLAND, R. P. 1997. Synthesis of fluorinated fluoresceins. *Journal of Organic Chemistry,* 62**,** 6469-6475.

SUTHERLAND, I. W. 2001. The biofilm matrix - an immobilized but dynamic microbial environment. *Trends in Microbiology,* 9**,** 222-227.

TAKAHASHI, N. & NYVAD, B. 2011. The role of bacteria in the caries process: Ecological perspectives. *Journal of Dental Research,* 90**,** 294-303.

TAKAHASHI, N. & WASHIO, J. 2011. Metabolomic effects of xylitol and fluoride on plaque biofilm *in vivo*. *Journal of Dental Research,* 90**,** 1463-1468.

TATE, S., MACGREGOR, G., DAVIS, M., INNES, J. A. & GREENING, A. P. 2002. Airways in cystic fibrosis are acidified: detection by exhaled breath condensate. *Thorax,* 57**,** 926-929.

TAUHARDT, L., FRANT, M., PRETZEL, D., HARTLIEB, M., BUCHER, C., HILDEBRAND, G., SCHROTER, B., WEBER, C., KEMPE, K., GOTTSCHALDT, M., LIEFEITH, K. & SCHUBERT, U. S. 2014. Amine end-functionalized poly(2-ethyl-2-oxazoline) as promising coating material for antifouling applications. *Journal of Materials Chemistry B,* 2**,** 4883-4893.

THIERBACH, S., WIENHOLD, M., FETZNER, S. & HENNECKE, U. 2019. Synthesis and biological activity of methylated derivatives of the *Pseudomonas* metabolites HHQ, HQNO and PQS. *Beilstein Journal of Organic Chemistry,* 15**,** 187-193.

TOYOFUKU, M., NOMURA, N., KUNO, E., TASHIRO, Y., NAKAJIMA, T. & UCHIYAMA, I. 2008. Influence of the Pseudomonas Quinolone Signal on denitrification in *Pseudomonas aeruginosa*. *Journal of Bacteriology,* 190**,** 7947-7956.

TSENG, B. S., ZHANG, W., HARRISON, J. J., QUACH, T. P., SONG, J. L., PENTERMAN, J., SINGH, P. K., CHOPP, D. L., PACKMAN, A. I. & PARSEK, M. R. 2013. The extracellular matrix protects *Pseudomonas aeruginosa* biofilms by limiting the penetration of tobramycin. *Environmental Microbiology,* 15**,** 2865-2878.

TURNBULL, L., TOYOFUKU, M., HYNEN, A. L., KUROSAWA, M., PESSI, G., PETTY, N. K., OSVATH, S. R., CARCAMO-OYARCE, G., GLOAG, E. S., SHIMONI, R., OMASITS, U., ITO, S., YAP, X., MONAHAN, L. G., CAVALIERE, R., AHRENS, C. H., CHARLES, I. G., NOMURA, N., EBERL, L. & WHITCHURCH, C. B. 2016. Explosive cell lysis as a mechanism for the biogenesis of bacterial membrane vesicles and biofilms. *Nature Communications,* 7**,** 1-13.

TUSON, H. H. & WEIBEL, D. B. 2013. Bacteria-surface interactions. *Soft Matter,* 9**,** 4368-4380.

TYLER, B. J., HOOK, A., PELSTER, A., WILLIAMS, P., ALEXANDER, M. & ARLINGHAUS, H. F. 2017. Development and characterization of a stable adhesive bond between a poly(dimethylsiloxane) catheter material and a bacterial biofilm resistant acrylate polymer coating. *Biointerphases,* 12**,** 1-12.

UNDEN, G., BECKER, S., BONGAERTS, J., SCHIRAWSKI, J. & SIX, S. 1994. Oxygen-regulated gene-expression in facultatively anaerobic-bacteria. *Antonie Van Leeuwenhoek International Journal of General and Molecular Microbiology,* 66**,** 3-22.

URIBE-ALVAREZ, C., CHIQUETE-FELIX, N., CONTRERAS-ZENTELLA, M., GUERRERO-CASTILLO, S., PENA, A. & URIBE-CARVAJAL, S. 2016. *Staphylococcus epidermidis*: metabolic adaptation and biofilm formation in response to different oxygen concentrations. *Pathogens and Disease,* 74**,** 1-15.

VACCA-SMITH, A. M., VENKITARAMAN, A. R., QUIVEY, R. G. & BOWEN, W. H. 1996. Interactions of streptococcal glucosyltransferases with α-amylase and starch on the surface of saliva-coated hydroxyapatite. *Archives of Oral Biology,* 41**,** 291-298.

VAN ALST, N. E., PICARDO, K. F., IGLEWSKI, B. H. & HAIDARIS, C. G. 2007. Nitrate sensing and metabolism modulate motility, biofilm formation, and virulence in *Pseudomonas aeruginosa*. *Infection and Immunity,* 75**,** 3780-3790.

VANDERWAL, A., NORDE, W., ZEHNDER, A. J. B. & LYKLEMA, J. 1997. Determination of the total charge in the cell walls of Gram-positive bacteria. *Colloids and Surfaces B: Biointerfaces,* 9**,** 81-100.

VANDERWAUVEN, C., PIERARD, A., KLEYRAYMANN, M. & HAAS, D. 1984. *Pseudomonas aeruginosa* mutants affected in anaerobic growth on arginine - evidence for a 4-gene cluster encoding the arginine deiminase pathway. *Journal of Bacteriology,* 160**,** 928-934.

VIGEANT, M. A. S., FORD, R. M., WAGNER, M. & TAMM, L. K. 2002. Reversible and irreversible adhesion of motile *Escherichia coli* cells analyzed by total internal reflection aqueous fluorescence microscopy. *Applied and Environmental Microbiology,* 68**,** 2794-2801.

VON OHLE, C., GIESEKE, A., NISTICO, L., DECKER, E. M., DEBEER, D. & STOODLEY, P. 2010. Real-time microsensor measurement of local metabolic activities in *ex vivo* dental biofilms exposed to sucrose and treated with chlorhexidine. *Applied and Environmental Microbiology,* 76**,** 2326-2334.

VROOM, J. M., DE GRAUW, K. J., GERRITSEN, H. C., BRADSHAW, D. J., MARSH, P. D., WATSON, G. K., BIRMINGHAM, J. J. & ALLISON, C. 1999. Depth penetration and detection of pH gradients in biofilms by two-photon excitation microscopy. *Applied and Environmental Microbiology,* 65**,** 3502-3511.

WALTERS, M. C., ROE, F., BUGNICOURT, A., FRANKLIN, M. J. & STEWART, P. S. 2003. Contributions of antibiotic penetration, oxygen limitation, and low metabolic activity to tolerance of *Pseudomonas aeruginosa* biofilms to ciprofloxacin and tobramycin. *Antimicrobial Agents and Chemotherapy,* 47**,** 317-323.

WATERS, M. S., KUNDU, S., LIN, N. J. & LIN-GIBSON, S. 2014. Microstructure and mechanical properties of *in situ Streptococcus mutans* biofilms. *ACS Applied Materials & Interfaces,* 6**,** 327-332.

WEBB, J. S., THOMPSON, L. S., JAMES, S., CHARLTON, T., TOLKER-NIELSEN, T., KOCH, B., GIVSKOV, M. & KJELLEBERG, S. 2003. Cell death in *Pseudomonas aeruginosa* biofilm development. *Journal of Bacteriology,* 185**,** 4585-4592.

WEI, Q. & MA, L. Y. Z. 2013. Biofilm matrix and its regulation in *Pseudomonas aeruginosa*. *International Journal of Molecular Sciences,* 14**,** 20983-21005.

WELCH, J. L. M., ROSSETTI, B. J., RIEKEN, C. W., DEWHIRST, F. E. & BORISY, G. G. 2016. Biogeography of a human oral microbiome at the micron scale. *Proceedings of the National Academy of Sciences of the United States of America,* 113**,** E791-E800.

WERNER, E., ROE, F., BUGNICOURT, A., FRANKLIN, M. J., HEYDORN, A., MOLIN, S., PITTS, B. & STEWART, P. S. 2004. Stratified growth in *Pseudomonas aeruginosa* biofilms. *Applied and Environmental Microbiology,* 70**,** 6188-6196.

WILTON, M., CHARRON-MAZENOD, L., MOORE, R. & LEWENZA, S. 2016. Extracellular DNA acidifies biofilms and induces aminoglycoside resistance in *Pseudomonas aeruginosa*. *Antimicrobial Agents and Chemotherapy,* 60**,** 544-553.

WOOD, T. K. 2016. Combatting bacterial persister cells. *Biotechnology and Bioengineering,* 113**,** 476-483.

WOOD, T. K., KNABEL, S. J. & KWAN, B. W. 2013. Bacterial persister cell formation and dormancy. *Applied and Environmental Microbiology,* 79**,** 7116-7121.

WORLITZSCH, D., TARRAN, R., ULRICH, M., SCHWAB, U., CEKICI, A., MEYER, K. C., BIRRER, P., BELLON, G., BERGER, J., WEISS, T., BOTZENHART, K., YANKASKAS, J. R., RANDELL, S., BOUCHER, R. C. & DORING, G. 2002. Effects of reduced mucus oxygen concentration in airway *Pseudomonas* infections of cystic fibrosis patients. *Journal of Clinical Investigation,* 109**,** 317-325.

WOZNIAK, D. J., WYCKOFF, T. J. O., STARKEY, M., KEYSER, R., AZADI, P., O'TOOLE, G. A. & PARSEK, M. R. 2003. Alginate is not a significant component of the extracellular polysaccharide matrix of PA14 and PAO1 *Pseudomonas aeruginosa* biofilms. *Proceedings of the National Academy of Sciences of the United States of America,* 100**,** 7907-7912.

WU, Y. L., KLAPPER, I. & STEWART, P. S. 2018. Hypoxia arising from concerted oxygen consumption by neutrophils and microorganisms in biofilms. *Pathogens and Disease,* 76**,** 1-10.

XIAO, J., HARA, A. T., KIM, D., ZERO, D. T., KOO, H. & HWANG, G. 2017. Biofilm three-dimensional architecture influences in situ pH distribution pattern on the human enamel surface. *International Journal of Oral Science,* 9**,** 74-79.

XIAO, J., KLEIN, M. I., FALSETTA, M. L., LU, B. W., DELAHUNTY, C. M., YATES, J. R., HEYDORN, A. & KOO, H. 2012. The exopolysaccharide matrix modulates the interaction between 3D architecture and virulence of a mixed-species oral biofilm. *PLOS Pathogens,* 8**,** 1-16.

XIAO, J. & KOO, H. 2010. Structural organization and dynamics of exopolysaccharide matrix and microcolonies formation by *Streptococcus mutans* in biofilms. *Journal of Applied Microbiology,* 108**,** 2103-2113.

XU, K. D., STEWART, P. S., XIA, F., HUANG, C. T. & MCFETERS, G. A. 1998. Spatial physiological heterogeneity in *Pseudomonas aeruginosa* biofilm is determined by oxygen availability. *Applied and Environmental Microbiology,* 64**,** 4035-4039.

YAMADA, T., TAKAHASHIABBE, S. & ABBE, K. 1985. Effects of oxygen on pyruvate formate-lyase *in situ* and sugar metabolism of *Streptococcus mutans* and *Streptococcus sanguis*. *Infection and Immunity,* 47**,** 129-134.

YATES, E. A., PHILIPP, B., BUCKLEY, C., ATKINSON, S., CHHABRA, S. R., SOCKETT, R. E., GOLDNER, M., DESSAUX, Y., CAMARA, M., SMITH, H. & WILLIAMS, P. 2002. N-acylhomoserine lactones undergo lactonolysis in a pH-, temperature-, and acyl chain length-dependent manner during growth of *Yersinia pseudotuberculosis* and *Pseudomonas aeruginosa*. *Infection and Immunity,* 70**,** 5635-5646.

YETERIAN, E., MARTIN, L. W., GUILLON, L., JOURNET, L., LAMONT, I. L. & SCHALK, I. J. 2010. Synthesis of the siderophore pyoverdine in *Pseudomonas aeruginosa* involves a periplasmic maturation. *Amino Acids,* 38**,** 1447-1459.

YOSHIDA, A. & KURAMITSU, H. K. 2002. Multiple *Streptococcus mutans* genes are involved in biofilm formation. *Applied and Environmental Microbiology,* 68**,** 6283-6291.

YU, S., WEI, Q., ZHAO, T. H., GUO, Y. & MA, L. Y. Z. 2016. A survival strategy for *Pseudomonas aeruginos*a that uses exopolysaccharides to sequester and store iron to stimulate Psl-dependent biofilm formation. *Applied and Environmental Microbiology,* 82**,** 6403-6413.

ZAPUN, A., CONTRERAS-MARTEL, C. & VERNET, T. 2008. Penicillin-binding proteins and beta-lactam resistance. *FEMS Microbiology Reviews,* 32**,** 361-385.
ZHAN, L. 2018. Rebalancing the caries microbiome dysbiosis: Targeted treatment and sugar alcohols. *Advances in Dental Research,* 29**,** 110-116.
ZHAN, L., FEATHERSTONE, J. D. B., GANSKY, S. A., HOOVER, C. I., FUJINO, T., BERKOWITZ, R. J. & DEN BESTEN, P. K. 2006. Antibacterial treatment needed for severe early childhood caries. *Journal of Public Health Dentistry,* 66**,** 174-179.
ZHANG, X. Q. & BISHOP, P. L. 2003. Biodegradability of biofilm extracellular polymeric substances. *Chemosphere,* 50**,** 63-69.
ZHANG, Z. S., NADEZHINA, E. & WILKINSON, K. J. 2011. Quantifying diffusion in a biofilm of *Streptococcus mutans*. *Antimicrobial Agents and Chemotherapy,* 55**,** 1075-1081.
ZHAO, X. L. & DRLICA, K. 2014. Reactive oxygen species and the bacterial response to lethal stress. *Current Opinion in Microbiology,* 21**,** 1-6.
ZHOU, C., WU, Y., THAPPETA, K. R. V., SUBRAMANIAN, J. T. L., PRANANTYO, D., KANG, E. T., DUAN, H. W., KLINE, K. & CHAN-PARK, M. B. 2017. *In vivo* anti-biofilm and anti-bacterial non-leachable coating thermally polymerized on cylindrical catheter. *ACS Applied Materials & Interfaces,* 9**,** 36269-36280.

10. Supplemental

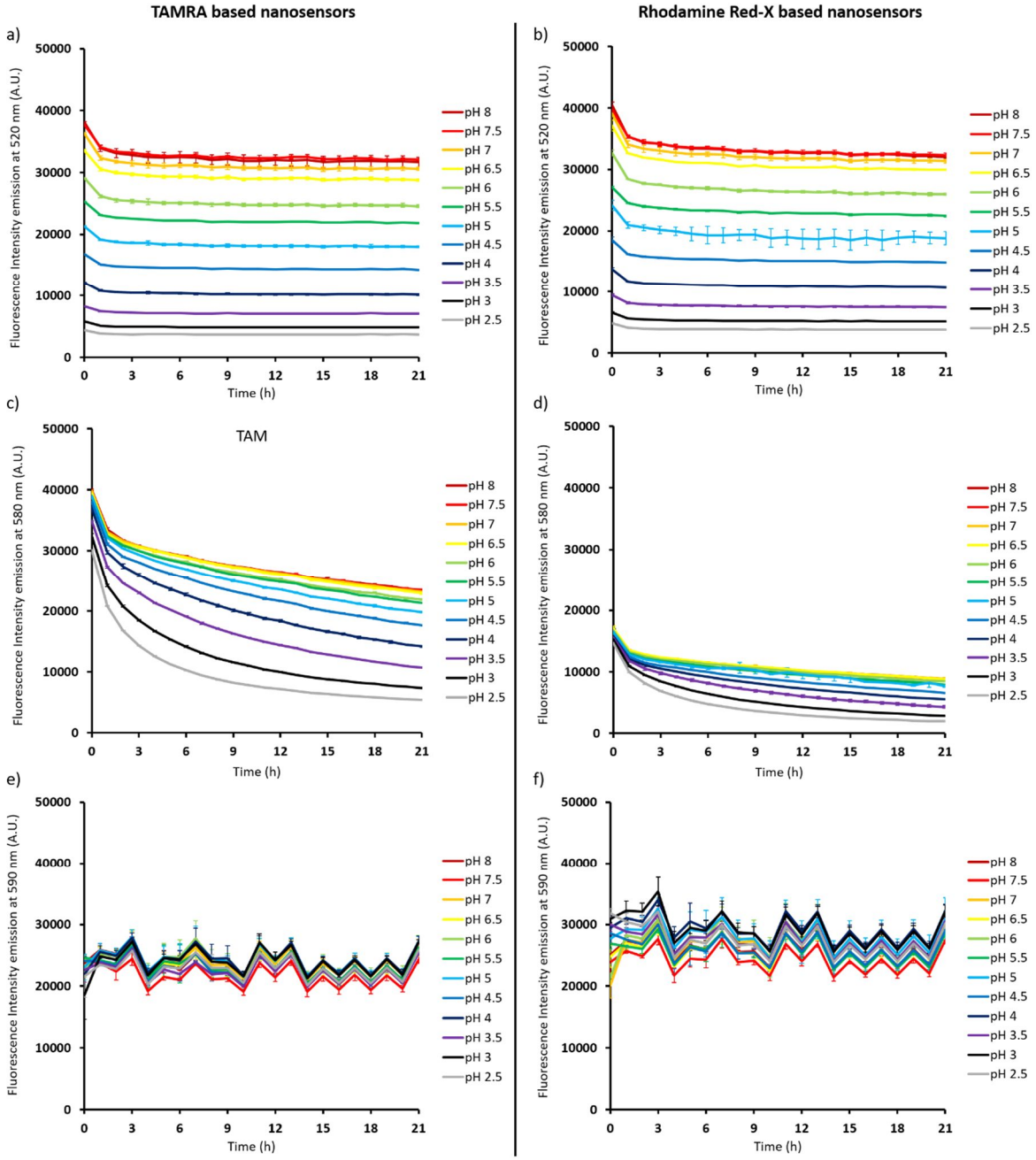

Supplemental Figure 10-1: Comparison between TAMRA-based and Rhodamine Red-X-based cationic polyacrylamide nanosensors shows reduced fluorescence intensity (photobleaching) over time (measured every hour) – 4 mg mL^{-1} cationic polyacrylamide nanosensors containing either TAMRA or Rhodamine Red- as a reference dye were suspended 1:10 PBS and diluted to a working concentration of 1 mg mL^{-1} in a range of pH buffers (2.5-8). Fluorescence intensity was measured every 1 h for 21 h at 37°C using: ex:488 nm, em:520 nm for **(a & b)**, ex:540 nm, em:580 nm for **(c & d)**, and ex:570 nm, em:590 nm for **(e & f)**. Error bars are ±1 S.D. n=1x3.

Click here to return to **5.2.5** or **5.3**

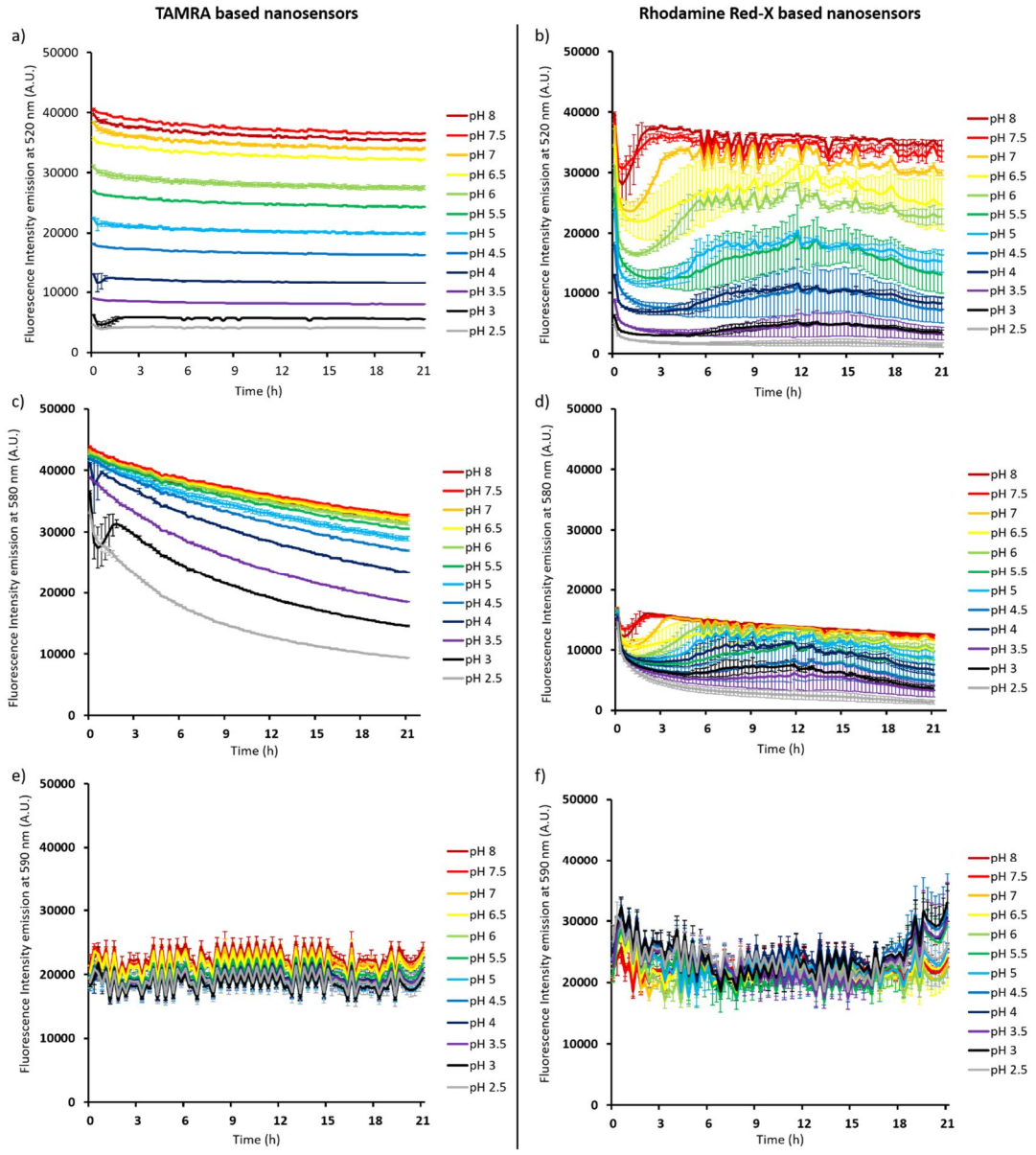

Supplemental Figure 10-2: Comparison between TAMRA-based and Rhodamine Red-X-based cationic polyacrylamide nanosensors shows reduced temperature (25°C) affects the fluorescence intensity of both OG, FAM, TAMRA and Rhodamine Red-X – 4 mg mL^{-1} cationic polyacrylamide nanosensors containing either TAMRA or Rhodamine Red- as a reference dye were suspended 1:10 PBS and diluted to a working concentration of 1 mg mL^{-1} in a range of pH buffers (2.5-8). Fluorescence intensity was measured every 15 min for 21 h at 25°C using: ex:488 nm, em:520 nm for **(a & b)**, ex:540 nm, em:580 nm for **(c & d)**, and ex:570 nm, em:590 nm for **(e & f)**. Error bars are ±1 S.D. n=1x3.

Click here to return to **5.2.5** or **5.3**

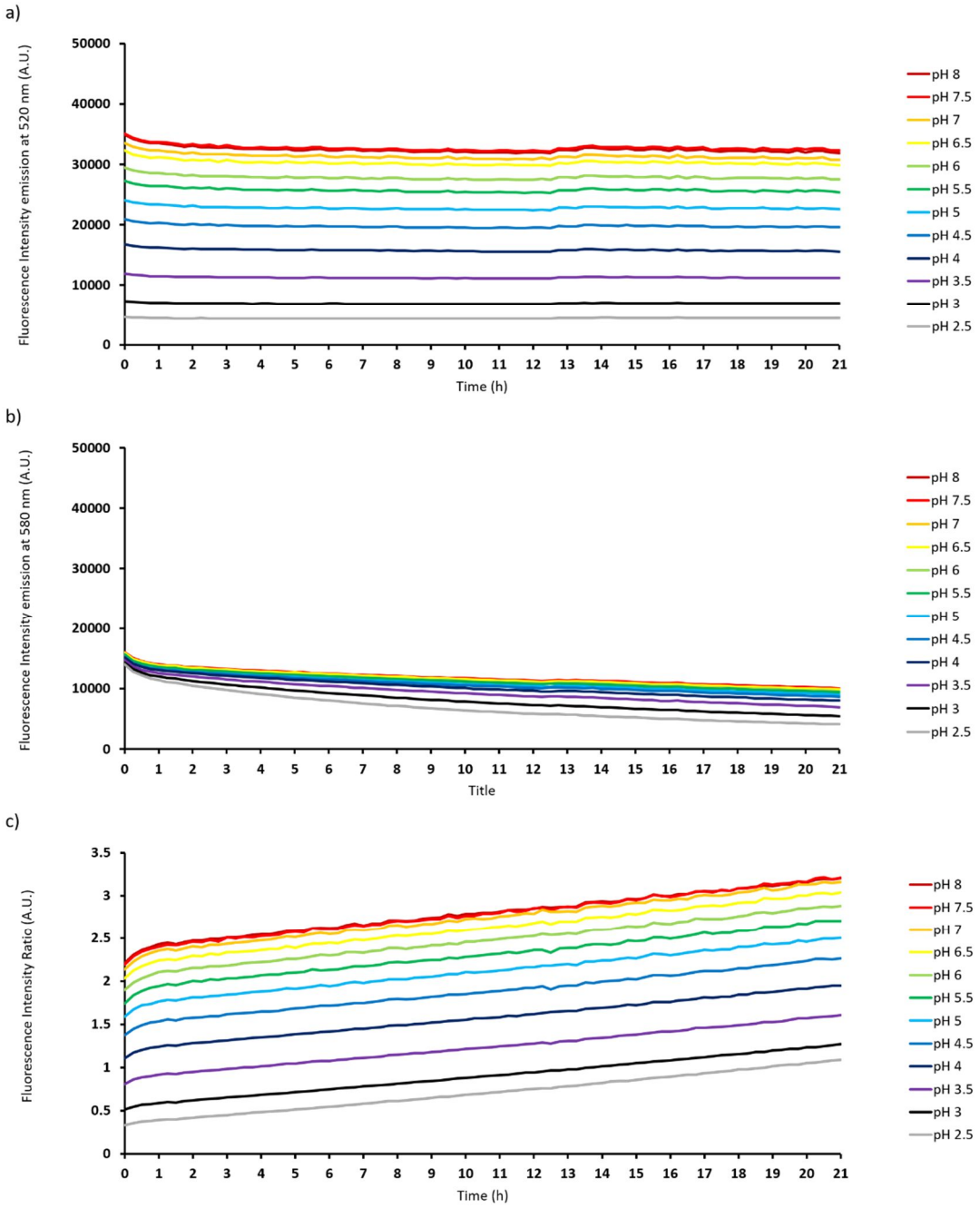

Supplemental Figure 10-3: Measuring fluorescence intensity of Rhodamine Red-X-based cationic polyacrylamide nanosensors for the calibration of fluorescence intensity readings from bacterial growth – 4 mg mL^{-1} cationic polyacrylamide nanosensors containing Rhodamine Red-X as a reference dye were suspended in M9 salts are diluted to a working concentration of 1 mg mL^{-1} in a range of pH buffers (2.5-8). Fluorescence intensity was measured every 15 min for 21 h at 37°C using: ex:488 nm, em:520 nm for **(a)** and ex:540 nm, em:580 nm for **(b)**. **(c)** Fluorescence intensity ratio calculated from the fluorescence intensity of **(a)** and **(b)**. Error bars are ±1 S.D. n=3x3.

Click here to return to **5.2.6** or **5.3**

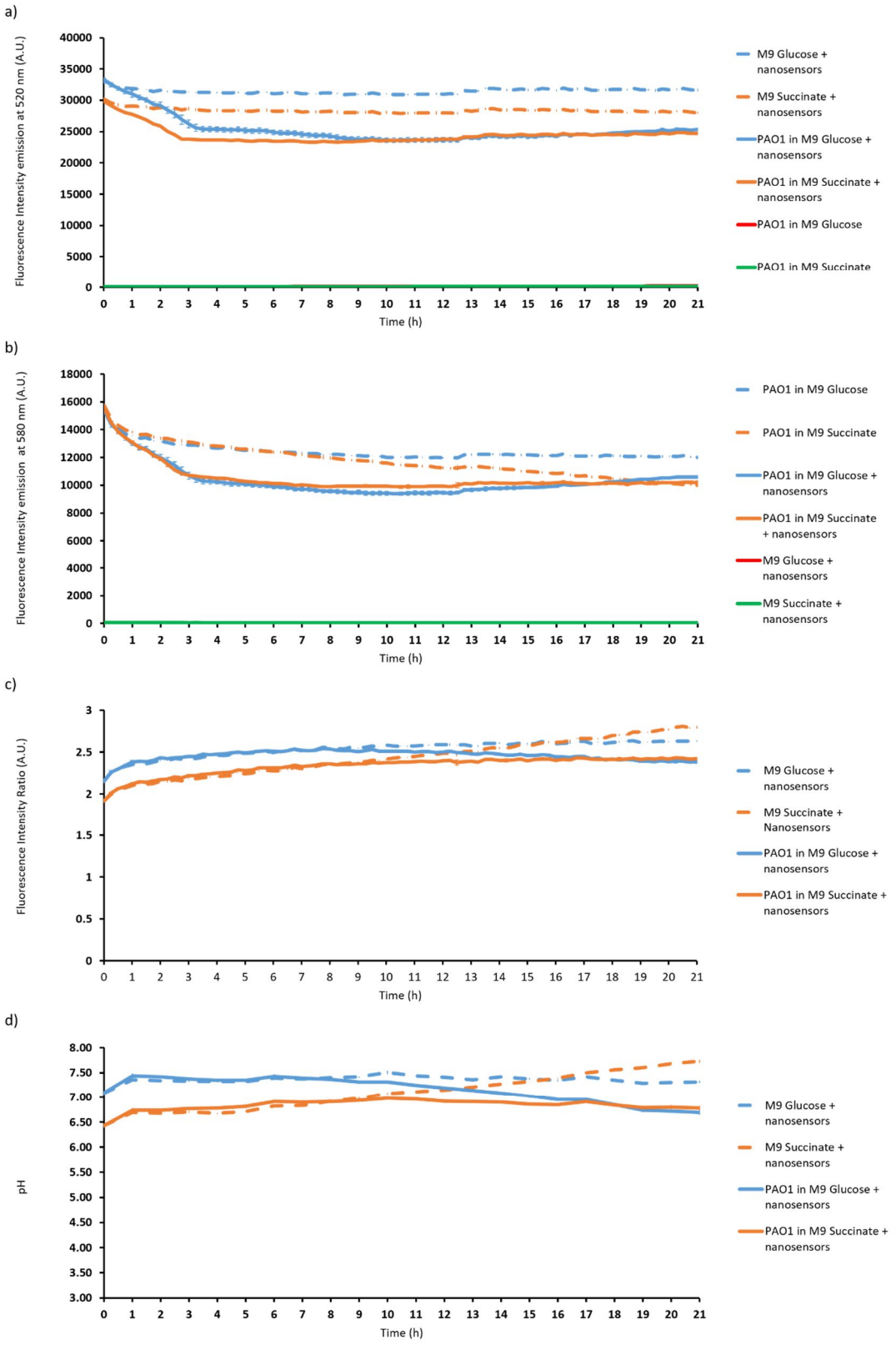

Supplemental Figure 10-4: Measuring fluorescence intensity of Rhodamine Red-X-based cationic polyacrylamide nanosensors incubated with PAO1-N WT – 4 mg mL^{-1} cationic polyacrylamide nanosensors containing Rhodamine Red-X as a reference dye were suspended in either M9 Glucose or M9 Succinate and diluted to a working concentration of 1 mg mL^{-1}. Nanosensors

were diluted in either PAO1-N WT at an OD of 0.05 (solid blue or orange) or M9 media alone (dashed blue or orange). PAO1-N WT was also measured in absence of nanosensors (red or green line). Fluorescence intensity was measured every 15 min for 21 h at 37°C using: ex:488 nm, em:520 nm for **(a)** and ex:540 nm, em:580 nm for **(b)**. **(c)** Fluorescence intensity ratio calculated from the fluorescence intensity of **(a)** and **(b)**. **(d)** pH calculated from fluorescence intensity ratio **(c)** and a 'rolling' linear regression from the fluorescence intensity ratio calculated in **Supplemental Figure 10-3**c. Error bars are ±1 S.D. n=3x3.

Click here to return to **5.2.6** or **5.3**

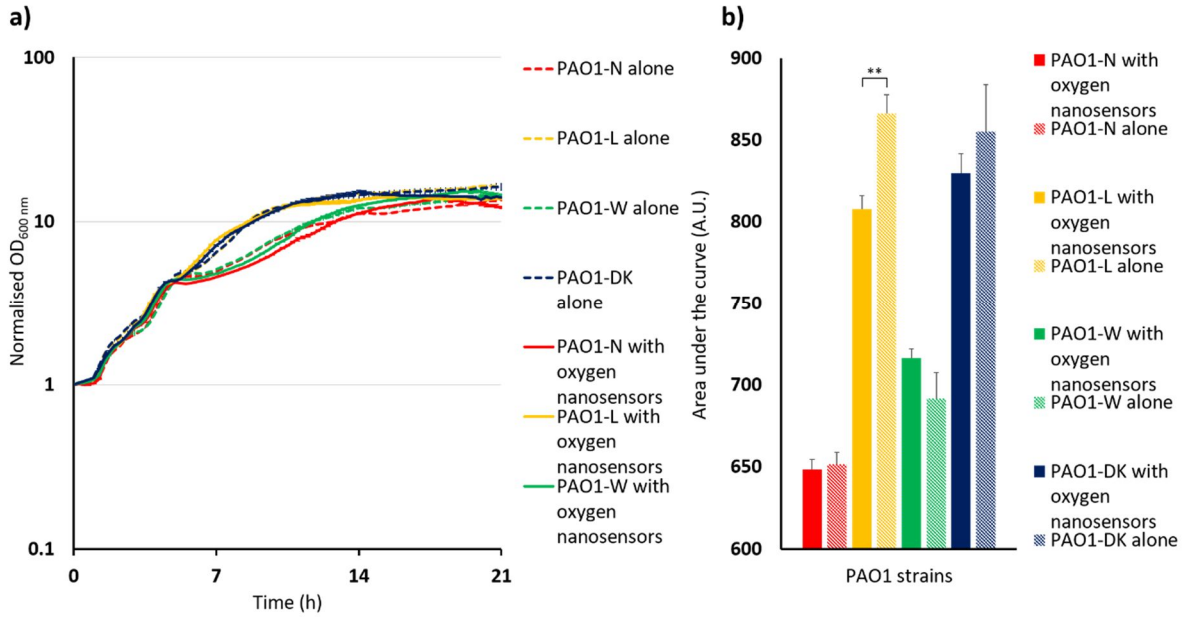

Supplemental Figure 10-5: Growth of PAO1 strains is uninhibited by oxygen nanosensors – PAO1 strains at OD_{600} of 0.05 were incubated in M9 succinate & 1% w/v casamino acids, with 1 mg mL^{-1} oxygen nanosensors as an additional condition. Absorbance at 600 nm was measured every 15 min. Error bars are ±1 S.D. n=2x3

Click here to return to **6.2.3** or **6.3**

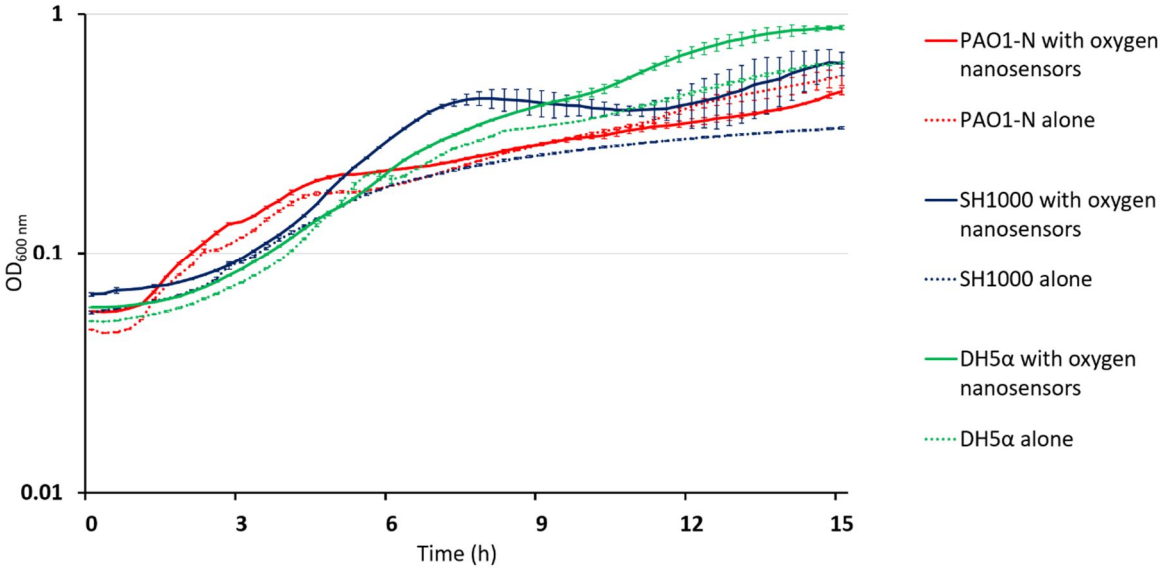

Supplemental Figure 10-6: Measuring growth for DH5α, SH1000 and PAO1-N grown in the presence and absence of oxygen nanosensors – Strains at OD_{600} of 0.05 were incubated in M9 glucose, with 1 mg mL^{-1} oxygen nanosensors as an additional condition. Absorbance at 600 nm was measured every 15 min. Error bars are ±1 S.D. n=2x3

Click here to return to **6.2.4**

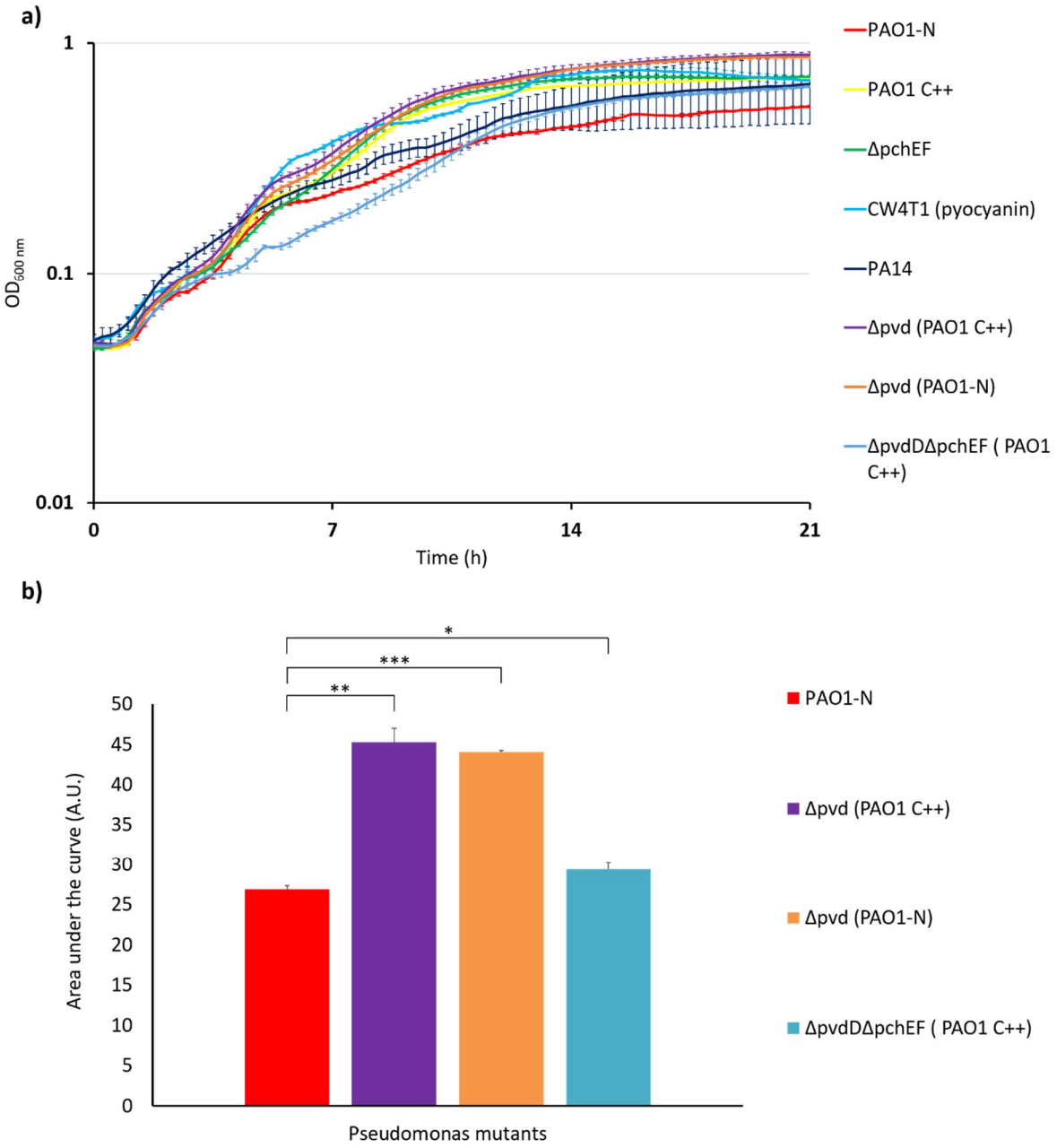

Supplemental Figure 10-7: Measuring the growth of *Pseudomonas aeruginosa* strains growth over 21 h - *P. aeruginosa* strains at OD_{600} of 0.05 were incubated in M9 succinate & casamino acids. Absorbance at 600 nm was measured every 15 min. **a)** OD of PAO1-N, PAO1 C++, PA14, CW4T1 (pyocyanin mutant), PAO1-NΔ*pchEF*, PAO1-NΔ*pvdD*, PAO1-C++Δ*pvdD* and PAO1-C++Δ*pvdD*Δ*pchEF* shows growth from all strains. **b)** Area under the curve of PAO1-N in comparison to PAO1-NΔ*pvdD*, PAO1-C++Δ*pvdD* and PAO1-C++Δ*pvdD*Δ*pchEF* shows significantly increased growth in the three mutants. ***=P<0.001, ** = P<0.005 & * = P<0.05. Error bars are ±1 S.D. n=2x3

Click here to return to **6.2.5**

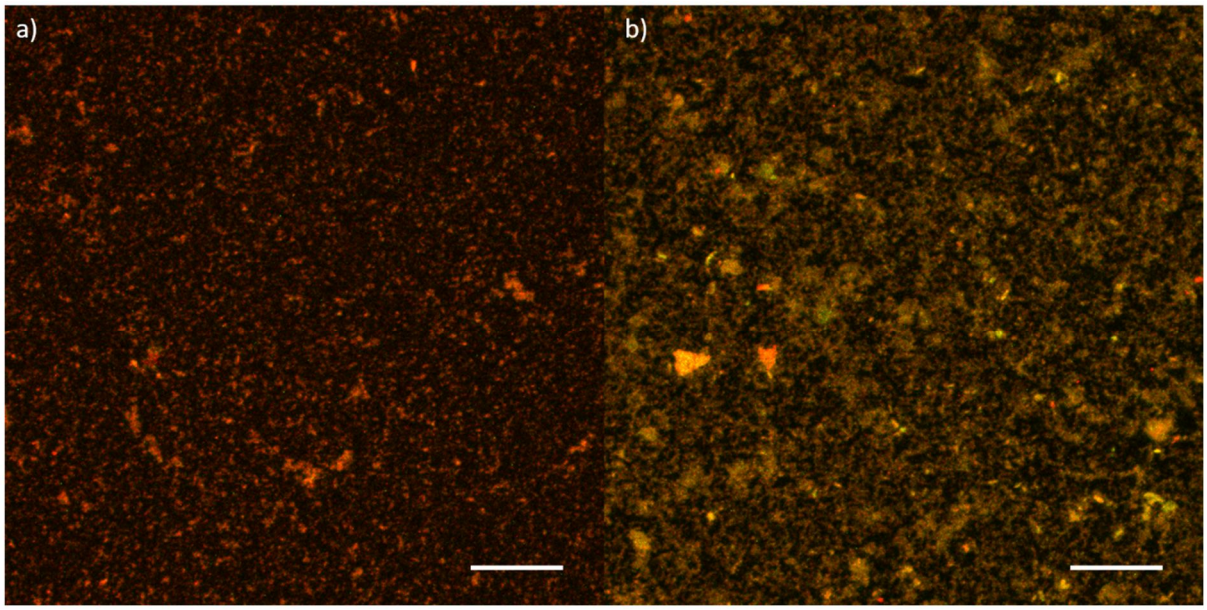

Supplemental Figure 10-8: Maximum Intensity Z-projections of (a) PAO1-N + 1 mg mL^{-1} oxygen nanosensors and (b) PAO1-NΔ*pvdD* + 1 mg mL^{-1} oxygen nanosensors shows increased nanosensor concentration and increased fluorescence intensity in PAO1-NΔ*pvdD* - Maximum intensity z-projections were produced in ImageJ using OG/FAM and TAMRA channels, removing slices where fluorescence intensity was absent. Each maximum intensity z-projection was used to calculate the average fluorescence intensity for OG/FAM and TAMRA (**Supplemental Table 10-1**) and a resultant fluorescence intensity ratio was calculated to determine an average fluorescence intensity ratio across the biofilm. **Scale bar 50 µm**.

Supplemental Table 10-1: Fluorescence Intensity emissions of OG, FAM & TAMRA, and the resultant fluorescence intensity ratio (FIR), calculated from the Maximum Intensity Z-projections of PAO1-N + 1 mg mL^{-1} oxygen nanosensors and PAO1-NΔ*pvdD* + 1 mg mL^{-1} oxygen nanosensors - Three ROIs were captured from each maximum intensity z-projection (**Supplemental Figure 10-8**) and the fluorescence intensity was measured for each ROI. The first P value represents a *t-test* between the OG/FAM measurements across the two conditions (green text) and the second P value is the corresponding TAMRA measurements across the two conditions (red text). The final P value represents a *t-test* between the two fluorescence intensity ratios calculated between the two conditions (black text).

		Fluorescence Intensity (A.U.)					
		ROI 1	ROI 2	ROI 3	Average	S.D. ±	P value
PAO1-N	OG/FAM	17.97	18.01	16.72	17.57	0.73	0.000383
	TAMRA	42.49	44.06	40.11	42.22	1.99	0.005363
	FIR	0.42	0.41	0.42	0.42	0.01	0.000298
PAO1-NΔ*pvdD*	OG/FAM	36.15	37.31	34.12	35.86	1.62	
	TAMRA	56.89	61.80	55.72	58.14	3.23	
	FIR	0.64	0.60	0.61	0.62	0.02	

Click here to return to **6.2.8**

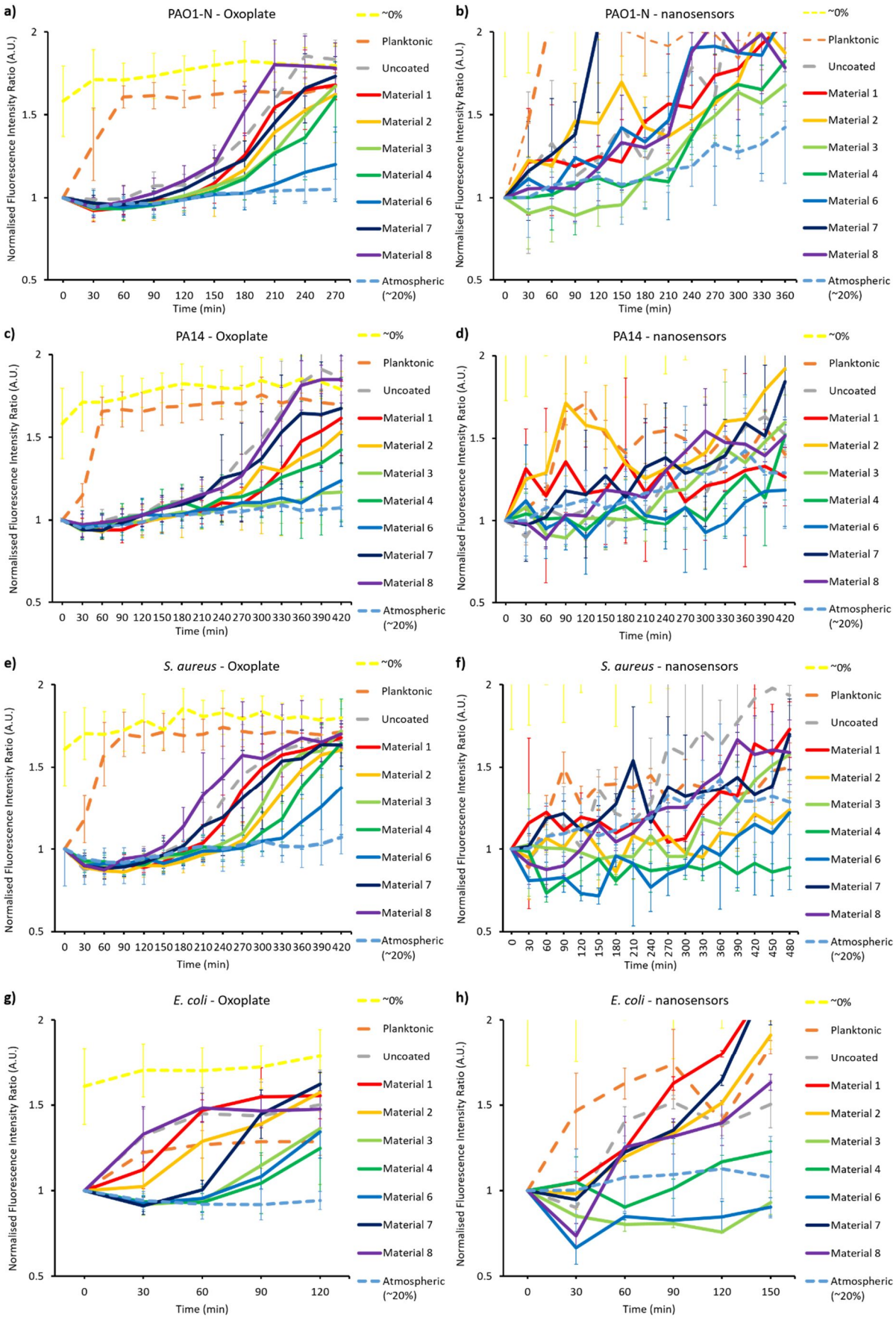
a)
PAO1-N - Oxoplate
b)
PAO1-N - nanosensors
c)
PA14 - Oxoplate
d)
PA14 - nanosensors
e)
S. aureus - Oxoplate
f)
S. aureus - nanosensors
g)
E. coli - Oxoplate
h)
E. coli - nanosensors
Normalised Fluorescence Intensity Ratio (A.U.)
Normalised Fluorescence Intensity Ratio (A.U.)
Normalised Fluorescence Intensity Ratio (A.U.)
Normalised Fluorescence Intensity Ratio (A.U.)
Normalised Fluorescence Intensity Ratio (A.U.)
Normalised Fluorescence Intensity Ratio (A.U.)
Normalised Fluorescence Intensity Ratio (A.U.)
Normalised Fluorescence Intensity Ratio (A.U.)
Time (min)
Time (min)
Time (min)
Time (min)
Time (min)
Time (min)
Time (min)
Time (min)
~0%
Planktonic
Uncoated
Material 1
Material 2
Material 3
Material 4
Material 6
Material 7
Material 8
Atmospheric (~20%)

Supplemental Figure 10-9: Measuring oxygen consumption with two methods to determine the effectiveness of anti-biofouling materials in preventing the attachment of different bacterial species (Rescaled) - Using a Calgary Biofilm Device (CBD) assay, peg-lids coated in a range of materials were incubated for 5 h in PAO1-N, PA14, *E.coli* strain ATCC 10536 or *S. aureus* strain ATCC 6538 culture. After incubation the peg-lids were transferred to either an OxoPlate with TSB media or oxygen nanosensors suspended in TSB. Fluorescence intensity at 540/590 nm and 540/650 nm (OxoPlate) or ex: 540, em:580 nm & ex:405 nm, em:650 nm was measured every 30 min for 20 h. The fluorescence intensity ratio (FIR) was plotted over time for each material until 'Uncoated' reached its plateau point. OxoPlate results are shown in **a)** (PAO1-N), **c)** (PA14), **e)** (*S. aureus*) & **g)** (*E. coli*) whilst oxygen nanosensor results are shown in **b)**, **d)**, **f)** & **h)**. Error bars are ±1 S.D. n=1x2

Click here to return to **6.2.9**

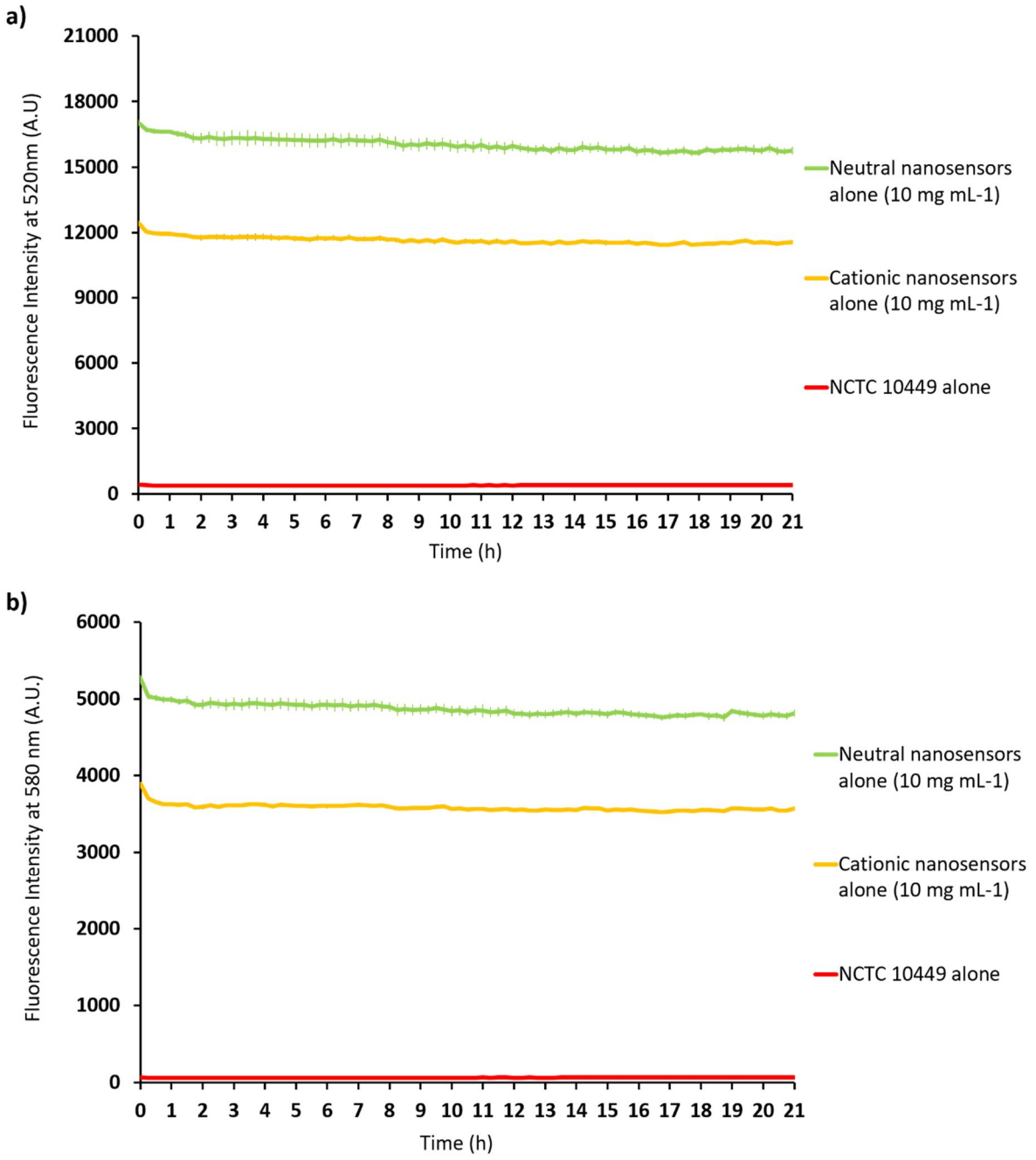

Supplemental Figure 10-10: *S. mutans* strain NCTC 10449 produces no auto-fluorescence – NCTC 10449 at OD_{600} of 0.05 was incubated in BHI media and nanosensors for 21 h. The fluorescence intensity (ex:488 nm, em:520 nm & ex:540 nm, 580 nm) was measured every 15 min. (**a**) Fluorescence intensity (520 nm) for NCTC 10449 alone and compared to neutral and cationic polyacrylamide nanosensors (10 mg mL^{-1}). (**b**) Fluorescence intensity (580 nm) for NCTC 10449 alone and compared to neutral and cationic polyacrylamide nanosensors (10 mg mL^{-1}). Error bars are ±1 S.D. n=2x3

Click here to return to **7.2.1**

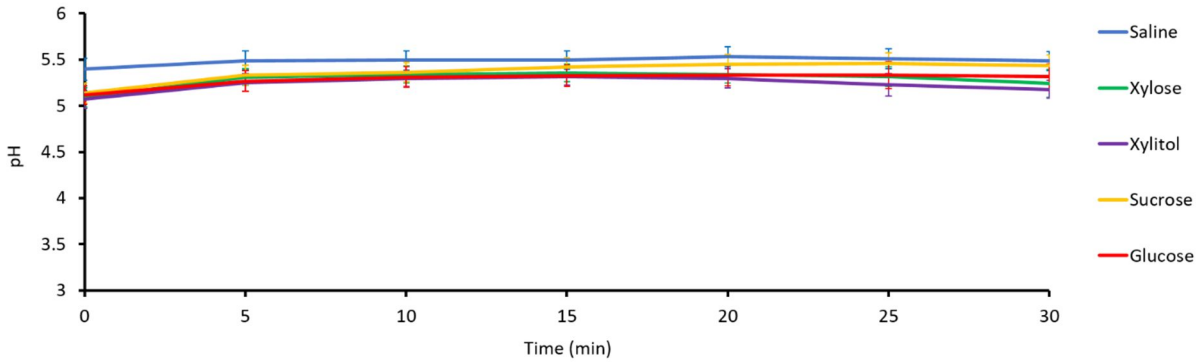

Supplemental Figure 10-11: No change to external pH was seen with addition of the carbohydrates to saline alone – Changes in fluorescence intensity were measured using fluorescent images of saline with 1 mg mL^{-1} cationic, pH-sensitive nanosensors. An initial image was taken at time point 0 min before either 1% w/v glucose, 1% w/v sucrose, 1% w/v xylose, 1% w/v xylitol or saline was added. Further images were then taken every 5 min for the remaining 30 min. All images were taken using a Nikon inverted fluorescence microscope. Error bars are ±1 S.D. n=3x2.

Click here to return to **7.2.2**

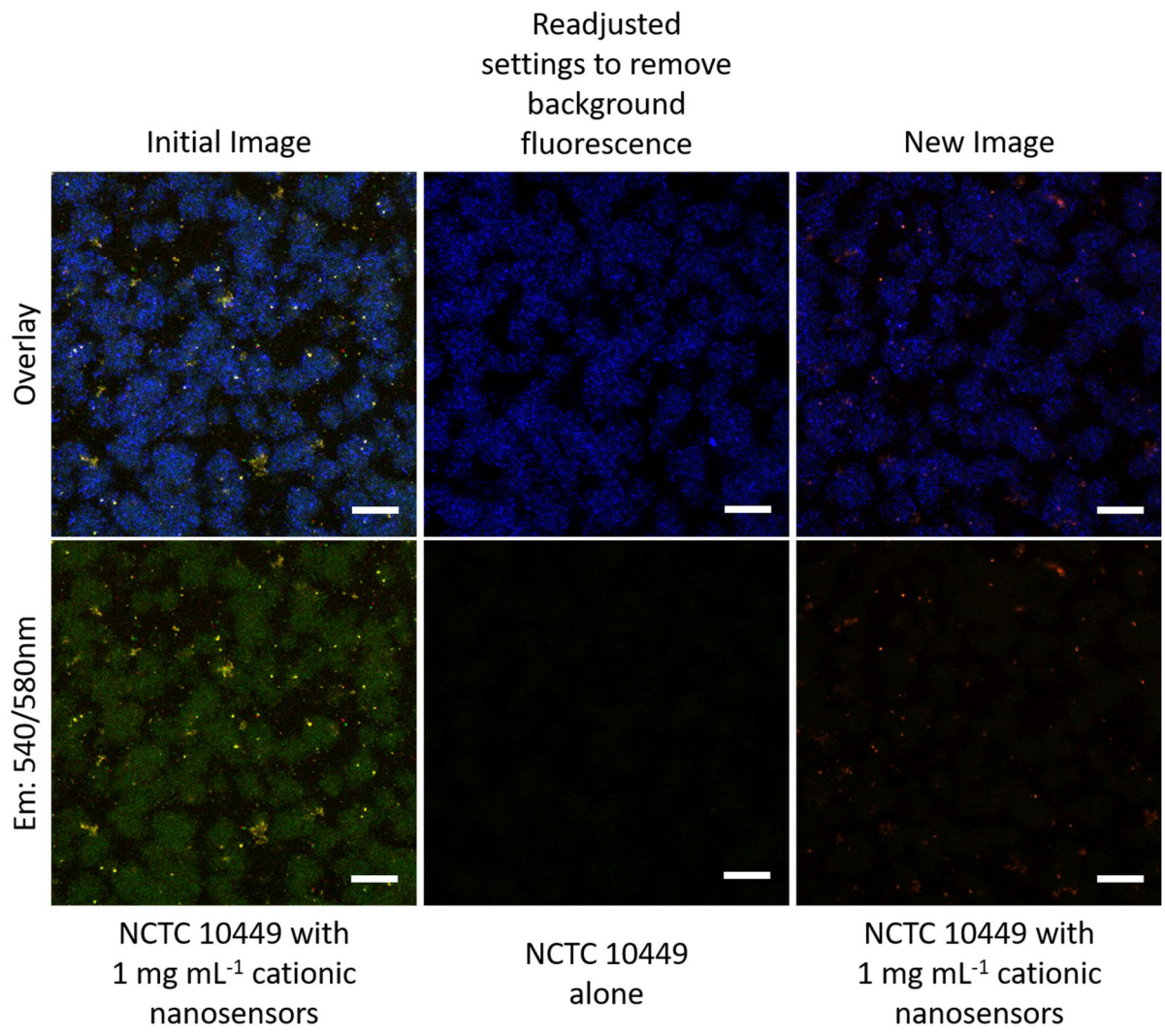

Supplemental Figure 10-12: *S. mutans strain* NCTC 10449 produces auto-fluorescence when grown in a biofilm – Representative images taken with a Zeiss confocal laser scanning microscope using a 40x/1.2na objective. NCTC 10449 was grown in BHI media with a 1% w/v sucrose supplement (**centre**) or with the addition of 1 mg mL^{-1} cationic polyacrylamide nanosensors (**left** & **right** panels) for 24 h at 37°C. After 24 h, the media was replaced with 50% BHI and re-incubated for 24 h at 37°C. (**Left**) A z-slice taken from an NCTC 10449 biofilm with 1 mg mL^{-1} cationic nanosensors; this image was taken with laser power 6.0 A.U. and gain settings 800 A.U. for both ex:488 nm, em:520 nm (OG/FAM) and ex:540 nm, em:580 nm (TAMRA). (**Centre**) A z-slice taken from an NCTC 10449 biofilm with no nanosensors; this image was taken with the TAMRA gain reduced to 700 A.U. and the OG/FAM gain reduced to 620 A.U. to remove background fluorescence. (**Right**) A z-slice taken from the same biofilm as the **left** panel; the image was taken with the same settings as the **centre** panel. **Scale bar 20 µm**. n=3x2

Click here to return to **7.2.3**